The building blocks of a quantum computer based on donor spins in silicon

Rachpon Kalra

A thesis in fulfilment of the requirements for the degree of
Doctor of Philosophy

UNSW
AUSTRALIA

School of Elec. Eng. and Telecom.
Faculty of Engineering

March 29, 2016

The University of New South Wales
Thesis/Dissertation Sheet

Surname: Kalra **First name:** Rachpon
Abbreviation for degree as given in University calendar: PhD
School: School of Elec. Eng. and Telecom. **Faculty:** Faculty of Engineering
Title: The building blocks of a quantum computer based on donor spins in silicon

Abstract 350 words maximum:

A computer with quantum mechanical building blocks, or qubits, promises a new class of computational capability and is a natural platform on which to simulate microscopic systems. Building a quantum computer, however, is a formidable challenge. The system chosen must be engineered to balance contradicting requirements. The fragile quantum states must be sufficiently protected from noise in the environment, while being accessible for accurate measurement and control. Moreover, the system must be scalable to millions of qubits that can be made to interact in complex sequences. Recent experimental breakthroughs have highlighted spin qubits in silicon as a promising platform. Firstly, fabrication of these semiconductor devices would capitalize on the expertise developed by the microelectronics industry. Secondly, and more fundamentally, silicon can provide a virtually noiseless environment for spin qubits while maintaining qubit addressability.

This thesis builds upon the foundational work on phosphorus donor electron spin qubits in silicon. We achieve dramatic improvements in the fundamental single qubit operations: the fidelities of readout, initialization and control of the electron spin are all enhanced to 99.9% simultaneously and we report a new record coherence time of 0.98 seconds. Furthermore, we provide novel theoretical proposals for the next steps in scaling this technology. We present a two-qubit operation that can be performed with fidelity exceeding 99%, robust to variability in donor positioning, and we devise a scheme for high-fidelity short-range qubit transport that may prove invaluable in the design of a quantum processor. The experimental setup required for scale-up is also addressed, as we report the first measurement of the silicon spin qubit device in a cryogen-free dilution refrigerator and present techniques to mitigate the noise induced by mechanical vibrations.

Our work has solved several crucial problems on the road-map towards a full-scale processor. It highlights the scalability and promise of this technology, which may result in the world's first quantum computer.

Declaration relating to disposition of project thesis/dissertation

I hereby grant to the University of New South Wales or its agents the right to archive and to make available my thesis or dissertation in whole or in part in the University libraries in all forms of media, now or here after known, subject to the provisions of the Copyright Act 1968. I retain all property rights, such as patent rights. I also retain the right to use in future works (such as articles or books) all or part of this thesis or dissertation.

I also authorise University Microfilms to use the 350 word abstract of my thesis in Dissertation Abstracts International (this is applicable to doctoral theses only).

....
Signature Witness Date: March 29, 2016

The University recognises that there may be exceptional circumstances requiring restrictions on copying or conditions on use. Requests for restriction for a period of up to 2 years must be made in writing. Requests for a longer period of restriction may be considered in exceptional circumstances and require the approval of the Dean of Graduate Research.

FOR OFFICE USE ONLY Date of completion of requirements for Award:

COPYRIGHT STATEMENT

'I hereby grant the University of New South Wales or its agents the right to archive and to make available my thesis or dissertation in whole or part in the University libraries in all forms of media, now or here after known, subject to the provisions of the Copyright Act 1968. I retain all proprietary rights, such as patent rights. I also retain the right to use in future works (such as articles or books) all or part of this thesis or dissertation.
I also authorise University Microfilms to use the 350 word abstract of my thesis in Dissertation Abstract International (this is applicable to doctoral theses only).
I have either used no substantial portions of copyright material in my thesis or I have obtained permission to use copyright material; where permission has not been granted I have applied/will apply for a partial restriction of the digital copy of my thesis or dissertation.'

Signed: .....
Date: March 29, 2016

AUTHENTICITY STATEMENT

'I certify that the Library deposit digital copy is a direct equivalent of the final officially approved version of my thesis. No emendation of content has occurred and if there are any minor variations in formatting, they are the result of the conversion to digital format.'

Signed: .....
Date: March 29, 2016

ORIGINALITY STATEMENT

'I hereby declare that this submission is my own work and to the best of my knowledge it contains no materials previously published or written by another person, or substantial proportions of material which have been accepted for the award of any other degree or diploma at UNSW or any other educational institution, except where due acknowledgement is made in the thesis. Any contribution made to the research by others, with whom I have worked at UNSW or elsewhere, is explicitly acknowledged in the thesis. I also declare that the intellectual content of this thesis is the product of my own work, except to the extent that assistance from others in the project's design and conception or in style, presentation and linguistic expression is acknowledged.'

Signed: .....
Date: March 29, 2016

Abstract

A computer with quantum mechanical building blocks, or qubits, promises a new class of computational capability and is a natural platform on which to simulate microscopic systems. Building a quantum computer, however, is a formidable challenge. The system chosen must be engineered to balance contradicting requirements. The fragile quantum states must be sufficiently protected from noise in the environment, while being accessible for accurate measurement and control. Moreover, the system must be scalable to millions of qubits that can be made to interact in complex sequences. Recent experimental breakthroughs have highlighted spin qubits in silicon as a promising platform. Firstly, fabrication of these semiconductor devices would capitalize on the expertise developed by the microelectronics industry. Secondly, and more fundamentally, silicon can provide a virtually noiseless environment for spin qubits while maintaining qubit addressability.

This thesis builds upon the foundational work on phosphorus donor electron spin qubits in silicon. We achieve dramatic improvements in the fundamental single qubit operations: the fidelities of readout, initialization and control of the electron spin are all enhanced to 99.9% simultaneously and we report a new record coherence time of 0.98 seconds. Furthermore, we provide novel theoretical proposals for the next steps in scaling this technology. We present a two-qubit operation that can be performed with fidelity exceeding 99%, robust to variability in donor positioning, and we devise a scheme for high-fidelity short-range qubit transport that may prove invaluable in the design of a quantum processor. The experimental setup required for scale-up is also addressed, as we report the first measurement of the silicon spin qubit device in a cryogen-free dilution refrigerator and present techniques to mitigate the noise induced by mechanical vibrations.

Our work has solved several crucial problems on the road-map towards a full-scale processor. It highlights the scalability and promise of this technology, which may result in the world's first quantum computer.

Acknowledgements

I write this the day after making the final corrections to my thesis. With great relief, I can now reflect on this journey they call a Ph.D. The past five years have challenged me in more ways than I anticipated. The experience has been greatly enriching and I have grown considerably. I know that I could not have done this alone. I am forever grateful to those who supported me, near and far.

To my supervisor. Andrea, I hope you know how much I appreciate everything you have done for me. The world knows you as the quantum spinmeister, the rockstar physicist. I know you as a caring leader, a mentor. Thank you for this character building experience. And for teaching me to write Hamiltonian of system. Thank you for lifting me, believing in me more than I did at times. It has been a privilege being your student for six and a half years.

To those on the ground with me. Arne. Thank you for teaching me the ropes, and for being patient during our countless discussions. You have been a great friend. Fahd. I will think of you whenever I see A3 paper. Thank you for being my travel partner through rotating and adiabatic frames. Juan. My big brother. Thank you for looking out for me and for being a role model. Kok Wai. This all started with you taking the time to teach me how to fabricate devices. Thank you for being my cleanroom mentor and friend. Sol. I have a feeling we are going to see great things from you, my friend. Gui, Juha, Stef and Jarryd, you have all been great friends and I have learned a lot from each one of you, thank you. Charles, thank you for taking the time to teach an engineer some theoretical physics. Dave and Rodrigo, the lab would not function without you, thank you. Fay, thank you for all your help and Andrew, thank you for your advice.

To my friends in Sydney. Thank you for the laughs and the opportunities to leave work aside. To my family. Papa, Pa, Didi, Jija, Pa Sandeep, Jeevna. Thank you for your constant love and support. I owe you everything. Mama, I miss you. Thank you for always being proud of me. To Raveena. Thank you for always being there for me, I could not have done this without you. I am truly grateful to have you in my life and I look forward to the rest of our lives together.

Publications

Patent

A. Morello, **R. Kalra**, and A. Laucht. 2013. Quantum Logic. International Patent Application PCT/AU2013/000886, filed August 2013. Patent Pending.

Peer reviewed journal articles

R. Kalra, A. Laucht, C. D. Hill, and A. Morello. "Robust two-qubit gates for donors in silicon controlled by hyperfine interactions." *Physical Review X* vol. 4 , no. 2, p. 021044, (2014).

J. T. Muhonen, J. P. Dehollain, A. Laucht, F. E. Hudson, **R. Kalra**, T. Sekiguchi, K. M. Itoh, D. N. Jamieson, J. C. McCallum, A. S. Dzurak, and A. Morello. "Storing quantum information for 30 seconds in a nanoelectronic device." *Nature Nanotechnology* vol. 9, no. 12, pp. 986-991, (2014).

J. T. Muhonen, A. Laucht, S. Simmons, J. P. Dehollain, **R. Kalra**, F. E. Hudson, S. Freer, K. M. Itoh, D. N. Jamieson, J. C. McCallum, A. S. Dzurak, and A. Morello. "Quantifying the quantum gate fidelity of single-atom spin qubits in silicon by randomized benchmarking." *Journal of Physics: Condensed Matter* vol. 27, no. 15, p. 154205, (2015).

J. P. Dehollain, S. Simmons, J. T. Muhonen, **R. Kalra**, A. Laucht, F. Hudson, K. Itoh, D. N. Jamieson, J. C. McCallum, A. S. Dzurak, and A. Morello. "Bell's inequality violation with spins in silicon." *Nature Nanotechnology* vol. 11, pp. 242-246, (2016).

A. Laucht, J. T. Muhonen, F. A. Mohiyaddin, **R. Kalra**, J. P. Dehollain, S. Freer, F. E. Hudson, M. Veldhorst, R. Rahman, G. Klimeck, K. M. Itoh, D. N. Jamieson, J. C. McCallum, A. S. Dzurak, and A. Morello. "Electrically controlling single-spin qubits in a continuous microwave field." *Science Advances* vol. 1, no. 3, p. 1500022, (2015).

A. Laucht, **R. Kalra**, J. T. Muhonen, J. P. Dehollain, F. A. Mohiyaddin, F. E. Hudson, J. C. McCallum, D. N. Jamieson, A. S. Dzurak and A. Morello. "High-fidelity adiabatic inversion of a ^{31}P electron spin qubit in natural silicon." *Applied Physics Letters* vol. 140, no. 9, p. 092115, (2014).

F. A. Mohiyaddin, R. Rahman, **R. Kalra**, G. Klimeck, L. C. L. Hollenberg, J. J. Pla, A. S. Dzurak, and A. Morello. "Noninvasive spatial metrology of single-atom devices." *Nano Letters* vol. 13, no. 5, pp. 1903-1909, (2013).

Articles submitted for publication

R. Kalra, A. Laucht, J. P. Dehollain, D. Bar, S. Freer, S. Simmons, J. T. Muhonen and A. Morello. "Vibration-induced electrical noise in a cryogen-free dilution refrigerator: characterization, mitigation, and impact on qubit coherence." *arXiv:1603.03146* (2016). Submitted to *Review of Scientific Instruments.*

F. A. Mohiyaddin, **R. Kalra**, A. Laucht, R. Rahman, G. Klimeck and A. Morello. "Transport of Spin Qubits with Donor Chains under Realistic Experimental Conditions." *arXiv:1602.07058* (2016). Submitted to *Physical Review B*.

A. Laucht, **R. Kalra**, S. Simmons, J. P. Dehollain, J. T. Muhonen, F. A. Mohiyaddin, S. Freer, F. E. Hudson, K. M. Itoh, D. N. Jamieson, J. C. McCallum, A. S. Dzurak and A. Morello. "A Dressed Spin Qubit in Silicon." *arXiv:1603.04800* (2016). Submitted to *Nature Nanotechnology*.

Journal articles in preparation

R. Kalra, S. Simmons, E. Petersen, J. T. Muhonen, A. Laucht, J. P. Dehollain, S. Freer, F. E. Hudson, K. M. Itoh, D. N. Jamieson, J. C. McCallum, A. S. Dzurak, S. A. Lyon and A. Morello. "Isotropic Dynamical Decoupling Sequences for a Single Electron Spin Qubit." *in preparation*

S. Freer, S. Simmons, A. Laucht, J. T. Muhonen, J. P. Dehollain, **R. Kalra**, F. A. Mohiyaddin, F. Hudson, K. Itoh, J. C. McCallum, D. N. Jamieson, A. S. Dzurak, and A. Morello. "Quantum memory in a single nucleus in silicon." *in preparation*

Conference Presentations

R. Kalra, A. Laucht, K. W. Chan, J. J. Pla, F. E. Hudson, J. C. McCallum, D. N. Jamieson, A. S. Dzurak, and A. Morello. "Ion-implanted 2-P-atom devices for spin-qubit coupling." Presented at:
- 2012 Quantum Computing Program Review. Denver, CO, USA (Poster)
- 2012 Australian Institute of Physics Congress. Sydney, Australia (Poster)

R. Kalra, A. Laucht, C. D. Hill, and A. Morello. "Robust two-qubit gates for donors in silicon controlled by hyperfine interactions." Presented at:
- 2013 S3NANO Winter School. Windsor, UK (Poster)
- 2013 Silicon Quantum Electronics Workshop. Villard de Lans, France (Poster)
- 2013 Centre for Quantum Computation and Communication Workshop. Sunshine Coast, Australia (Oral)
- 2014 IEEE Technologies of the Future Poster Competition. Sydney, Australia (Poster)
- 2014 UNSW Faculty of Engineering Dean's Award for Research Excellence Poster Competition. Sydney, Australia (Poster)

R. Kalra, F. A. Mohiyaddin, A. Laucht, R. Rahman, G. Klimeck and A. Morello."Transport of Spin Qubits with Donor Chains under Realistic Experimental Conditions." Presented at:
- 2014 Quantum Computing Program Review. Arlington, VA, USA (Poster)
- 2014 Silicon Quantum Electronics Workshop. Albuquerque, NM, USA (Poster)

R. Kalra, S. Simmons, E. Petersen, J. T. Muhonen, A. Laucht, J. P. Dehollain, S. Freer, F. E. Hudson, K. M. Itoh, D. N. Jamieson, J. C. McCallum, A. S. Dzurak, S. A. Lyon and A. Morello. "Isotropic Dynamical Decoupling Sequences for a Single Electron Spin Qubit." Presented at:
- 2015 American Physical Society March Meeting, San Antonio, TX, USA (Oral)
- 2015 Centre for Quantum Computation and Communication Workshop. Kingscliff, Australia (Poster)

Awards

Best poster of research theme and overall runner up at 2014 UNSW Faculty of Engineering Dean's Award for Research Excellence Poster Competition. Research theme: "Digital Services."

Winner at 2014 IEEE Technologies of the Future Poster Competition. Category: "Physical Modeling & Simulations."

Research Highlights

Pairing up single atoms in silicon for quantum computing, Article on Phys.org, June 16, 2014.

Abbreviations

2D	2-dimensional
2DEG	2-dimensional electron gas
AC	Alternating current
ADC	Analog-to-digital converter
Al	Aluminium
ANFF	Australian National Fabrication Facility
ARB	Arbitrary waveform generator
AWG	American wire gauge
CDD	Concatenated dynamical decoupling
CN	Cupronickel
CP	Carr Purcell
CPMG	Carr Purcell Meiboom Gill
CQC2T	Centre for Quantum Computation & Communication Technology
DC	Direct current
DD	Dynamical decoupling
DOS	Density of states
EBL	Electron beam lithography
ESEEM	Electron spin echo envelope modulation
ESR	Electron spin resonance
FEP	Fluorinated ethylene propylene
FET	Field effect transistor
FWHM	Full width at half maximum

MOS	Metal-oxide-semiconductor
MW	Microwave
NMR	Nuclear magnetic resonance
P	Phosphorus
PCB	Printed circuit board
PIRS	Pulse induced resonance shift
PMMA	Polymethyl methacrylate)
QND	Quantum non-demolition
RMS	Root mean square
RF	Radio frequency
SEM	Scanning electron microscope
SET	Single electron transistor
Si	Silicon
SIM	Small instrumentation module
SiO_2	Silicon dioxide
SMA	Sub-Miniature version A
SRS	Stanford Research Systems
SS	Stainless steel
STM	Scanning tunneling microscope
UNSW	University of New South Wales
UV	Ultraviolet

Contents

Abstract . . . vii
Acknowledgements . . . ix
Publications . . . xi
Abbreviations . . . xv

1 An introduction to quantum computing with donor spins in silicon 7
1.1 Quantum computing . . . 8
1.2 Background knowledge . . . 10
1.2.1 The electron spin qubit . . . 10
1.2.2 The ^{31}P:Si quantum computer . . . 13
1.3 Breakthroughs towards a ^{31}P:Si spin-based quantum computer . . . 16
1.3.1 Single-shot electron spin readout . . . 16
1.3.2 Electron and nuclear spin control . . . 16
1.4 Scope of this Thesis . . . 17
1.4.1 Thesis Outline . . . 18

2 Device fabrication and experimental methods 21
2.1 Device fabrication and packaging . . . 22
2.1.1 Silicon wafer preparation . . . 22
2.1.2 Electron beam lithography . . . 23
2.1.3 Donor implantation . . . 24
2.1.4 Final processing steps . . . 25
2.2 Experimental setup . . . 26
2.2.1 Cables and filtering . . . 26
2.2.2 Instrumentation . . . 28
2.3 Summary . . . 29

3 Improving the fundamental single qubit operations on the electron spin 31
3.1 Qubit control . . . 32
3.2 State preservation and coherence times . . . 34
3.3 Readout . . . 38
3.4 Initialization . . . 40
3.5 Summary and Outlook . . . 44

4 Isotropic dynamical decoupling **45**
4.1 Bulk magnetic resonance experiments . . . 46
4.2 The debate about the validity of CPMG . . . 48
4.3 Our system: single spin approximation . . . 49
4.4 Single spin simulations . . . 50
4.5 Strategy: isotropic dynamical decoupling . . . 53
4.5.1 Sequences vs N (Simulations) . . . 54
4.6 Sequence robustness assessment (Simulations) . . . 56
4.7 Experimental results . . . 59
4.8 Sequence variations . . . 61
4.9 Pulse induced resonance shift . . . 62
4.10 Summary and Outlook . . . 67

5 Robust two-qubit gates controlled by hyperfine interactions **69**
5.1 Proposed system and theoretical representation . . . 71
5.2 Hyperfine-regulated SWAP gates . . . 72
5.3 CROT gates . . . 75
5.4 System calibration from the ESR spectrum . . . 80
5.5 Summary and Outlook . . . 83

6 Transport of spin qubits with donor chains under realistic experimental conditions **85**
6.1 Construction of a donor chain . . . 87
6.1.1 Nuclear spins . . . 89
6.1.2 Source and target donor qubits . . . 90
6.2 Calibration of the system . . . 91
6.2.1 Calibration of the donor chain in the bulk-like mode . . . 94
6.3 Spin transport . . . 96
6.3.1 Singlet initialization for adiabatic transport . . . 98
6.4 Adiabatic transport under realistic experimental conditions . . . 101
6.4.1 Errors in $J_{\max}$ and T_{AP} . . . 102
6.4.2 The effect of ΔB_z . . . 105
6.4.3 Limited tunability of exchange couplings . . . 105
6.4.4 Noise on the qubit energy splittings ϵ_i . . . 108
6.4.5 Noise in the qubit-chain couplings J_s and J_t . . . 110
6.5 Summary and Outlook . . . 111

7 Vibration-induced electrical noise in a cryogen-free dilution refrigerator **113**
7.1 Measurement setup . . . 114
7.2 Pulse tube noise . . . 116
7.3 Cable comparison . . . 120

7.4 Effect of noise on qubit coherence 126
7.5 Summary and Outlook 129

8 Conclusion **131**
8.1 Summary of achievements 132
8.2 Chapter 3 - Improving single qubit operations 132
8.3 Chapter 4 - Isotropic dynamical decoupling 132
8.4 Chapter 5 - Two-qubit gate proposal 133
8.5 Chapter 6 - Spin transport under realistic experimental conditions 133
8.6 Chapter 7 - Noise in a cryogen-free dilution refrigerator 134
8.7 Future work and Outlook 134

References **136**

List of Figures

1.1 Spin qubit represented on the Bloch sphere. 11
1.2 Donor-based quantum computer. 15

2.1 Layout of the features patterned during the stock preparation stage. 23
2.2 Drawing of the alignment markers used for electron beam lithography. 24
2.3 Device images. 25
2.4 Pictures of the DC and AC filter boxes and the device enclosure. 27
2.5 Schematic of the instrumentation setup. 28

3.1 π-rotation about the y-axis in the absence and presence of noise. 32
3.2 Linewidths and qubit control fidelity. 33
3.3 Frequency spectrum of the noise seen by the qubit. 35
3.4 Limiting coherences as a function of plunge level. 36
3.5 Electron spin coherence time approaching 1 second. 37
3.6 Electron readout and initialization errors due to thermal effects. 39
3.7 Steered initialization of the electron spin. 43

4.1 Simulations of CPMG with the noise spectrum from the experiment. 51
4.2 Experimental results of CPMG with fixed offsets in the rotation angle. 53
4.3 Simulations of dynamical decoupling with the noise spectrum from the experiment. 55
4.4 Effects of offsets in rotation angle and detuning. 57
4.5 Sequence robustness to offsets in detuning. 58
4.6 Echo traces obtained from the XY family of dynamical decoupling sequences. . . 60
4.7 BB1 pulses and concatenated XY. 62
4.8 Pulse induced resonance shift. 64
4.9 The $A_{\mathrm{PIRS}}\tau_{\mathrm{PIRS}}$ product. 65
4.10 PIRS sequence comparison. 66
4.11 Overlay of PIRS simulations with traces from the experiment. 67

5.1 Hyperfine-regulated SWAP gate. 74
5.2 Conditional-rotation gate. 78
5.3 ESR fingerprint for system calibration. 81

6.1 Schematic of a spin chain. 87
6.2 The yield of functioning chains given donor placement errors. 88
6.3 Schematic of the system used for transport. 92
6.4 The ESR spectra for calibration in the interface mode. 93
6.5 The ESR spectra for calibration in the bulk-like mode. 95
6.6 Overview of the adiabatic transport protocol. 97
6.7 Initialization of the near-singlet state. 98
6.8 State precession in the adiabatic frame. 101
6.9 Adiabatic transport fidelity. 102
6.10 The effect of ΔB_z and $J_{\min}$ on transport fidelity. 106
6.11 The effect of noise on transport fidelity. 109
6.12 Spin chains in a surface-code compatible architecture. 112

7.1 Schematic of the cryogen-free dilution refrigerator measurement setup. 115
7.2 Electrical noise induced by vibrations from the pulse tube. 117
7.3 Spectrogram of the noise signal. 118
7.4 Temperature dependence of the noise magnitude. 119
7.5 Comparison of the noise induced in four types of semi-rigid cables. 122
7.6 Comparison of the noise induced in four types of flexible cables. 123
7.7 Comparison of the frequency response of the eight cables tested. 125
7.8 Coherence measurements of the electron spin qubit in different dilution refrigerator setups. 127

Chapter 1

An introduction to quantum computing with donor spins in silicon

---

"... and by golly it's a wonderful problem, because it doesn't look so easy."

–Richard P. Feynman

The fundamental building block of the digital revolution is the transistor, the hardware responsible for representing a single bit of binary information. All computer processing is essentially a series of logic operations performed with these transistors, where the bit is the voltage at the gate of the transistor. The driving force behind the progress made since the transistor was first invented in 1947 has been the ability of the microelectronics industry to shrink its size and therefore fit more onto a single chip. In fact, the number of transistors in a dense integrated circuit has been doubling every two years since the 1960s. This rate of progress is known as Moore's law, named after Gordon E. Moore, the co-founder of Intel. The smallest feature size in the transistors in commercially available chips today is 14 nm. However, Moore's law cannot continue forever [1]. Quantum mechanical phenomena will inhibit the standard function of transistors as they approach the length-scales of their constituent atoms.

The focus of this thesis is the fundamental building block of what may lead to a new revolution, the quantum computer. The idea of a computational device that exploits the laws of quantum mechanics was first explored over three decades ago. In 1982, Richard P. Feynman explained how simulations of quantum physics could be naturally performed on a computer with quantum mechanical building blocks [2]. In 1985, David Deutsch discussed how such a machine allows for general purpose quantum computation [3]. Serious interest in working towards building a quantum computer began in the mid-1990s, when Peter Shor presented two important results. The first was an algorithm for a quantum computer to factorize large numbers in polynomial time [4], which has major implications on modern data encryption. The second was a scheme for quantum error correction, which shows that a certain level of error can be tolerated and corrected for in a processor [5]. This was a key result as quantum systems are extremely susceptible to noise.

In Section 1.1, we outline the requirements for building such a machine, and briefly address progress made by researchers around the world. Section 1.2 describes key concepts relevant to the focus of this thesis: donor spin qubits in silicon. Finally, Section 1.3 presents the recent achievements made in silicon quantum computing here at UNSW, prior to the start of this thesis. These advancements are the foundation for the work presented here.

1.1 Quantum computing

In the same way that a classical computer processes bits, a quantum computer processes quantum bits, or qubits. A qubit is a quantum mechanical two-level system, which can be embodied through many physical implementations. Indeed, spin qubits in silicon represent only one of many platforms currently being investigated for their potential to scale to a full quantum processor. At its core, the platform must satisfy 5 basic requirements as outlined by David DiVincenzo [6].

Requirements for a Quantum Computer [6]

1. The qubit is the first requirement. A well-defined quantum mechanical system must be chosen and the number of qubits in the computer must be precisely known, i.e. not a statistical quantity.

2. One must have the ability to initialize the qubit into a known state with high fidelity. Fidelity is defined as the probability that the resulting quantum state following an operation (such as initialization) matches the desired quantum state.

3. Fluctuations in the environment can alter the state of fragile quantum systems, resulting in a loss of state coherence that builds over time. The qubit must be therefore be sufficiently isolated from the noisy environment such that an algorithm can be performed before coherence is lost.

4. One must be able to perform "a controlled sequence of unitary transformations" [6] which make up the quantum algorithm. These include operations on the single qubit as well as operations that induce entanglement between two qubits.

5. High fidelity measurement, or readout, of the state of each qubit is necessary to learn the result of the algorithm.

Physical Platforms

A qubit can be defined in many physical systems. Here, we briefly address the progress made in the most popular platforms being investigated for quantum computing. One such implementation uses photons with the goal of building an all-optical quantum computer, where the polarization of a single photon defines the qubit [7]. Photonic qubits have the advantage that they are largely free from decoherence, but a great challenge remains in creating high-efficiency single-photon sources. Most experimental demonstrations have been performed using macroscopic optical elements, while a full-scale quantum processor will require the shift towards microscopic optical waveguide circuits [8].

Another example of a qubit relatively free of environmental noise is the orbital state or spin of a laser-cooled ion in an electromagnetic trap in vacuum. To date, this system has achieved the largest processors, demonstrating entanglement between 14 qubits [9] and implementing Shor's algorithm to factorize the number '15' [10]. However, scaling this system requires substantial engineering development beyond the current state-of-the-art. In this aspect, solid-state qubits have an advantage.

There are two categories of solid-state qubits that hold considerable promise for a full-scale processor in which significant progress has already been made: superconducting qubits and spin qubits. Between the two, superconducting qubits are ahead in the race. The qubit can be encoded onto a superconducting circuit in several ways. They have the advantage that they are fabricated on-chip and can be coupled via superconducting resonators [11]. Recent

achievements show the implementation of elements of Kitaev's surface code, an important step towards realizing a fault-tolerant system [12–14]. Perhaps the key challenge that remains is the experimental demonstration of a scalable architecture that allows for efficient quantum error correction [15].

Spin qubits in the solid-state, while currently behind their superconducting counterparts, are particularly promising for their long coherence times. The spins of electrons have been used to form qubits in several ways, including the singlet-triplet qubit [16], the double-dot hybrid qubit [17] and the exchange-only qubit [18]. The qubit at the center of this thesis is the bare spin of an electron.

1.2 Background knowledge

The focus of this thesis is the electron spin qubit confined to a donor in silicon as the building block for a quantum computer. This section is thus divided into two sub-sections, introducing (i) the bare spin qubit and (ii) an architecture for a processor based on donor spins in silicon.

1.2.1 The electron spin qubit

The experiment carried out by Otto Stern and Walther Gerlach in 1922 [19] was the first observation of spin. The trajectory of a beam of silver atoms through an inhomogeneous magnetic field revealed an intrinsic angular momentum in the atoms. Furthermore, the deflection observed showed that the magnetic moment is quantized into two values, $\pm\hbar/2$.

Mathematical representation

While the spins of atomic nuclei vary, the electron has a spin of 1/2 (i.e. the magnetic moment is $\pm\hbar/2$). The eigenstates of the electron spin in a magnetic field $\mathbf{B}_0$ are $|\downarrow\rangle$ and $|\uparrow\rangle$, corresponding to the spin being aligned or anti-aligned with $\mathbf{B}_0$, respectively. Their eigenenergies are determined by the Zeeman energy, $-\hbar\gamma_e|\mathbf{B}_0|$ and $+\hbar\gamma_e|\mathbf{B}_0|$, respectively, where $\gamma_e/2\pi = 28$ GHz/T is the gyromagnetic ratio of the electron. The Hamiltonian, H_0, can be represented in terms of the spin operators, $\mathbf{S}$, which are related to the Pauli operators by $\mathbf{S} = (\hbar/2)\boldsymbol{\sigma}$.

$$H_0 = \gamma_e\left(\mathbf{B}_0 \cdot \mathbf{S}\right) = \gamma_e B_0 S_z = \frac{\hbar\gamma_e B_0}{2}\begin{pmatrix} 1 & 0 \\ 0 & -1 \end{pmatrix} \tag{1.1}$$

where S_z is the spin operator in the direction of the magnetic field and $B_0 = |\mathbf{B}_0|$. The Hamiltonian represents the total energy of the system, and is thus expressed in units of energy. However, parts of this thesis will define Hamiltonians in units of angular frequency (by setting $\hbar = 1$) or in units of frequency (by setting $\hbar = 1/2\pi$). The units used will be stated explicitly.

It is useful to represent the spin state on the Bloch sphere, which allows both superposition and the evolution of the state due to the given Hamiltonian to be visualized. Figure 1.1(a) shows the Bloch sphere representation of the Hamiltonian in Equation 1.1. Here, the $+z'$ and

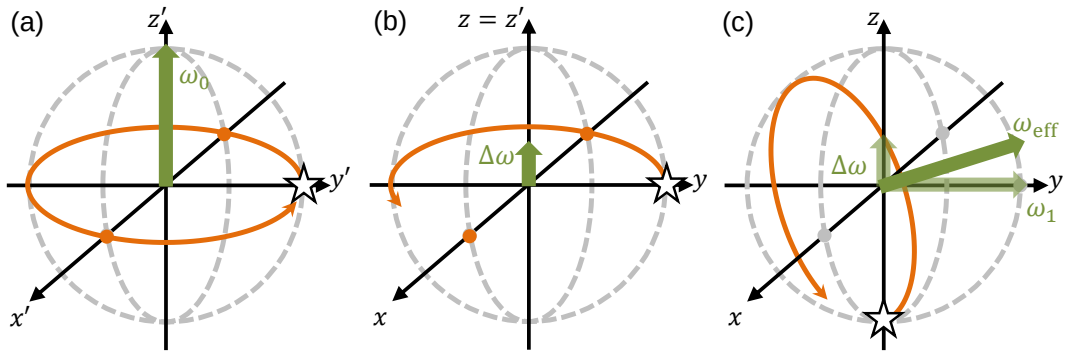

Figure 1.1: **Spin qubit represented on the Bloch sphere.** The initial state is indicated by the star. (a) In the laboratory frame, the spin precesses around the externally applied magnetic field with frequency ω_0. (b) In the frame rotating about the z'-axis at frequency ω, the spin, the field along the z-axis reduces to $\Delta\omega = \omega_0 - \omega$. (c) A magnetic field rotating at frequency ω appears static in the rotating frame, as shown by ω_1. Given the non-zero detuning, the spin initialized in the $|\downarrow\rangle$ precesses about the vector sum of $\Delta\omega$ and ω_1, ω_{eff}.

$-z'$ axes correspond to the $|\uparrow\rangle$ and $|\downarrow\rangle$ states, respectively. The initial state, indicated by the star, is $(|\uparrow\rangle + i|\downarrow\rangle)/\sqrt{2}$. The field is drawn in units of angular frequency, where $\omega_0 = \gamma_e B_0$. The spin undergoes Larmor precession around the field with frequency ω_0, as illustrated by the orange curve.

Magnetic resonance

Magnetic resonance provides the experimentalist with the ability to control the spin qubit. To understand this, it is helpful to move to a different frame of reference, where the representation in Figure 1.1(a) corresponds to the laboratory frame. We can instead define our Hamiltonian in a frame rotating at an angular frequency ω about the z'-axis. In this frame, the spin state appears to instead precess at a frequency $\Delta\omega = \omega_0 - \omega$, as represented in Figure 1.1(b). Mathematically, the result comes from the change of basis operator, given by

$$A = e^{i\omega t \sigma_z/2}, \tag{1.2}$$

where $|\phi\rangle = A|\psi\rangle$, defining $|\phi\rangle$ and $|\psi\rangle$ as the states represented in the rotating and laboratory frames, respectively. The effect of changing bases on the Hamiltonian is easily derived by substitution into the Schroedinger equation.

$$i\hbar \frac{d|\psi\rangle}{dt} = H|\psi\rangle \tag{1.3a}$$

$$i\hbar \frac{d|\phi\rangle}{dt} = \left[AHA^{-1} - i\hbar A \frac{dA^{-1}}{dt} \right] |\phi\rangle = H'|\phi\rangle, \tag{1.3b}$$

where H' is the Hamiltonian in the new frame. Using the change of basis operator for the

rotating frame A, the second term in the definition of H' yields

$$-i\hbar A\frac{dA^{-1}}{dt} = -\hbar\frac{\omega}{2}\sigma_z = -\omega S_z, \tag{1.4}$$

which is responsible for the effect observed in Figure 1.1(b). It is then simple to understand magnetic resonance in the rotating frame. Consider the effect of an externally applied oscillating field perpendicular to $\mathbf{B}_0$, of the form $2B_1\cos(\omega_t)S_x$ in the lab frame. This can be separated into two rotating fields with frequency ω and amplitude B_1: one in the direction of the Larmor precession and one opposite, which can be ignored. In the frame rotating at the same frequency as the rotating field, this appears as a static field $\omega_1 = \gamma_e B_1$ in the x-y plane of the Bloch sphere along a direction defined relative to an arbitrary phase.

Figure 1.1(c) shows the effect of this field in the off-resonant case where $\Delta\omega \neq 0$ with the spin initialized in the $|\downarrow\rangle$ state. The evolution of the state $|\psi(t)\rangle$ is described by Rabi's formula,

$$|\langle\uparrow|\psi(t)\rangle|^2 = \frac{\omega_1^2}{\omega_1^2 + (\Delta\omega)^2}\sin^2\left(\frac{\sqrt{\omega_1^2 + (\Delta\omega)^2}}{2}t\right). \tag{1.5}$$

$|\langle\uparrow|\psi(t)\rangle|^2$ is the probability that the state is found in the $|\uparrow\rangle$ state. To achieve a perfect spin flip, $|\langle\uparrow|\psi(t)\rangle|^2 = 1$, the oscillating field must be in resonance with the qubit splitting, i.e. $\Delta\omega = 0$.

Decoherence

Our qubits are defined in the resonant rotating frame, $\omega = \omega_0$, where any time-independent superposition of the basis states appears static. If $B_0 = 1$ T, for example, $\omega/2\pi = 28$ GHz which is in the microwave range. Using magnetic resonance, the spin qubit can be rotated about an arbitrary axis on the x-y plane, achieved with a phase shift with respect to the arbitrarily defined rotating (qubit) frame. A rotation of angle ϕ is achieved by switching on B_1 for a time ϕ/ω_1.

Unfortunately, in practice, the states do not remain static in the qubit frame. The resonance frequency of the qubit, ω_0, can be modified by noise in the environment. This may come in the form of classical magnetic field noise, the effect of fluctuations from nearby spins or even electric field noise if there is a mechanism that couples this to the qubit level splitting. This noise causes the state to precess in the rotating frame. This is called dephasing, as it causes us to lose track of the phase of the qubit. For a particular system, one can quote the time over which the state remains coherent. We address the measurement of this quantity in the next section.

Spin echoes and Dynamical decoupling

The techniques described in this section come from decades of research on bulk (ensemble) nuclear magnetic resonance (NMR) and electron spin resonance (ESR) experiments. The co-

herence time, T_2, of a spin qubit can be measured in several ways, potentially yielding different quantities. One standard method is using the Hahn echo [20]. From a spin initialized in the ground state ($|\downarrow\rangle$), it is rotated to the $+y$-axis with a $(\pi/2)_x$ pulse, which is a rotation of angle $\pi/2$ about the x-axis in the qubit (rotating) frame. A delay of time $\tau/2$ then follows, during which a fixed offset $\Delta\omega$ may cause the spin to dephase. After this time, a $(\pi)_x$ pulse is applied. Another delay of time $\tau/2$ follows, where the evolution of the spin due to $\Delta\omega$ is effectively reversed. The expectation value of the spin along the y-axis, $\langle S_y \rangle$, is then measured (the *echo*) and this is repeated to obtain statistics. The way in which $\langle S_y \rangle$ is measured will be clarified in the next section when we introduce our device. The experiment is repeated for different τ to obtain an echo trace of $\langle S_y \rangle$ as a function τ, where noise will eventually cause the signal to decay for long τ. The Hahn echo coherence time T_2^{HE} is extracted from the decay curve.

This leads to dynamical decoupling, a technique that can be used to combat decoherence by filtering out the effect of parts of the noise. In our explanation of the Hahn echo, we stated that the refocusing pulse in the middle of the sequence removes the effect of a fixed offset, $\Delta\omega$. In fact, it filters out the effect of any noise that appears static over that time, which is equivalent to noise with frequency much slower than $\nu = 1/\tau$: a high-pass filter characteristic. In total, the sequence acts as a bandpass filter as it also filters noise at frequencies much larger than ν. This is easily understood by considering the evolution of the qubit during each delay segment τ. The phase accumulated by the qubit in that time is given by $\int_0^\tau \Delta\omega(t)dt$. The integral is inherently a low-pass filter, averaging out noise at frequencies much greater than ν, thus explaining the low-pass cut-off of the band-pass filter.

Dynamical decoupling (DD) [21] is a technique to shift the center frequency of the bandpass filter [22]. While DD sequences come in many forms, we consider those involving the repetition of the sequence $(\tau/2 - \pi - \tau/2)$, N times. A DD sequence thus achieves a targeted total free precession time T_{FP} with $\tau = T_{\mathrm{FP}}/N$, whereas $\tau = T_{\mathrm{FP}}$ for the Hahn echo. This is beneficial in the case where the noise level decreases with frequency, as the center of the bandpass filter ν is pushed to N/T_{FP}.

DD is the focus of Chapter 4. The Carr-Purcell-Meiboom-Gill (CPMG) sequence is one used often in this thesis [23]. For spins initialized in the spin-$|\downarrow\rangle$ state, an N-pulse CPMG sequence is defined as $(\pi/2)_x - N \times (\tau/2 - \pi_y - \tau/2) - echo$. The *echo* is the measurement of $\langle S_y \rangle$, which differs between bulk experiments and our single spin experiments and will be discussed in Chapter 4.

1.2.2 The ^{31}P:Si quantum computer

The first proposal for a quantum processor using phosphorus donor spin qubits in silicon was made by Bruce Kane in 1998, here at UNSW [24]. Silicon as a host material for spin qubits has two key advantages. Firstly, bulk ESR and NMR experiments have shown that the dominant source of decoherence for a spin is its coupling to a spin bath. Naturally abundant silicon has $\sim 92.2\%$ ^{28}Si, $\sim 4.7\%$ ^{29}Si and $\sim 3.1\%$ ^{30}Si, of which only the ^{29}Si isotope has a nuclear

spin. The concentration of this isotope can be reduced through isotopic purification, essentially reducing the concentration of the background spin bath. Bulk measurements of the ^{31}P electron spin in isotopically purified silicon report a coherence time $T_2 > 1$ s [25].

The second advantage of silicon in relation to the Kane proposal is related to the fabrication of the proposed processor. A schematic from Reference [24] is reproduced here in Figure 1.2(a). Gate electrodes on top of an oxide are used to control the donors in the silicon substrate. Fabrication of such metal-oxide-semiconductor (MOS) structures has been perfected over decades by the microelectronics industry, allowing this platform to capitalize on their expertise.

The qubit in the Kane proposal is actually the spin of the nucleus of the single phosphorus (^{31}P) donor, as opposed to the electron. The coupling of two nuclear spin qubits would be achieved via the electrons. The spins of the electron and nucleus of the ^{31}P donor are coupled by the hyperfine interaction A, while two electrons are coupled by the exchange interaction J, given by the overlap of their wavefunctions. Kane proposed that the magnitudes of the couplings could be tuned by J and A gates, shown in Figure 1.2(a).

This inspired other proposals based on the same ^{31}P:Si system, but using the electron spin as the qubit instead [26–28]. This has the advantage of faster single-qubit rotations due to its larger gyromagnetic ratio and faster two-qubit gates, as inter-qubit coupling comes directly from the exchange interaction. This also allows the nuclear spin to be used as a resource, as will be discussed in this thesis. Figure 1.2(b) shows the two-dimensional architecture for a quantum processor employing the donor electron spin qubit outlined by Hollenberg *et al.* [26]. We point out two of the labeled sections in this figure: 'quantum logic gates' and 'coherent electron spin transport.' It is proposed that the spin qubits are transported to interaction regions where two-qubit logic gates can be performed. This thesis proposes techniques that could be used to realize these experimentally.

The ^{31}P in Si spin Hamiltonian

The electron orbital ground state for the single ^{31}P donor in silicon is 45 meV below the conduction band edge and the nearest excited state is separated by over 10 meV [30]. As we will show in the next section, the devices are operated in a dilution refrigerator (base temperature $T_{\text{base}} \approx 30$ mK and electron temperature $T_{\text{el}} \approx 200$ mK [31]). At such low temperatures, the electron is safely confined to the orbital ground state (10 meV $\approx$ 116 K). The spin Hamiltonian of the ^{31}P donor in an external magnetic field is written below in units of angular frequency, setting $\hbar = 1$.

$$H = \gamma_e B_0 S_z - \gamma_n B_0 I_z + \mathbf{S} \cdot \mathbf{A} \cdot \mathbf{I} = \gamma_e B_0 S_z - \gamma_n B_0 I_z + A\,(\mathbf{S} \cdot \mathbf{I}) \tag{1.6a}$$

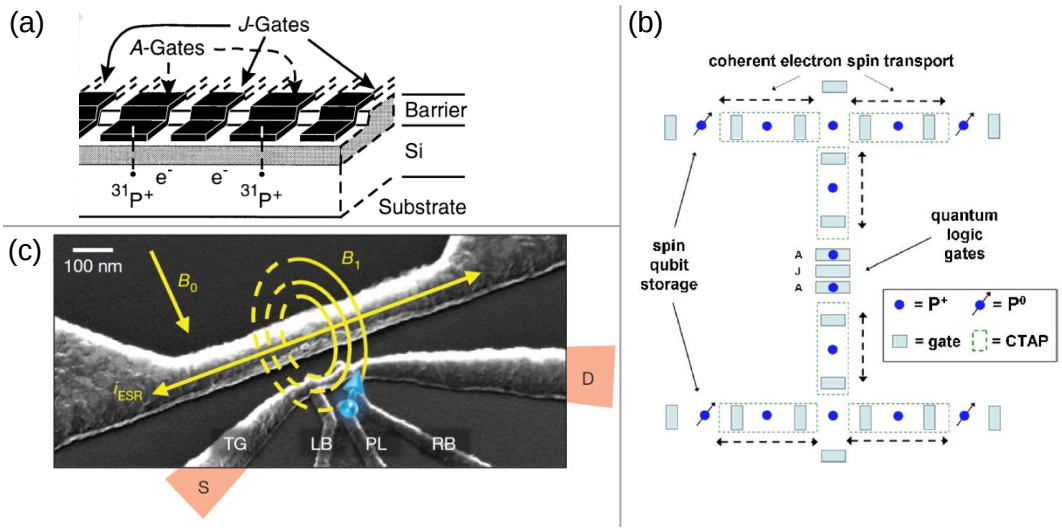

Figure 1.2: **Donor-based quantum computer.** (a) Reproduced from Reference [24]. The schematic of the Kane quantum computer. (b) Reproduced from Reference [26]. A schematic for a 2D architecture based on the donor electron spin qubit. (c) Reproduced from Reference [29]. An SEM of the donor qubit device fabricated on natural silicon. The donor is depicted by the blue circle.

$$= \frac{1}{2}\begin{pmatrix} (\gamma_e - \gamma_n)B_0 + A/2 & 0 & 0 & 0 \\ 0 & (\gamma_e + \gamma_n)B_0 - A/2 & A & 0 \\ 0 & A & (-\gamma_e - \gamma_n)B_0 - A/2 & 0 \\ 0 & 0 & 0 & (-\gamma_e + \gamma_n)B_0 + A/2 \end{pmatrix}, \tag{1.6b}$$

where $\mathbf{I}$ is the nuclear spin operator with z-operator I_z. The hyperfine tensor $\mathbf{A}$ is isotropic, allowing its replacement with the scalar $A/2\pi = 117$ MHz, as measured in bulk silicon. The gyromagnetic ratio of the nucleus is $\gamma_n/2\pi = 17.2$ MHz/T. The Hamiltonian is also shown in matrix form. Recall that the basis states implicit from using the spin operators as defined are $\{|\uparrow\Uparrow\rangle, |\uparrow\Downarrow\rangle, |\downarrow\Uparrow\rangle, |\downarrow\Downarrow\rangle\}$, where $|\Uparrow\rangle$ and $|\Downarrow\rangle$ are the nuclear spin states. We observe that A couples the $|\uparrow\Downarrow\rangle$ and $|\downarrow\Uparrow\rangle$ states, while they are detuned by $(\gamma_e + \gamma_n)B_0$. As we will show in the next section, we operate our devices in a large magnetic field $B_0 \approx 1.5$ T. The detuning between the $|\uparrow\Downarrow\rangle$ and $|\downarrow\Uparrow\rangle$ states is thus over an order of magnitude larger than the coupling. The eigenstates are therefore approximately the separable tensor products of the individual electron and nuclear spin qubit states.

1.3 Breakthroughs towards a ^{31}P:Si spin-based quantum computer

Several major breakthroughs were made by the Morello group at UNSW in the years preceding the start of this thesis. The first major milestones towards realizing the Kane quantum computer were achieved: (i) single-shot readout of the donor electron spin [31], (ii) coherent control of the donor electron spin [29] and (iii) nuclear spin readout and control [32]. This section presents measurement techniques used in these reports, as the same principles are used for the work of this thesis.

1.3.1 Single-shot electron spin readout

A scanning-electron micrograph of the device used by Pla *et al.* [29] is shown in Figure 1.2(c). The aluminium gates 'TG,' 'LB,' and 'RB' and the Ohmic contacts 'S' and 'D' form a single-electron transistor (SET) [33], whose highly nonlinear current-voltage characteristics [34] allow it to be used as an excellent charge sensor [35]. Phosphorus donors are implanted through the thin oxide (5-10 nm SiO_2) [36]. Given the ion implantation parameters, it is expected that $\sim$ 3 donors are tunnel-coupled to the SET island [31]. A specific donor can be selected by tuning (with the gate 'PL') its electrochemical potential to be in resonance with that of the SET island for readout. Readout is achieved via spin-to-charge conversion [37]. A large field B_0 ($\sim$ 1.5 T) Zeeman splits ($\sim$ 42 GHz) the electrochemical potentials of the $|\uparrow\rangle$ and $|\downarrow\rangle$ electron states, $\mu_\uparrow$ and $\mu_\downarrow$. The electrochemical potential of the SET island μ_{SET} is aligned such that only a spin-$|\uparrow\rangle$ donor electron can tunnel out to the island, leaving behind the positive charge of the phosphorus ion. This shifts the bias of the SET causing a current to flow ($\sim$ 1 nA), until a spin-$|\downarrow\rangle$ electron from the island tunnels on to the donor, switching off the current. The 'blip' in the current signal beyond a discrimination threshold, e.g. 0.5 nA, therefore signals the readout of a spin-$|\uparrow\rangle$ electron and the subsequent initialization of the electron spin into the $|\downarrow\rangle$ state.

Of course, the spin-selectivity of the spin-to-charge conversion requires that the thermal broadening of the SET island is much smaller than the electron Zeeman energy splitting, thus requiring the use of a dilution refrigerator ($T_{\mathrm{el}} \approx 200$ mK ≈ 4 GHz).

1.3.2 Electron and nuclear spin control

At $B_0 \approx 1.5$ T, an oscillating magnetic field at the site of the donor at MHz and GHz frequencies is required for NMR and ESR, respectively. This is delivered via a coplanar waveguide terminating in a short-circuit antenna [38], as shown in Figure 1.2(c).

In the experiment, the electrochemical potential of the donor electron is set to one of two phases. The readout and initialization phase is as described before, where it is brought into resonance with the electrochemical potential of the island. Once initialized, it is 'plunged' far

below that of the island, such that ESR and NMR can be performed while the electron is safely confined to the donor [29]. Upon completion of a sequence, the electron is brought back to the readout phase for measurement of its spin. Recall that the experiment only has access to measurement of the z-component of the electron spin. If the y-component needs to be measured at the end of a sequence, for example, then a $(\pi/2)_x$ rotation is used to map this onto the z-axis.

The measurement of the nuclear spin is achieved via the electron spin, through its influence on the ESR frequency [32]. The transition frequencies of the donor spin Hamiltonian (Equation 1.6) are given below to first order.

$$\omega_{e\Uparrow} = \gamma_e B_0 + A/2 \tag{1.7a}$$

$$\omega_{e\Downarrow} = \gamma_e B_0 - A/2 \tag{1.7b}$$

$$\omega_{n\uparrow} = -\gamma_n B_0 + A/2 \tag{1.7c}$$

$$\omega_{n\downarrow} = -\gamma_n B_0 - A/2 \tag{1.7d}$$

For example, $\omega_{e\Uparrow}$, is the ESR frequency when the nucleus is in the $|\Uparrow\rangle$ state. The spin of the nucleus is thus measured by checking whether $\omega_{e\Uparrow}$ or $\omega_{e\Downarrow}$ is in resonance with the electron spin [32]. This constitutes a quantum non-demolition measurement (QND) of the nuclear spin [39], allowing the measurement protocol to be repeated to reduce the effect of errors in single-shot electron spin readout [31] and obtain high-fidelity nuclear spin readout [32].

The resonance frequencies in the experiment are not precisely known *a priori* and are found by performing an 'ESR sweep' experiment, which is used frequently in this thesis. The electron is initialized in the $|\downarrow\rangle$ state and then tuned to the control phase. A long pulse, beyond the expected coherence time, at frequency ω_{ESR} is applied. If the magnetic resonance condition is met, then the spin state will be randomized. This single shot is repeated many times to obtain the expectation value in the z-direction, $P_\uparrow$. ω_{ESR} is then swept over a range in order to find the resonance frequency.

The results presented above were obtained from devices fabricated on natural silicon substrate [29, 31, 32]. Given the 4.7% abundance of the ^{29}Si isotope, the control fidelity of the electron spin was limited to 57% [29]. The next step towards building a full-scale quantum processor is to improve upon this work.

1.4 Scope of this Thesis

At the time of starting this thesis, the single-donor electron and nuclear spin qubits had just been demonstrated in natural silicon [29, 31, 32]. This was a landmark result for silicon quantum computation as envisioned by Kane [24]. The aim of this thesis is to advance progress towards building a quantum computer in silicon. Unlike the Kane proposal, we focus on the electron

spin qubit rather than that of the nucleus.

Given the road-map towards building a full-scale processor, each chapter focuses on overcoming a selected hurdle. The problems chosen vary in kind, embodying the interdisciplinary nature of the challenge to build a quantum computer. The beginning chapters focus on qubit measurements aimed at improving upon the achievements made in natural silicon. The middle chapters present theoretical proposals for the realistic implementation of key components of current processor architectures. The final chapter addresses an important change in the experimental setup that will be necessary as the field progresses from few-qubit devices to a full-scale processor.

1.4.1 Thesis Outline

- Chapter 2 details the steps involved in device fabrication and the experimental setup used for qubit measurements. The results presented in Chapters 3, 4 and 7 are obtained from a device fabricated as part of this thesis. The complete recipes for electron beam lithography and device preparation are disclosed. The details of the measurement instrumentation setup including wiring and filtering are provided.

- Chapter 3 presents measurements of a single electron spin qubit device fabricated on isotopically purified silicon. We focus on four key achievements in single-qubit operations. (i) Qubit control fidelities and (ii) coherence times are dramatically improved as a result of the isotopic purification. Methods devised as part of this thesis substantially improve (iii) readout and (iv) initialization fidelities of the electron spin qubit. We also perform experiments on qubit coherence times that reveal behavior that is not currently understood.

- Chapter 4 continues with measurements on the same device, addressing a contested claim made in the previous chapter. There, the coherence times reported for the electron spin are measured with the CPMG sequence. This sparked two points of criticism in regards to its validity. This chapter concludes this debate by measuring the coherence times with an isotropic dynamical decoupling sequence. Our investigations also reveal a phenomenon present in our device that is detrimental to qubit control fidelities.

- Chapter 5 considers the implementation of logic operations with donor electron spin qubits. We present theoretical proposals for two types of two-qubit gates that are more robust to fabrication uncertainties than those previously proposed in the literature. We highlight the advantage provided by the availability of the donor nuclear spin as a resource. Calculations of the expected gate fidelities are presented, followed by a protocol to calibrate relevant parameters for a proof-of-principle device.

- Chapter 6 continues with considerations of another key component for scale-up: qubit transport. We combine various ideas developed in the literature to form a scheme for transport in a donor-based processor. An assessment of the transport scheme under realistic experimental considerations is provided. A calibration protocol is also presented for its incorporation into a full-scale processor.

- Chapter 7 address the shift to measurement of these qubit devices in a cryogen-free dilution refrigerator setup. We present a characterization of the electrical noise observed on our cables in such a setup which comes from the vibrations created by the pulse-tube cryocooler. A comparison of the noise induced in different cables is performed, which serves to diagnose the coupling mechanism of the vibrations to the electrical signal as well as identify a cable that mitigates this noise as much as possible. We then measure the same electron spin qubit device in this setup, demonstrating the effect of the noise on the coherence of the qubit.

- Chapter 8 summarizes the achievements of this thesis and presents an outlook on future work required to advance progress towards building a full-scale quantum computer based on donors in silicon.

Chapter 2

Device fabrication and experimental methods

This first part of this chapter outlines the processes used to fabricate the devices discussed in this thesis. The isotopically-purified stock was provided by K. Itoh of Keio University. Donor implantation for these particular devices was performed at the Australian National University by J. C. McCallum of the University of Melbourne. The majority of the remaining processes were carried out at the Australian National Fabrication Facility at the University of New South Wales. The second part of this chapter covers the experimental setup used to measure these devices. Measurements were performed at the low-temperature facilities at the Centre for Quantum Computation and Communication Technology at the University of New South Wales.

The devices created and measured at UNSW have propelled silicon quantum computation forward with respect to more established platforms. One of the key advantages of this platform is the fact that the fabrication processes used are compatible with those of the multi-trillion dollar microelectronics industry, whose techniques have been optimized for decades. The ability to capitalize on this wealth of expertise will prove paramount when attempting to scale up to a fully functional quantum computer.

In Section 2.1, we walk through the device fabrication process, starting from a bare silicon wafer to a complete qubit device.

In Section 2.2, we provide an overview of the experimental setup used to measure these qubit devices. This will provide insight into how the results in Chapters 3 and 4 are obtained.

2.1 Device fabrication and packaging

Two of the devices fabricated as part of this thesis have yielded results that are now either published or in preparation for publication. The two devices are identical apart from the stock silicon on which they were fabricated. The first device was fabricated on high purity natural silicon while the second was fabricated on isotopically-purified silicon.

2.1.1 Silicon wafer preparation

The details of preparation of the silicon stock wafers is outside the scope of this thesis, as the author did not carry out these particular steps. However, an overview is provided for the reader to understand the layout of the stock on which these devices are fabricated. Figure 2.1 shows a drawing of the main features prepared during this stage in the 1.2 mm $\times$ 1.2 mm pixel that can host one qubit device. The process begins by obtaining silicon wafers. For the ^{nat}Si device, high purity silicon wafers with low residual p-type background doping ($\sim 10^{12}$ cm^{-3}) were purchased from Topsil. For the ^{28}Si device, wafers were provided by K. Itoh that consist of an epitaxial layer of isotopically purified ^{28}Si grown on top of a 500 μm thick high purity natural silicon wafer. The ^{28}Si layer is 0.8 μm thick and has residual concentrations of 730 ppm of ^{29}Si and 30 ppm of ^{30}Si. The remaining steps for device preparation are identical for both devices.

The wafer first undergoes a standard cleaning process. Titanium-platinum (Ti-Pt) alignment markers are then defined with ultraviolet (UV) lithography for subsequent patterning. A $\sim$ 200 nm thick field oxide is grown in a wet thermal oxidation furnace that acts as a mask for the following diffusion of n+ and p regions. Boron is diffused to form a guard ring around each device, as shown in Figure 2.1, to block possible leakage paths at the Si-SiO_2 interface under the thick oxide due to trapped positive charges in the oxide that may induce a two-dimensional electron gas (2DEG) at the interface [40, 41]. Phosphorus is diffused to form the source and drain regions for each device. Two source-drain pairs are present as these pixels were originally intended for two smaller devices. Finally, a 5-10 nm high quality gate oxide (SiO_2) is grown in an ultra-dry furnace.

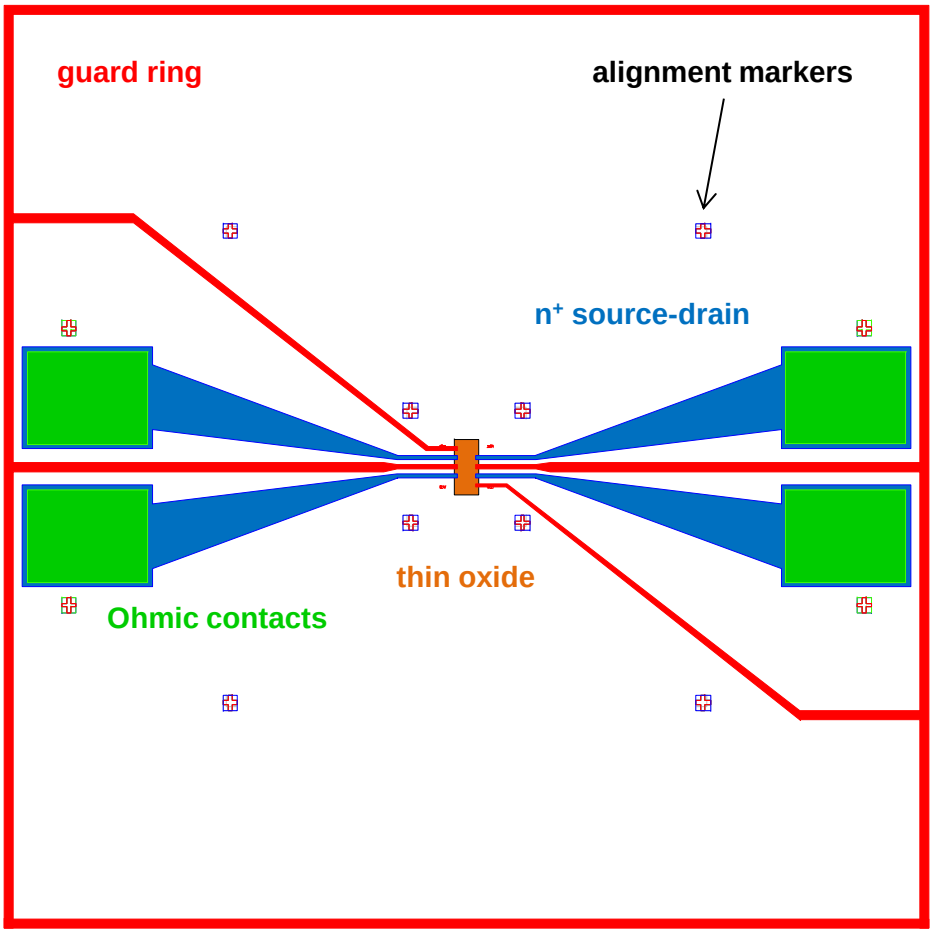

Figure 2.1: **Layout of the features patterned during the stock preparation stage.** The key features shown are the (i) Ti-Pt alignment markers, (ii) the guard ring created by diffusion of boron, (iii) the source and drain regions created by diffusion of phosphorus, (iv) the Ohmic contacts to the source and drain and (v) the high quality thin oxide.

2.1.2 Electron beam lithography

Once the stock has been prepared, it is divided into pieces for the purpose of making different types of devices. Smaller Ti-Pt alignment markers, as shown in Figure 2.2, are defined with electron beam lithography (EBL) to be used for all subsequent EBL steps.

The recipe used to define patterns with EBL was developed at ANFF over many years. The piece is cleaned with acetone followed by isopropyl alcohol (IPA). It is then placed in a Deton Vacuum oxygen plasma asher to remove organic residue such as photoresist or polymethyl methacrylate (PMMA) from the surface. A spin clean with acetone and IPA precedes the application of PMMA, the EBL resist. PMMA A4 is dropped on to the piece and it is spun at 7500 rpm for 30 seconds (achieving a thickness of $\sim$ 150 nm) followed by a 90 second post-bake

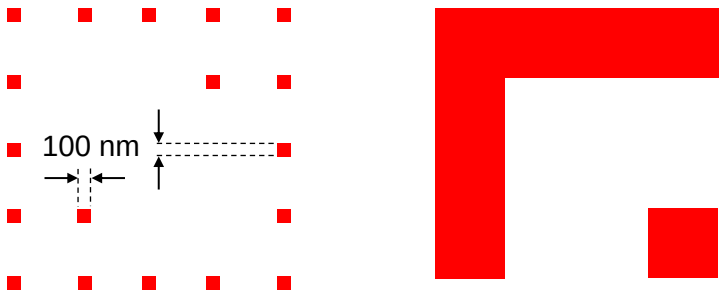

Figure 2.2: **Drawing of the alignment markers used for electron beam lithography.** Typical alignment errors are less than 10 nm.

at 180°C. Droplets of colloidal gold solution are placed at the corners of the piece on top of the PMMA that serve as focus markers. The pattern is then written in a FEI scanning electron microscope (SEM) system that is fitted for EBL via the Nanometer Pattern Generation System (NPGS) from J. C. Nabity. The nanometer-scale features are written with an acceleration voltage of 30 kV. Following patterning, development is achieved using a 1:3 solution of methyl-isobutyl-ketone (MIBK) and IPA. The piece is placed in the solution for 40 seconds, during which ultrasonic agitation is applied for 15 seconds. The piece is then transferred to IPA, which is a weak developer, for 20 seconds.

In the patterning of alignment markers, the titanium and platinum are deposited using an electron-beam evaporator. In the patterning of the device electrodes, aluminium is evaporated onto the piece using an Edwards thermal evaporator at a rate of 2-5 Å/s. The devices in this thesis consist of two stacked aluminium layers. The thickness of the first and second layers are 35 nm and 100 nm, respectively. Finally, N-methyl-2-pyrollidone (NMP) heated to 75°C is used to perform lift off. These steps are repeated for each layer. After the completion of each aluminium layer, the chip is placed on a hotplate at 150°C for 5 minutes to form a ∼2-3 nm thick layer of aluminium oxide. This is necessary to electrically insulate the stacked layers.

2.1.3 Donor implantation

Prior to the patterning of the aluminium electrodes, the donors must be implanted. 90 nm × 90 nm apertures in a PMMA mask are defined by EBL in each pixel. This forms the 'active region' of each pixel, around which the aluminium gates will be fabricated. Note that one piece generally has $\sim 10 \times 10$ pixels, so that this implanted piece can be used for several device designs. Implantation was carried out by Jeffrey McCallum at the ion accelerator facility at the Australian National University. The devices discussed in this thesis were originally intended for two-donor coupling experiments. Therefore, P_2^+ was implanted at 20 keV (10 keV per ion) with a fluence of 5×10^{10} cm^{-2} ($\sim$ 4 donor pairs in the aperture). The intention was that

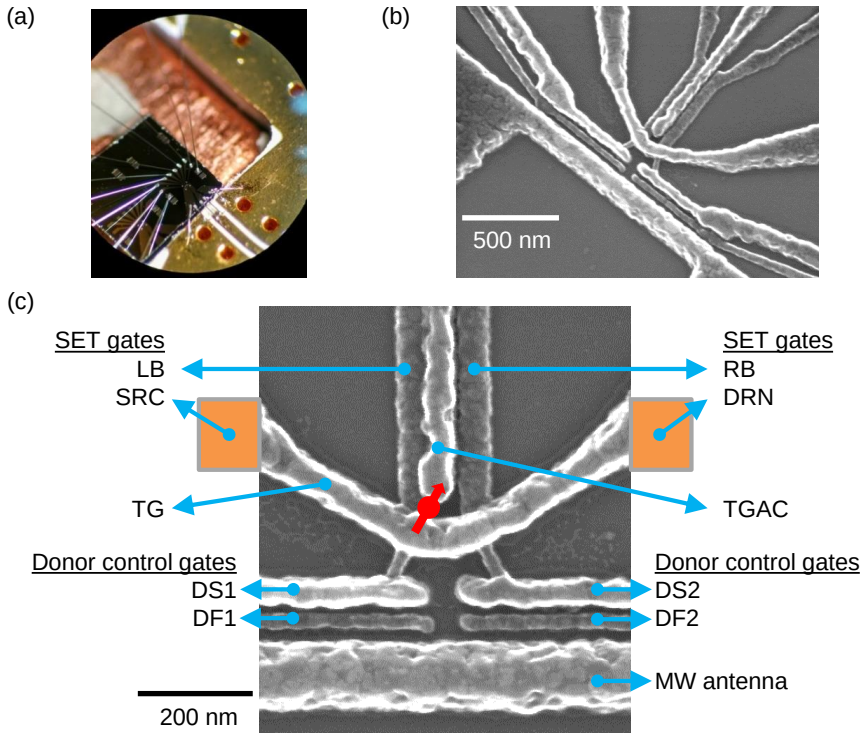

Figure 2.3: **Device images.** (a) A photo of the wire-bonded 2×2 chip taken through the microscope at the bonder. The layout of this PCB is slightly different to the one shown in Figure 2.4. The silver paint can be seen (out of focus) connecting the body of the chip to the copper stage. (b) Scanning electron micrograph of the device. (c) Zoom-in of the active region with gates labeled. The location of the donor is indicated with the red circle and arrow, as determined by device modeling [44].

each implanted molecule would form a coupled donor pair. Although a donor pair was not found in our measurements, isolated donors were found which have been used to perform many experiments, some of which are presented in this thesis.

Following implantation and removal of the PMMA mask, the piece undergoes a rapid thermal anneal (RTA) for 5 seconds at 1000°C to activate the donors and repair the damage caused by implantation [42]. The aluminium Ohmic contacts to the source and drain diffused regions are then defined. The piece is then divided into smaller pieces of $\sim 2 \times 6$ pixels each so that the devices can be fabricated in smaller batches.

2.1.4 Final processing steps

Once both layers have been patterned for a batch with $\sim$ 10-16 devices, the piece is further divided into chips of 2×2 pixels to fit the space available in the enclosure. The final processing step is to perform a forming gas anneal (FGA). The chip is loaded into a clean furnace preset to 400°C with forming gas (95% N_2 and 5% H_2) for 15 minutes. The purpose of this step is to reduce the trap density at the Si-SiO_2 interface [43].

At this stage, the chip is ready to be adhered to the enclosure using PMMA. We will cover the details of the enclosure and printed circuit board (PCB) used in the next section. As there is a layer of PMMA beneath the chip, we use silver paint for thermal contact between the body of the chip and an uncoated part of the copper stage. A Kulicke & Soffa aluminium wedge bonder is used for wire bonding the gates to the PCB. Extreme care is taken at this stage to confirm that the tools used are grounded so as to not damage the device through electrostatic discharge. Once bonded, the device and enclosure are ready to be transferred to the experimental setup. Figure 2.3 shows (a) the bonded chip in the enclosure and (b) an SEM of the completed device. Sub-figure (c) shows a zoom-in of the active region with the gates labeled as they will be referred to in the next section. The SET is formed by the two barriers (LB and RB) and the top gate (TG) that creates a 2DEG from electrons connected to the source (SRC) and (DRN). The TGAC gate is used to pulse the potential of the SET island. Donor fast (DF1 and DF2) and slow (DS1 and DS2) gates are used to control the potential of the donor electron. The antenna is used for NMR and ESR.

2.2 Experimental setup

For the majority of the results presented in this thesis, the device was measured in an Oxford Kelvinox 100 dilution refrigerator. Our group later acquired a BlueFors LD400 cryogen-free dilution refrigerator, but this setup and the device measurements performed in this fridge will be discussed separately in Chapter 7. The Oxford fridge is a traditional wet dilution refrigerator with a superconducting magnet which we run at ~ 1.55 T. The enclosure is secured to a cold-finger attached to the mixing chamber plate of the fridge, such that the sample sits directly at the center of the magnet.

2.2.1 Cables and filtering

Part of the work of this thesis was designing filter boxes for the lines that connect to the device, as they carry thermal radiation. The purpose of the filter boxes is to minimize the amount of radiation that comes through while still allowing the intended electrical signal to reach the device. The material for the wires or cables used are also chosen to minimize thermal conductance from the room-temperature stage. The required lines are split into three categories: DC, AC and microwave. With reference to the gate labels in Figure 2.3(c), the DC lines include the TG, RB, LB, DS1 and DS2 gates, while the AC lines include the SRC, DRN, TGAC, DF1 and DF2 gates.

The microwave line carries the MHz to GHz signals to the antenna for NMR and ESR. The coaxial cable used for this line is a semi-rigid stainless steel UT85 cable. The outer shield of the cable is thermalized at every temperature stage by anchoring it to the stage with copper wire. Attenuators are installed at two temperature stages in the fridge to thermalize the inner conductor (10 dB at 1.5 K and 3 dB at the mixing-chamber plate). This line goes to the

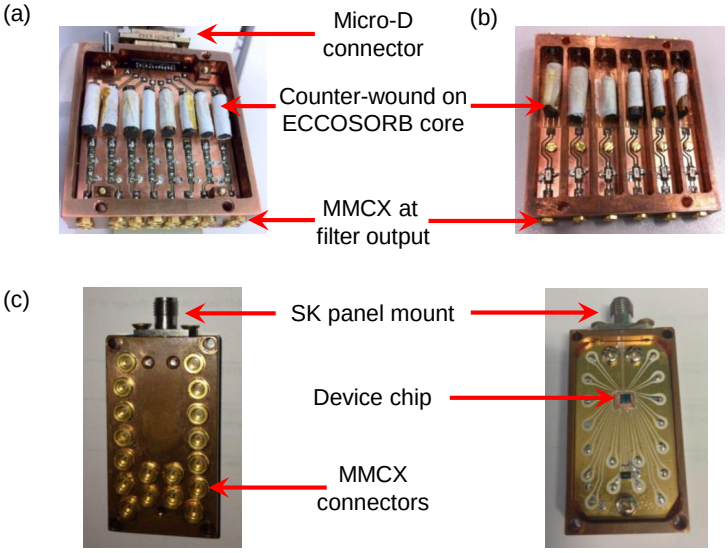

Figure 2.4: **Pictures of the DC and AC filter boxes and the device enclosure.** These pictures were taken before the filter boxes were potted with copper powder. (a) Each line in the DC box has two passive RC filters in series with cut-off frequencies of 20 Hz and 8 MHz. (b) Each line in the AC box has an integrated LC-pi filter with a cut-off frequency of 80 MHz. (c) The device is mounted as shown. The microwave line connects to the 2.92 mm K connector on the panel without passing through a filter box.

enclosure directly, without passing through a filter box.

The AC and DC lines, however, each have a dedicated filter box to attenuate as much high frequency noise as possible. The AC lines are used for gates which are pulsed. We use cupronickel UT85 coaxial cables which are also thermally anchored to every temperature stage with copper wire. The DC lines are used for gates that only require a fixed voltage bias. We use constantan twisted pairs that are accessed at room-temperature with a 24-pin Fischer connector and connect to the filter box through a micro-D connector. These insulated wires are wrapped around rods and glued with varnish at each temperature stage of the fridge for thermalization.

The DC and AC boxes are similar in their response to high-frequency noise ($\sim$GHz) but differ in their lower cutoff-frequency low-pass filter. The PCB in the DC box has two passive first-order RC filters in series. The resistors used are 20 kΩ thin-film nichrome and the capacitors used are 470 nF and 1 pF ceramic (X7R or NP0) for cut-off frequencies of 20 Hz and 8 MHz, respectively. The PCB in the AC box hosts the LFCN-80+ LC-pi filter from Mini-Circuits with a cut-off frequency of 80 MHz. To attenuate high-frequency noise, we make use of both ECCOSORB, a high loss microwave absorber, and copper powder. A counter-wound coil around an ECCOSORB core is included in series with the low-pass filters mentioned previously. Two meters of wire is used for the coil to maximize the length of contact with the ECCOSORB material and it is counter-wound to minimize inductance. The box is then potted with copper

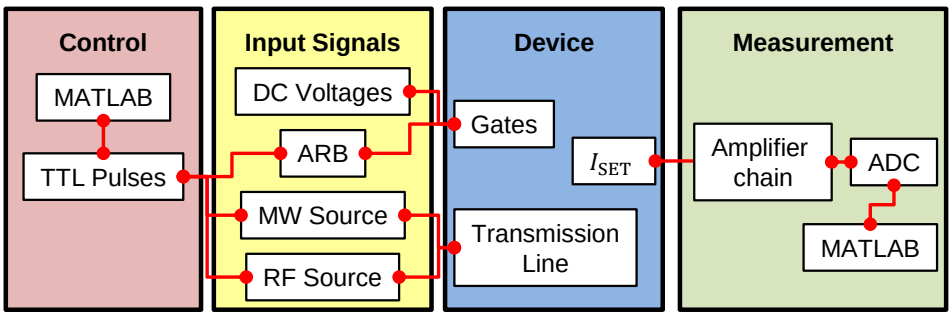

Figure 2.5: **Schematic of the instrumentation setup.** The TTL signal generator is responsible for the trigger timing of the arbitrary waveform generator, microwave source and RF source. The signals are fed to to the device and the measured signal is the current through the SET. This is amplified and acquired at room temperature.

powder, which attenuates high frequencies through skin effect damping due to its large effective surface area, as the grains are insulated by a natural oxide layer [45].

At the output of the filter boxes, the lines have been thermalized as best as possible and unwanted high frequency noise has been attenuated. We use thin (EZ47) semi-rigid coaxial cables to connect the lines from the output of the filter box to the lines on the enclosure. Coaxial cables are used here to shield the inner conductor from thermal radiation. The cables are connected to pins on the enclosure with MMCX connectors, as they are compact enough to fit the required number of lines. The microwave line, however, is connected to the enclosure using a 2.92 mm K connector, for its superior frequency response.

The enclosure is milled out of a single block of oxygen-free copper for maximum thermal conductance. The connectors on the body of the enclosure connect to a PCB that is designed in-house. The chip is mounted on a copper stage carved out of the enclosure, in a small aperture in the middle of the PCB. The track for the microwave line is a matched coplanar waveguide and the dielectric used for the PCB is Rogers 3010, suitable for high frequency applications.

2.2.2 Instrumentation

Figure 2.5 shows a schematic of the instrumentation setup used. Our measurement scripts are written in MATLAB. A 200 MHz TTL pulse generator (SpinCore PulseBlasterESR-PRO) is responsible for the triggering of the remaining equipment, and therefore the timing of the measurement sequence. DC voltages are applied to the gates in the device using Stanford Research Systems (SRS) SIM928 Isolated Voltage Source modules in a SIM900 mainframe. Voltage pulses are applied to gates using the Lecroy ArbStudio arbitrary waveform generator (ARB). The microwave (MW) signals for electron spin resonance are supplied by the Agilent E8267D Vector Source (MW source). The radio-frequency (RF) signals for nuclear magnetic resonance are supplied by the SpinCore PulseBlasterDDS-II-300 (RF source).

The measured signal from the device is solely the current flowing through the SET. The

magnitude of the current under normal operation is ~ 1 nA, and therefore must be amplified. We use the FEMTO DLPCA-200 transimpedance amplifier set at 10^7 V/A, which has an input impedance of 150 Ω and a passband from DC to 50 kHz. The signal is further amplified with a SIM910 voltage amplifier with a gain of 10 V/V, which allows us to opto-isolate the input from the output, preventing the creation of a large ground loop. A SIM965 analog filter module set to a low-pass fourth order Bessel filter with a cut-off frequency of 40 kHz provides the final filtering of the signal. The signal is acquired by an AlazarTech ATS9440 PCI digitizer card, or analog-to-digital converter (ADC).

2.3 Summary

This chapter provided an overview of the process (Section 2.1) used to fabricate the device on which all measurements presented in this thesis are performed. The exact experimental setup described (Section 2.2) is used to perform the measurements presented in Chapters 3 and 4. Our efforts in filtering and cable thermalization result in a device electron temperature $T_{\mathrm{el}} \approx 100$ mK.

Chapter 3

Improving the fundamental single qubit operations on the electron spin

This chapter focuses on improving the fidelities of the fundamental operations for a single donor electron spin qubit. Coherence times and control fidelities are dramatically increased for a device fabricated on isotopically-purified silicon as compared to one on natural silicon. For readout, the electron spin is mapped onto that of the nucleus, whose state is measured with very high fidelity owing to quantum non-demolition measurement. A scheme is devised and implemented to achieve high-fidelity electron spin initialization based on measurement back-action. Combining these improvements, the fidelities of the fundamental operations of electron spin initialization, readout and control all exceed 99.9%.

This chapter includes results from the following publications:

J. T. Muhonen, J. P. Dehollain, A. Laucht, F. E. Hudson, **R. Kalra**, T. Sekiguchi, K. M. Itoh, D. N. Jamieson, J. C. McCallum, A. S. Dzurak, and A. Morello. "Storing quantum information for 30 seconds in a nanoelectronic device." *Nature Nanotechnology* vol. 9, no. 12, pp. 986-991, (2014).

J. T. Muhonen, A. Laucht, S. Simmons, J. P. Dehollain, **R. Kalra**, F. E. Hudson, S. Freer, K. M. Itoh, D. N. Jamieson, J. C. McCallum, A. S. Dzurak, and A. Morello. "Quantifying the quantum gate fidelity of single-atom spin qubits in silicon by randomized benchmarking." *Journal of Physics: Condensed Matter* vol. 27, no. 15, p. 154205, (2015).

J. P. Dehollain, S. Simmons, J. T. Muhonen, **R. Kalra**, A. Laucht, F. Hudson, K. Itoh, D. N. Jamieson, J. C. McCallum, A. S. Dzurak, and A. Morello. "Bell's inequality violation with spins in silicon." *Nature Nanotechnology* vol. 11, pp. 242-246, (2016).

The author acknowledges (i) J. T. Muhonen, J. P. Dehollain and A. Laucht for leading the measurements presented in Figures 3.2 and 3.3, (ii) S. Simmons for leading the measurement presented in Figure 3.7, and (iii) F. E. Hudson and S. Freer for their work in device fabrication and preparation.

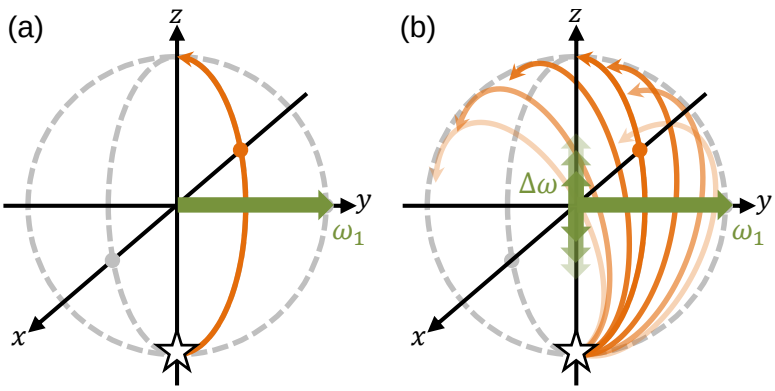

Figure 3.1: **π-rotation about the y-axis in the absence and presence of noise.** A $|\downarrow\rangle$ state (as indicated by the star) is rotated (a) exactly to the $|\uparrow\rangle$ state in the absence of noise. (b) A non-zero $\Delta\omega$ can result from noise, causing errors in the rotation axis and angle.

At the time of starting this thesis, complete donor electron and nuclear qubit control in silicon had just been achieved in the span of a few years. This laid the foundation for a quantum computer based on donors in silicon. However, development of single qubit control had only just begun. To be scalable, the fidelities of the key operations had to be improved. In this chapter, we present progress made in improving the fidelities of qubit control, state preservation, measurement and initialization for the electron spin qubit. All of the measurements presented in this chapter were performed on the device shown in Figure 2.3, which was fabricated as part of this thesis.

3.1 Qubit control

Qubit control, or rotations about arbitrary axes on the Bloch sphere, is necessary for any quantum algorithm. The control fidelity is defined as the probability that the resulting state after an attempted rotation matches the intended final state. In other words, if a rotation is performed that is designed to rotate Ψ_a to Ψ_b, but an error occurs such that the resulting state is actually Ψ_c, then the control fidelity is equal to $F_c = |\langle\Psi_c|\Psi_b\rangle|^2$. It is instructive to start by picturing a rotation of angle π about the y-axis.

Figure 3.1(a) shows the qubit Bloch sphere in the rotating frame at the drive frequency ω which matches the qubit resonance frequency ω_0, such that $\Delta\omega = 0$. We assume that the drive ω_1 can be pulsed on for exactly $T_\pi = \pi/\omega_1$ such that a spin-$|\downarrow\rangle$ is perfectly flipped, following the trajectory outlined by the orange curve. The control fidelity can be limited by fluctuations in the qubit resonance frequency. If the expected magnitude of $\Delta\omega$ due to fluctuations, or $\langle|\Delta\omega|\rangle$, is significant compared to ω_1, there will be an error in the rotation achieved as shown in Figure 3.1(b).

$\langle|\Delta\omega|\rangle$ can be estimated by performing an ESR sweep experiment to obtain $P_\uparrow$ as a function

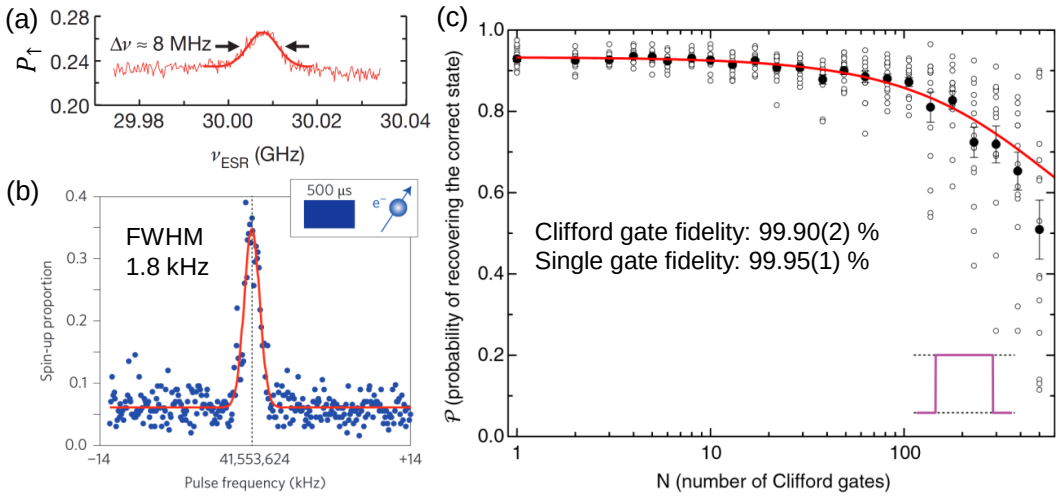

Figure 3.2: **Linewidths and qubit control fidelity.** (a) Reproduced from Reference [29], this plot shows the linewidth measured in the natural silicon device. (b) and (c) Reproduced from [46] and [47], these plots show the linewidth measured and qubit control fidelity achieved, respectively, in an isotopically-purified silicon device.

of ω (Chapter 1). The shape of the resulting curve will depend on the ratio $\omega_1/\langle|\Delta\omega|\rangle$. In the power-broadened case where this ratio is large, it will follow the Lorentzian envelope given in Rabi's formula, $\omega_1^2/[\omega_1^2 + (\omega_0 - \omega)^2]$ (Chapter 1), not allowing a measurement of $\langle|\Delta\omega|\rangle$. A low amplitude ω_1 is required to capture the effect of $\langle|\Delta\omega|\rangle$. In practice, the drive is applied for a time longer than the expected coherence time so that the rotation angle achieved is randomized, and the curve obtained is a Gaussian whose linewidth is a measure of the inhomogeneous broadening due to noise [29].

Figure 3.2(a), reproduced from Reference [29], shows that the linewidth measured in the natural silicon device is 8 MHz. This is greater than the 3 MHz magnitude of ω_1 ($\div 2\pi$) achieved in that experiment, resulting in a poor control fidelity $F_c = 57\%$.

The qubit control fidelity was improved dramatically by moving from natural silicon to isotopically-purified silicon, with a ^{29}Si concentration of < 800 ppm [46]. The linewidth was measured to be 1.8 kHz as shown in Figure 3.2(b). With a Rabi frequency over two orders of magnitude larger than the linewidth, the intrinsic control fidelity would be of order 99.9999%. In practice, the fidelities achieved are instead limited by the technical limitations of the room-temperature electronics [47]. The limited bandwidth of the instrumentation gating the duration of the ω_1 pulse leads to a finite time resolution, and therefore a finite precision in the rotation angle of the qubit.

To quantify the qubit control fidelity, Muhonen *et al.* [47] employed the randomized benchmarking protocol [48]. Unlike quantum process tomography, randomized benchmarking is able to extract the control fidelity alone while remaining insensitive to state initialization and measurement errors. The protocol involves applying a sequence of N randomly chosen gates from

the Clifford group. A universal set of gates can be constructed when the single qubit rotations from the Clifford group are combined with a two-qubit gate [49]. Figure 3.2(c), reproduced from Reference [47], plots the probability of recovering the desired state as a function of N. The eventual decay in the state recovery is due to errors accumulated by the gates in combination with decoherence, allowing a gate fidelity to be extracted that includes both these effects. The average gate fidelities for the electron spin obtained exceed 99.9%.

This control fidelity is certainly beyond the threshold for fault-tolerant architectures such as the surface code [50]. It could be enhanced further by improving the room-temperature electronics, and obtaining a high-bandwidth solution for gating the microwave pulses.

3.2 State preservation and coherence times

The coherence times measured in the isotopically-purified silicon device set a new benchmark for solid-state qubits: 0.56 seconds for the electron spin as measured by a 16,384-pulse CPMG. The CPMG sequence is defined in Chapter 1. For a complete picture of the noise affecting the coherence of a qubit, it is useful to obtain the spectrum of the noise as a function of frequency. Figure 3.3(a) shows the noise spectrum for the electron spin qubit, reproduced exactly from Reference [46]. The technique used to obtain the noise spectrum involves the use of the CPMG sequence as a bandpass filter, as explained in Chapter 1.

The procedure for obtaining one point in the plot of Figure 3.3(a) is as follows. To determine the magnitude of the noise at a certain frequency ν, we must extract a coherence time from CPMG sequences with $\tau = 1/\nu$. A coherence time is measured by plotting the probability of state recovery as a function of the total free-precession time during the CPMG sequence, $N\tau$. With τ fixed, the total time is instead swept by varying N. The coherence time can then be translated to a noise power at ν. Note that the filter function picture of dynamical decoupling is only valid if the sources of noise are themselves not affected by the sequence and if the refocusing pulses achieve perfect π rotations.

It is clear from the spectrum that the power of dynamical decoupling is, in this case, the ability to filter out the high-magnitude low-frequency noise. Again, the coherence time of the electron spin was measured to be $T_2 = 0.56$ seconds with a 16,384-pulse CPMG. For comparison of this sequence to the noise spectrum, $\nu \approx 30$ kHz at $T_{\mathrm{FP}} = 0.56$ s. Note however that there is some debate as to whether or not CPMG provides a valid measure of coherence times. We address this debate and present work done to resolve it in Chapter 4.

Muhonen *et al.* [46] also addressed the possible sources of noise, attributing the frequency-dependent component to instability in the externally applied magnetic field, and the noise floor to Johnson-Nyquist noise delivered to the qubit by the ESR line. The short-circuit termination of the transmission line (the antenna) should ideally be parallel to the external magnetic field, such that the oscillating field produced B_1 would always be perpendicular to B_0. Due to experimental constraints, however, this was not the case in this device. A component of the

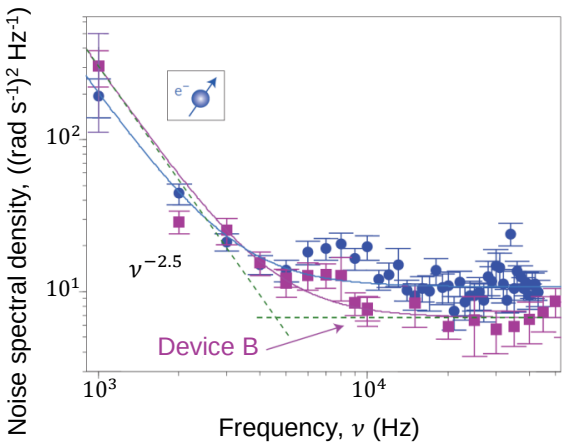

Figure 3.3: **Frequency spectrum of the noise seen by the qubit.** This plot is reproduced from Reference [46], where the noise spectrum is measured on two devices. Device B, labeled, is the device measured in this thesis.

field created by the short is in the direction of B_0, and therefore, current noise in the antenna contributes to dephasing. Work is currently underway in an enclosure where the device is rotated to achieve perfect alignment in the hope of improving the coherence times.

Since the work presented by Muhonen *et al.*, however, we have performed measurements that suggest the noise floor shown in Figure 3.3 is not limited by thermal radiation alone. This work was done in the context of the investigation of dynamical decoupling sequences on the electron qubit as will be presented in Chapter 4. While optimizing experimental parameters to achieve the longest possible coherences, we found that T_2 is dependent on the plunge level. The plunge level is the magnitude of the voltage pulse used to lower the potential of the donor with respect to the SET island, in order to move from the initialization phase to the qubit control phase. We quote the quantity in units of 'ARB V', which corresponds to the instruction sent to the Lecroy ArbStudio arbitrary waveform generator (ARB). The ARB actually delivers twice this voltage, as it has an output resistance of 50 Ω and expects to be delivering the voltage to a 50 Ω load. We use the output from two channels which are equal for the settings of this particular experiment. These outputs are then passed through voltage dividers before being connected to the cables in the cryostat. Channel 1 is passed through a 50:1 divider and is connected to the TGAC gate while Channel 2 is passed through a 40:1 divider and is connected to the DF1 and DF2 gates, as labeled in Figure 2.3.

Figure 3.4(a) presents the coherence times as a function of plunge level. Note that at the range of plunge levels investigated, the current through the SET is switched off. For each plunge level, we perform a 16,384-pulse CPMG to measure the coherence times, which should be limited by the noise floor shown in Figure 3.3(a). To obtain a point for a particular value of T_{FP}, we prepare the spin in the $|\downarrow\rangle$ state, pulse to the specified plunge level to perform the

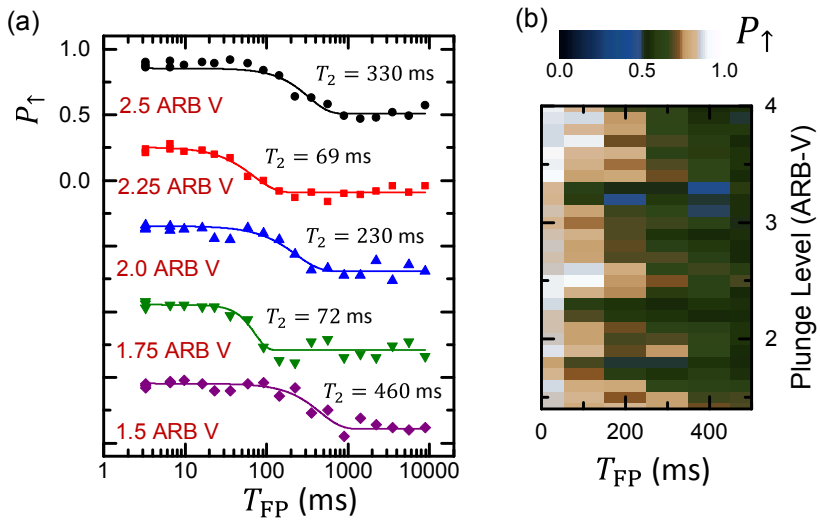

Figure 3.4: **Limiting coherences as a function of plunge level.** (a) At five different plunge levels, a 16,384-pulse CPMG sequence is used to measure the coherence time of the electron qubit. T_2 is not constant as a function of plunge level. (b) The same 16,384 pulse CPMG is used for a finer scan of a wider range of plunge levels. Due to time constraints, this experiment only uses six values of T_{FP} (10, 100, 200, 300, 400 and 500 ms) to reveal an indication of the coherence time.

16,384-pulse CPMG sequence with $\tau = T_{\mathrm{FP}}/16384$ and then pulse back to read the electron spin. Recall that the frequency being sampled in the noise spectrum shown in Figure 3.3(a) is $1/\tau$. Therefore, as we increase T_{FP}, the sequence samples lower frequencies in the noise spectrum. At $T_{\mathrm{FP}} = 1$ s, the frequency sampled is 16,384 Hz, which is still at the noise floor in Figure 3.3(a).

Note that before applying the CPMG sequence, the electron is taken to the equator of the Bloch sphere with a $(\pi/2)_x$ pulse, and the same pulse is applied at the end of the sequence to take it to the $|\uparrow\rangle$ state if it remained coherent. T_{FP} is the total free-precession time during the sequence as it does not include the time taken to apply the refocusing pulses. This is repeated 100 times to obtain the probability that the spin is found in the $|\uparrow\rangle$ state, $P_\uparrow$. The labels on the y-axis on the right correspond to $P_\uparrow$ for the 2.5 ARB V trace, and the remaining traces are offset for clarity. The traces start at $P_\uparrow \sim 0.85$ and once T_{FP} passes the coherence time, they decay to $P_\uparrow \sim 0.5$. Note also that we recalibrate the qubit resonance frequency at each plunge level to account for Stark shifts of the hyperfine interaction [44].

The traces are fit to $P_\uparrow(T_{\mathrm{FP}}) = P_f + (P_i - P_f)\exp[-(T_{\mathrm{FP}}/T_2)^n]$, with P_f and P_i forced to be equal for all five traces. The coherence times T_2 extracted show a clear plunge-level dependence, as shown in Figure 3.4(a). Note that the Hahn echo coherence time T_2^{HE} is also measured and is found to be independent of plunge level (data not shown). We then attempt to observe the dependence of T_2 for a finer scan and wider range of plunge levels. However, this scan would take over a day to complete, as each of the traces in sub-figure (a) take over an hour to acquire. Instead, we obtain a rough snapshot of the coherence times by focusing

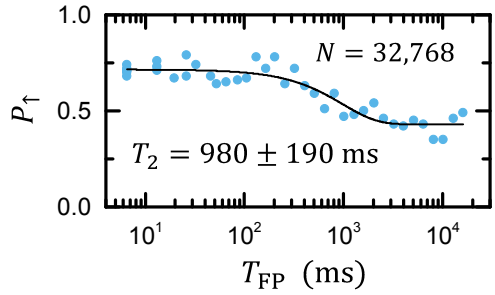

Figure 3.5: **Electron spin coherence time approaching 1 second.** $T_2 = 980 \pm 190$ ms for a 32,768-pulse CPMG sequence with optimized plunge-level.

on key points of T_{FP} around the expected values of T_2. We essentially acquire an echo trace with $T_{FP} = 50$, 100, 200, 300, 400 and 500 ms. Figure 3.4(b) shows these results for plunge levels between 1.5 and 4 ARB V. If we look at the echo snapshots (horizontal slice) at 1.8 and 2.3 ARB V, we observe that $P_\uparrow$ decays to ~ 0.6 at $T_{FP} = 0.1$ s, which means that $T_2 \lesssim 0.1$ s. This agrees with the values for T_2 at 1.75 and 2.25 ARB V presented in sub-figure (a), indicating that the plunge-dependence is repeatable and stable. The longer values of T_2 reported for 1.5, 2.0 and 2.5 ARB V also agree with the snapshots at these values. The snapshot also shows that the T_2 is short at 3.3 ARB V, confirming that the plunge dependence continues past the range investigated in sub-figure (a).

This study implies that the noise past ~ 10 kHz in Figure 3.3 is plunge-level dependent. As an additional experiment, we carefully tune the plunge-level and perform a 32,768-pulse CPMG sequence to sample the lowered noise floor. We obtain a new record electron spin coherence time in our system: $T_2 = 980 \pm 190$ ms, as shown in Figure 3.5. Note that the reduced contrast between the initial and final values of $P_\uparrow$ are likely due to a combination of less care taken in tuning the readout-phase and pulse errors accumulating at this higher N. On another note, this coherence time is approaching the spin relaxation $T_1 \approx 3$ s at this magnetic field (data not shown), recalling that T_2 is ultimately limited to $T_2^{\max} = 2T_1$.

To obtain a $T_2 \approx 1$ s, the noise floor can not be greater than $\sim$2 (rad/s)^{2}Hz^{-1}. The tuning-dependence of T_2 indicates that the noise floor cannot be solely from Johnson-Nyquist noise delivered by the antenna as suggested by Muhonen *et al.* [46]. It is possible that the radiation provides a baseline noise floor <2 (rad/s)^{2}Hz^{-1}, while at certain plunge levels, the qubit is exposed to a greater level of noise. However, we have not identified the source of the increased level of noise. The shape of the dependence of the coherence time on tuning level is reminiscent of the shape of the density of states (DOS) in the source and drain leads. We have always referred to the source or drain leads as a two-dimensional electron gas. However, in these devices, the narrow dimensions of the leads actually "give rise to quasi-one-dimensional DOS with highly nonuniform characteristics," as reported in Reference [51]. Indeed, we have found that the donor being probed in our measurements is in fact tunnel-coupled to the drain

lead, as will be elaborated upon in Section 3.4. It is possible that this coupling is the cause of the plunge-level dependence observed. Tuning the relative potentials of the donor electron and the drain result in the donor electron moving in and out of resonance with maxima in the DOS of the drain lead. We do not offer a model of how this results in the reduction in the observed coherence time as this is outside the scope of this thesis. However, we do point out an observation made in Reference [52], which shows the coherence times of two individual electron spin qubits confined in separated gate-defined quantum dots in the same isotopically-purified silicon substrate used for our devices. Veldhorst *et al.* found that the coherence time of the electron spin closer to the electron-reservoir lead exhibited a shorter coherence time. Perhaps our observations and theirs have the same physical origin.

3.3 Readout

The method used to readout the spin of the electron is simple and effective. The measurement fidelities achieved so far have been good, but the errors ($> 1\%$) are still an order-of-magnitude larger than the errors for qubit control ($\sim 0.1\%$). The readout method and associated analysis of the measurement signal has been described in Chapter 1. Pla *et al.* analyzed the sources of error and separated them into two categories: thermal effects and electrical errors. Electrical errors come from the electrical noise on the measurement signal and the filtering we install to reduce this noise. On the one hand, noise can cause a sample in the measurement signal to lie above the discriminating current threshold, leading us to erroneously conclude that it was a blip from a spin-up electron. On the other hand, the low-pass filtering can cause us to miss a blip. The blip widths follow a distribution given by the tunnel-rate of an electron on the SET island back on to the donor. The height of blips that are too narrow given the cut-off of the low-pass filtering will be attenuated and missed if they are below the discrimination current threshold. This leads us to erroneously conclude the electron was in the spin-down state. Pla *et al.* estimated the electrical readout error to be 18% in the ^{nat}Si device [29], while the error in the improved setup for the ^{28}Si device was estimated to be 2% by Muhonen *et al.* [46].

There is another source of error that could be categorized under electrical errors. In the readout phase, the electron spin is probed for a finite time T_{read}. The donor electron has a characteristic tunnel-out time, τ_{out}, such that the probability that the electron has not tunneled out after a time t is equal to $\exp(-t/\tau_{\mathrm{out}})$. Therefore, a true spin-up electron can be missed (identified as spin-down) if T_{read} is short compared to τ_{out}.

A readout error due to thermal effects is summarized in Figure 3.6(a). A spin-down electron may be allowed to tunnel out of the donor due to a state in the SET at that energy becoming available as a result of a non-zero electron temperature. In the measurements of Pla *et al.* [29], this error was estimated to be 28%, resulting in a total average measurement fidelity of 77% when combined with electrical errors. For the ^{28}Si device with improved electron temperature, however, investigations were not carried out to separate measurement and initialization errors

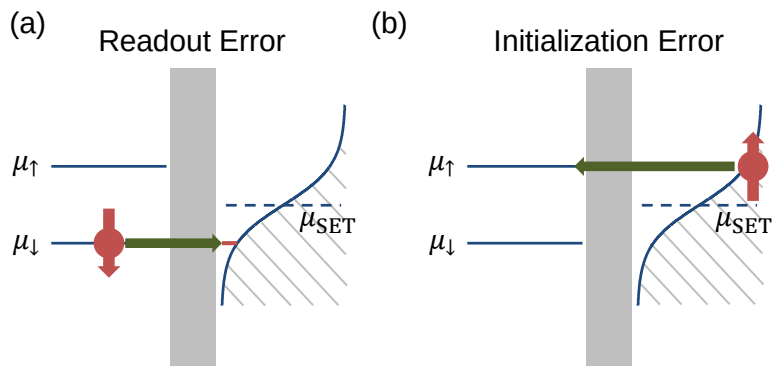

Figure 3.6: **Electron readout and initialization errors due to thermal effects.** A non-zero electron temperature depopulates states below μ_{SET} and populates states above μ_{SET}. (a) A spin-down donor electron is able to tunnel to an available state in the SET. (b) An electron in the SET has enough energy to initialize the donor with a spin-up electron.

due to thermal effects. Instead, the combined fidelity encompassing both state preparation and measurement fidelities is approximately 95-97% [46, 53] . This will be discussed in the next section of this chapter where we focus on initialization of the electron qubit. As experiments stand, electron measurement errors are of the order of 2-5%.

Here, we outline our method to achieve a higher electron readout fidelity. We utilize a tool inherently present in our setup to enhance the fidelity to $\sim 99.9\%$: the nucleus. The protocol simply involves mapping the electron spin onto the nuclear spin, and then reading the state of the nucleus instead, as proposed by Reference [39]. When we read the electron spin, the electron tunnels to the SET and is not recoverable. In contrast, the readout of the nuclear spin is a quantum non-demolition measurement, as described in Chapter 1. Therefore, the single-shot readout of the nuclear spin can be repeated arbitrarily many times to significantly reduce the probability of obtaining an error from the readout of the electron state.

The power of quantum non-demolition measurements is easy to understand. To illustrate this, we determine the probability of incorrectly measuring the nuclear state as a function of the number of times the readout is repeated, N. We define the measurement error ϵ_{qnd} to be the probability of obtaining at least $N/2$ incorrect individual readouts. The error per readout is ϵ_1, which can come from the incorrect rotation of the electron conditional upon the nucleus or an incorrect reading of the electron state. The probability of error ϵ_{qnd} is thus given by

$$\epsilon_{\mathrm{qnd}} = \sum_{k=\lceil N/2 \rceil}^{N} \binom{N}{k} \epsilon_1^k (1-\epsilon_1)^{k-1} \approx \binom{N}{\lceil N/2 \rceil} \epsilon_1^{\lceil N/2 \rceil}. \tag{3.1}$$

The approximation on the right-hand side of the above equation is valid for $\epsilon \ll 1$. From the approximation, it is easy to see the exponential power of quantum non-demolition measurement in reducing the probability of a readout error. For example, a 5% single-shot error probability

ϵ_1 repeated 13 times yields $\epsilon_{\text{qnd}} \approx 1$ ppm. Note that in this model, we have assumed that the nuclear spin does not change. The nuclear spin relaxation times T_{1n} are extremely long and have not been measured. However, in the presence of repeated donor electron tunneling events, the lifetimes of the nuclear states are reduced and are different for the $|\Downarrow\rangle$ and $|\Uparrow\rangle$ states. The $|\Downarrow\rangle$ state is relatively short-lived due to a flip-flop process through which the $|\uparrow\Downarrow\rangle$ state decays to the $|\downarrow\Uparrow\rangle$ state [32]. As we have not quantified the lifetimes in our device, we use the value measured by Pla *et al.* in the natural-silicon device: 65 s. This limits the fidelity of the measurement scheme as the probability that the nucleus remains in the same state is $\exp(-t/65)$. Even still, in the conservative example of $\epsilon_1 = 5\%$, the measurement fidelity can exceed 99.9% with 7 repeated measurements. Thus, in practice, the fidelity of this scheme is limited by the fidelity of mapping the electron spin on to the nuclear spin.

This mapping can be achieved in several ways. One example is shown below for an arbitrary electron state, $\alpha|\uparrow\rangle + \beta|\downarrow\rangle$, and an arbitrary nucleus state, $\gamma|\Uparrow\rangle + \lambda|\Downarrow\rangle$. The swap between their states is achieved by the application of three consecutive pulses: $\nu_{n\uparrow}$, $\nu_{e\Uparrow}$ and $\nu_{n\uparrow}$, in the notation defined in Chapter 1.

$$\begin{pmatrix}\alpha\\ \beta\end{pmatrix} \otimes \begin{pmatrix}\gamma\\ \lambda\end{pmatrix} = \begin{pmatrix}\alpha\gamma\\ \alpha\lambda\\ \beta\gamma\\ \beta\lambda\end{pmatrix} \xrightarrow{\nu_{n\uparrow}} \begin{pmatrix}\alpha\lambda\\ \alpha\gamma\\ \beta\gamma\\ \beta\lambda\end{pmatrix} \xrightarrow{\nu_{e\Uparrow}} \begin{pmatrix}\beta\gamma\\ \alpha\gamma\\ \alpha\lambda\\ \beta\lambda\end{pmatrix} \xrightarrow{\nu_{n\uparrow}} \begin{pmatrix}\alpha\gamma\\ \beta\gamma\\ \alpha\lambda\\ \beta\lambda\end{pmatrix} = \begin{pmatrix}\gamma\\ \lambda\end{pmatrix} \otimes \begin{pmatrix}\alpha\\ \beta\end{pmatrix} \tag{3.2}$$

The probability of an error being introduced in this mapping is a combination of imperfect rotations and non-zero excitation probabilities at the unintended transitions. The selectivity is very high in our system, where the ESR transitions are split by ~ 100 MHz with excitation bandwidth ~ 1 MHz, and the NMR transitions are split by ~ 30 MHz with excitation bandwidth ~ 30 kHz. Therefore the fidelity of the entire scheme is limited to the electron control fidelity, $F_c \approx 99.9\%$.

This method of reading the electron spin desensitizes the measurement to electrical noise and thermal effects and has already been used in Reference [53] to achieve readout fidelities $\sim 99.9\%$.

3.4 Initialization

Here we present work done to improve initialization fidelities. In the previous section on readout, we stated that the bare fidelity for electron spin state preparation and measurement (SPAM) is approximately 95-97% [46, 53]. The error in initialization is approximately 2-4%. Figure 3.6(b) shows how thermal effects can lead to loading a spin-up electron onto the donor. However, one should note that if μ_{SET} is between $\mu_\uparrow$ and $\mu_\downarrow$ as shown in the figure, then the expected error due to thermal effects is much lower than observed. For an electron temperature of 100 mK,

both readout and initialization errors should be approximately 30 ppm (at 1.55 T). In his Ph.D. thesis, J. P. Dehollain states that SPAM errors were unchanged at lower fields, reinforcing that thermal effects are not limiting fidelities. Given this information, we realize that we do not have an accurate model of the exact mechanism responsible for electron qubit readout and initialization.

Nevertheless, we have devised a scheme to improve initialization fidelities by over an order of magnitude. Combined with the readout technique of mapping the electron spin onto the nucleus, our SPAM errors are reduced to less than 0.1%. Before presenting the details of the technique and the results obtained, we mention two other possible schemes for initializing the electron spin with high fidelity. The first possibility is to load the donor electron and wait for a time that is many multiples of T_1, the spin-relaxation time. Given that T_1 is in the order of seconds for our electron spin qubit, the initialization time would be in the order of a minute. This would not be suitable for quantum algorithms employing rounds of error correction, as ancillary qubits would need to be initialized multiple times during the computation [50]. Another option is to employ the same strategy we have for high-fidelity readout, but in reverse. We can initialize the nucleus in an eigenstate with high fidelity using strong projective measurements. Its prepared state could then be mapped on to the electron spin using the swapping protocol described in the previous section. The disadvantage is that, while the electron is initialized with high fidelity, the nucleus is not. This may be an issue in schemes where the nuclear spin is to be used as a resource for the electron qubit [54], as we propose in Chapter 5.

Our scheme to achieve high fidelity electron spin initialization, without the use of the nucleus, is based on measurement of the electron spin. There are two equally applicable explanations of the mechanism: one is in the context of the knowledge of the prepared state, and the other is in the context of the back-action that the measurement has on the spin state [55, 56]. We begin by explaining the scheme in the first context. In the readout stage, we align μ_{SET} to be between $\mu_\uparrow$ and $\mu_\downarrow$ for some time T_{read}. If we detect a blip in the current, then we know with some high probability that the electron that tunneled out was in the spin-up state. However, if we do not detect a blip, then we know with a high probability that the electron that is on the donor is in the spin-down state. As T_{read} increases with respect to τ_{out}, the tunnel-time of the donor electron, we can assign an increasing probability to the electron being in the spin-down state. Thus, the probability that we have initialized a $\mu_\downarrow$ state is controlled by the ratio $T_{\mathrm{read}} : \tau_{\mathrm{out}}$, assuming that no blip occurred. This relation will be quantified from the experimental data.

We can also think of the measurement steering the electron spin into the desired eigenstate [55, 57]. Consider a weak measurement, where $T_{\mathrm{read}} < \tau_{\mathrm{out}}$. The basic idea is that if, in our example, there is no blip in the current, then the arbitrary qubit state will be steered towards the $|\downarrow\rangle$ state. Extending this to $T_{\mathrm{read}} \gg \tau_{\mathrm{out}}$ results in a state that is increasingly kicked towards the $|\downarrow\rangle$ state.

The protocol, in practice, is simple. First, we move to the readout level to load a spin-down electron in the usual manner, where the initialization fidelity is not sufficiently high. Then, we

wait until there is no blip for $N\tau_{\text{out}}$, where N is set to achieve a targeted initialization fidelity. If a blip occurs before $N\tau_{\text{out}}$, the clock is restarted. Once no blip has been detected for a time $N\tau_{\text{out}}$, the qubit can be pulsed away from the readout level, as it has been steered to the $|\downarrow\rangle$ state with the targeted fidelity. Note that this protocol can take a long time to be successful, as the clock may need to be restarted several times. This is the one drawback of the protocol, though it would still be faster than waiting for the spin to relax into its ground state.

Clearly, this protocol requires real-time feedback based on the measured current. For our proof-of-principle demonstration, however, we employ post-processing as we do not yet have real-time feedback capabilities in our setup. Our sequence, shown in Figure 3.7(a), starts by moving to the readout level for 20 ms. This serves as our initialization stage. We then plunge the level of the donor below that of the SET, moving out of the measurement phase such that back-action stops for 1 ms. The electron qubit is then pulsed back to the readout level once again to measure the state of the electron prepared in the initialization stage. The sequence is repeated 40,000 times to obtain statistics. We then post-process the current traces to extract t, the length of time between the end of the last blip in the initialization stage and the pulsing to the plunge phase, as illustrated in Figure 3.7(a). We bin t in 1 ms bins, only taking traces with $t > 0$. In other words, we exclude those traces where an electron has not been loaded onto the donor before pulsing to the plunge stage.

Figure 3.7(b) plots $P_\uparrow$ as a function of t, where $P_\uparrow$ is the fraction of current traces with a blip in the electron spin readout stage. We fit the data to an exponential decay $P_\uparrow = P_{\uparrow 0}\exp(-t/\tau) + P_{\uparrow\text{min}}$. We find that the data fits well with $\tau = 2.1$ ms, which is approximately equal to the tunnel-out time of the donor electron τ_{out}. One striking result is that the initial spin-up probability $P_{\uparrow 0} = 0.77$. Recall that initialization is achieved by aligning μ_{SET} directly between $\mu_\uparrow$ and $\mu_\downarrow$ such that, to a high probability, a spin-$|\downarrow\rangle$ is loaded. Our model therefore must be incomplete, as $P_{\uparrow 0}$ represents a 77% error in the initialization fidelity prior to steering.

For now, we focus on the initialization error achieved with steering, $P_{\uparrow\text{min}} = 4\%$. However, this does not mean that our initialization fidelity is 96%. It is likely that the initialization fidelity is actually higher than this, but errors during the readout stage cause us to mistake some spin-$|\downarrow\rangle$ electrons as spin-$|\uparrow\rangle$ electrons due to the electrical or thermal effects, as described in Section 3.3.

To measure the true initialization fidelity, we employ the measurement technique introduced in the previous section to improve the readout fidelity. In reference to Figure 3.7(a), the measurement stage no longer consists of a single-shot electron spin readout. During the plunge, the electron spin is mapped on to the nucleus, which is then measured with high fidelity. The results are shown in Figure 3.7(c), where $P_\uparrow$ is plotted as a function of t normalized to $\tau_{\text{out}} = 2.1$ ms. Firstly, we point out that $P_{\uparrow 0}$ obtained from the fits in sub-figures (a) and (b) are not equal, reinforcing that our model for electron spin initialization must be incomplete. Nevertheless, the fit shows that the initialization error achieved is $P_{\uparrow\text{min}} = 0.7\%$. Given that the readout fidelity is $> 99.9\%$, the saturation value truly represents the fidelity with which the

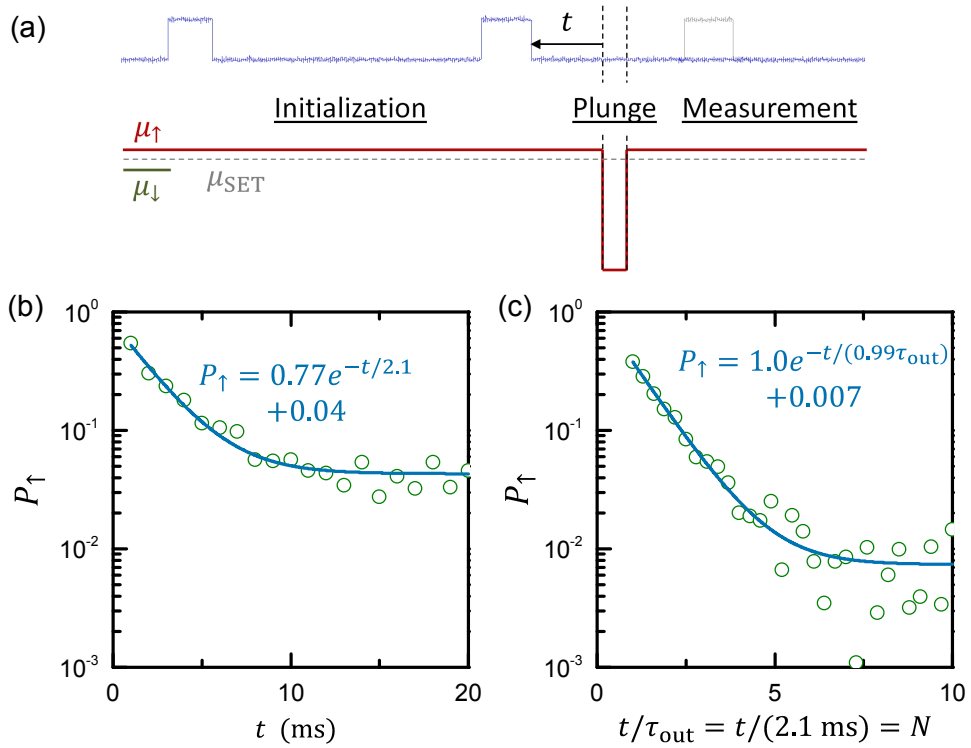

Figure 3.7: **Steered initialization of the electron spin.** (a) In the initialization stage μ_{SET} is aligned between $\mu_\uparrow$ and $\mu_\downarrow$. t is the time over which the electron spin is steered towards the $|\downarrow\rangle$ state. After plunging for 1 ms, the electron is pulsed to the measurement stage. (b)-(c) The results of the steering protocol are plotted. In (b), readout of the electron is performed as illustrated in (a), i.e. via single-shot readout of the electron spin. In (c), readout of the electron spin is achieved via the nucleus, to remove the effect of errors in the electron spin measurement.

electron was initialized in the spin-$|\downarrow\rangle$ state: 99.3%.

In further work carried out by S. Simmons, the initialization fidelity was improved to exceed 99.9%. This was based on the hypothesis that the 99.3% initialization fidelity (Figure 3.7(c)) was limited by missed blips in the initialization stage (Figure 3.7(a)). For example, consider a current trace in the experiment that shows a blip with $t = 20$ ms. We would expect that the loaded electron would be 'steered' towards the spin-$|\downarrow\rangle$ state for 20 ms. However, it is possible that the donor electron tunneled out and was re-initialized during that time, but no blip was detected due to the finite amplifier bandwidth (Section 3.3). This missed blip then resets the electron spin, such that the time for which it is actually steered is less than recorded, thus reducing the fidelity of the initialization protocol. As we will explain, S. Simmons managed to reduce the probability that the the spin-$|\downarrow\rangle$ electron tunnels out, thereby reducing the probability that a missed blip occurred during the steering phase.

Our standard model for a spin-$|\downarrow\rangle$ electron tunneling out is based on the thermal broadening of the SET island, as illustrated in Figure 3.6(a). However, the observed rate of these tunneling

events is orders of magnitude higher than the expected rate given the electron temperature measured in the device. S. Simmons discovered that a significant portion of these tunneling events were coming from tunnel-coupling of the donor electron directly to the drain lead, whose electrochemical potential was aligned below $\mu_{\downarrow}$. Thus, a spin-$|\downarrow\rangle$ electron could tunnel out to the drain, and then be reset by an electron from the SET island. By lowering the electrochemical potentials of the donor electron and the SET island with respect to that of the drain, the frequency of these tunneling events were significantly reduced. Therefore, the probability that a tunneling-event occurs during the initialization stage and is missed due to the finite amplified bandwidth is reduced. Repeating the steering experiment, S. Simmons was able to achieve an initialization fidelity $> 99.9\%$. Note that this data is not shown as the experiment with this modification was performed independent of the author.

3.5 Summary and Outlook

Our recent advancement in improving the fidelities of the fundamental operations on a single electron spin qubit have consolidated donors in silicon as a serious candidate for a full-scale quantum computer. The most significant change made was fabricating a device on isotopically-purified silicon. The improvement that this would bring with respect to natural silicon was already realized by Kane [24] in 1998. The near-elimination of the ^{29}Si bath reduced the linewidth of the qubit resonance frequency by over 3 orders of magnitude. The control fidelity ($F_c \approx 99.9\%$) is now limited by the experimental setup rather than the intrinsic device. It is likely that this will improve as the instrumentation technology and techniques improve.

The ability to use the nuclear spin has enhanced electron spin measurement fidelities to the level of the control fidelity, $\approx 99.9\%$. This simple technique adds to the list of advantages that donors have as a base for a quantum computer. We have successfully used measurement back-action on the state of the electron spin to initialize it with high fidelity. While the protocol is slow relative to requirements for error correction, we hope that this first step will lead to further advancements. Overall, we have simultaneously achieved fidelities of 99.9% for electron qubit initialization, control and measurement in one device.

This work reveals that there are two aspects of the behavior of our donor devices that require further study. Firstly, we have seen that the electron spin coherence time is dependent on device tuning. This may be a result of the tunnel-coupling of the donor electron to the drain lead which is likely to exhibit a nonuniform quasi-one-dimensional DOS, as discussed in Section 3.2. Secondly, our model for electron spin readout and initialization must be incomplete. The bare readout and initialization fidelities (not using the schemes discussed in this chapter) are worse than expected by thermal broadening given the electron temperature measured in the device. Solving these puzzles may lead to even further enhancements in the fidelities of the fundamental single qubit operations.

Chapter 4

Isotropic dynamical decoupling

In the previous chapter, we showed the results of coherence measurements on the electron spin qubit in isotopically purified silicon. The value obtained by CPMG sparked debate as to whether or not it was a suitable number to report in the context of quantum information processing. In this chapter, we aim to resolve this debate. We thus compare the performance of isotropic dynamical decoupling sequences from the XY family to CPMG. We find that a high order XY sequence, e.g. XY128, is capable of matching the coherence time measured by CPMG, confirming that the number published in Reference [46] is valid. In doing so, we have also established an appropriate isotropic sequence that is robust to the experimental imperfections in our system and suitable for quantum information processing purposes. Our investigation also reveals a phenomenon where the resonance frequency of the electron spin is modified following the application of microwave pulses. The mechanism responsible is not understood and will need to be addressed before scaling up to many-qubit systems.

The work presented in this chapter is currently being prepared for publication.

The author acknowledges (i) S. Simmons, with whom the measurements presented in this chapter were performed and (ii) S. A. Lyon for insightful discussions.

In Reference [46], we reported a coherence time of 560 ms for the electron spin qubit, as shown in Chapter 3. This was measured with a 16,384-pulse CPMG sequence, while the coherence time obtained with a Hahn echo was $T_2^{\mathrm{HE}} \approx 1$ ms. The use of CPMG sparked two points of criticism. The first is in regards to the fact that CPMG does not effectively preserve an arbitrary qubit state, and is therefore unsuitable for quantum information processing. Recall that the CPMG sequence initializes the qubit in the $|+y\rangle$ state (the state oriented along the $+y$-axis on the qubit Bloch sphere) and uses refocusing pulses oriented along that same axis. Given experimental imperfections, the sequence is known to only be effective at preserving the magnetization along that y-axis, such that an arbitrary input state would not be protected from decoherence. Therefore, such a sequence, where all refocusing pulses are of the same phase, is unsuitable for use in a quantum processor. An isotropic dynamical decoupling sequence would be required for the protection of an arbitrary state. In this chapter, we investigate the effectiveness of isotropic dynamical decoupling sequences from the XY family on our electron spin qubit. These sequences employ refocusing pulses along a combination of the x and y axes. We assume that the magnetization along the z-axis does not need to be actively preserved, as typically $T_1 \gg T_2$ in our system. The refocusing pulses in the sequences we discuss all have a delay τ between them. We do not include a discussion of sequences with varying inter-pulse spacing such as Uhrig dynamical decoupling [58].

In our previous work [46], CPMG was used for its simple execution, solely to quantify the coherence time in our system. This leads to the second point of criticism. In bulk NMR experiments, CPMG has been known to produce anomalously long echoes that do not reflect the usable coherence times of the systems tested. This cast doubt as to whether or not the coherence time we reported using CPMG was a valid quantity. In this chapter, we show empirically that the $T_2 = 560$ ms reported earlier was, in fact, valid, by matching it with an isotropic sequence that does not exhibit anomalous echoes in bulk.

In carrying out this investigation, we also uncovered a non-ideal phenomenon present in our device that is unrelated to the debate of the suitability of CPMG. We find that each pulse of microwave excitation delivered to the qubit has the undesired effect of shifting its resonant frequency. This has important implications for the testing of isotropic dynamical decoupling sequences, as will be discussed at the end of the chapter.

We begin this chapter by providing a brief introduction to bulk magnetic resonance experiments, in contrast to the single spin measurements presented in this thesis.

4.1 Bulk magnetic resonance experiments

Newly entering the spin qubit community today, it is easy to fall under the impression that magnetic resonance experiments have always been performed with single spins. This is, of course, not true. The field of magnetic resonance experiments on ensembles of spin-centers has been established for decades. The first experiments were conducted by Rabi in 1938 with a beam

of lithium chloride molecules. In 1946, two further experiments [59, 60] laid the foundation for the experimental setups for NMR on liquids and solids. The concept of a spin echo was then established by Hahn in 1950 [20]. Bulk electron spin resonance experiments were developed in parallel with their NMR counterparts.

Magnetic resonance in a single molecule had only just been achieved in 1993 [61, 62]. The key hurdle to be overcome was the detection of the tiny magnetic moment. In ensemble experiments, the collective magnetization of the spins can be detected directly when the ensemble contains $\sim 10^{10}$ electrons or $\sim 10^{16}$ nuclei. In the experiments of Wrachtrup [61] and Kohler [62], on the other hand, an optical detection scheme was employed. The technique used to detect a single electron spin in this thesis is spin-to-charge conversion with subsequent charge detection, as described in Chapter 1.

Before proceeding, we highlight two differences between single spin and bulk measurements. The first relates to inhomogeneities in the experiment. In a bulk experiment, each spin is in a different position in the sample, and can therefore experience different magnitudes of the inhomogeneous static and oscillating fields. This is referred to as a spatial ensemble. For a single spin measurement, no such spatial sampling occurs. Instead, inhomogeneities arise through changes in experimental parameters with time. This is referred to as a time ensemble. Note that bulk measurements would also have a component of the time ensemble. The other key difference is in the Hamiltonian of the system. In bulk measurements, interactions between like-spins are often the key terms that limit coherence times. For a single spin experiment, there would ideally be no other like-spins in the vicinity, and the limiters of coherence would depend on the particular system.

In the next section, we provide a history of the anomalous echoes produced by the CPMG sequence in bulk experiments. It is useful to first understand the difference in the way these measurements are performed in bulk as compared to the spin-to-charge conversion technique we use. The difference lies in the way the *echo* at the end of the sequence is measured, as defined in Chapter 1. As we have seen, we can directly readout the spin state of the electron by energetically discriminating between its $|\uparrow\rangle$ and $|\downarrow\rangle$ states. As a result, we only have access to measurement of the z-magnetization. If we apply a sequence to our qubit and want to measure the expectation value in the y-direction, for example, we must map this to the z-axis with a $(\pi/2)_x$-pulse. In contrast, in bulk experiments, induction coils are used to directly measure the magnetization in both the x and y axes.

A Hahn echo experiment is performed similarly in both cases. The spins start initialized in their ground state. The sequence applied is then $(\pi/2)_x - \tau/2 - (\pi)_x - \tau/2 - echo$. In a bulk experiment the echo occurs when the spins 'rephase' and their magnetizations align on the y-axis, producing a signal in the detection circuitry. In our experiment, however, we map the echo onto the z-axis with another $(\pi/2)_x$ pulse. We then repeat this measurement to gain statistics on the mapped expectation value. This translates to the echo height obtained in a single run in a bulk experiment. In both cases, the experiment is repeated for varying τ to

extract the coherence time T_2^{HE}.

For a CPMG experiment, the process is the same as described for the Hahn echo in our single spin case, except that N refocusing pulses are applied along the y-axis. To obtain the decay as a function of time, we must repeat the experiment for each value of τ or N used. On the other hand, in a bulk experiment, an echo occurs after each π pulse, and there is no requirement to disrupt the sequence to obtain the echo. Therefore, in a single run, N echoes can be obtained from an N-pulse CPMG to observe the decay of the amplitude of the echo with time up to $N\tau$ seconds.

4.2 The debate about the validity of CPMG

The purpose of this section is to provide the reader with a historical background of the anomalous echoes produced by CPMG in bulk experiments as well as to provide legitimacy to the doubt over the validity of the coherence time we measured using CPMG.

The anomalous echo obtained by applying a many-pulse CPMG sequence was first independently reported by both Dementyev [63] and Watanabe [64] in 2003. The spin of choice was the ^{29}Si isotope which has a natural abundance of 4.7%. T_2^{HE} was measured to be ≈ 5.6 ms, while the CPMG echoes persist to over $100 \times T_2^{\mathrm{HE}}$. At first glance, it seems that this could be a result of the CPMG sequence sampling a different portion of the noise spectrum, as we claim for our system [46]. However, the anomalous echoes appear for a range of τ in the CPMG, such that the noise sampled is over the same frequency range as sampled by the Hahn echo. Although an explanation is not provided in the original papers, Dementyvev, of the Barrett group, states that their "results strongly suggest that the effects are due principally to the ^{29}Si homo-nuclear dipolar coupling [63]."

If the effect is a result of the dipolar coupling between the spins in the ensemble, then it should not be of concern to an experiment probing a single isolated spin that is not coupled to a bath of identical spins. However, in 2005, Franzoni and Levstein reproduced the anomalous echo with polycrystalline C_{60}, and provided an explanation of the phenomenon that does not rely on dynamics due to dipolar coupling. In their paper, they state that the two system requirements for the observation of the anomalous echoes are "(i) an RF field inhomogeneity or a highly inhomogeneous line able to produce different tilting angles in different sites of the sample and (ii) the absence of spin diffusion (noneffective flip-flop interactions) [65]." Their explanation compared the long-lived CPMG tails to stimulated echoes [20], where "some magnetization is preserved in the direction of the external magnetic field, having a decay time" [65] much longer than the coherence time. With this, one would conclude that the effect would be visible for a single spin as well. Condition (ii) is met quite easily, as the absence of a bath of like-spins leads to an absence of spin diffusion. Condition (i) could also be achieved considering inhomogeneities in the time ensemble, rather than the spatial ensemble relevant to bulk experiments.

A debate on the mechanism responsible for the anomalous echoes then ensued. In 2007 and

2008, the Barrett group published two papers on their explanation of the phenomenon [66, 67]. They calculated the evolution of the system subject to the dynamical decoupling sequences for up to 9 spins (limited by computation capabilities) using average Hamiltonian theory. They showed that the anomalous echoes were not expected analytically when the sequence was treated using the ideal δ-pulse approximation (zero-duration π-pulses). They stated that "the dipolar coupling has a many-body effect during any real, finite pulse [66]." Figure 4 of Reference [66] highlights the 'coherence transfer pathways' that cause the long-lived tails. The effect is not trivial to understand, but the key point is that dipolar couplings are a necessary ingredient for the phenomenon.

We will also mention that the anomalous echo was observed in GaAs, with the ^{75}As nuclear spin by Watanabe [68], which is the only naturally abundant isotope. Therefore, in the sample, every other atom is an ^{75}As being probed, which certainly does not fall under the dilute ensemble limit required by the Levstein explanation. However, we have not found this work referenced or discussed in the literature. We refer the interested reader to a more recent paper, Reference [69], that compares the Barret and Levstein explanations and offers its own insight.

A detailed explanation of the phenomenon is beyond the scope of this thesis. However, it does appear that the dipolar coupling is a crucial ingredient, which is not present for an isolated single spin. We proceed by simulating the effect of pulse errors on a single spin to confirm that the anomalous echoes should not be observed.

4.3 Our system: single spin approximation

In the following sections, we will numerically simulate the application of dynamical decoupling sequences on a single electron spin. Before proceeding, we acknowledge that, while the simulations we will present in this section are for a truly isolated single spin, the donor electron investigated does have other spins in its local environment. Other electrons may couple to the probed electron through exchange or dipolar coupling. They could be confined either by traps at the oxide-semiconductor interface or by donors, as the ion implantation parameters were designed for eight donors (four pairs) to be implanted through the mask. However, resonant exchange or flip-flops are unlikely to occur, as the highly inhomogeneous electric fields in the device [70] severely Stark shift the donors, resulting in strong detuning. For example, the investigated donor has a hyperfine coupling of 98 MHz, whereas two other donors that have been measured in the same device have hyperfine interactions closer to the bulk value of 117 MHz. Having said that, we have searched for coupling to the investigated electron in an attempt to work towards two-qubit coupling. We carried out spin-echo double resonance (SEDOR) experiments to look for couplings as low as 50 Hz. As this yielded a negative result, we have not included the data in this thesis. In summary, our experimental results indicate that the investigated electron is not coupled with any significant magnitude to any other electrons.

As for nuclear spins in the environment, the electron is first and foremost coupled to its donor

nuclear spin via the hyperfine interaction. Nevertheless, the omission of the donor nuclear spin from the simulations is justified as experiments have shown the nuclear spin state to be static over long timescales [32]. The only other spins in the environment would be other nuclear spins in the lattice (^{29}Si or ^{31}P). Hyperfine interactions greater than 1 kHz would present themselves in the scans of electron spin resonance frequency [46, 71], but no such couplings were found. Therefore, we know that no nuclei with coupling stronger than 1 kHz are present in the vicinity of the donor electron. In conclusion, the treatment of the investigated electron as a truly isolated single spin is justified for our purposes of determining the performance of applied dynamical decoupling sequences.

4.4 Single spin simulations

In this section, we numerically simulate the application of CPMG sequences on a single spin. The aim of the simulations is to verify that the anomalous echoes do not appear for a single spin and that the coherence time obtained with CPMG is a valid measure of the true coherence. We focus on the Levstein explanation, as that of the Barrett group clearly does not apply to a single isolated spin. In reference to the spatial ensemble, they state that an inhomogeneity is required to 'produce different tilting angles in different sites of the sample [65]'. We interpret this to mean static inhomogeneities. In other words, in an inhomogeneous field, spins at different sites will experience an error in their respective rotations, but this error is systematic and repeatable. The inhomogeneity could lie in the static magnetic field B_0 and/or the oscillating field B_1. The equivalent phenomenon for a single spin is a slow fluctuation in the Hamiltonian parameters or the power of the microwave excitation, such that the rotation angle is different at each repetition.

We therefore simulate the echoes obtained for a single spin in the presence of static errors in B_0 and B_1, independently. We perform our simulations in the rotating frame. As described in Chapter 1, the Hamiltonian (angular frequency units) of a spin-1/2 qubit in an external magnetic field B_0 in the frame rotating at a frequency ω is $H_0 = \Delta\omega(\sigma_z/2)$. A *rotating* magnetic field B_1 with frequency ω then contributes the term $\omega_1(\cos(\theta)(\sigma_x/2) + \sin(\theta)(\sigma_y/2))$, where θ is its phase with respect to the rotating frame. For example, $\theta = \pi/2$ yields a pulse oriented along the $+y$ axis.

The qubit is initialized in the $|{+y}\rangle = (|\uparrow\rangle + i|\downarrow\rangle)/\sqrt{2}$ state. The CPMG sequence for the simulations is then defined to be $(\tau/2 - \pi_y - \tau/2) \times N$. During the delays, $\tau/2$, the Hamiltonian is H_0, which is equal to 0 in the resonant case. The π_y pulses are simulated by adding the term $\omega_1(\sigma_y/2)$ to the Hamiltonian for a time $T_\pi = \pi/\omega_1$.

To simulate the echo traces that would be seen in the experiment, we add noise to the term $\Delta\omega$, as it is the noise along z that contributes to dephasing. We can separate $\Delta\omega$ into two terms, $\Delta\omega = \Delta\omega_{DC} + \delta\omega$, where $\Delta\omega_{DC}$ is a fixed offset and $\delta\omega$ is zero-mean noise. $\delta\omega$ is shaped to have the same power spectrum as reported by Muhonen *et al.* [46], $(9 \times 10^{11})/(\omega_n)^{-2.5} + 6$

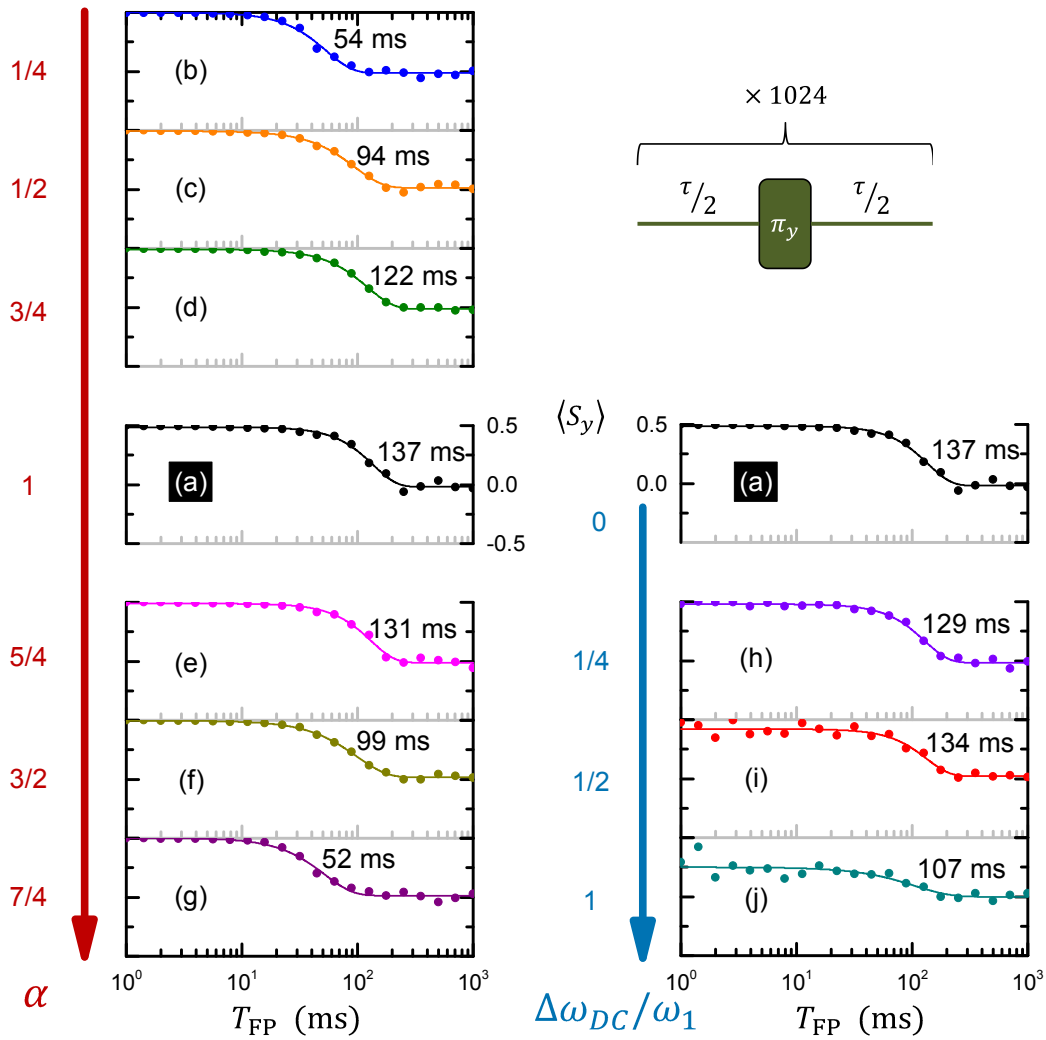

Figure 4.1: **Simulations of CPMG with the noise spectrum from the experiment.** (Top right) Pulse sequence used in the simulations. $\langle S_y \rangle$ is plotted against T_{FP} to extract coherence times for the 1,024-pulse CPMG sequence. (a) The control sequence is simulated without offsets in the rotation angle or detuning. (b-g) The echo traces for varying α, the rotation angle factor. (h-k) The echo traces for varying $\Delta\omega_{DC}$, normalized to ω_1.

$(\mathrm{rad/s})^2\mathrm{Hz}^{-1}$, where ω_n is the frequency in the noise spectrum. We then simulate the CPMG sequence with the noise added, repeating this 100 times to obtain statistics for the final state, $|\psi\rangle$. The output 'echo' is calculated as the average $\langle S_y \rangle$ over the 100 repetitions. Note that $\langle S_y \rangle$ is used since the qubit is initialized in the $|+y\rangle$ state. We have defined the Hamiltonian in units of angular frequency, such that $\langle +y|S_y|+y\rangle = 0.5$. This is directly related to the fidelity of the sequence. As the sequence should ideally return the spin back to the initial state, the fidelity is defined as the squared-projection of the final state onto the initial state: $\langle S_y \rangle = |\langle +y|\psi\rangle|^2 - 0.5$. We choose to plot $\langle S_y \rangle$ to remind the reader that these are simulations

and are not to be confused with $P_\uparrow$ used for the experiment. The echo trace is obtained by plotting the average $\langle S_y \rangle$ as a function of T_{FP}. Recall that T_{FP} is the total free-precession time, equal to $N\tau$.

Figure 4.1(a) shows the echo curve obtained for a 1,024-pulse CPMG, where $\Delta\omega_{DC} = 0$ and the π_y pulses are set to achieve a perfect π rotation in the absence of noise. We see a coherence time of 137 ms, matching the value reported in Figure 4(b) of Reference [46]. We then introduce systematic errors in the rotation angle by replacing the term ω_1 with $\alpha\omega_1$, such that a rotation angle of $\alpha\omega_1 T_\pi$ is performed. Figure 4.1(b,c,d,e,f,g) show the echoes obtained for the same simulation performed for $\alpha = 1/4$, $1/2$, $3/4$, $5/4$, $3/2$ and $7/4$, respectively. We see that the coherence times are not artificially extended for $\alpha \neq 1$, confirming that an anomalous echo is *not* produced for a single spin in the presence of ω_1 inhomogeneity.

Figure 4.1(h,i,j) show the echoes obtained for $\alpha = 1$, but $\Delta\omega_{DC}/\omega_1 = 1/4$, $1/2$ and 1, respectively, with $\omega_1/2\pi = 1$ MHz. This simulates the effect of an inhomogeneity in the static magnetic field. Again, the coherence times are not artificially extended, and we can conclude that this inhomogeneity is not sufficient to produce the anomalous echo.

Our first thought was to test exactly this in the experiment to rule out the idea that inhomogeneities give rise to anomalous echoes for a single spin. In other words, we would measure the echo as a function of intentional offsets in the experiment, as done in the simulations shown. However, if such significant inhomogeneities in the time ensemble are present in our system, then introducing fixed offsets would not represent a controlled study. Nevertheless, we test this out of curiosity. (Note that this was performed prior to the simulations). Instead of modifying the power, as done in the simulations, it is simpler in the experiment to modify the pulse duration T_p. T_p is modified to perform a rotation angle of $\beta\pi$, where β is swept from 1/2 to 3/2. This is achieved by setting $T_p = \beta T_\pi + 0.69$ μs. The additional 0.69 μs accounts for zero-padding of the pulse shape as well as rise and fall times. T_π is calibrated to be 1.44 μs from Rabi nutation experiments to achieve a π-pulse ($T_p = 2.13$ μs).

As shown in Figure 4.1(a), the coherence time for $\beta = 1$ is $T_2 \approx 350$ ms. Note that this is lower than reported by Muhonen *et al.* [46]. However, as we have shown in Chapter 3, the coherence time varies with device tuning which drifts over time. This was not optimized prior to this measurement, which could explain the discrepancy. This could also explain the behavior observed for the two points with the highest βT_π in the figure. We see that the coherence time corresponding to the orange point ($T_p = 2.67$ μs) is ≈ 560 ms and that of the purple point ($T_p = 2.85$ μs) is ≈ 70 ms. These measurements were carried out sequentially in a single run, in increasing order of βT_π. As the measurement spanned several hours, it is likely that the tuning of the device shifted by this point. Figure 4.1(b) shows the raw echo signals used to extract the coherence times. Comparing the first and last curves, corresponding to $\beta = 1/2$ and $3/2$, respectively, we see a clear difference in their quality. The low-T_{FP} half of the $\beta = 1/2$ curve is relatively flat, while that of the $\beta = 3/2$ oscillates. The simulations in Figure 4.1 show that the curves should be similar for symmetric offsets from a perfect π-pulse. The tuning of the device

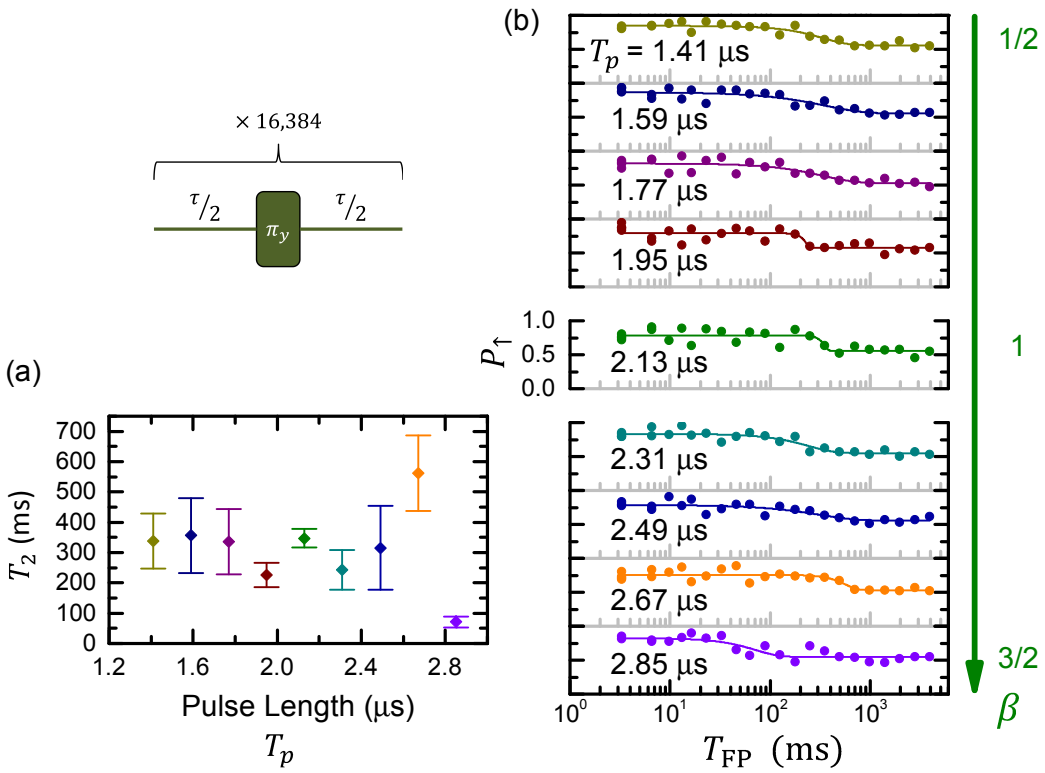

Figure 4.2: **Experimental results of CPMG with fixed offsets in the rotation angle.** (Top left) Pulse sequence used in the simulations. (a) Coherence times are plotted as a function of the length of the refocusing pulse. Given zero-padding in the pulses, $T_p = 1.41$ μs results in a $\pi/2$ pulse while $T_p = 2.85$ μs results in a $3\pi/2$ pulse. The coherence times are extracted from the data shown in (b), where $P_\uparrow$ is plotted as a function of T_{FP}. T_p is labeled for each trace, corresponding to β ranging from 1/2 to 3/2.

likely drifted during this measurement.

Nevertheless, it is fair to say that introducing a fixed offset in the intended rotation angle has not artificially extended the coherence time. However, unlike the simulations, this is not a controlled study of experimental conditions to confirm that the coherence time obtained by CPMG is a valid quantity. For that, we require a different strategy.

4.5 Strategy: isotropic dynamical decoupling

Our strategy to confirm the validity of the coherence time measured by CPMG is to check if it can be matched by a sequence that is known not to produce an anomalous echo in ensemble measurements. From the papers that reported the observation of these anomalous echoes [63, 65], it would seem that the Carr-Purcell (CP) sequence would be a suitable choice for a valid measure of the coherence time, as it does not exhibit an anomalous echo. However, it is known to suffer greatly from pulse errors, leading to the state being destroyed rather than

preserved [72]. We thus turn to sequences from the XY family, which have an additional crucial advantage. XY-type sequences involve pulses being applied on both the x and y axes, which makes them isotropic in preserving both the x and y components of the spin. This is necessary for use in a quantum computer, where an arbitrary input state would need to be preserved, as stated earlier. Therefore, if we are able to find an isotropic XY-type sequence that matches the coherence time measured by CPMG, then we both confirm the validity of the quoted quantity and determine a dynamical decoupling sequence that could be used in a full-scale quantum computer given the experimental imperfections in our system.

4.5.1 Sequences vs N (Simulations)

We begin with simulations of sequences from the XY-family to determine one that would be suitable given the noise spectrum present in our system. We use the simulation technique outlined in Section 4.4, where a single spin is considered in the rotating frame, with noise shaped to have the power spectrum reported in Reference [46]. The sequences we initially simulate are the (a) CPMG, (b) CP and (c) XY4 (or XYXY) sequences. With the qubit initialized in the $|+y\rangle$ state, the CP sequence is defined as $(\tau/2 - \pi_x - \tau/2) \times N$. The CP and CPMG sequences only differ in the phase of the applied pulses with respect to the initial state. The XY4 sequence is defined as $(\tau/2 - \pi_x - \tau - \pi_y - \tau - \pi_x - \tau - \pi_y - \tau/2) \times N/4$. Note here that the Rabi frequency $\omega_1/2\pi$ is chosen to be 500 kHz.

The results for $N = 16{,}384$ are shown in Figure 4.3(a-c). The CPMG yields $T_2 = 340$ ms, consistent with the maximum obtainable coherence time given the 6 $(\text{rad/s})^2\text{Hz}^{-1}$ noise floor. Note that this does not match the experimental value of 550 ms reported in Reference [46]. This observation is also pointed out by Muhonen *et al.* [46]. From the work of this thesis, we understand that the cause for this may be differences in the plunge level (Chapter 3) arising from drift between measurements. We see from Figure 4.3(b-c) that the CP sequence fails to preserve coherence past 20 ms while the XY4 sequence shows a coherence time of ~ 50 ms. The longer coherence time of CPMG should not be interpreted as an anomalous echo. As we will show, the CP and XY4 sequences are suffering from errors during the π-pulses.

To demonstrate this, we repeat the simulation but remove the noise in $\Delta\omega$ during the π-pulses such that the desired rotation is achieved perfectly. The coherence times from the three sequences, as shown in Figure 4.3(d-f), now all match at ≈ 330 ms. Therefore we can say that when ideal pulses are considered, the dynamical decoupling sequence can be treated as a filter for the noise spectrum independent of the phase of the constituent pulses [22]. However, when real pulses are considered, errors are introduced by the sequence itself that appear as a reduced coherence time. The robustness of the sequence to these errors is the key to the differences seen in Figure 4.3(a-c).

Before directly investigating sequence robustness, we repeat this simulation using other sequences from the XY family. The aim is to find an XY sequence that matches the performance of CPMG given the noise spectrum simulated. We look towards higher-order XY sequences,

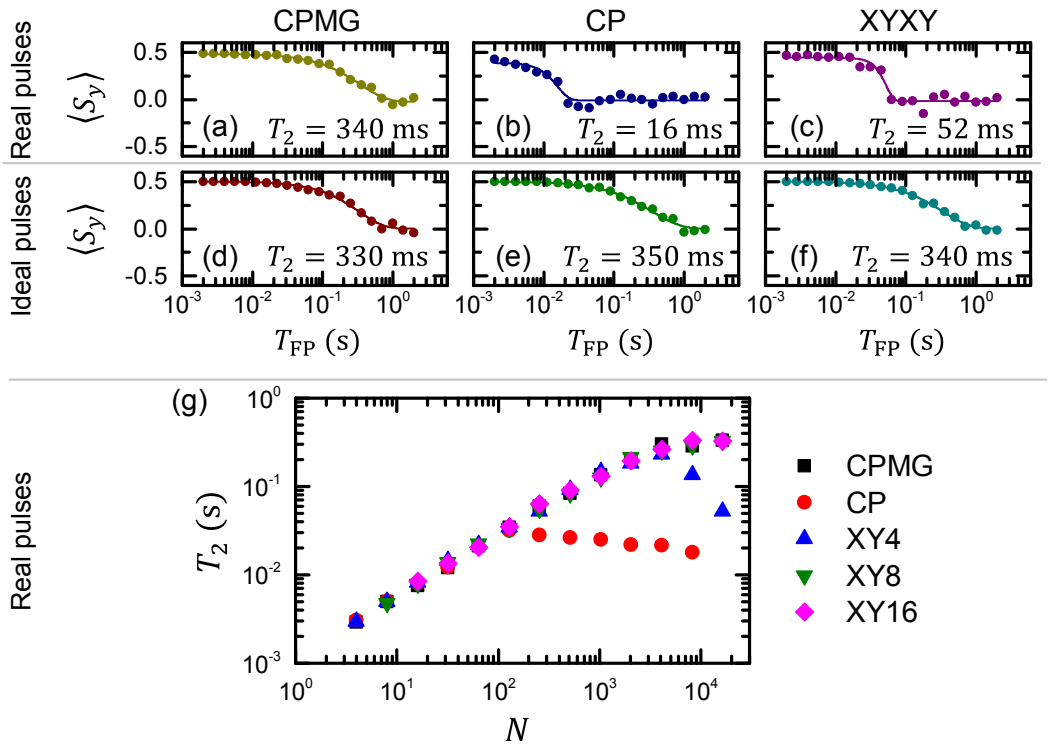

Figure 4.3: **Simulations of dynamical decoupling with the noise spectrum from the experiment.** (a-f) 16,384-pulse CPMG, CP and XYXY (or XY4) sequences are simulated with the initial state oriented along the $+y$-axis. $\langle S_y \rangle$ is plotted as a function of T_{FP} to extract coherence times using (a-c) real pulses and (d-f) ideal pulses. (g) The coherence times from a full set of simulations are plotted as a function of N. XY8 and XY16 match CPMG up to N = 16,384, while CP and XY4 deviate at lower N.

which are defined by the recursive function [73] defined in Algorithm 1.

Algorithm 1 seqXY(M)

```
if M == 4 then
    seqXY = XYXY;
else {if log2(M) is odd}
    subseqXY = seqXY(M/2);
    seqXY = [subseqXY subseqXY(end) subseqXY(1:(end-1))];
else {if log2(M) is even}
    subseqXY = seqXY(M/2);
    seqXY = [subseqXY π+subseqXY];
end if
```

This allows us to create the sequences XY8, XY16, XY32, and so on. For example, XY8 is XYXY-YXYX and XY16 is XYXY-YXYX-$\bar{X}\bar{Y}\bar{X}\bar{Y}$-$\bar{Y}\bar{X}\bar{Y}\bar{X}$. We simulate these sequences with real pulses, as done for Figure 4.3(a-c), and plot the extracted coherence times in Figure 4.3(g). We see that for low N, all sequences considered are able to match those of CPMG. We observe

that CP deviates at $N = 256$ pulses. After this point, the coherence slightly decreases with increasing N as, presumably, the errors from the pulses accumulate. XY4 only begins to deviate at $N = 4{,}096$, while XY8, XY16 and XY32 all match CPMG up to $N = 16{,}384$.

This is encouraging, as it suggests that even XY8 will be sufficient to match CPMG in the experiment. Before presenting the results of the experiment, we address the idea of the robustness of a sequence to errors with some additional simulations.

4.6 Sequence robustness assessment (Simulations)

In essence, the simulations above (Figure 4.3) are an assessment of the robustness of the sequence to jitter, or fluctuations, in $\Delta\omega$. Here, we simulate these sequences in the presence of fixed offsets in $\Delta\omega$ and ω_1, but without noise ($\delta\omega = 0$). We acknowledge that robustness to a fixed offset is not directly translatable to robustness to jitter. Nevertheless, for the purpose of gaining an appreciation of sequence robustness, a systematic analysis of fixed offsets will suffice.

We begin with offsets in the rotation angle, by modifying the magnitude of ω_1 by a factor α in our simulations. For this, we set the detuning frequency $\Delta\omega$ to 0, which means that the Hamiltonian in the rotating frame is equal to 0 when a pulse is not being applied. The operation of the sequence is therefore very easily understood as a series of rotations for the initialized $|{+y}\rangle$ state. For CPMG, the rotations about the y axis have no effect and the sequence is therefore completely 'robust' to errors introduced by a non-unity α. For CP, the rotations about the x-axis simply cause a total rotation of $N\alpha\pi$. The effect is difficult to visualize for the XY sequences, so we simulate the spin recovery for XY4, XY8 and XY16. Figure 4.4(a-c) plots $\langle S_y \rangle$ as a function of α and N. Consider the 32-pulse XY4 sequence, sub-figure (a), as an example. We see that the state is recovered (yellow) for α ranging from 0.9 to 1.1. Outside this range, $\langle S_y \rangle$ drops. Although it then later increases from the net effect of the errors, we clip the data to highlight the range over which the sequence is robust. As errors accumulate with an increasing number of pulses, we see this range decrease for increasing N. The XY8 sequence is more robust than XY4, as shown in sub-figure (b). XY16 is completely robust to any errors in α, as shown in sub-figure (c). This is easy to understand by looking at the sequence: XYXY-YXYX-$\bar{\mathrm{X}}\bar{\mathrm{Y}}\bar{\mathrm{X}}\bar{\mathrm{Y}}$-$\bar{\mathrm{Y}}\bar{\mathrm{X}}\bar{\mathrm{Y}}\bar{\mathrm{X}}$. The second half of the sequence is the mirror image of the first half, where each pulse is replaced by its negative. The 9th pulse undoes the error introduced by the 8th pulse, the 10th pulse undoes the error introduced by the 7th pulse, and so on. At the end of an XY16 period, the errors are reversed, such that α has no effect. This would not be true for XY32 and beyond, however, as their halves would not be mirror images. Nevertheless, the general trend holds (apart from XY16) that sequences of higher order are more robust.

The next parameter to test is $\Delta\omega$. For this, the evolution during the wait times is important in determining the effect of the sequence on the spin. We must therefore first understand how $\langle S_y \rangle$ behaves as a function of T_{FP} (or τ). While the result is intuitive and will be explained soon, we illustrate the behavior with the aid of simulations. We simulate the XY8 and XY32

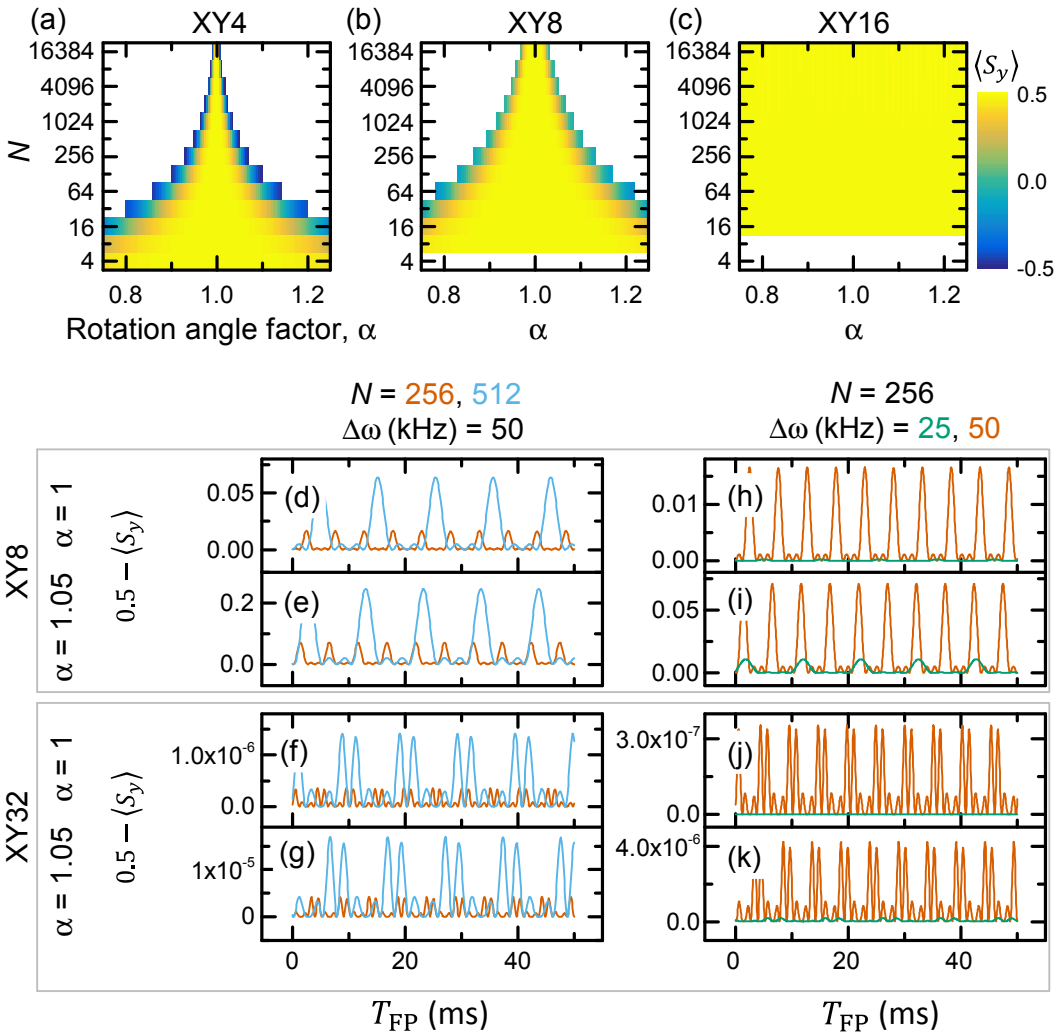

Figure 4.4: **Effects of offsets in rotation angle and detuning.** (a-c) Simulations are performed for XY4, XY8 and XY16 with the initial state oriented along the $+y$-axis. The state recovery, $\langle S_y \rangle$, is plotted as a function of the number of pulses and the rotation angle factor. Recall that XY8, for example, cannot be performed for $N < 8$. (d-k) The error in state recovery, $0.5 - \langle S_y \rangle$ is plotted for combinations of XY8 and XY32 with $\alpha = 1$ and 1.05 as a function of T_{FP}. The first column shows the effect of doubling N with a fixed detuning of 50 kHz. The second column shows the effect of doubling the detuning with $N = 256$.

sequences and plot the results in Figure 4.4(d-k), for $\alpha = 1$ and 1.05 with 1 μs π-pulse. Note here that we plot the error of the sequence, which is 'one minus the fidelity,' where the fidelity is defined as before. We plot this instead of $\langle S_y \rangle$ as the errors in spin recovery being investigated are $\ll 1$.

In the first column, sub-figures (d) to (g), the detuning is fixed at 50 kHz, while N is varied between 256 and 512. Firstly, we see that the fidelities are periodic with respect to T_{FP}. The key observation from all four sub-figures in this column is that when N is doubled, the fundamental

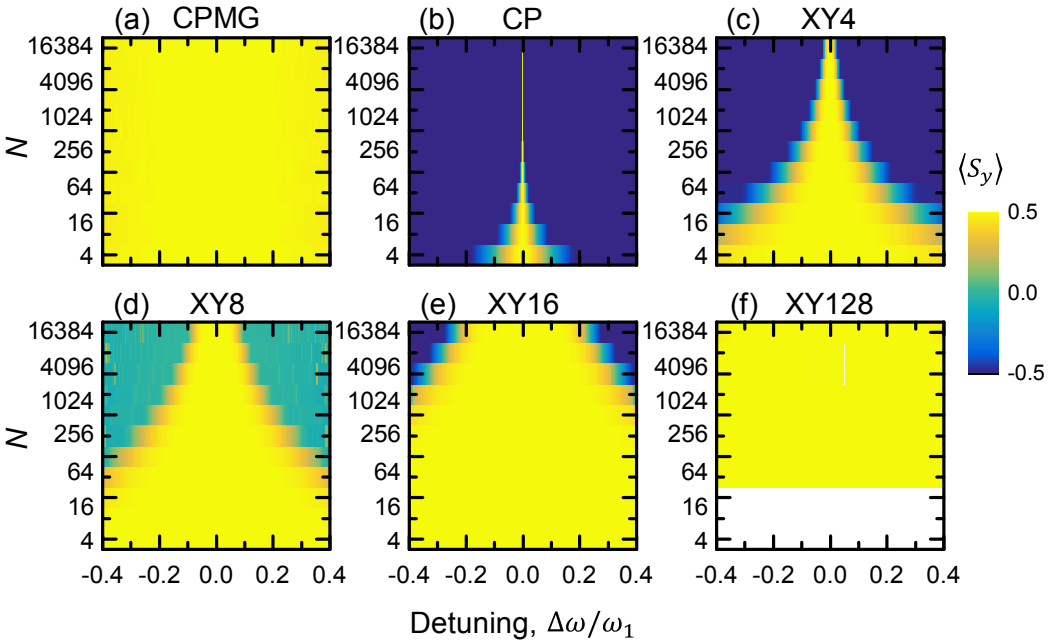

Figure 4.5: **Sequence robustness to offsets in detuning.** Simulations are performed for CPMG, CP, XY4, XY8, XY16 and XY128 with initial state oriented along the $+y$ axis. The state recovery, $\langle S_y \rangle$, is plotted as a function of the number of pulses and the detuning frequency. For each point, τ is varied to extract a minimum spin recovery, in accordance with the periodic behavior shown in Figure 4.4(d-k).

frequency of the oscillations is halved. Additionally, changing the sequence from XY8 to XY32 does not affect the fundamental frequencies. This has been tested and found true for arbitrary input states and all other sequences discussed (data not shown). Incidentally, comparison of the scales of the y-axes between XY8 and XY32 already illustrates the superiority of the higher order sequence.

In the second column, sub-figures (h) to (k), we fix $N = 256$, and vary the detuning between 25 and 50 kHz. Although less clear in sub-figures (h) and (j), we observe from (i) and (k) that the fundamental frequency of the oscillations is halved when $\Delta\omega$ is halved. Again, this holds true regardless of the input state (data not shown), the sequence, and α. From these plots, we deduce that the fundamental frequency is equal to $\Delta\omega/N$ when plotted against T_{FP}, or equal to $\Delta\omega$ when plotted against τ $(= T_{\mathrm{FP}}/N)$.

This is simple to understand. During the wait times, the state precesses with a frequency $\Delta\omega$. If τ is increased by $2\pi/(\Delta\omega)$, then the spin will simply accumulate a phase of 2π during the wait times such that the resulting state, immediately before the next refocusing pulse is to be applied, is unaffected. The periodicity of the fidelity with respect to τ (or T_{FP}) will be important to remember for Section 4.9.

For the purpose of quantifying sequence robustness, we use the knowledge of the fundamental frequency to extract a worst-case fidelity by simulating each sequence for one full period in τ.

We plot the results, as $\langle S_y \rangle$, in Figure 4.5 for CPMG, CP, XY4, XY8, XY16 and XY128. This is plotted as a function of N and $\Delta\omega$ (normalized to ω_1). We define the 'sequence bandwidth' to be the range of detuning over which the sequence successfully recovers the state. We clearly see that CPMG is highly robust against offset errors in the detuning, while CP is extremely sensitive, as the sequence bandwidth almost completely diminishes past 256 pulses. The robustness of the XY sequences is increased as the order is increased. Although not visible on this color scale, XY128 actually outperforms CPMG.

4.7 Experimental results

Armed with the evidence that higher order XY sequences should be able to match the coherence times measured by CPMG, we seek to verify this in the experiment. Figure 4.6 plots the echo traces obtained with XY4, XY8, XY16, XY32, XY64 and XY128. In each plot, the probability of spin recovery, $P_\uparrow$, is plotted as a function of the total free precession time, T_{FP}. Based on the simulations presented in Figure 4.3, we expect that XY4 will match CPMG up to $N = 4{,}096$, beyond which it would exhibit a shorter coherence time. Furthermore, XY8 should be sufficient to match CPMG up to 16,384 pulses. However, we find this not to be the case.

The first row of Figure 4.6 shows the echo traces for XY4, for $N = 128$, 256, 512 and 1,024. At $N = 512$, the coherence time is $T_2 = 74$ ms, which is still in line with that of CPMG. However, at $N = 1{,}024$, we see that the spin is not recovered at all for the range of T_{FP} in the scan. Firstly, the deviation from the ideal coherence time in the experiment occurs at a lower value of N than we predicted. Secondly, the simulations showed that past this critical value of N, a standard echo trace would still be obtained, just with a shorter coherence time. The result of the 1,024-pulse XY4 sequence is not expected.

The second row shows the results for XY8. This matches CPMG up to $N = 2{,}048$, with a coherence time of 160 ms. The 4,096-pulse XY8 sequence, however, fails to recover the spin state. While the behavior differs from that of the 1,024-pulse XY4 sequence, we see that $P_\uparrow$ is erratic before the state loses coherence. The characteristic behavior is clearer for the XY16, XY32 and XY64 sequences. Past their respective critical values of N, $P_\uparrow$ appears to exhibit reproducible oscillations before decoherence is reached. We indicate this critical value of N in Figure 4.6 by fitting a standard exponential decay to that plot for each XY sequence. The points are obtained in random order to exclude the possibility of the oscillations originating from a slow drift in experimental parameters. We have taken great care to calibrate the rotation angle and resonance frequency as best as possible. Despite this, these oscillations are reliably reproduced. We speculate on a possible explanation of this phenomenon in Section 4.9. For now, we shift our focus away from these oscillations and towards the last row in Figure 4.6, corresponding to the XY128 sequence. We see that XY128 successfully yields a standard echo trace for $N = 16{,}384$, where all lower-order XY sequences failed. Clearly, this must be due to the fact that it is more robust to the limiting errors in the system, which we address in Section 4.9.

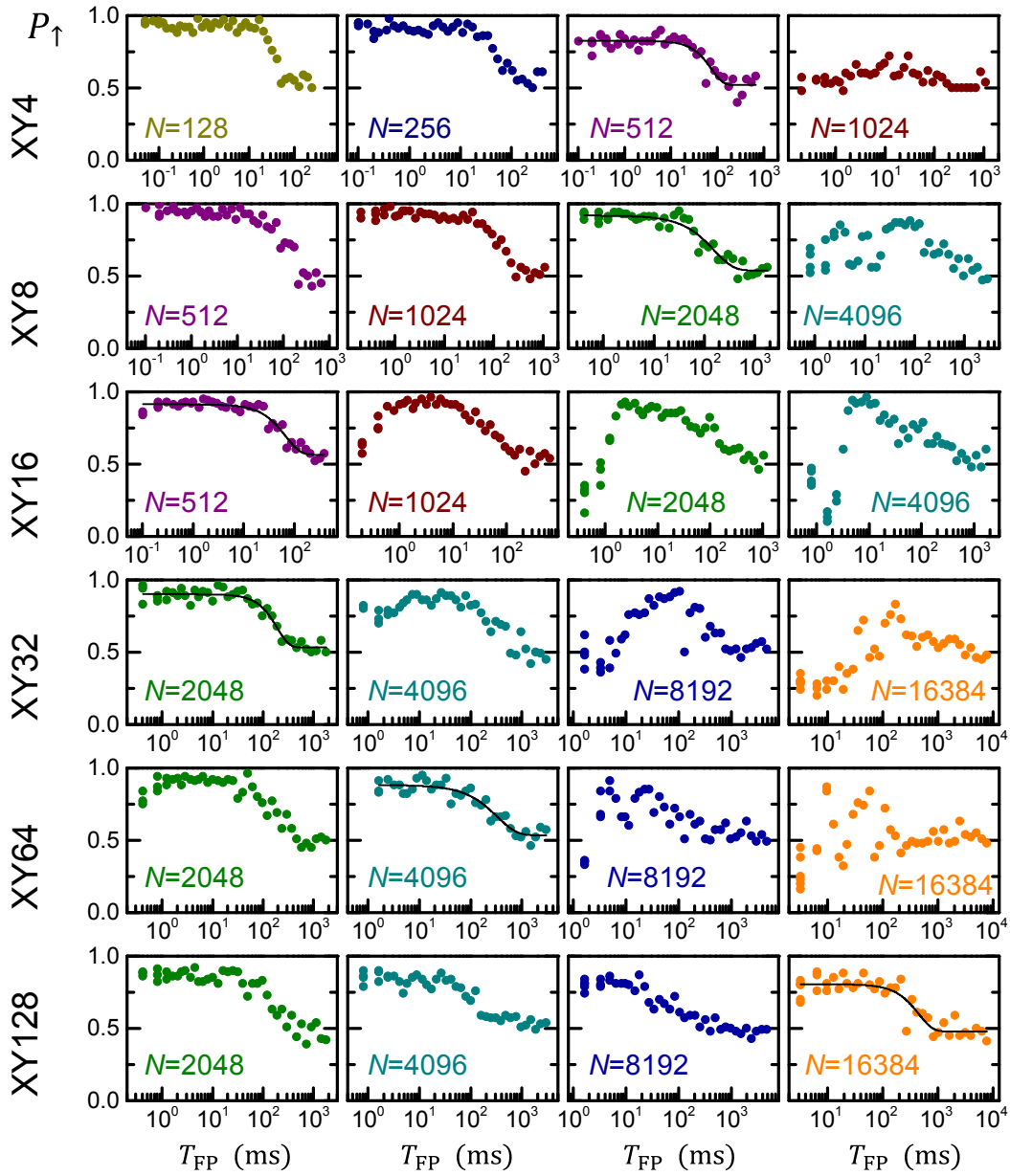

Figure 4.6: **Echo traces obtained from the XY family of dynamical decoupling sequences.** Each row corresponds to a particular base sequence, ranging from XY4 to XY128. For each sequence, four values of N are selected to show the maximum N for which the particular base sequence yields a standard echo trace. Beyond this, coherent oscillations appear in the traces. XY128 is successful in matching the performance of CPMG at $N = 16{,}384$, with $T_2 = 450$ ms.

We do point out, however, that the echo trace for the 8,192-pulse XY128 sequence has a very long stretch ($n < 1$ in the exponential fit) and thus yields an abnormally low coherence time. This is sometimes observed when there is a jump in device tuning. We did not retake this trace as it was only noticed after the experiment was completed. Nevertheless, the trace for XY128 with $N = 16{,}384$ appears as expected.

The coherence time obtained with the 16,384-pulse XY128 sequence is $T_2 = 450$ ms. Given the variability in the coherence times measured with CPMG at this value of N with device tuning, we conclude that XY128 successfully matches the performance of CPMG. Thus we have accomplished the goal set at the beginning of the chapter. We have found an isotropic dynamical decoupling sequence that is robust to the specific experimental imperfections in our system. We have also confirmed that the coherence time measured by CPMG is a valid measure of the qubit coherence, not suffering from anomalous echoes.

4.8 Sequence variations

In this section, we briefly address other strategies that failed in our attempt to have an XY sequence match CPMG. Our first hypothesis was that the sequence performance was suffering from rotation-angle errors. We thus tried to use BB1 pulses to account for these errors. The BB1 pulse is defined in Reference [74], where each π pulse is replaced by five pulses (as we use the symmetric version) designed to achieve the desired π rotation in spite of a systematic error in the magnitude of ω_1. The echo trace obtained for a XY16 using BB1 pulses with $N = 1{,}024$ is shown in Figure 4.7(a). Here, N refers to the number of wait-times τ that are present in the sequence, as there are actually 5,120 pulses. We observe reproducible oscillations as seen before. This, in fact, behaves worse than the 1,024-pulse XY16 sequence with standard π pulses shown in Figure 4.6. This suggests that rotation angle errors are not the cause for poor sequence performance. In hindsight, we should have also tried CORPSE pulses [75], which are designed to be robust to detuning errors. However, this was not done due to time constraints.

In this chapter, we have only investigated XY sequences constructed from Algorithm 1. Another family of sequences investigated in the bulk-NMR literature is concatenated dynamical decoupling (CDD), which is obtained through concatenation of the base sequence, XYXY [76–78]. CDD sequences are also isotropic and are expected to be quite robust to pulse errors. In the same way that we have used Algorithm 1 to find higher order XY sequences, increasing the level of concatenation for CDD increases the number of pulses in the base sequence. For completeness, we test if CDD can be used to match CPMG at 16,384 pulses. Note that we use the symmetric version of CDD as compared to the definition in Reference [76]. Concatenation level-1, 2, 3 and 4 yield base sequences with 4, 20, 84 and 340 pulses, respectively. Concatenation level-4 already has more pulses in its base sequence than XY128 (128 pulses). In the context of CDD, we use N to refer to the number of wait-times τ, not the number of pulses. For example, CDD level-4 corresponds to $N = 256$ even though it has 340 pulses. Level-4 with $N = 16384$

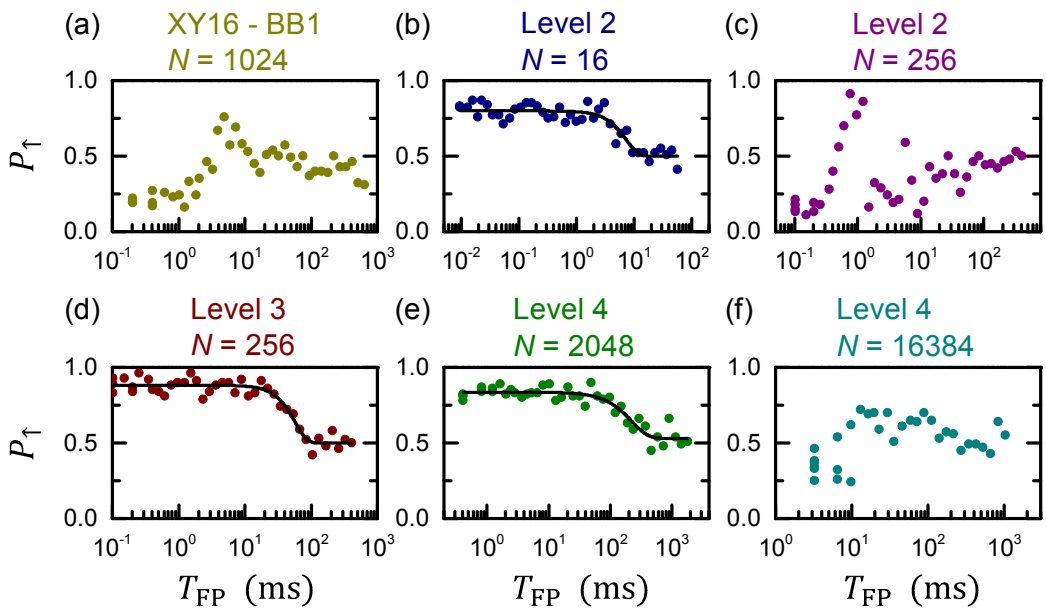

Figure 4.7: **BB1 pulses and concatenated XY.** (a) The echo trace is plotted for a 1,024-pulse XY16 sequence where each π-pulse is replaced with BB1 pulses. The spin state is not successfully recovered. (b-f) The echo traces are plotted for concatenated XY with varying levels of concatenation and N. Even at four levels of concatenation, the spin state is not successfully recovered for $N = 16{,}384$.

then corresponds to the base sequence being repeated 64 times.

We repeat the type of experiment presented in Figure 4.6, but with CDD. Figure 4.7(b-f) show the echo traces obtained. The values of N presented have been selected to provide a meaningful snapshot of the performance of CDD. We see that while level-2 succeeds at (b) 16 pulses, it eventually fails at (c) 256 pulses. Indeed, moving to level-3 concatenation does improve the performance, as shown by the successful echo trace obtained in sub-figure (d). Level-4 succeeds at (e) 2,048 pulses, but fails at (f) 16,384 pulses. Considering that CDD level 4 has more than twice the number of pulses as compared to XY128, we conclude that the family of sequences defined by Algorithm 1 outperforms CDD given the specific experimental imperfections in our system. Concatenated dynamical decoupling has similarly been studied in the context of singlet-triplet qubits [79] and found to fail in comparison to CPMG at a high number of pulses.

4.9 Pulse induced resonance shift

This section addresses the unexpected echo traces observed in Section 4.7. We offer an explanation for this phenomenon that is based on an observation made during measurements of this device in a different context. We then perform simulations based on our model which match the echo traces reasonably well.

The echo traces presented in Figure 4.6 exhibit reproducible oscillations as a function of T_{FP} before decoherence is reached. At first glance, this is reminiscent of electron spin echo envelope modulation (ESEEM) as studied in bulk ESR experiments [80]. ESEEM is caused by anisotropy in the hyperfine coupling between the electron and nearby nuclei. However, the depth of the modulation (deviation of $P_{\uparrow}$ from 1) of the echo traces in Figure 4.6 is much greater than we would expect from ESEEM [77]. More importantly, the oscillations observed in Figure 4.6 are certainly not periodic as is predicted by ESEEM. In fact, the oscillations almost seem periodic with $\log(T_{\mathrm{FP}})$.

We have explored the effect of the introduction of a fixed detuning $\Delta\omega$ in Figure 4.4(d-k) and found that this causes periodic oscillations as a function of T_{FP}. This leads to the hypothesis that the oscillations could be explained by a detuning $\Delta\omega$ whose magnitude decreases as T_{FP} is increased. This idea leads us to link our data to an observation made by our colleagues on the same device, but in a different context.

Our team has performed several experiments with this device, either probing the electron spin qubit or the nuclear spin qubit individually [44, 46, 47, 81]. In only one case have we performed an experiment that utilizes both qubits at the same time [53]. This required the application of both RF pulses in the MHz range to control the nuclear spin and microwave pulses in the GHz range to control the electron spin within a single sequence. An unexpected observation was made during these experiments. The resonance frequency of the electron qubit is shifted after the application of an RF pulse. This shift decays after some time of order 100 μs to 1 ms after the end of the pulse and its magnitude is correlated with the power of the RF pulse. We will refer to this phenomenon as pulse-induced resonance shift (PIRS). Our team does not have an explanation for the mechanism by which the RF pulse can induce such a shift that persists beyond the end of the pulse. For the measurement reported by Dehollain *et al.* [53], the sequences were tailored to minimize the effect of PIRS on the fidelity of the experiment.

Up until now, the discussion of PIRS within our team has only been in the context of the effect of the RF (MHz) pulses on the electron qubit resonance frequency. Typically in our experiments, the power delivered to the device by a MHz pulse is significantly higher than for a GHz pulse. This is easily understood by comparing the lengths of the π-pulses used for the electron and nuclear spins. The π-pulse lengths are between 1 μs and 10 μs for the electron, and between 30 μs and 100 μs for the nucleus. Given that $\gamma_e = 28$ GHz/T and $\gamma_n = 17$ MHz/T, the magnitude of the oscillating field B_1 at the site of the donor is 16 to 550 times larger for the MHz pulses as compared to the GHz pulses. This could easily be the reason PIRS had not been observed after a GHz pulse.

Here, we propose that PIRS in the context of microwave pulses could explain the oscillations in the echo traces in Figure 4.6. Assume a simple model where the application of a π-pulse on

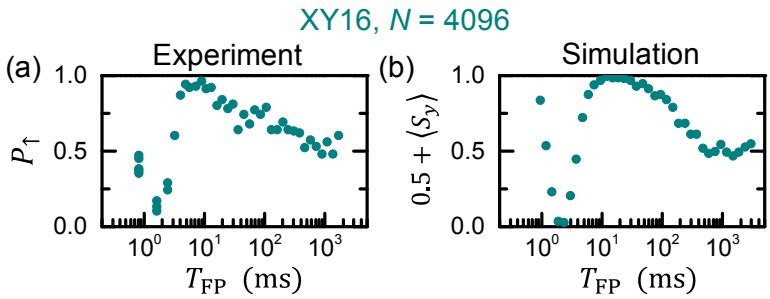

Figure 4.8: **Pulse induced resonance shift.** (a) Echo trace obtained in the experiment for XY16 with $N = 4{,}096$, reproduced from Figure 4.6. (b) Simulated echo trace with the usual noise spectrum in addition to PIRS with parameters $\tau_{\text{PIRS}} = 100$ μs and $A_{\text{PIRS}} = 1.4$ kHz.

the electron (GHz pulse) contributes a shift in the resonance frequency of the form

$$\Delta\omega_{\text{PIRS}} = \begin{cases} 0 & t < t_0 \\ A_{\text{PIRS}} e^{(-(t-t_0)/\tau_{\text{PIRS}})} & t \geq t_0 \end{cases}, \tag{4.1}$$

where t_0 is the time at end of the pulse, A_{PIRS} is the initial magnitude of the shift and τ_{PIRS} is the decay time constant. Assume that A_{PIRS} induced by a single microwave pulse is too small to be detected. We can foresee that a dynamical decoupling sequence with a low number of pulses N will not be affected by PIRS. On the other hand, for large N, the $\Delta\omega_{\text{PIRS}}$ contributed by each refocusing pulse can accumulate to a significant magnitude. This effect is mainly relevant to shorter T_{FP}, where the time between pulses τ is short compared to τ_{PIRS}. For longer T_{FP}, $\Delta\omega_{\text{PIRS}}$ has time to decay before the application of another π-pulse. This yields an average detuning that decreases as T_{FP} increases, which may explain the apparently linear oscillations on a logarithmic scale of T_{FP}.

We simulate the noise introduced by PIRS, $\Delta\omega_{\text{PIRS}}$, in addition to the usual noise spectrum [46] for a 4,096-pulse XY16 sequence. The magnitude of ω_1 is calculated to match the experimental π-pulse time of ≈ 1.5 μs. We set $\tau_{\text{PIRS}} = 100$ μs, based on the first observations of PIRS with RF pulses. Through trial and error, we find that $A_{\text{PIRS}} = 1.4$ kHz yields an echo trace that closely resembles the experimental data. Figure 4.8(a) shows the experimental echo trace and (b) shows the results of this simulation. The close match between experiment and simulations suggest that PIRS could indeed be the cause of the observed oscillations.

We find from further simulations (not shown) that the oscillations in the echo trace due to PIRS are solely due to the presence of $\Delta\omega_{\text{PIRS}}$ during the pulses. This is tested by simulating the sequence with perfect pulses which results in a standard echo trace without these oscillations. In contrast, we re-simulate the echo traces but remove the wait times τ between pulses. We find that the oscillations are reproduced almost exactly, allowing us to remove the wait times in the following simulations.

To gain insight into the effect of each of the PIRS parameters, we simulate the 4,096-pulse

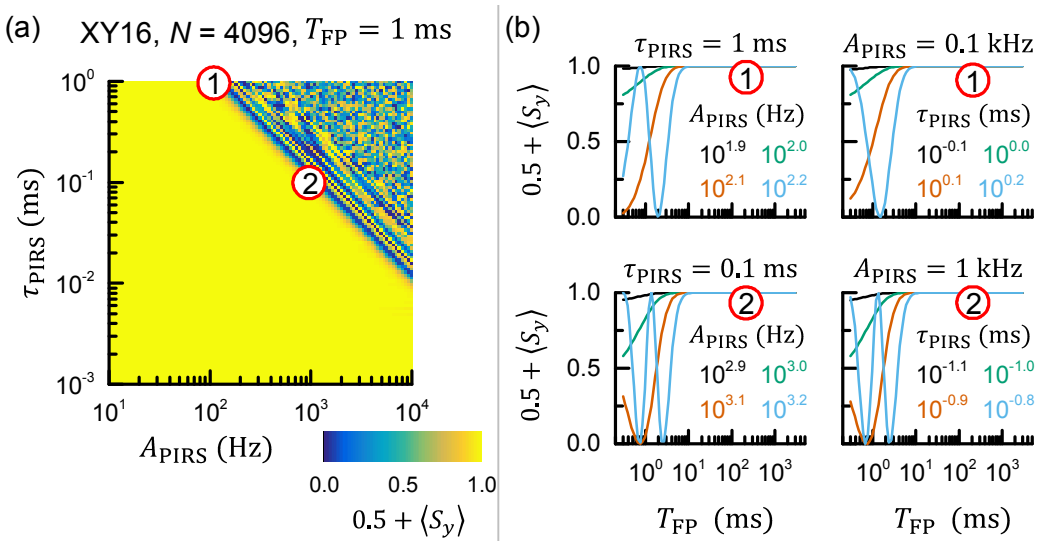

Figure 4.9: **The $A_{\text{PIRS}}\tau_{\text{PIRS}}$ product.** (a) The fidelity of the 4,096-pulse XY16 sequence is plotted as a function of A_{PIRS} and τ_{PIRS}, for $T_{\text{FP}} = 1$ ms. The line separating the high and low fidelity regions indicate that the PIRS oscillations are dependent on the product $A_{\text{PIRS}}\tau_{\text{PIRS}}$. (b) Plots of the echo traces for A_{PIRS} and τ_{PIRS} indicated by the points labeled "1" and "2" in (a). Each panel in the left (or right) column shows echo traces for four values of A_{PIRS} (or τ_{PIRS}).

XY16 sequence as a function of both τ_{PIRS} and A_{PIRS}. For these simulations, we exclude the usual noise spectrum that is responsible for qubit decoherence to save on computation time. We plot the fidelity, $0.5 + \langle S_y \rangle$, for $T_{\text{FP}} = 1$ ms in Figure 4.9(a). As we will illustrate, the choice of T_{FP} is not critical. Note that the axes are plotted in logarithmic scale. We observe a line separating the yellow region from the low-fidelity region. This indicates that, for this sequence, so long as the product $\tau_{\text{PIRS}}A_{\text{PIRS}}$ is below $\approx 10^2$ ms-Hz, the spin-recovery at $T_{\text{FP}} = 1$ ms is not affected.

Figure 4.9(b) shows the echo traces, i.e. the spin recovery as a function of T_{FP}, for certain values of τ_{PIRS} and A_{PIRS}. We focus on the region over which the sequence just begins to suffer from PIRS oscillations, given by the $\tau_{\text{PIRS}}A_{\text{PIRS}} \approx 10^2$ ms-Hz line. Point "1" is where $\tau_{\text{PIRS}} = 1$ ms and $A_{\text{PIRS}} = 100$ Hz and point "2" is where $\tau_{\text{PIRS}} = 0.1$ ms and $A_{\text{PIRS}} = 1$ kHz. The top and bottom rows show the echo traces for point "1" and "2," respectively, as shown by the green lines. We also show the effect of varying A_{PIRS} (left column) or τ_{PIRS} (right column) slightly, as plotted by the other curves in each graph. In other words, the panels in the left (or right) column show the echo traces for points along a vertical (or horizontal) line in Figure 4.9(a). From the similarity in the four panels, we can say that, to a good approximation, the PIRS oscillations are described by the product $A_{\text{PIRS}}\tau_{\text{PIRS}}$.

Additionally, observe from the panels in Figure 4.9(b) that the oscillations are only present below some critical value of T_{FP}. Therefore, the choice of T_{FP} in sub-figure (a) is not important, as long as it is below this critical value. For a given sequence, this critical value of T_{FP} is found

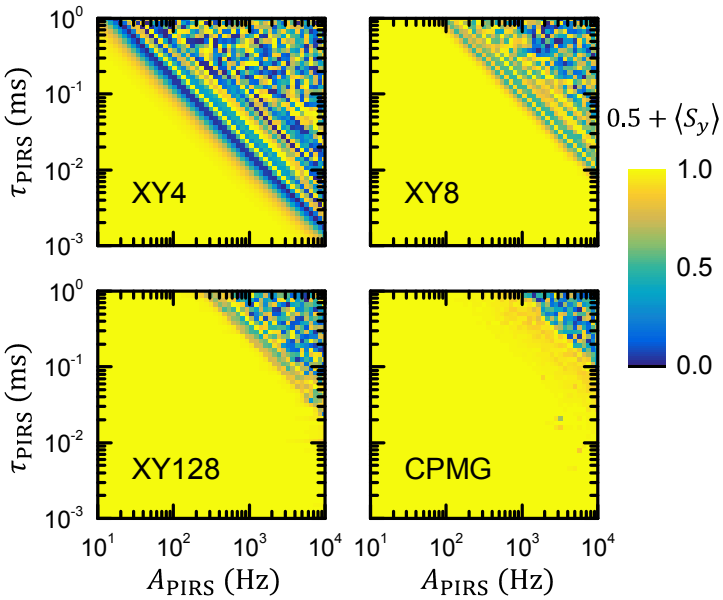

Figure 4.10: **PIRS sequence comparison.** Four sequences are tested for their robustness to PIRS. The fidelity is plotted as a function of A_{PIRS} and τ_{PIRS}, for $T_{\mathrm{FP}} = 1$ ms. $N = 4{,}096$ for comparison to Figure 4.9(a).

to be dependent on ω_1, as we would expect. Referring back to Figures 4.8(a) and (b), where experimental data is compared to a PIRS simulation, the critical values of T_{FP} match very closely. This is simply the result of using the value of ω_1 used in the experiment. This is further evidence supporting the hypothesis that PIRS is responsible for the observed oscillations.

In order for this model to fit with our data, we should see that increasing the order of the XY sequence or moving to CPMG reduces the PIRS oscillations. We thus repeat the simulations performed for Figure 4.9(a) for XY4, XY8, XY128 and CPMG, and plot the results in Figure 4.10. As expected, we see the border move to a higher value of the A_{PIRS}-τ_{PIRS} product as we increase the order of the XY sequence. Interestingly, we see that CPMG is significantly more robust than XY128 to PIRS.

Figure 4.8 showed a simulation of PIRS that closely resembled the experimental echo trace for XY16 with $N = 4{,}096$. We check whether these parameters, $\tau_{\mathrm{PIRS}} = 100$ μs and $A_{\mathrm{PIRS}} = 1.4$ kHz, match the rest of the data. Figure 4.11 plots the experimental echo traces (reproduced from Figure 4.6) in gray, and the simulated traces in color. To minimize computation time, we do not add the usual noise spectrum on top of PIRS. Instead, we shape the traces obtained from PIRS simulations with the expected coherence time T_2 as a function of N. The first row shows the results for XY16, where $N = 1{,}024$, 2,048 and 4,096. The simulations match the experiment at low T_{FP} remarkably well. We highlight that the critical value of T_{FP} changes with N, and the simulations capture this effect almost exactly. This strongly supports our PIRS hypothesis. The simulations also match the other sequences shown up to $N = 4{,}096$.

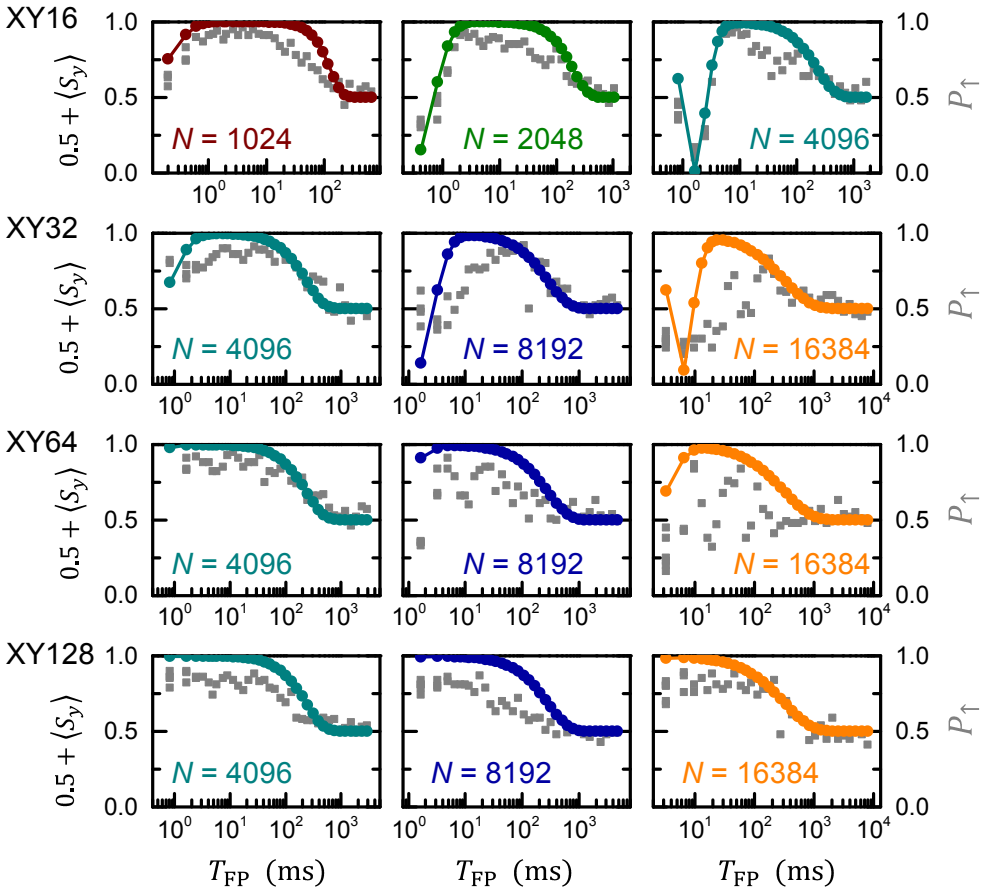

Figure 4.11: **Overlay of PIRS simulations with traces from the experiment.** The experimental traces are reproduced from Figure 4.6 in gray, corresponding to the y-axis labeled $P_\uparrow$. The fidelity, $0.5 + \langle S_y \rangle$, from PIRS simulations are shown in color, with $\tau_{\text{PIRS}} = 100$ μs and $A_{\text{PIRS}} = 1.4$ kHz. The data is shaped to have the expected coherence times. The simulations match the experiment well for XY16 and XY128.

However, the model fails for $N \geq 8{,}192$ for the XY32 and XY64 sequences. Recall that we do no yet understand the cause for PIRS and the model we use is very simplistic (Equation 4.1). There may be other effects responsible for the behavior shown for $N \geq 8{,}192$. Nevertheless, the simulations and experiment match for XY128 (bottom row), in that neither exhibit oscillations in the echo trace.

4.10 Summary and Outlook

This chapter aimed to answer one question. Can an XY-type sequence match the performance of CPMG in our experiment? We have found the answer to be yes, the XY128 sequence matches the coherence time measured by CPMG at 16,384 pulses. In doing so, we have confirmed that the coherence time reported by CPMG is a valid quantity and is not a result of an anomalous

echo as observed in ensemble measurements. This was also determined by single spin simulations with pulse errors, strongly suggesting that the dipolar coupling in ensemble measurements is the key ingredient for anomalous echoes.

Additionally, we have determined an isotropic dynamical decoupling sequence that is sufficiently robust to our particular experimental imperfections. An isotropic sequence is necessary for quantum processing in order to preserve arbitrary qubit states. Our search for this sequence led us to discover an imperfection in our device. Prior to this work, it had been observed that the application of an RF pulse induces a shift in the resonance frequency of the electron spin qubit. While this was believed to be exclusive to RF pulses, we have strong evidence that such a shift exists for the microwave pulses used to control the electron spin as well. The reason we have observed it in this study is that the many-pulse dynamical decoupling sequences cause this shift to accumulate. It was not observed in Reference [46] because only CPMG was performed, which is significantly more robust to this effect.

We do not currently understand the cause for this pulse-induced resonance shift, nor have we characterized the effect thoroughly. While we have managed to match CPMG with XY128 for a single qubit, it will be important to determine the mechanism responsible and, if possible, mitigate the effect.

Chapter 5

Robust two-qubit gates controlled by hyperfine interactions

The work presented in the previous chapters has solidified that the electron spin qubit confined to a donor atom in silicon is an exceptional qubit where readout, initialization, control and protection from decoherence can be performed with high fidelity. The natural next step is to move from single qubit operations to two-qubit logic gates, which are necessary for quantum computation. Here, we present two strategies for performing two-qubit operations with electron spins, relying on the ability to set the donor nuclear spins in arbitrary states. The effective magnetic detuning of the two electron qubits is provided by the hyperfine interaction when the two nuclei are prepared in opposite spin states. This can be exploited to switch on and off SWAP operations with modest tuning of the electron exchange interaction. Furthermore, the hyperfine detuning enables high-fidelity conditional rotation gates based on selective resonant excitation. The latter requires no dynamic tuning of the exchange interaction at all, and offers a very attractive scheme to implement two-qubit logic gates in a full-scale processor.

The work presented in this chapter has been published in:
R. Kalra, A. Laucht, C. D. Hill, and A. Morello. "Robust two-qubit gates for donors in silicon controlled by hyperfine interactions." *Physical Review X* vol. 4 , no. 2, p. 021044, (2014).

The author acknowledges the contributions of A. Laucht and C. D. Hill to the work presented in this chapter.

Chapter 3 highlighted our work in achieving fidelities of greater than 99.9% in the fundamental single qubit operations of readout, initialization and control of the donor electron spin. Chapter 4 confirmed that the long coherence time reported in Reference [46] is suitable for quantum computation. The next step in scaling this technology to a quantum processor is to consider two-qubit logic operations. All quantum algorithms can be implemented with the ability to perform both arbitrary single-qubit rotations and *any* entangling two-qubit logic gate [82]. While several proposals for the implementation of a two-qubit gate with donor electrons exist [26, 27, 83], they pose very challenging demands on the tunability of the spin exchange interaction J, assumed to be switchable from ~ 0 to > 1 GHz. It is also predicted that J can vary strongly upon displacing a donor by even a single lattice site [84, 85], thus requiring true atomic precision in the placement of the donors. These considerations have contributed to create some skepticism on the viability of donor spin qubits for large quantum computer architectures.

Here we propose two implementations of entangling two-qubit gates that overcome these challenges. Our proposals are based on exploiting the hyperfine interaction A with the donor nuclear spins, and the ability to initialize the nuclear spin state. As stated in Chapter 4, our team has experimentally established high-fidelity control of the donor nuclear spin and shown that, when prepared in an eigenstate, the spin state is very long lived [32, 46]. The core of the idea is to prepare the nuclei in opposite spin eigenstates, so that the hyperfine coupling provides a substantial difference in the effective local magnetic field experienced by the electrons. In a many-qubit quantum processor, it will be possible to prepare the state of individual nuclear spins by selectively ionizing the donors whose nucleus we wish to control, since an ionized donor has a resonance frequency that differs from the two nuclear resonances of a neutral donor by several MHz [32]. Magnetically detuning the energies of electron spin qubits has been proposed [86] and implemented in several ways, including the fabrication of a micro-magnet adjacent to the qubits [87], introducing a difference in g-factors [88], or dynamically polarizing the background nuclear spin bath [89]. In comparison, the initialization of the two nuclei in the two-donor system presents an extremely compact and consistent source of magnetic detuning. It also avoids additional decoherence channels that can arise from the transverse component of an external magnetic field gradient [90].

Section 5.2 outlines the first proposal, focusing on using the hyperfine interaction to switch the amplitude of exchange oscillations to perform a $\sqrt{\text{SWAP}}$ gate. This requires a reasonable two orders of magnitude control of J, which could be achieved with an easily fabricated device design. Section 5.3 presents the second two-donor gate, which is a prototypical implementation of a conditional rotation (CROT), as demonstrated for superconducting qubits [91] and spin-qubits in diamond [92]. This is the resonant rotation of one qubit conditional upon the state of the other. We show that this entangling two-qubit gate can be performed with high fidelity in the two-donor system. Dynamic control of the exchange coupling is not required at all in this case, and high-fidelity gates can be achieved for a wide range of coupling strengths. Under

suitable conditions, the CROT gate is also expected to be well protected from charge and gate noise [93]. These gates can tolerate over two orders of magnitude of variability in J, which means that atomically-precise donor placement is not required. The two-qubit gates described here can be applied locally in separate interaction regions, as defined in the framework proposed by Hollenberg *et al.* [26] for a scalable quantum computing architecture.

5.1 Proposed system and theoretical representation

In this section, we introduce the spin Hamiltonian of the two-donor system. Recall that the computational basis states of the single electron spin qubit are defined to be the $|\uparrow\rangle$ and $|\downarrow\rangle$ states. For two qubits, the computational basis is $\{|\uparrow\uparrow\rangle, |\uparrow\downarrow\rangle, |\downarrow\uparrow\rangle, |\downarrow\downarrow\rangle\}$. Of course, the two-donor system also includes the spins of the donor nuclei. The coupling of the two electron spin qubits arises from the overlap of the electron wavefunctions which results in an isotropic Heisenberg exchange interaction J. The magnitude of J is a function of donor separation, their planar alignment and respective electrochemical potentials [84, 94]. For the convenience of the discussions in this chapter, we define the spin Hamiltonian H in units of frequency, with $\mathbf{S}_i = \boldsymbol{\sigma}_i/2$.

$$\begin{aligned} H &= \gamma_e B_0 \left(S_{1_z} + S_{2_z}\right) - \gamma_n B_0 \left(I_{1_z} + I_{2_z}\right) \\ &\quad + A_1 \left(\mathbf{S}_1 \cdot \mathbf{I}_1\right) + A_2 \left(\mathbf{S}_2 \cdot \mathbf{I}_2\right) + J \left(\mathbf{S}_1 \cdot \mathbf{S}_2\right), \end{aligned} \tag{5.1}$$

where subscript 1 (or 2) refers to donor-1 (or 2), γ_n is the nuclear gyromagnetic ratio, $\mathbf{S}$ (or $\mathbf{I}$) is the electron (or nuclear) spin operator with z-component S_z (or I_z), and A is the hyperfine interaction. While we focus on a pair of ^{31}P donors in silicon, the conclusions of this chapter are also valid for other donor species in silicon. For the ^{31}P nucleus, $\gamma_n = 17.2$ MHz/T. We allow for different values of A in the two donors, since the different local electric field can Stark-shift the hyperfine coupling [44, 95]. We define $\Delta A = (A_2 - A_1)/2$ and $\bar{A} = (A_1 + A_2)/2$. The bulk value for A for ^{31}P donors is 117 MHz and we assume $|\Delta A|/\bar{A}$ to be in the range of 1-4%, i.e. $\Delta A \sim$ a few MHz, as expected for ^{31}P donors spaced by $\sim$ 20 nm in a gated nanostructure [70]. The parameters J, A_1, A_2 depend on local electric fields and the exact positions of the two donors, and can be extracted from an experiment which we describe in Section 5.4.

The coupled donor-pair spin Hamiltonian has been studied in bulk ESR experiments in References [96–100] in a high magnetic field such that $\gamma_e B_0 \gg J$ and $\bar{A}$. Recall that at high fields, where $(\gamma_e + \gamma_n)B_0 \gg \bar{A}$, the electrons and nuclei are sufficiently detuned from hyperfine mixing such that their eigenstates can mostly be treated separately. The effect of the relative strengths of J and $\bar{A}$ on the dynamics of the electrons is the foundation of the proposals of this chapter.

5.2 Hyperfine-regulated SWAP gates

The $\sqrt{\text{SWAP}}$ operation between two qubits is the prototypical entangling quantum logic gate in the context of exchange interaction. Its physical implementation with single-spin qubits requires J to be tunable.

Previous donor-based qubit proposals suggested tuning J via direct modification of the tunnel-barrier [24, 26, 85], requiring precise placement of a J-gate between the coupled donors. Instead we suggest tuning J by detuning the donor potentials by an amount $\varepsilon = E_1^0 - E_2^0$, where E^0 is the electrochemical potential of each donor in the neutral donor state D^0 [see Figure 5.1(a-b)]. This method is widely used in double quantum dot systems in the singlet-triplet configuration [101], however there the 'detuning' is defined as the energy difference between the (1,1) and (0,2) charge configurations. Since in our scheme each donor spin represents a qubit, we do not advocate coming too close to the (0,2) charge configuration – this would correspond to moving the donor pair from a (D^0,D^0) to a (D^+,D^-) state. Nevertheless $J(\varepsilon)$ can be significantly tuned [102] from its minimum value at $\varepsilon \approx 0$, to a higher value at $\varepsilon < E_c$, where $E_c \sim 35$ meV is the donor charging energy [94, 103]. This significantly relaxes the requirements on nanofabrication, since the control gates only need to be adjacent to the donor pair, not between them.

In the first proposal of this chapter, we show how SWAP operations can be switched on and off with modest control of $J(\varepsilon)$. A perfect SWAP$^\alpha$ operation is a rotation of angle $\alpha\pi$ exactly about the J-axis in the S-T_0 Bloch sphere [see Figure 5.1(c)], where $S = (|\uparrow\downarrow\rangle - |\downarrow\uparrow\rangle)/\sqrt{2}$ and $T_0 = (|\uparrow\downarrow\rangle + |\downarrow\uparrow\rangle)/\sqrt{2}$. For example, the entangling $\sqrt{\text{SWAP}}$ operation is a rotation of angle $\pi/2$ about the J-axis. The $|\uparrow\uparrow\rangle$, $|\downarrow\downarrow\rangle$ states are unaffected by the exchange interaction.

Existing proposals rely on gate-control of J to vary the frequency of the exchange oscillations from (ideally) zero to a maximum value J_{on}. Any residual interaction J_{off} after the SWAP$^\alpha$ operation would result in further – unwanted – evolution of the qubits. For example, the qubit readout method based on spin-dependent tunneling requires a wait time of order 10 μs – 1 ms between the end of the operation and the readout event [31]. Performing a $\sqrt{\text{SWAP}}$ operation in 10 ns requires $J_{\text{on}} = 25$ MHz, but ensuring that the resulting states have not changed by more than 1% after 1 ms requires $J_{\text{off}} < 32$ Hz: a six order of magnitude dynamic range which may be extremely challenging to achieve [94]. Our proposal focuses on controlling the amplitude of the exchange oscillations instead.

We first note that the nuclear spins are also subject to a mutual coupling J_n mediated by A and J [24]. However this coupling is very small – a few kHz even for $J \gg 1$ GHz, so we can assume J_n to be negligible relative to the other energy terms of the nuclear states. Recalling that the nuclear states have negligible mixing with the electronic states in a high magnetic field, we can say that the nuclear eigenstates are, to a very good approximation, the separable $|\Uparrow\Uparrow\rangle$, $|\Uparrow\Downarrow\rangle$, $|\Downarrow\Uparrow\rangle$ and $|\Downarrow\Downarrow\rangle$ states. The nuclei can be initialized in any of their eigenstates with very high fidelity [32, 46]. Once initialized, the individual nuclei can be treated as static, such that nucleus i contributes an additional local magnetic field $A_i/2$ or $-A_i/2$ to its respective electron

when in the $|\Uparrow\rangle$ or $|\Downarrow\rangle$ state. This results in a magnetic field difference for the two electrons, $\Delta B_z = |\langle\uparrow\downarrow|H|\uparrow\downarrow\rangle - \langle\downarrow\uparrow|H|\downarrow\uparrow\rangle|$. When the nuclei are parallel ($|\Uparrow\Uparrow\rangle$ or $|\Downarrow\Downarrow\rangle$), $\Delta B_z = \Delta A$, and when they are anti-parallel ($|\Uparrow\Downarrow\rangle$ or $|\Downarrow\Uparrow\rangle$), $\Delta B_z = \bar{A}$. We can, therefore, switch the strength of ΔB_z by $1-2$ orders of magnitude – in a 'digital' fashion – through preparation of the nuclear states. However, dynamically switching the nuclear states requires relatively long timescales (~ 10 μs for a π-pulse), making it unsuitable to be performed during the operation of a two-qubit gate.

Once the nuclei have been prepared such that ΔB_z is known, a SWAP$^\alpha$ operation can be implemented. Note that we address calibration of experimental parameters including ΔB_z in Section 5.4. The SWAP$^\alpha$ operation is implemented by rapidly gate-tuning J until it becomes larger than ΔB_z [see Figure 5.1(e)]. After a time $\tau = \alpha/(2\sqrt{J^2 + \Delta B_z^2}) \approx \alpha/(2J)$, the system is pulsed back to the low regime $J \ll \Delta B_z$ where the exchange oscillations are frozen [see Figure 5.1(d)], completing the SWAP$^\alpha$ operation. For $\Delta B_z = \bar{A} \approx 120$ MHz, pulsing J to $10 \times \Delta B_z$ would yield a $\sqrt{\text{SWAP}}$ operation in $\approx$200 ps.

We calculate the fidelity of spin exchange oscillation and suppression in the 'on' and 'off' regimes, respectively, as a function of $J/\Delta B_z$. Simulations are performed using the full Hamiltonian (Equation 5.1) with the electrons initialized in the $|\psi_0\rangle = |\downarrow\uparrow\rangle$ state and $B_0 = 1$ T. The nuclei are initialized in the $|\Uparrow\Downarrow\rangle$ state, such that ΔB_z is ΔA. The insets of Figure 5.1(f) show the evolution of the expectation value of the two electrons, where $\langle S_z\rangle$ is plotted for electron 1 (blue curve) and 2 (red curve) for two values of $J/\Delta B_z$ to illustrate when exchange oscillations are allowed or suppressed. The fidelity of spin exchange is then calculated by taking the squared-projection of the state after a π-rotation in the S-T_0 Bloch sphere onto the exchanged state, or $|\langle\psi_\pi|\uparrow\downarrow\rangle|^2$. This fidelities obtained from these simulations are plotted as the blue circles in Figure 5.1(f). The fidelity of spin exchange, valid in the regime $J/\Delta B_z \gg 1$, is equal to 'one minus' the fidelity (or the error) of exchange suppression, which is valid in the regime $J/\Delta B_z \ll 1$. The simulations have been repeated for the nuclei initialized in parallel states, and the behavior observed is identical when J is renormalized to the new $\Delta B_z = \Delta A$.

The Rabi formula for precession in the S-T_0 Bloch sphere, $J^2/(J^2 + \Delta B_z^2)$, is plotted as the red curve, following the results of the time evolution simulations very closely. This validates the mapping of the four-spin system onto the truncated picture illustrated by the S-T_0 Bloch sphere. The results in Figure 5.1(f) show that SWAP operations can be switched on and off with a fidelity of 99% by pulsing J between $\Delta B_z/10$ and $10\Delta B_z$ – two orders of magnitude control of J is sufficient. An alternative method to perform SWAP$^\alpha$ operations would be to use Euler angle construction [16], allowing for exact rotations about the J-axis and further reducing the tuning capabilities required.

Note that the blue circles represent the process fidelity for a full SWAP operation. This provides a conservative estimate of the $\sqrt{\text{SWAP}}$ operation, which is the actual two-qubit entangling operation. Also, while this represents the inherent fidelity achievable, in practice, the fidelity will depend on the accuracy of the pulse calibration, and the stability of the value of

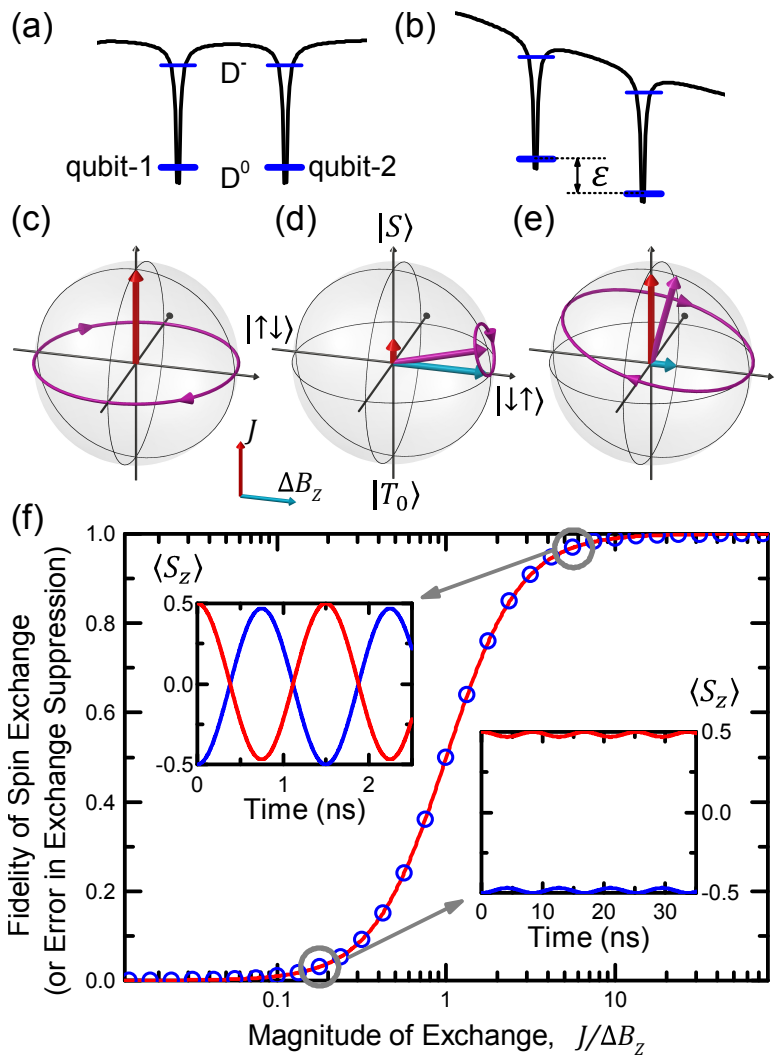

Figure 5.1: **Hyperfine-regulated SWAP gate.** (a),(b) Schematic of the conduction band profile of the coupled donor pair with qubit-1 and qubit-2 (a) in resonance and (b) detuned by ε. (c)-(e) Precession on the S-T_0 Bloch spheres with initial state $|\downarrow\uparrow\rangle$ for exchange-coupled electrons (c) in the absence of coupling to nuclei, (d) where $J < \Delta B_z$ and (e) where $J > \Delta B_z$. Here, we use the convention of the field pointing towards the lower-energy state where precession follows the left-hand rule. (f) The fidelity of spin-state exchange, valid for $J \gg \Delta B_z$, is equal to the error in exchange suppression, valid for $J \ll \Delta B_z$. The probability of spin exchange is plotted as a function of J normalized to ΔB_z. The insets show the time evolution of the expectation value of the electrons initialized as $|\downarrow\uparrow\rangle$ for two values of J, illustrating the ability to control the amplitude of exchange oscillations.

J during the operation. Fluctuations in J can arise from electric field noise in the environment. The proposal calls for a gate to tune J by two-orders-of-magnitude, which means J will especially be sensitive to the voltage noise on that gate. Furthermore, this gate electrode will require a high bandwidth as it will need to be pulsed at a high frequency. This removes the possibility of using a low-frequency low-pass filter to reduce voltage noise on the gate.

5.3 CROT gates

The CROT operation is another two-qubit gate that can be achieved with the exchange-coupled two-donor system. Most importantly, our proposed realization of the operation does not require any tuning of J, further simplifying its practical implementation. In demonstrating how the system can be used to implement a CROT gate, we make some necessary approximations to the Hamiltonian and quantify the associated errors.

Fidelity is most often calculated as average gate fidelity over all input states [74]. Perhaps a more meaningful quantity is the minimum fidelity considering all possible input states, though this is more difficult to calculate. We choose to provide an intuitive measure of the operator fidelity that approximates the minimum fidelity. Our method is to calculate the total fidelity F by adding, as independent events, the worst-case errors associated with each approximation we make to the Hamiltonian of the system. The worst-case fidelity for each approximation is defined as $\min_{\psi_i}(|\langle\psi_{actual}|\psi_{ideal}\rangle|^2)$, where ψ_{ideal} and ψ_{actual} are the output states of the operator with and without the approximation, given an input state ψ_i. The input state that yields the minimum fidelity is easy to identify for each individual approximation. The total fidelity F is then plotted in Figure 5.2(c-d) as a function of J and T_{CROT}, the gate operation time. The two panels show the fidelities for two concentrations of ^{29}Si, as will be explained later.

We propose to operate the CROT gate under the condition $J < \bar{A} \ll \gamma_e B_0$. We prepare the nuclei in either the $|\Uparrow\Downarrow\rangle$ or $|\Downarrow\Uparrow\rangle$ eigenstate, where they are static and do not participate in the dynamics of the electrons. The ΔB_z experienced by the two electrons for this nuclear configuration is $\bar{A}$. We thus define an electron-only Hamiltonian in the computational basis with the nuclei initialized in the $|\Downarrow\Uparrow\rangle$ state,

$$H_1 = \begin{bmatrix} E_{\uparrow\uparrow} & 0 & 0 & 0 \\ 0 & E_{\uparrow\downarrow} & J/2 & 0 \\ 0 & J/2 & E_{\downarrow\uparrow} & 0 \\ 0 & 0 & 0 & E_{\downarrow\downarrow} \end{bmatrix}, \tag{5.2}$$

where $E_{\uparrow\uparrow} = \gamma_e B_0 + \frac{J}{4} + \frac{\Delta A}{2}$, $E_{\uparrow\downarrow} = \frac{-J}{4} + \frac{-\bar{A}}{2}$, $E_{\downarrow\uparrow} = \frac{-J}{4} + \frac{\bar{A}}{2}$ and $E_{\downarrow\downarrow} = -\gamma_e B_0 + \frac{J}{4} + \frac{-\Delta A}{2}$. We rotate away the J-terms leaving the Hamiltonian diagonalized using the change of basis matrix with the eigenstates of the Hamiltonian: $|\uparrow\uparrow\rangle$, $|\downarrow\downarrow\rangle$ and

$$|\widetilde{\uparrow\downarrow}\rangle = \cos\theta|\uparrow\downarrow\rangle - \sin\theta|\downarrow\uparrow\rangle, \tag{5.3}$$

$$|\widetilde{\downarrow\uparrow}\rangle = \cos\theta|\downarrow\uparrow\rangle + \sin\theta|\uparrow\downarrow\rangle, \tag{5.4}$$

where $\tan 2\theta = J/\bar{A}$. The corresponding eigenenergies are $E_{\widetilde{\uparrow\downarrow}} = -J/4 - \sqrt{\bar{A}^2 + J^2}/2$ and $E_{\widetilde{\downarrow\uparrow}} = -J/4 + \sqrt{\bar{A}^2 + J^2}/2$.

Figure 5.2(a) shows a level diagram of the four eigenstates of the system including the allowed

ESR transitions, and Figure 5.2(b) shows a schematic of the corresponding ESR spectrum. We define the notation e.g. $\nu_{\uparrow\updownarrow}$ to be the transition frequency corresponding to rotating the second electron when the first electron is $|\uparrow\rangle$. Recall that in this chapter, the Hamiltonian is defined in units of frequency, as opposed to energy or angular frequency. The transition frequencies are given by

$$\nu_{\uparrow\updownarrow} = \gamma_e B_0 + \frac{\Delta A}{2} + \frac{J}{2} + \frac{\sqrt{\bar{A}^2 + J^2}}{2}, \tag{5.5}$$

$$\nu_{\downarrow\updownarrow} = \gamma_e B_0 + \frac{\Delta A}{2} - \frac{J}{2} + \frac{\sqrt{\bar{A}^2 + J^2}}{2}, \tag{5.6}$$

$$\nu_{\updownarrow\uparrow} = \gamma_e B_0 + \frac{\Delta A}{2} + \frac{J}{2} - \frac{\sqrt{\bar{A}^2 + J^2}}{2}, \tag{5.7}$$

$$\nu_{\updownarrow\downarrow} = \gamma_e B_0 + \frac{\Delta A}{2} - \frac{J}{2} - \frac{\sqrt{\bar{A}^2 + J^2}}{2}. \tag{5.8}$$

We define our CROT operation to be a π-rotation at $\nu_{\downarrow\updownarrow}$. An ideal CROT, however, would be a π-rotation between $|\downarrow\downarrow\rangle$ and $|\downarrow\uparrow\rangle$, not between $|\downarrow\downarrow\rangle$ and $|\widetilde{\downarrow\uparrow}\rangle$. Using the protocol outlined earlier for calculating the associated error, clearly ψ_{actual} and ψ_{ideal} are $|\widetilde{\downarrow\uparrow}\rangle$ and $|\downarrow\uparrow\rangle$. The inherent error introduced in the operation is thus $\sin^2\theta$. This error increases with J and is independent of T_{CROT} and the ^{29}Si concentration, thus appearing as a vertical boundary in the high-J region of both the fidelity plots, Figure 5.2(c-d).

The CROT operation is obtained by applying a magnetic field, rotating at frequency ν in the plane perpendicular to the $\mathbf{B}_0$, with time-dependent amplitude $B_1(t)$. Recall that this rotating field is practically achieved by applying an oscillating magnetic field perpendicular to $\mathbf{B}_0$ with double the desired amplitude, $2B_1(t)$. Transforming this into our altered basis and into the rotating frame at frequency ν, the Hamiltonian is given by

$$H_2 = \begin{bmatrix} E_{\uparrow\uparrow} - \nu & \gamma_e B_1(t)\mu_S & \gamma_e B_1(t)\mu_T & 0 \\ \gamma_e B_1(t)\mu_S & E_{\widetilde{\uparrow\downarrow}} & 0 & \gamma_e B_1(t)\mu_S \\ \gamma_e B_1(t)\mu_T & 0 & E_{\widetilde{\downarrow\uparrow}} & \gamma_e B_1(t)\mu_T \\ 0 & \gamma_e B_1(t)\mu_S & \gamma_e B_1(t)\mu_T & E_{\downarrow\downarrow} + \nu \end{bmatrix}, \tag{5.9}$$

where $\mu_S = (\cos\theta - \sin\theta)/2$ and $\mu_T = (\cos\theta + \sin\theta)/2$. These two terms appear as a result of the altered basis states ($|\widetilde{\downarrow\uparrow}\rangle$ and $|\widetilde{\uparrow\downarrow}\rangle$). We now have $\gamma_e B_1(t)$ coupling the four transitions $\nu_{\uparrow\updownarrow}$, $\nu_{\downarrow\updownarrow}$, $\nu_{\updownarrow\uparrow}$ and $\nu_{\updownarrow\downarrow}$, with different apparent amplitudes $[\gamma_e B_1(t)(\cos\theta \pm \sin\theta)/2]$ depending on the states involved. Our next approximations to the Hamiltonian will be to remove these coupling terms in the Hamiltonian for the three off-resonant transitions. To quantify the error associated with these approximations, we treat each transition as an independent qubit system with relevant coupling and detuning, and determine the transition probability given $\gamma_e B_1(t)$. Non-zero probabilities at $\nu_{\uparrow\updownarrow}$, $\nu_{\updownarrow\uparrow}$ and $\nu_{\updownarrow\downarrow}$ are considered errors. Additionally, a non-unity probability at $\nu_{\downarrow\updownarrow}$ (the chosen CROT transition) is also an error-event.

We assume that the CROT gate at frequency $\nu_{\downarrow\updownarrow}$ is obtained by applying a resonant mi-

crowave pulse with a Gaussian envelope. Its excitation profile, f_V, is given by Reference [104] and is many orders of magnitude more selective than that of a square pulse at large detuning, which is crucial for the CROT gate which is based on selectivity. Other shapes with similar selectivity, such as the Hermite pulse, are also possible candidates [74] for the CROT gate. The excitation amplitude we choose is defined as:

$$B_1(t) = B_1^{\max}\exp\left(\frac{(t - T_{\mathrm{CROT}}/2)^2}{2(T_{\mathrm{CROT}}/6)^2}\right), t \in [0, T_{\mathrm{CROT}}], \tag{5.10}$$

where the pulse length T_{CROT} is six times the standard deviation of the Gaussian to sufficiently approximate the function. The time T_{CROT} necessary for a π-rotation is inversely related to $B_1^{\max}$ – the complete relationship is given in Reference [104]. For example, to perform a π-rotation in 100 ns, $B_1^{\max}$ would need to be 0.43 mT for a Gaussian pulse and 0.18 mT for a square pulse. We also take into account the modification of the apparent amplitude of B_1 depending on the states involved, $\mu(\theta)$. We define the probability that a π-rotation occurs for a certain transition, with frequency ν_i and corresponding $\mu(\theta)$, as:

$$p_\pi = \int_{-\infty}^{\infty} f_V(\nu_{\downarrow\updownarrow}, T_{\mathrm{CROT}}, \mu(\theta), \nu) P(\nu_i, \sigma, \nu) d\nu. \tag{5.11}$$

The excitation profile $f_V(\nu_{\downarrow\updownarrow}, T_{\mathrm{CROT}}, \mu(\theta), \nu)$ is the probability that a transition with frequency ν is excited by the Gaussian pulse with T_{CROT} at frequency $\nu_{\downarrow\updownarrow}$. Here, $P(\nu_i, \sigma, \nu)$ describes the broadening of the resonance frequency, a normalized Gaussian distribution with standard deviation σ, centered at ν_i. In other words, it is the probability the a transition with nominal resonance frequency ν_i has been shifted to ν due to fluctuations in the environment. The first source of this broadening is fluctuations in the surrounding bath of ^{29}Si spins [105], which is why we calculate F for qubits in both natural silicon (^{nat}Si), which contains 4.7% spin-carrying ^{29}Si nuclei [see Figure 5.2(c)], and in isotopically purified ^{28}Si with 800 ppm residual ^{29}Si atoms (^{iso}Si) [see Figure 5.2(d)]. Further possible sources of broadening are magnetic noise that couple directly into the spin qubit frequency and electric field noise, which couple via modulation of A, γ_e or J. We extract the values for σ from the linewidths measured in each material. In ^{nat}Si, the dynamics of the nuclear spin bath are the dominant source of broadening, resulting in $\sigma = 3.2$ MHz [29]. In ^{iso}Si, the experiment reported in Chapter 3 found the linewidth to be dependent on the experimental setup, which resulted in $\sigma = 1.8$ kHz [46]. These experimental values inherently include broadening due to the spin bath, and the modulation of A and γ_e via electric field noise, but not of J. We address the issue of noise in J at the end of this section.

Looking at the fidelity plots, we can see the error associated with the partial excitation (non-zero p_π) of off-resonant transitions. The diagonal fidelity-boundary at the top-left is due to the proximity of $\nu_{\uparrow\updownarrow}$ to $\nu_{\downarrow\updownarrow}$. Faster gates, corresponding to shorter T_{CROT} and broader excitation profiles, require a higher J to separate the two resonances. The diagonal fidelity-boundary at the top-right is due to the $\nu_{\updownarrow\uparrow}$ coming closer to $\nu_{\downarrow\updownarrow}$ as J increases. Hence, these two boundaries are orthogonal. They appear at the same positions for both ^{nat}Si and ^{iso}Si, since they mainly

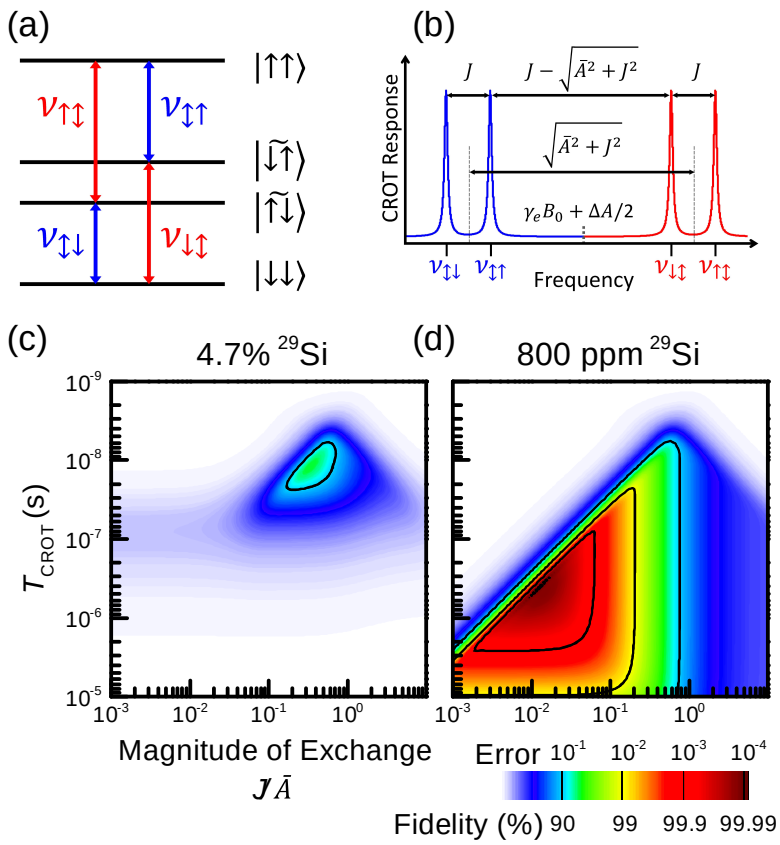

Figure 5.2: **Conditional-rotation gate.** (a) Schematic of the level diagram for the two-donor system with the nuclei prepared in the $|\Downarrow\Uparrow\rangle$ state. (b) Schematic of the corresponding ESR spectrum. (c),(d) Contour plots of the fidelity of the proposed CROT gate as a function of J and T_{CROT}, calculated on the basis of the experimental values of the ESR linewidths in (c) natural silicon and (d) isotopically-purified silicon.

depend on the spectral separation of the lines given by J and $\bar{A}$ which, in both cases, is larger than the quoted linewidths..

The final type of error is the incomplete excitation (non-unity p_π) of the CROT transition. The excitation profile must be sufficiently wide (short T_{CROT}) as compared to the inhomogeneous broadening to successfully drive the π-rotation at $\nu_{\downarrow\updownarrow}$. This results in the horizontal fidelity-boundary at the bottom of Figure 5.2(c-d). We see that this boundary allows for significantly longer T_{CROT} in ^{iso}Si [Figure 5.2(d)] as compared to ^{nat}Si [Figure 5.2(c)] due to the narrow linewidth, effectively 'unveiling' a large region of high fidelities. In natural silicon, fidelities of ∼95% are achievable for a range of J values over almost an order of magnitude, with gate times around 30 ns. In the isotopically-purified material, the peak fidelity achievable exceeds 99.99% with a gate time of 400 ns. Fidelities greater than 99.9% are achievable for a range of J values over ∼1.5 orders of magnitude, with gate times as short as 80 ns. From a practical perspective, the important result is that fidelities greater than 99% are achievable

for a range of J values varying over ∼2.6 orders of magnitude. This means that even ion implantation [36, 106, 107], which inherently suffers from imprecisions in the donor placement, becomes realistically suitable for multi-qubit donor structures. Also, a recent proposal shows that donor pairs can be exchange-coupled via an intermediate multi-electron quantum dot [108]. The typical coupling strengths $J \sim 100$ kHz in that proposal would yield $\sim 99.9\%$ fidelity for the CROT gates in ^{iso}Si described here. Given the demonstrated ability to fabricate top-gated few-electron quantum dots in silicon [109] that can be tunnel-coupled to donors [31], donor-dot hybrids could constitute an appealing new strategy for fabrication and scale-up [108].

We have quantified the errors associated with applying the excitation to off-resonant transitions and the effect of noise on the intended CROT transition. We thus make the secular approximation to the Hamiltonian with $\nu = \nu_{\downarrow\updownarrow} = E_{\widetilde{\downarrow\uparrow}} - E_{\downarrow\downarrow}$,

$$H_3 = \begin{bmatrix} E_{\uparrow\uparrow} - (E_{\widetilde{\downarrow\uparrow}} - E_{\downarrow\downarrow}) & 0 & 0 & 0 \\ 0 & E_{\widetilde{\uparrow\downarrow}} & 0 & 0 \\ 0 & 0 & E_{\widetilde{\downarrow\uparrow}} & \gamma_e B_1(t)\mu_T \\ 0 & 0 & \gamma_e B_1(t)\mu_T & E_{\widetilde{\downarrow\uparrow}} \end{bmatrix}. \tag{5.12}$$

The Hamiltonian above is suitable to perform a conditional rotation, where the errors arising from the three classes of approximations have been summed to provide a conservative estimate of the overall fidelity. The resulting gate rotates the spin by an angle $2\phi = \int 2\pi\gamma_e B_1(t)(\cos\theta + \sin\theta)dt$ within time t, described by the time evolution operator,

$$U(t) = \begin{bmatrix} e^{(i\gamma_1)} & 0 & 0 & 0 \\ 0 & e^{(i\gamma_2)} & 0 & 0 \\ 0 & 0 & e^{(i\gamma_3)}\cos\phi & -ie^{(i\gamma_3)}\sin\phi \\ 0 & 0 & -ie^{(i\gamma_3)}\sin\phi & e^{(i\gamma_3)}\cos\phi \end{bmatrix}, \tag{5.13}$$

where we have made the substitutions $\gamma_1 = -t(E_{\uparrow\uparrow} - (E_{\widetilde{\downarrow\uparrow}} - E_{\downarrow\downarrow}))$, $\gamma_2 = -t(E_{\widetilde{\uparrow\downarrow}})$ and $\gamma_3 = -t(E_{\widetilde{\downarrow\uparrow}})$ for compactness. A single pulse of the above operator with $U(t : 2\phi = \pi)$ yields an operation that closely resembles the CROT,

$$U_2 = \begin{bmatrix} e^{(i\gamma_1)} & 0 & 0 & 0 \\ 0 & e^{(i\gamma_2)} & 0 & 0 \\ 0 & 0 & 0 & -ie^{(i\gamma_3)} \\ 0 & 0 & -ie^{(i\gamma_3)} & 0 \end{bmatrix}. \tag{5.14}$$

The above operation successfully rotates the spin of the second electron conditional upon the state of the first. In order to complete the CROT operation, however, the resulting phases must be accounted for. The operator causes a phase shift for each of the four basis states $(\theta_{\uparrow\uparrow}, \theta_{\uparrow\downarrow}, \theta_{\downarrow\uparrow}, \theta_{\downarrow\downarrow})$ which can be easily extracted by taking the phase of the non-zero element in the associated column for each basis state. It is useful to analyze, instead, the phases associated

with electron-1 (θ_1) and electron-2 (θ_2), the phase due to the interaction (θ_{12}) and the global phase (θ_g). Only θ_1, θ_2 and θ_g can be corrected for with single-qubit rotations, requiring that our CROT have $\theta_{12} = 0$. For the above operator, $\theta_{12} = \frac{1}{4}(\theta_{\uparrow\downarrow}+\theta_{\downarrow\uparrow}-\theta_{\uparrow\uparrow}-\theta_{\downarrow\downarrow}) = \frac{1}{4}(\gamma_2-\gamma_1) \neq 0$. One possible solution is to use a refocusing pulse to correct for this phase as follows:

$$U_3 = X_2 U_{\sqrt{CROT}} X_2 U_{\sqrt{CROT}} \ , \tag{5.15}$$

where $U_{\sqrt{CROT}}$ is $U(t : 2\phi = \pi/2)$ and X_2 unconditionally flips the spin of the second (target) electron. For the phase to be refocused, X_2 must have $\theta_{12} = 0$. The two transitions, $\nu_{\uparrow\updownarrow}$ and $\nu_{\downarrow\updownarrow}$ must both undergo a π-rotation in the same amount of time. This is satisfied by the operator

$$X_2 = \begin{bmatrix} 0 & -ie^{(i\gamma_2)} & 0 & 0 \\ -ie^{(i\gamma_2)} & 0 & 0 & 0 \\ 0 & 0 & 0 & -ie^{(i\gamma_3)} \\ 0 & 0 & -ie^{(i\gamma_3)} & 0 \end{bmatrix}, \tag{5.16}$$

where $\theta_{12} = 0$. This may be implemented as a two-tone pulse at the frequencies $\nu_{\downarrow\updownarrow}$ and $\nu_{\uparrow\updownarrow}$ with amplitude adjusted for the $(\cos\theta + \sin\theta)$ difference in the transition matrix elements between the two pairs of states. The result of Equation 5.15 yields the full operator for the CROT that successfully completes a conditional rotation and cancels out the phase due to the interaction.

In the analysis above we have made a realistic estimate of the CROT gate errors that could arise from fluctuations of the qubits' resonance frequencies. Once an exchange interaction J acts in the 2-qubit Hamiltonian, electrical noise from switching charges and gate voltage fluctuations [93] can introduce further shifts of the instantaneous operation frequencies, and therefore constitute an additional source of error. We do not attempt here to estimate the magnitude of such errors, but we note that our CROT scheme can be implemented while the two donors are at the same electrochemical potential, $\varepsilon = 0$. A thorough noise analysis of exchange-coupled singlet-triplet qubits has unambiguously shown that the dephasing time T_2^* is inversely proportional to $\mathrm{d}J/\mathrm{d}\varepsilon$, whereas no effects of charge or gate noise on the tunnel barrier height could be observed [110]. Since J is minimum when $\varepsilon = 0$ [102] and $\mathrm{d}J/\mathrm{d}\varepsilon = 0$ in that circumstance [111–113], CROT operations can be performed while the coupled 2-qubit system is to first-order immune from fluctuations in ε. In this context, the lateral gates could be used to tune the system to the $\mathrm{d}J/\mathrm{d}\varepsilon = 0$ condition, even in the presence of static local disorder [114]. Additionally, the fact that J does not need to be tuned allows the gate electrodes to be heavily low-pass filtered, thus reducing the electric field noise present in the device.

5.4 System calibration from the ESR spectrum

The exchange coupling J between the two donors in each interaction region needs to be calibrated in order to perform either of the proposed two-qubit logic gates. Given a Hamiltonian

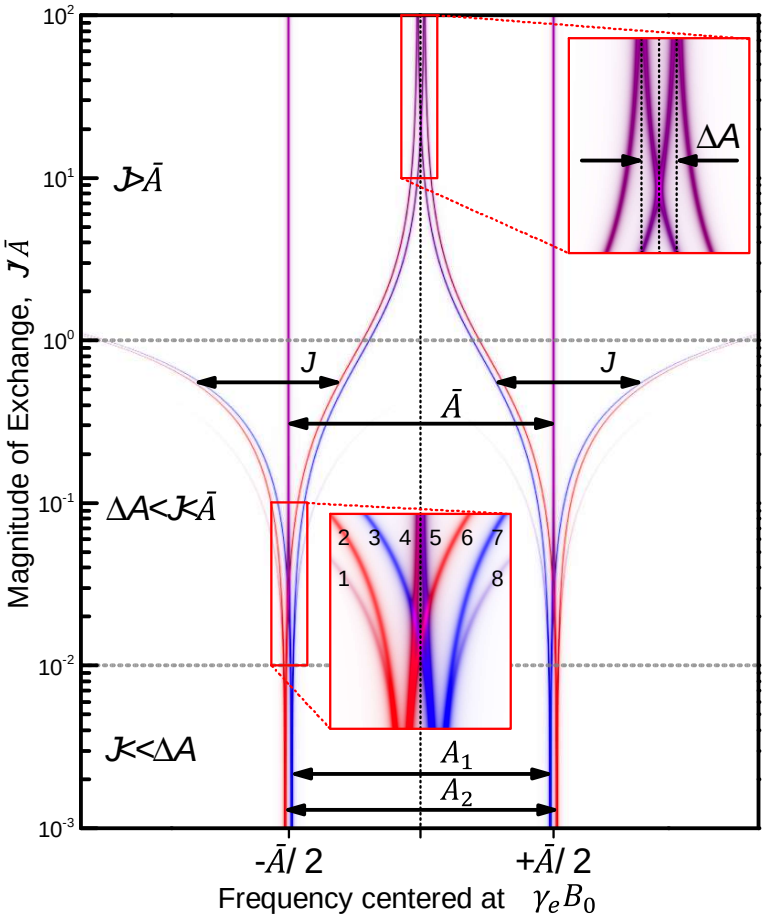

Figure 5.3: **ESR fingerprint for system calibration.** The ESR spectrum of $H(J)$ plotted as a function of the exchange-hyperfine interaction ratio, $J/\bar{A}$. Branches are labeled from left to right (1 to 16) on the $J = 10^{-1}\bar{A}$ line, with 1 to 8 shown.

$H(J)$, J can be extracted from the ESR spectrum obtained by performing ESR sweeps as shown in Chapter 1 and References [29, 46]. This 'ESR fingerprint' [see Figure 5.3] is calculated by considering all transitions between the eigenstates of $H(J)$ in the regime $J < \gamma_e B_0$. Their respective intensities are weighted with (i) the electronic transition dipole matrix elements, $\langle\psi_i|(\sigma_{x_{S1}} + \sigma_{x_{S2}})|\psi_f\rangle$, where $\sigma_{x_{Sn}}$ is the Pauli operator for electron n, and (ii) the readout contrast, i.e. the change in expectation value of spin-z projection of each electron upon excitation of the ESR transition, $\Delta\langle S_{n_z}\rangle = \langle\psi_f|S_{n_z}|\psi_f\rangle - \langle\psi_i|S_{n_z}|\psi_i\rangle$. The transitions in Figure 5.3 are color-coded such that the blue and red intensities are proportional to $\Delta\langle S_{1_z}\rangle$ and $\Delta\langle S_{2_z}\rangle$, respectively. In the example of an allowed electronic transition, $|\downarrow\downarrow\rangle \rightarrow |T_0\rangle$, the line is drawn in purple as it has equal, non-zero contributions from both $\Delta\langle S_{1_z}\rangle$ and $\Delta\langle S_{2_z}\rangle$. We plot in Figure 5.3 an example where $A_2 > A_1$ and $\Delta A/\bar{A} = 2.5\%$. The linewidth is taken to be smaller than ΔA such that this splitting can be resolved.

In the $J \ll \Delta A$ region, where the eigenstates are simply the combinations of logical electronic and nuclear states, we see a pair of blue and red lines that correspond to rotations of electron 1 and 2, respectively. The transitions at $\gamma_e B_0 - A_i/2$ and $\gamma_e B_0 + A_i/2$ rotate electron i when its binding nucleus is in the $|\Downarrow\rangle$ and $|\Uparrow\rangle$ state, respectively. Thus, the red line at $\gamma_e B_0 - A_2/2$ includes the following four transitions: $|\downarrow\downarrow\Downarrow\Downarrow\rangle \rightarrow |\downarrow\uparrow\Downarrow\Downarrow\rangle$ (branch 1), $|\uparrow\downarrow\Downarrow\Downarrow\rangle \rightarrow |\uparrow\uparrow\Downarrow\Downarrow\rangle$ (branch 4), $|\downarrow\downarrow\Uparrow\Downarrow\rangle \rightarrow |\downarrow\uparrow\Uparrow\Downarrow\rangle$ (branch 2) and $|\uparrow\downarrow\Uparrow\Downarrow\rangle \rightarrow |\uparrow\uparrow\Uparrow\Downarrow\rangle$ (branch 6). In the following, we will focus our description of the transitions to the red branches on the left-hand side of the spectrum, noting that the same reasoning can directly be transferred to the other branches.

As J becomes larger than the linewidth (region $J < \bar{A}$), we observe the exchange-splitting between transitions $|\downarrow\downarrow\Downarrow\Downarrow\rangle \rightarrow |\downarrow\uparrow\Downarrow\Downarrow\rangle$ (branch 1) and $|\uparrow\downarrow\Downarrow\Downarrow\rangle \rightarrow |\uparrow\uparrow\Downarrow\Downarrow\rangle$ (branch 4), and between transitions $|\downarrow\downarrow\Uparrow\Downarrow\rangle \rightarrow |\downarrow\uparrow\Uparrow\Downarrow\rangle$ (branch 2) and $|\uparrow\downarrow\Uparrow\Downarrow\rangle \rightarrow |\uparrow\uparrow\Uparrow\Downarrow\rangle$ (branch 6). The electronic $|\uparrow\downarrow\rangle$ and $|\downarrow\uparrow\rangle$ states tend towards either the $|T_0\rangle$ and $|S\rangle$ states as $J/\Delta B_z$ increases for each particular nuclear configuration. Branches 1 and 2 fade away for $J \sim \Delta A$ and $J \sim \bar{A}$, respectively, as they involve the state approaching a magnetically-inaccessible singlet state. Their J-split counterparts, branches 4 and 6, involving states approaching $|T_0\rangle$, tend towards $\gamma_e B_0 - \bar{A}/2$ and $\gamma_e B_0 - \Delta A/2$ (region $J > \bar{A}$), respectively.

A transition involving a fully entangled state would have $\Delta\langle S_{1_z}\rangle = \Delta\langle S_{2_z}\rangle = 0.5$. Accordingly, the region where the branches become purple indicate where a participating state tends towards the $|T_0\rangle$ or $|S\rangle$.

With the ability to independently prepare and readout the electron of each donor, it would be possible to observe every transition for a given $H(J)$. The protocol would involve preparing or, at least randomizing, the nuclear spins using appropriate NMR pulses, then extracting the ESR spectrum for both electrons as in Reference [29].

For a proof-of-principle device, we make the conservative assumption that only donor-2 is tunnel-coupled to a charge reservoir so that its electron spin can be read out in single-shot and initialized electrically in the ground state [31]. In this case, performing ESR experiments would only reveal those transitions involving the $|\downarrow\downarrow\rangle$ state and result in $\Delta\langle S_{2_z}\rangle > 0$. In the $J \lesssim \Delta A$ regime, branches 1, 2, 11 and 13 could be observed. In the $\Delta A \lesssim J \lesssim \bar{A}$ regime, branch 1 fades away and branch 5 emerges as its $\Delta\langle S_{2_z}\rangle$ increases. Finally, in the $J \gtrsim \bar{A}$, branch 2 fades away while branch 10 emerges. The relative spacing between the lines should make it easy to extract the value of J. To be certain, slightly modifying J by shifting the electrostatic environment will allow comparison to the fingerprint in Figure 5.3, ensuring correct interpretation of the observed resonances. Operating in the $\gamma_e B_0 \gg \bar{A}$ regime, the resonant frequencies of these transitions are determined by four parameters ($\gamma_e B_0$, $\bar{A}$, ΔA and J) so that the determination of four resonant frequencies is sufficient to extract these parameters.

5.5 Summary and Outlook

We have analyzed the system of two exchange-coupled donor spin qubits, and shown how we can harness the hyperfine interaction with the ^{31}P donor nuclei to implement two different types of two-qubit logic gates that form a universal set of operations when combined with single-qubit rotations. In the first method, we show that the amplitude of exchange oscillations can be controlled by exploiting the presence of the magnetic detuning, ΔB_z, provided by the hyperfine interaction with the donor nuclei. These oscillations can be switched on and off to form a $\sqrt{\text{SWAP}}$ gate of 99% fidelity upon tuning J by just two orders of magnitude. However, this implementation is susceptible to electric field noise coupling modulating J. In the second method, a two-qubit gate is implemented as the resonant rotation of one electron conditional upon the spin state of the other. This method has the significant advantage that J does not need to be tuned and a wide range of coupling strengths yields high-fidelity CROT gates in isotopically-purified silicon (>99% for over two-orders of magnitude variability in J). The CROT gate can be operated at zero electrostatic detuning, which renders the system minimally susceptible to charge noise.

Compared to previous proposals, the CROT gate greatly relaxes the requirements on the accuracy of donor positioning and the alignment of control gates. This makes it ideal for incorporation into a full-scale quantum processor architecture based on donors in silicon.

Chapter 6

Transport of spin qubits with donor chains under realistic experimental conditions

The ability to transport a qubit is essential to many quantum processor architectures. For a spin-based computer, one dimensional spin chains have been proposed as a compact medium to realize short-range transport. In this chapter, we model odd-sized donor chains under a range of experimental imperfections including variability of donor position within the chain. The role of donor-nuclear spins in the transport of the electron spin across the donor chain is addressed. We then estimate the required timescales and exchange couplings, and the level of noise that can be tolerated to achieve high fidelity transport. We also propose a protocol to calibrate and initialize the chain, thereby providing a complete guideline for realizing a functional donor chain and utilizing it for spin transport.

The work presented in this chapter has been submitted for publication:
F. A. Mohiyaddin, **R. Kalra**, A. Laucht, R. Rahman, G. Klimeck and A. Morello. "Transport of Spin Qubits with Donor Chains under Realistic Experimental Conditions." *arXiv:1602.07058* (2016). Submitted to *Physical Review B*.

The author acknowledges F. A. Mohiyaddin, with whom the work presented in this chapter was completed.

In Chapter 5, we proposed a method to perform a two-qubit logic gate with donors in silicon that takes advantage of the hyperfine interaction. Together with the single-qubit operations already experimentally demonstrated, this would form a universal set of quantum gates. One ingredient remains that would complete the set of capabilities required for the architecture described by Hollenberg *et al.* [26]: qubit transport. While transport is not explicitly required by newer proposals based on the promising surface code layout, it is known that long-distance links can help in raising the fault-tolerant threshold [115]. Moreover, they can simplify the layout of a quantum processor by allowing extra space between the physical qubits to accommodate control electronics and other components.

For a solid-state electron-spin-based processor, several proposals outline how the spin-carrying electron itself can be transported, whether by shuttling its confinement potential [116], or by adiabatic passage [117, 118]. Other schemes involve spin-to-spin coupling between electrons such that transport is essentially achieved via a SWAP operation as described in Chapter 5. This may come from direct exchange coupling, magnetic dipolar interaction [27], electric dipoles [119], or a coupling mediated via an intermediate quantum dot [108], a ferromagnet [120] or a resonant cavity [119, 121, 122].

The infrastructure dedicated to qubit transport should be compact, scalable and robust. One-dimensional spin chains have been studied in the literature as a compact medium to couple distant spin qubits [123]. If the number of spins in the chain is odd, the chain forms an extended spin-1/2 qubit [124, 125], providing a link between qubits coupled to either end, as shown in Figure 6.1. A spin state can then be transported from a source qubit to the distant target through (i) sequential SWAP operations [123] or (ii) the adiabatic protocol described by Oh *et al.* [126–129].

Earlier theoretical work on spin chains [123, 127–129] has given general guidelines on design rules and operation schemes for their use in quantum information processing. However, the practical implementation of a spin chain requires a system-specific appraisal of its physical properties and parameters, and a careful analysis of the manufacturability, error rate and speed of operation under realistic experimental conditions. Here we provide an extensive analysis of the feasibility of spin chains based on donors in silicon.

The chapter is organized as follows. In Section 6.1, we outline the requirements for a donor chain to form the desired extended qubit. Moreover, we address the precision with which the donors need to be positioned and the effect of the donor nuclear spins. In Section 6.2, we detail a protocol to calibrate the chain for transport. Finally, in Section 6.3, we assess the fidelity of the adiabatic transport protocol [126] in the presence of several experimental imperfections. Our results therefore provide a complete guideline for realizing a functional donor chain and utilizing it for spin transport.

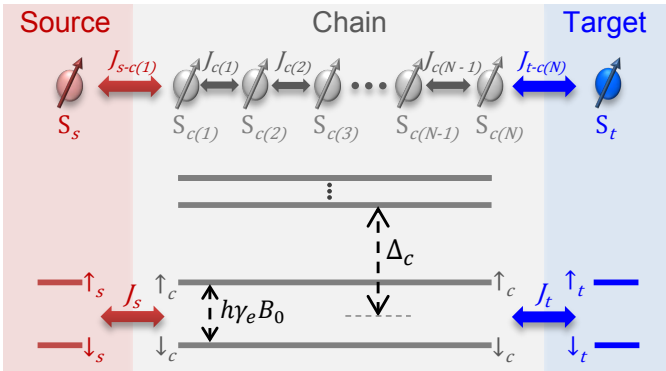

Figure 6.1: **Schematic of a spin chain.** The spins at the edges ($S_{c(1)}$ and $S_{c(N)}$) of the chain (gray) are exchange-coupled to source and target qubits (S_s and S_t). When $\Delta_c \gg h\gamma_e B_0$, the chain forms an extended qubit, allowing spin transport from the source to the target. The magnitude of the effective coupling between the chain and source qubits, J_s, approaches $J_{s-c(1)}/\sqrt{N}$ for large N [123].

6.1 Construction of a donor chain

We begin our analysis by considering a chain solely made up of electrons, and will only include the donor nuclei later in Section 6.1.1. The spin Hamiltonian for an odd number N of electrons with nearest-neighbor exchange couplings $J_{c(i)}$ in an externally applied static magnetic field B_0 is:

$$H_{c_e} = h\gamma_e B_0 \sum_{i=1}^{N} \frac{\sigma_{z,c(i)}}{2} + \sum_{i=1}^{N-1} J_{c(i)} \frac{\boldsymbol{\sigma}_{c(i)}}{2} \cdot \frac{\boldsymbol{\sigma}_{c(i+1)}}{2}, \tag{6.1}$$

where $\gamma_e \approx 28$ GHz/T is the gyromagnetic ratio of the electron. $\boldsymbol{\sigma}_{c(i)}$ is the vector Pauli operator for the ith electron spin in the chain and $\sigma_{z,c(i)}$ is the Pauli z-operator for the i-th spin, with z defined as the direction of the external field B_0. For example, for a chain with $N = 3$, $\sigma_{z,c(2)} = I_2 \otimes \sigma_z \otimes I_2$, where σ_z is the Pauli z-matrix, and I_2 is the 2×2 identity matrix. In contrast to previous chapters, we define the Hamiltonian in energy units here to avoid confusion later in Section 6.3.

The energy spectrum of an odd-number chain consists of a low-energy doublet of states, separated from the nearest excited states by a gap Δ_c (see Figure 6.1), that depends on the intra-chain exchange interaction strengths $J_{c(i)}$. The chain can be treated as an effective two-level system, i.e. a spin-1/2 qubit, under the condition [123]

$$\Delta_c \gg h\gamma_e B_0 \tag{6.2}$$

where $h\gamma_e B_0$ is the Zeeman splitting of the ground doublet. Therefore we label the two lowest energy states of the chain as $|\uparrow_c\rangle$ and $|\downarrow_c\rangle$. Assuming $J_{c(i)} = J_c \; \forall \; i$, Δ_c is given by [125]

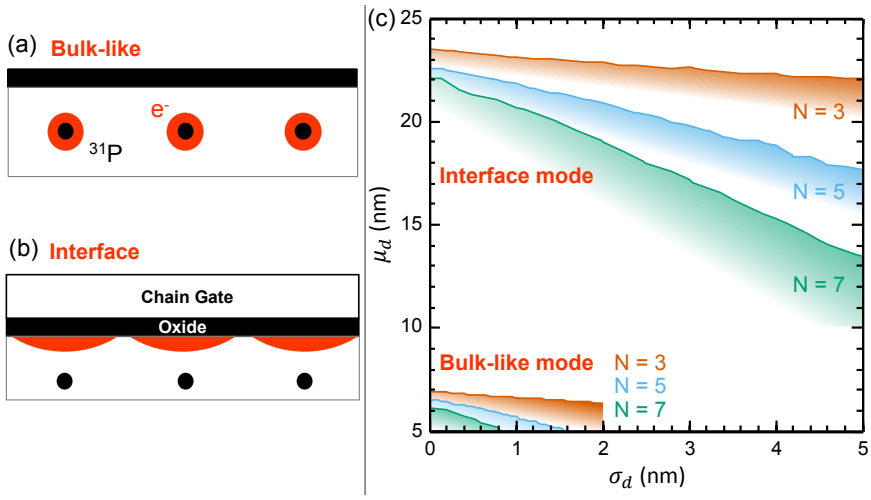

Figure 6.2: **The yield of functioning chains given donor placement errors.** (a)-(b) Schematics of electron orbital wavefunctions in a three-donor chain operated in the (a) bulk-like and (b) interface modes. The electrons and ^{31}P nuclei are represented in red and black, respectively. (c) Targeted inter-donor separation μ_d to obtain at least 90% yield, as a function of donor placement error σ_d. Chains are simulated for the bulk-like and interface modes for $N = 3$, 5 and 7, with $B_0 = 1$ T. Pulling electrons to the Si-SiO$_2$ interface with a chain gate increases the robustness of the chain to donor placement inaccuracies.

$$\Delta_c \approx \frac{J_c \pi^2}{2N} \tag{6.3}$$

Notice that Δ_c is inversely proportional to the number of spins in the chain. If the intra-chain exchange couplings are not all equal, Δ_c needs to be calculated from the numerical diagonalization of Equation 6.1. One typically finds that, with inhomogeneous $J_{c(i)}$, Δ_c is mostly limited by the weaker couplings within the chain. Regardless of the details of the intra-chain couplings, the chain will function as an extended qubit provided the condition in Equation 6.2 is satisfied. The key point in practice is that the chain serves as an effective spin-1/2 as long as $J_{c(i)} \gg h\gamma_e B_0 \ \forall \ i$.

Recall from Chapter 1 that a minimum $B_0 \sim 1$ T is required for high-contrast qubit readout where the electron temperature in our devices is typically $\sim$ 100 mK. This value of B_0 sets a challenging requirement for the minimum $J_{c(i)}$ in the chain according to Equation 6.2. For the example of a 7-electron chain, the minimum $J_{c(i)}/h$ must be $>$ 400 GHz to satisfy $\Delta_c > 10h\gamma_e B_0$. Donor placement inaccuracies during fabrication [130] can lead to large variability in $J_{c(i)}$ [84]. In our paper [131], we calculate the required positioning accuracy to obtain the desired chain qubit. As this portion of the work was carried out by F. A. Mohiyaddin, only a brief summary is presented here.

Figure 6.2 plots the targeted inter-donor separation such that at least 90% of the chains successfully form the extended qubit, as a function of donor placement error. Close to atomic precision in donor placement is required for a chain barely exceeding 20 nm in length, when the

donors are operated in the 'bulk-like mode.' We define this mode to be the operating regime in which no large electric field is applied at the donor site, such that the donor electron is confined to its nucleus. Alternatively, the chain can be operated in the 'interface mode,' where the electrons are pulled towards the Si-SiO_2 interface with a gate voltage [132]. Our calculations show that with 5 nm precision in donor placement, a chain qubit can be formed approaching 100 nm in length when operated in the 'interface mode' [131], making this operating regime the clear choice in the experiment. For completeness, however, we discuss both cases in this chapter.

6.1.1 Nuclear spins

Thus far, we have only included the electron spins in our Hamiltonian, which resulted in a chain-qubit splitting $\epsilon_c = h\gamma_e B_0$. We now include the donor nuclei, which are hyperfine coupled to their respective electrons, and can affect the chain-qubit splitting. The complete chain Hamiltonian is given by

$$H_c = H_{c_e} - \sum_{i=1}^{N} h\gamma_n B_0 \frac{{}^{\text{nuc}}\sigma_{z,c(i)}}{2} + \sum_{i=1}^{N} A_{c(i)} \frac{\boldsymbol{\sigma}_{c(i)}}{2} \cdot \frac{{}^{\text{nuc}}\boldsymbol{\sigma}_{c(i)}}{2} \tag{6.4}$$

where H_{c_e} is given by Equation 6.1, ${}^{\text{nuc}}\boldsymbol{\sigma}_{c(i)}$ is the Pauli operator for the ith chain nucleus with z-component ${}^{\text{nuc}}\sigma_{z,c(i)}$. $A_{c(i)}$ is the hyperfine coupling between the electron and nuclear spins of the ith chain donor. In the interface mode where the electrons are pulled away from their respective nuclei, $A_{c(i)} = 0, \forall i$. The nuclear spins therefore have no effect on the chain qubit. The energy separation between the $|\uparrow_c\rangle$ and $|\downarrow_c\rangle$ chain qubit states is equal to $h\gamma_e B_0$. In the following, we detail the effect of the nuclear spins on ϵ_c in the bulk-like case.

Nuclear spin contribution in the bulk-like mode

Recall that for a large magnetic field, e.g. $B_0 = 1$ T, the electron and nuclear spin states can be treated separately. The N electrons form the extended qubit described in Section 6.1, provided Equation 6.2 is satisfied. For each state of the chain qubit, there are therefore 2^N eigenstates for the nuclei. The resulting ESR spectrum of the chain consists of 2^N resonances, where the chain qubit state is flipped conditional on the state of the nuclear system.

For example, we plot the ESR spectrum for the example of a 3-donor spin chain operated in the bulk-like mode with $B_0 = 1$ T in Figure 6.5(a). The eight ESR transitions reveal the hyperfine shifts in the chain qubit resonance frequency from $\gamma_e B_0 = 28$ GHz. The frequency shift, which we denote as $\Delta\nu_c$, is a function of the nuclear state and the individual hyperfine couplings.

We can provide an expression for this shift by first determining the eigenstates of the nuclei. The chain nuclei are mutually coupled by an electron-mediated super-exchange coupling, J_n, which is a function of the individual hyperfine couplings $A_{c(i)}$ and the electronic exchange couplings $J_{c(i)}$ [24]. For a 3-donor chain with $J_{c(i)}/h = 1$ THz and $A_{c(i)}/h = 100$ MHz, we

numerically calculate that J_n/h between the first and third nuclei is $\sim$ 100 kHz. However, in realistic devices, local electric fields and strain can introduce a Stark shift of order a few MHz in the individual hyperfine couplings $A_{c(i)}/h$ [44, 70], which in turn detune the nuclei from each other by an amount that typically exceeds the magnitude of their mutual couplings. We account for this by introducing variations in the hyperfine couplings of order 1 MHz in Equation 6.4. The $\sim$MHz detuning dominates over the weak coupling J_n/h, such that the nuclear eigenstates are almost exactly the tensor products of their individual $|\Uparrow\rangle$ and $|\Downarrow\rangle$ states. We can thus calculate $\Delta\nu_c$ to first order using the equation below.

$$\Delta\nu_c = \sum_{i=1}^{N} U(i) A_{c(i)} C_{c(i)}/h, \tag{6.5}$$

where $U(i)$ equals 1 or -1 when the ith nuclear spin is $|\Uparrow\rangle$ or $|\Downarrow\rangle$, respectively. $2C_{c(i)} = \langle\uparrow_c|\sigma_{zc(i)}|\uparrow_c\rangle = -\langle\downarrow_c|\sigma_{zc(i)}|\downarrow_c\rangle$ represents the 'effective contribution' of the ith chain electron to the chain spin-1/2 ground states. With this result, we can map the effect of the nuclei for a chain operated in the bulk-like mode onto a shift in ϵ_c by an amount $h\Delta\nu_c$.

6.1.2 Source and target donor qubits

We have simplified the donor chain to a single chain qubit with an energy splitting, ϵ_c, determined by the external magnetic field and the hyperfine coupling to the nuclei. We now include the source and target donor qubits, with their electron spins exchange-coupled to either end of the chain by $J_{s-c(1)}$ and $J_{t-c(N)}$, respectively. Provided $J_{s-c(1)}$ and $J_{t-c(N)} \ll J_c$, the effective exchange coupling between the source (or target) and chain qubits is given by $J_s \approx J_{s-c(1)}/\sqrt{N}$ (or $J_t \approx J_{t-c(N)}/\sqrt{N}$) [123]. Given realistic values of J_c/h of order 100 GHz, the maximum value of J_s/h and J_t/h would be $\sim$ 10 GHz. The source, chain and target electron qubits can then be mapped on to the following Hamiltonian.

$$\begin{aligned} H_{s-c-t} = \epsilon_s \frac{\sigma_{z,s}}{2} + \epsilon_c \frac{\sigma_{z,c}}{2} + \epsilon_t \frac{\sigma_{z,t}}{2} + \\ J_s \frac{\boldsymbol{\sigma}_s}{2} \cdot \frac{\boldsymbol{\sigma}_c}{2} + J_t \frac{\boldsymbol{\sigma}_c}{2} \cdot \frac{\boldsymbol{\sigma}_t}{2}, \end{aligned} \tag{6.6}$$

where $\boldsymbol{\sigma}_i$ is the Pauli operator with z component $\sigma_{z,i}$. ϵ_i is the energy splitting between the qubit states, where the subscript i denotes the source, chain or target.

While we consider both interface and bulk-like modes for the chain, we assume that the source and target donors are operated in the bulk-like mode, where the electron and nuclear spins are coupled by the hyperfine interaction A. For a single donor, recall from Chapter 5 that the nuclear spin can be prepared to yield source and target qubit splittings (ϵ_s and ϵ_t) equal to $h\gamma_e B_0 + A/2$ or $h\gamma_e B_0 - A/2$ when the nucleus is in the $|\Uparrow\rangle$ state or $|\Downarrow\rangle$ state, respectively. In the analysis below, we set $\epsilon_s = \epsilon_t$, which can be realized by preparing the nuclear spins of the source and target donors in the same state, and tuning their hyperfine couplings with local

electrostatic gates [44] until they acquire identical values.

We define the energy detuning between the source and chain qubits as $\Delta B_z = |\epsilon_s - \epsilon_c|$. In the case of an interface-mode chain, $\Delta B_z = A/2$ regardless of the source qubit nuclear state. We use the notation ΔB_z to highlight that this detuning coincides with the energy difference between the $|\uparrow_s\downarrow_c\rangle$ and $|\downarrow_s\uparrow_c\rangle$ source-chain states, and has the same physical origin as the energy difference between the $|\uparrow\downarrow\rangle, |\downarrow\uparrow\rangle$ states in a singlet-triplet qubit [101]. In the interface case, $\Delta B_z = A/2$, as $\epsilon_c = h\gamma_e B_0$ and $\epsilon_s = h\gamma_e B_0 \pm A/2$.

6.2 Calibration of the system

Spin transport across the chain requires control over the exchange couplings J_s and J_t, as will be described in Section 6.3. This control may come from tuning the tunnel barriers between the donor electrons directly [85], or detuning their respective electrochemical potentials [94], with gate electrodes. It is however extremely unlikely, even with atomically precise donor placement, that the magnitude of exchange couplings will match the values targeted during fabrication. Therefore, it will be necessary to first calibrate J_s and J_t to the voltages of the respective gate-electrodes designed to tune them (exchange-gates). For spin transport, the key quantities to record are the minimum and maximum values of the exchange couplings that can be achieved. In addition, it is also important to measure ϵ_i for each qubit, as it can vary due to magnetic field inhomogeneities and DC Stark shifts of the electron g-factor [133] and donor hyperfine interaction [44, 70].

Before providing a calibration protocol, we first introduce the way in which a spin chain might be incorporated into a quantum processor architecture, such as the one presented by Hollenberg *et al.* [26]. A source donor at the edge of the quantum processor is tunnel-coupled to a single-electron transistor (SET) for initialization and readout of its electron and nuclear spins [31–33], as illustrated in Figure 6.3. This donor is then exchange coupled to a donor chain, which is in turn coupled to a target donor. The target donor is linked to the remaining entities of the processor. Due to layout constraints, it may not be possible to fabricate an SET for every donor qubit in the processor for initialization and readout. We have thus developed a protocol to calibrate and initialize the qubits, regardless of their distance from the edge of the processor.

Our calibration protocol relies on the assumption that any qubit or a pair of qubits can be effectively isolated from the remainder of the processor. For example, when the source donor is being calibrated, one must ensure that the chain does not alter its dynamics. Similarly, when J_s is being calibrated, the target should not alter the dynamics of the source-chain system. This isolation may be achieved in two steps. We present these steps using the example of isolating the source donor. First, J_s should be minimized by pulsing its exchange-gate appropriately. However, it would be unrealistic to assume that $J_s = 0$. The source qubit, therefore, is not completely separated from the dynamics of the chain. The second step utilizes J_t to minimize

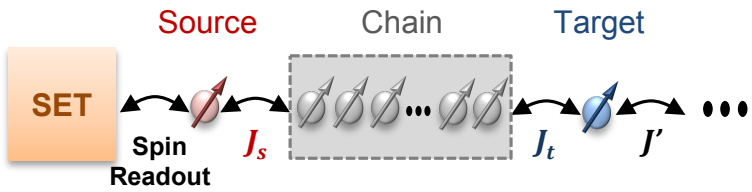

Figure 6.3: **Schematic of the system used for transport.** A source donor is exchange-coupled to a donor chain, which is in turn coupled to a target donor. The target donor is then linked to the remainder of the quantum processor. A single-electron transistor (SET) tunnel-coupled to the source donor serves to initialize and measure the state of the source electron spin qubit.

the effect of a non-zero J_s. Maximizing J_t, i.e. strongly coupling the chain and target qubits, has the effect of isolating the dynamics of the source qubit. This is because the eigenstates of the system will then approximately be the tensor products of the uncoupled source qubit states with the singlet-triplet states of the chain and target, similar to the case where $J_s = 0$. The required ratio of J_t to J_s for this isolation will be quantified in Section 6.4.3. We assume that the above steps are sufficient to isolate any qubit (or pair of qubits) in the processor that is being calibrated.

We begin by determining ϵ_s of the isolated source donor. The spin state of the source electron is measured and initialized using spin-dependent tunneling to the SET [31]. ϵ_s can then be extracted via an ESR sweep experiment as described in Chapter 1.

The next step is to calibrate J_s with its exchange-gate (J_s-gate) voltage. For this, the chain is first isolated from the target, by minimizing J_t and maximizing J' (Figure 6.3). Then, the ESR spectrum of the source qubit is measured while varying the J_s-gate voltages. The exchange coupling J_s modifies the source resonance frequencies and provides a unique 'fingerprint' that can be compared to the theoretically calculated ESR spectrum described below, resulting in an accurate map of J_s as a function of J_s-gate voltage.

Figure 6.4(a) shows the ESR spectrum of the source electron as a function of J_s, with the chain operated in the interface mode, calculated by solving for the eigenstates of the Hamiltonian:

$$H_{s-c(\text{interface})} = h\gamma_e B_0 \left(\frac{\sigma_{z,s}}{2} + \frac{\sigma_{z,c}}{2}\right) - h\gamma_n B_0 \frac{{}^{\text{nuc}}\sigma_{z,s}}{2} + A\frac{\boldsymbol{\sigma}_s}{2} \cdot \frac{{}^{\text{nuc}}\boldsymbol{\sigma}_s}{2} + J_s \frac{\boldsymbol{\sigma}_s}{2} \cdot \frac{\boldsymbol{\sigma}_c}{2}, \tag{6.7}$$

where ${}^{\text{nuc}}\boldsymbol{\sigma}_s$ is the Pauli operator for the source nucleus with z-component ${}^{\text{nuc}}\sigma_{z,s}$, and $\gamma_n \approx 17.2$ MHz/T is the nuclear gyromagnetic ratio for the ^{31}P donor. To obtain a model ESR spectrum that would match the experiment described, for each value of J_s, we weigh all possible transitions between the eigenstates of $H_{s-c(\text{interface})}$ with the product of the transition probability and spin readout contrast of the source qubit [54]. This corresponds to the read-

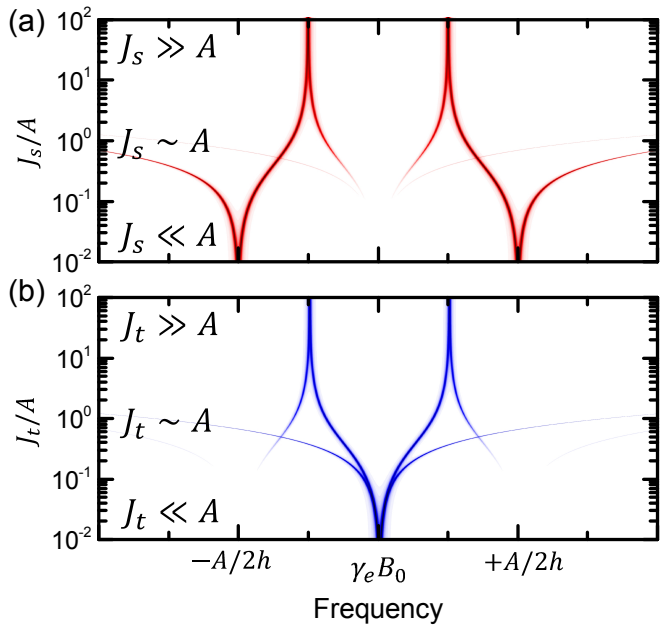

Figure 6.4: **The ESR spectra for calibration in the interface mode.** The spectra are calculated for a donor electron coupled to a chain qubit, assuming that measurement of only (a) the donor electron or (b) the chain qubit is possible. (a) and (b) are used to calibrate J_s and J_t, respectively.

out signal available in the experiment, which is the spin of the source electron (Chapter 5). The resonance frequencies obtained in the experiment at a particular voltage on the J_s-gate corresponds to a horizontal slice in the plot.

We now briefly describe the physics in Figure 6.4(a). For $J_s \ll A/2$, the ESR spectrum is that of the isolated source donor, where the two hyperfine-split peaks [29] correspond to the two possible frequencies of $\epsilon_s/h = \gamma_e B_0 \pm A/2h$. As J_s is increased with its exchange-gate, each of the peaks split into two branches corresponding to the two possible states of the chain qubit, $|\uparrow_c\rangle$ and $|\downarrow_c\rangle$. This splitting is equal to J_s/h, allowing its magnitude to be directly obtained in the low J_s ($< A/2$) regime. As J_s is increased further ($> \Delta B_z = A/2$), the eigenstates of the coupled source and chain qubits evolve towards the spin-singlet $|S\rangle$ and the triplet states, $|T_0\rangle$, $|T_+\rangle$ and $|T_-\rangle$. The branches that involve the $|S\rangle$-like state fade away as their transition probabilities tend to zero. In contrast, the branches that involve the $|T_0\rangle$-like state tend towards a frequency that is the average of the isolated source and chain qubit frequencies, i.e. $(\epsilon_s + \epsilon_c)/2h$. This is equal to $\gamma_e B_0 \pm A/4h$ as shown at the top of Figure 6.4(a), depending on the spin of the source nucleus.

While the low ($< A/2$) values of J_s can be extracted directly from the ESR spectrum, a different technique is required to estimate them when $J_s > A/2$. In this regime, J_s can be measured using a SWAP-style experiment, as detailed in the sequence below.

i. Initialize the source-chain system in anti-parallel states while J_s is minimized. For this,

the chain qubit needs to be read out using a conditional-rotation (CROT) on the source qubit [54]: with the source initialized in the $|\downarrow\rangle$ state and J_s pulsed to $\ll A/2$, an ESR π-pulse is applied at the frequency where the source qubit flips only if the chain is in the $|\downarrow\rangle$ state. If the source has not flipped, then the chain has been determined to be in the $|\uparrow\rangle$ state. The source qubit should then be initialized in the opposite state to the chain qubit.

ii. Measure the frequency of exchange oscillations. With the system initialized in anti-parallel states, J_s is pulsed high ($> A/2$) for a time τ, and then minimized thereafter. The source qubit is then readout to see if it has flipped. This is repeated several times to obtain a flip-probability. The flip-probability can be plotted as a function of τ, and will display exchange oscillations at frequency J_s.

The chain qubit splitting ϵ_c is calibrated by measuring its ESR spectrum, using the fact that its spin state can be read out via CROT of the source qubit in the $J_s \ll A/2$ regime. Similarly, access to the spin state of the chain qubit allows the calibration of J_t to its associated exchange-gate with the same method used to calibrate J_s. Figure 6.4(b) shows the ESR spectrum of the chain qubit as a function of J_t. This spectrum is obtained by solving the Hamiltonian in Equation 6.7, but where the source is replaced by the target and the readout contrast is based on the chain qubit instead. In the low J_t regime, the ESR spectrum is that of the isolated chain qubit, whereas the spectra of Figure 6.4(a) and (b) converge in the high J_s or J_t regime.

The above techniques can thus be used recursively to (i) initialize and readout any qubit, (ii) measure ϵ_i of each qubit, and (iii) calibrate the exchange interaction to its associated gate for any pair of qubits in the processor. As we will explain below, a particularly important parameter for the operation of the chain is the maximum exchange coupling achievable between chain and qubits, $J_{\max}$.

Note that our analysis in this section focused on a donor chain operated in the interface mode. For completeness, we also present the calibration protocol and ESR spectra for the case where the chain is operated in the bulk-like mode here.

6.2.1 Calibration of the donor chain in the bulk-like mode

The difference between the interface and bulk-like modes first appears when measuring the exchange coupling J_s between the source and chain qubits. The ESR spectrum of the source electron will not only show contributions from the state of the chain qubit, but also from the state of the chain nuclei. Figure 6.5(b) shows the ESR spectrum for a source donor coupled to a 3-donor chain, as a function of the exchange coupling $J_{s-c(1)}$ between the source and the first element of the chain. This spectrum is calculated by numerically solving for the eigenstates of the following Hamiltonian.

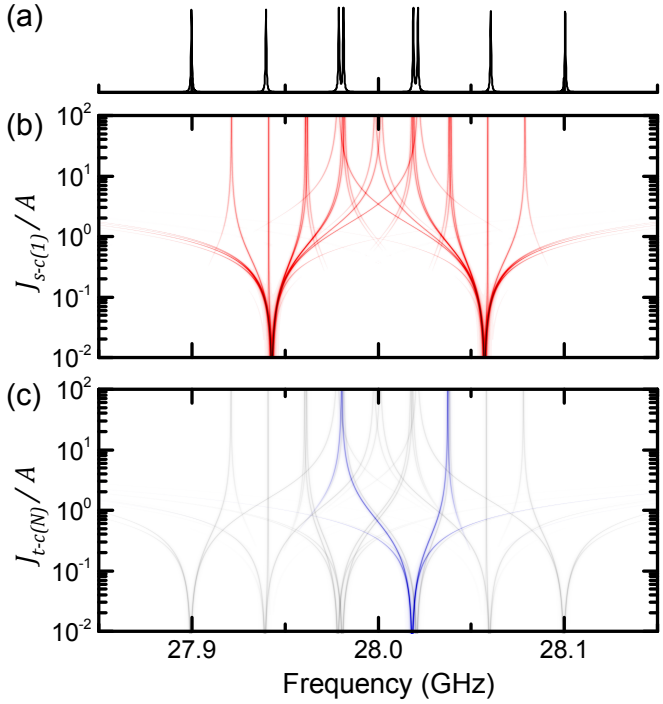

Figure 6.5: **The ESR spectra for calibration in the bulk-like mode.** (a) The ESR frequencies for a three-donor chain, with $B_0 = 1$ T and $J_c/h = 1$ THz. (b) ESR spectrum of a donor coupled to the edge of a $N = 3$ donor chain. (c) ESR spectrum of a $N = 3$ chain qubit coupled to a single donor, i.e. assuming that the chain, not the donor, is being measured. Highlighted in blue are the branches corresponding to the $|\Downarrow\Downarrow\Uparrow\rangle$ nuclear configuration of the chain.

$$\begin{aligned} H_{s-c(\text{bulk})} = H_c + h\gamma_e B_0 \frac{\sigma_{z,s}}{2} - h\gamma_n B_0 \frac{{}^{\text{nuc}}\sigma_{z,s}}{2} + \\ A_s \frac{\boldsymbol{\sigma}_s}{2} \cdot \frac{{}^{\text{nuc}}\boldsymbol{\sigma}_s}{2} + J_{s-c(1)} \frac{\boldsymbol{\sigma}_s}{2} \cdot \frac{\boldsymbol{\sigma}_{c(1)}}{2}, \end{aligned} \tag{6.8}$$

Note that $J_s \propto J_{s-c(1)}$ as described in Section 6.1. For each value of $J_{s-c(1)}$, we find all allowed transitions between eigenstates of $H_{s-c(\text{bulk})}$ and weigh them with the product of the transition probability and the spin readout contrast of the source qubit, as done for the interface mode.

Experimentally, to observe all transition frequencies in the ESR spectrum, the chain qubit and nuclei need to be randomized. The NMR frequencies of an N-donor chain are bound between 0 and $\gamma_n B_0 + A/2h$, as will be explained in the next section. This makes it possible to randomize the nuclei with non-adiabatic sweeps over the NMR frequencies. Similarly, non-adiabatic sweeps over the ESR frequencies in Figure 6.5(a) can be used to randomize the chain qubit.

Figure 6.5(b) shows that in the low $J_{s-c(1)}$ regime, the ESR spectrum of the source electron

consists of two transition frequencies corresponding to the two states of its nuclear spin. As $J_{s-c(1)}$ is increased slightly, these split into a pair of branches due to the coupling to the chain qubit, which can be in either the $|\uparrow_c\rangle$ or $|\downarrow_c\rangle$ state. The branches are split by J_s/h, allowing J_s to be calibrated from the ESR spectrum. For large $J_{s-c(1)}$ ($\gg A$), the branches involving the $|T_0\rangle$-like state tend towards the average of the uncoupled source and chain qubit frequencies, $(\epsilon_s + \epsilon_c)/2h$. This results in 2×2^N possible frequencies, since there are N nuclei in the chain. For $J_s \gg A$, J_s can be calibrated using the SWAP-style experiments outlined in Section 6.2. Once J_s has been calibrated, ϵ_c (and therefore ΔB_z) can be determined by performing ESR on the isolated chain qubit, as explained in Section 6.2.

Figure 6.5(c) then shows the ESR spectrum of the chain qubit coupled to a target donor, for the purpose of calibrating J_t. In the low J_t regime, the chain qubit has eight possible transition frequencies corresponding to those in Figure 6.5(a). Highlighted in bright blue are the branches corresponding to a particular nuclear configuration ($|\Downarrow\Downarrow\Downarrow\Uparrow\rangle$) of the chain. This was done to simplify the understanding of the spectrum, as well as to show that J_t can be obtained even if the chain nuclei are not randomized.

NMR frequencies of a donor chain in the bulk-like mode

In calibration of the system where the chain is operated in the bulk-like mode, it is desirable to randomize the nuclei. Recall that the nuclear eigenstates of a realistic donor chain in the bulk-like mode would be tensor products of the $|\Uparrow\rangle$ and $|\Downarrow\rangle$ states of the chain nuclei. The NMR frequency ν_{ni} for flipping the ith chain nucleus to first order is given by

$$\nu_{ni} = |-\gamma_n B_0 \pm C_{c(i)} A/h|, \tag{6.9}$$

where $C_{c(i)}$ is as defined in Equation 6.5. The sign is $+$ or $-$ when the chain qubit state is $|\uparrow_c\rangle$ or $|\downarrow_c\rangle$, respectively.

$C_{c(i)}$ takes its maximum value of 0.5 when $N = 1$. Hence the maximum value of ν_{ni} is $(\gamma_n B_0 + A/2h)$ for any N. Thus randomized non-adiabatic NMR frequency sweeps from DC to past this maximum value would be sufficient to randomize the nuclei for a donor chain of any size. Practically, the sweep involves applying a frequency-modulated excitation where the rate of change of frequency is faster than, but comparable to, the expected Rabi frequency of a nuclear spin [134].

6.3 Spin transport

Thus far, we have outlined the requirements for an extended qubit to be formed by a chain of donors. We have detailed a protocol to calibrate the chain and its parameters in the experiment. In this section, we analyze the transport of a source qubit to the target qubit via the chain. For our analysis, we define the transport fidelity as:

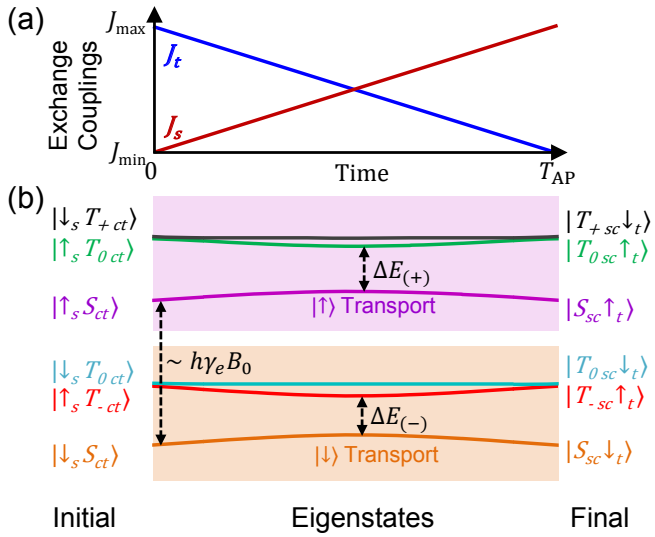

Figure 6.6: **Overview of the adiabatic transport protocol.** (a) Pulsing scheme. (b) Sketch of the time evolution of the eigenenergies (y-axis not to scale). The approximate eigenstates are labeled at the start and end of the protocol. The $|\uparrow\rangle$ and $|\downarrow\rangle$ states are transported via the two labeled adiabatic passages. They belong to two independent blocks of the Hamiltonian as grouped by the shaded boxes.

$$F = |\langle \Psi_f | \Psi_r \rangle|^2, \tag{6.10}$$

where $|\Psi_r\rangle$ is the required final state of the source-chain-target system and $|\Psi_f\rangle$ is the actual final state of the system after transport.

An intuitive method for transporting the source qubit to the target is via sequential SWAP operations [123], where the spin state is first transferred to the chain and then to the target. The SWAP operation can be achieved as discussed in Chapter 5. Defining $\bar{J}$ as the mean exchange coupling during a SWAP operation, the transport fidelity is given by

$$F_{\text{SWAP}} \approx \sin^4 (\pi T_{\text{SWAP}} \bar{J}/h). \tag{6.11}$$

While the SWAP operation is fast, F_{SWAP} is sensitive to noise in J and timing imperfections. Equation 6.11 shows that an accuracy of $\bar{J}T_{\text{SWAP}}$ to within 2% is required to obtain $F_{\text{SWAP}} > 99\%$. In the example where $J(t)/h = 10$ GHz and $T_{\text{SWAP}} = 50$ ps, this translates to a requirement of pulses with picosecond precision. To circumvent this timing constraint, an adiabatic transport protocol robust to pulsing errors was proposed by Oh *et al.* [126].

An adiabatic process is one in which the instantaneous eigenstates of the system are modified at a rate much slower than the energy separations between them. The Hamiltonian H_{s-c-t} in Equation 6.6 is block diagonal, as explained in Reference [126]. We analyze the adiabatic transport process by starting with $J_s = 0$ and $J_t = J_{\text{max}}$ at $t = 0$. At this point, the eigenstates are the uncoupled source spin state and the chain-target singlet and triplet states, as labeled

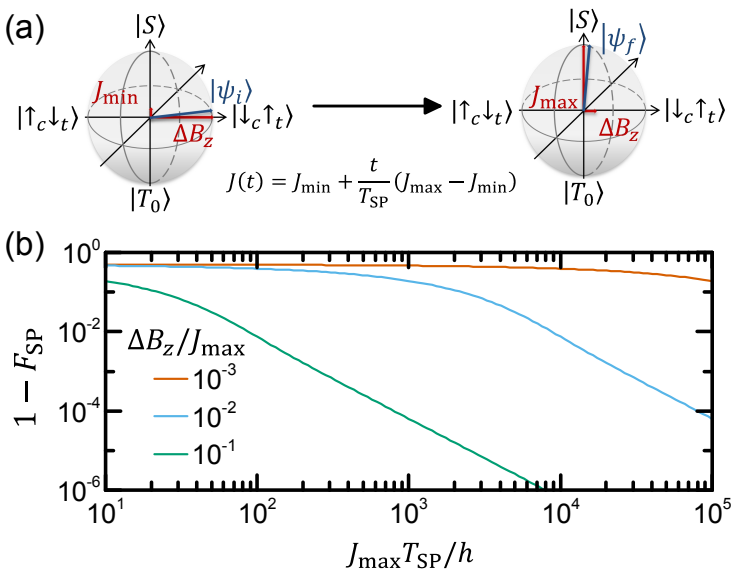

Figure 6.7: **Initialization of the near-singlet state.** (a) Protocol for initializing the chain and target qubits into the near-singlet $|\varphi_{S_{ct}}\rangle$ state of chain and target qubits. (b) Initialization error as a function of the product of T_{SP} and $J_{\max}$, for three values of $\Delta B_z/J_{\max}$. The fidelities are approximately given by Equation 6.12.

on the left side of Figure 6.6(b). The source holds the qubit state to be transported, $|\psi_s\rangle$, and the chain and target qubits must be initialized in the singlet state $|S_{ct}\rangle$ (Section 6.3.1). The system is thus in a superposition of the $|\uparrow_s\ S_{ct}\rangle$ and $|\downarrow_s\ S_{ct}\rangle$ eigenstates, which belong to two independent three-state blocks in the Hamiltonian. These blocks are grouped by the shaded boxes in Figure 6.6(b). Note here that we have omitted the $|\uparrow_s\ T_{+ct}\rangle$ and $|\downarrow_s\ T_{-ct}\rangle$ states in the figure as they are in separate blocks of H_{s-c-t} and do not play a role in transport.

Once initialized, the transport protocol is completed by ramping J_s towards $J_{\max}$ and J_t towards 0 over a time T_{AP}, as shown in Figure 6.6(a). The evolution of the eigenenergies as a function of time is shown in Figure 6.6(b), revealing that the $|\uparrow_s\rangle$ and $|\downarrow_s\rangle$ components follow two independent adiabatic passages. The two passages are identical if $\Delta B_z = 0$. At the end of the protocol, the eigenstates are essentially reflections of the $t = 0$ states. The source qubit is transported to the target, and the prepared singlet is reflected on to the source and chain qubits.

Prior to estimating the fidelity of the adiabatic protocol (Section 6.4), we outline a method to initialize the target and chain for transport.

6.3.1 Singlet initialization for adiabatic transport

Recall from Section 6.1 that the required magnetic field is ~ 1 T and the maximum value of J_s/h and J_t/h is ~ 10 GHz. Therefore, the ground-state of the chain-target system when J_t is at its maximum is the $|T_{-ct}\rangle$ state, rather than the singlet $|S_{ct}\rangle$ state. This rules out several

well-established techniques to initialize two qubits in the singlet state that require it to be their ground state [101]. Below we show that we can nevertheless initialize a singlet state by making use of the presence of a finite ΔB_z. The idea is similar to the way in which the $|\uparrow\downarrow\rangle$ or $|\downarrow\uparrow\rangle$ states are initialized in singlet-triplet qubits [101].

For ease of explanation, we assume that the nuclei of the source and target donors are both initialized in the $|\Downarrow\rangle$ state. We begin with the chain and target qubits in the ground $|T_{-ct}\rangle$ state with minimal J_s and J_t, using the techniques described in Section 6.2. ESR is then used to excite the two qubits to $|\psi_i\rangle$ as labeled in Figure 6.7(a). $|\psi_i\rangle$ is the lower-energy state of the two anti-parallel eigenstates in the low-J regime, equal to $|\widetilde{\downarrow_c\uparrow_t}\rangle = \cos(\theta_2)|\downarrow_c\uparrow_t\rangle + \sin(\theta_2)|\uparrow_c\downarrow_t\rangle$, where $\tan(2\theta_2) = J_{\min}/\Delta B_z$. J_t is then increased adiabatically to $J_{\max}(\gg \Delta B_z)$ over a timescale T_{SP} such that the initialized state $|\psi_i\rangle$ evolves to $|\psi_f\rangle$, as shown in Figure 6.7(a).

Observe that the prepared state $|\psi_f\rangle$ is not exactly equal to the singlet state. ΔB_z modifies the eigenstate of the chain-target system from the exact singlet to a 'near singlet' state, $|\varphi_{S_{ct}}\rangle = \cos(\theta_1)|S_{ct}\rangle - \sin(\theta_1)|T_{0ct}\rangle$, where $\tan(2\theta_1) = \Delta B_z/J_{\max}$. The effect of the discrepancy between the $|\varphi_{S_{ct}}\rangle$ state and the ideal initial state $|S_{ct}\rangle$ on the adiabatic transport protocol will be addressed later in Section 6.4.2. Here, we only focus on the fidelity with which this initialization protocol prepares the $|\varphi_{S_{ct}}\rangle$ state.

The fidelity F_{SP} is calculated as a function of T_{SP}, the time over which J_t is ramped. F_{SP} is defined as the squared-projection of the final chain-target state onto the required $|\varphi_{S_{ct}}\rangle$ state. Figure 6.7(b) plots the error $1 - F_{\mathrm{SP}}$ as a function of the product $J_{\max}T_{\mathrm{SP}}/h$ for $\Delta B_z/J_{\max} = 10^{-1}$, 10^{-2} and 10^{-3}. For simplicity we assume $J_{\min} = 0$. Recall that the adiabaticity of an adiabatic protocol is enhanced when the minimum energy separation between the eigenstates and/or the duration of the protocol is increased. Therefore the fidelity improves as T_{SP} is increased, as long as dephasing can be neglected. This is illustrated in Figure 6.7(b) by considering a fixed $J_{\max}$ and ΔB_z. In addition, the fidelity improves by increasing ΔB_z, since it determines the minimum energy separation between the two eigenstates in this Bloch sphere during the adiabatic protocol. This is also observed in the figure by considering a fixed $J_{\max}$ and T_{SP}. The expression below, derived in the following sub-section, is an approximation for F_{SP} in the adiabatic regime:

$$1 - F_{\mathrm{SP}} \approx \frac{1}{4\left(J_{\max}T_{\mathrm{SP}}/\hbar\right)^2}\left(\frac{J_{\max}}{\Delta B_z}\right)^4. \tag{6.12}$$

Figure 6.7(b) shows that high initialization fidelities are achievable with this protocol. For example, an initialization error of $< 10^{-4}$ can be obtained for $\Delta B_z/h = 100$ MHz, $J_{\max}/h = 10$ GHz, and $T_{\mathrm{SP}} > 10$ μs. However, we note that the required T_{SP} are several orders of magnitude larger than the timescales for the transport protocol, as will be discussed in the next section. Nonetheless, the initialization protocol need only be performed once, since the prepared state can be reused. This is due to the fact that the transport protocol reflects the $|\varphi_{S_{ct}}\rangle$ state on to the source and chain qubits, as illustrated in Figure 6.6(b).

Derivation of analytical approximation

The singlet initialization protocol involves initializing the chain-target system in the $|\widetilde{\downarrow_c\uparrow_t}\rangle$ state, as discussed above, and ramping the exchange coupling between the chain and target qubits. The $|\uparrow_c\uparrow_t\rangle$ and $|\downarrow_c\downarrow_t\rangle$ states are not coupled to either the $|\uparrow_c\downarrow_t\rangle$ or $|\downarrow_c\uparrow_t\rangle$ states. Therefore, the dynamics of the protocol can be represented in the S-T_0 Bloch sphere, as illustrated in Figure 6.7(a). The truncated Hamiltonian in the basis $\{|T_{0ct}\rangle, |S_{ct}\rangle\}$ is given by

$$H_{\mathrm{SP}}(t) = J(t)\frac{\sigma_z}{2} + \Delta B_z \frac{\sigma_x}{2}, \tag{6.13}$$

where $J(t)$ is the exchange coupling between the chain and target, and is linearly ramped from 0 to $J_{\max}$. The aim is to have the system in the $|\varphi_{S_{ct}}\rangle$ eigenstate at the end of the protocol, as defined in Section 6.3.1. Therefore, to quantify the fidelity of the protocol, we translate the Hamiltonian into the adiabatic frame. The translated Hamiltonian $H^A_{\mathrm{SP}}(t)$ is obtained by applying the following operation from the change of basis states (Chapter 1),

$$H^A_{\mathrm{SP}}(t) = AH_{\mathrm{SP}}A^{-1} - i\hbar A\frac{d}{dt}(A^{-1}), \tag{6.14}$$

where the row vectors of A are the time-varying eigenvectors of $H_{\mathrm{SP}}(t)$.

$$H^A_{\mathrm{SP}}(t) = \sqrt{J(t)^2 + (\Delta B_z)^2}\frac{\sigma_z}{2} - \hbar\frac{d\chi_{\mathrm{SP}}}{dt}\frac{\sigma_y}{2}, \tag{6.15}$$

where $\tan(\chi_{\mathrm{SP}}) = \Delta B_z/J(t)$. To gain insight into the energy terms in H^A_{SP}, it is instructive to compare the system in the adiabatic frame onto a spin in a magnetic field (Figure 6.8). In this picture, the field in the z-direction is the energy separation of the eigenstates of H_{SP}. The field in the y-direction is proportional to the rate of change of the angle of the eigenstate in the Bloch sphere of H_{SP} (the laboratory frame). The eigenvectors of $H^A_{\mathrm{SP}}(t)$ are given by

$$|\Phi_{1_{\mathrm{SP}}}(t)\rangle = \begin{pmatrix} \cos(\alpha_{\mathrm{SP}}) \\ -i\sin(\alpha_{\mathrm{SP}}) \end{pmatrix}, \tag{6.16a}$$

$$|\Phi_{2_{\mathrm{SP}}}(t)\rangle = \begin{pmatrix} \sin(\alpha_{\mathrm{SP}}) \\ i\cos(\alpha_{\mathrm{SP}}) \end{pmatrix}, \tag{6.16b}$$

where $\tan(2\alpha_{\mathrm{SP}}) = \hbar\frac{d\chi_{\mathrm{SP}}}{dt}/\sqrt{J(t)^2 + \Delta B_z^2}$. The fidelity is determined by the closeness of the state at the end of the protocol to the $+z$-axis in the adiabatic frame, which is equivalent to the eigenstate of H_{SP}.

The dynamics of the system in the adiabatic frame, H^A_{SP}, is shown in Figure 6.8. Figure 6.8(a) shows the initial state of the system, which is oriented along z, as we start in an eigenstate of H_{SP}. However, the field along y is non-zero at this point, such that the eigenstate $|\Phi_{1_{\mathrm{SP}}}(t)\rangle$ is at an angle $\alpha_{\mathrm{SP}}(0)$ from the z-axis. If we consider the protocol to be in the adiabatic limit, then the precession frequency of the initial state around the eigenstate $|\Phi_{1_{\mathrm{SP}}}(t)\rangle$ is much

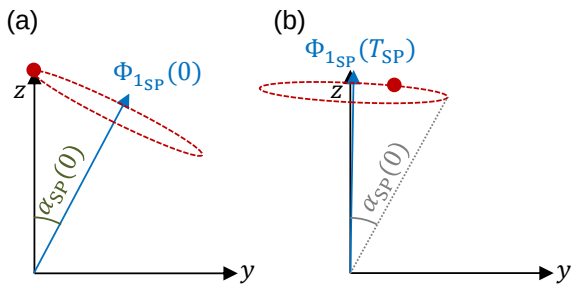

Figure 6.8: **State precession in the adiabatic frame.** The Bloch spheres are shown at the (a) start and (b) end of the singlet initialization protocol. The red dot represents the instantaneous state. The initial state of the system is oriented along the z-axis. In the adiabatic limit, the 'circle of precession' (dashed red circle) around the eigenstate $|\Phi_{1_{\rm SP}}(t)\rangle$ (blue arrow) follows the evolution of $|\Phi_{1_{\rm SP}}(t)\rangle$ and does not change in diameter.

faster than $d\alpha_{\rm SP}(t)/dt$. Hence, we can picture the precession trajectory of the state to be a circle around $|\Phi_{1_{\rm SP}}(t)\rangle$ (dashed red circle in Figure 6.8). In the adiabatic limit, the center of this 'circle of precession' follows $|\Phi_{1_{\rm SP}}(t)\rangle$, and therefore the projection of the instantaneous state onto $|\Phi_{1_{\rm SP}}(t)\rangle$ remains constant.

From Equation 6.16, we see that $\alpha_{\rm SP}$ tends towards zero at $t = T_{\rm SP}$, as also illustrated in Figure 6.8(b). At the end of the protocol, the circle of precession is centered close to the z-axis, with its diameter set by $\alpha_{\rm SP}(0)$. Therefore, the squared-projection of the eigenstate at $t = 0$ on to the z-axis is an estimate of the fidelity of the protocol, and is given by

$$1 - F_{\rm SP} \approx \sin^2(\alpha_{\rm SP}(0)) = \frac{1}{2}\left(1 - \sqrt{\frac{K}{1+K}}\right), \tag{6.17}$$

where $K = (\Delta B_z/J_{\rm max})^4 \times (J_{\rm max}T_{\rm SP}/\hbar)^2$. In the limit where $K \gg 1$, this can be simplified to

$$1 - F_{\rm SP} \approx \frac{1}{4\,(J_{\rm max}T_{\rm SP}/\hbar)^2}\left(\frac{J_{\rm max}}{\Delta B_z}\right)^4. \tag{6.18}$$

6.4 Adiabatic transport under realistic experimental conditions

With an understanding of the adiabatic transport protocol and the ability to initialize the system, we will now investigate the influence of the following experimental parameters on the adiabatic transport protocol: (i) Errors in $T_{\rm AP}$ and/or $J_{\rm max}$; (ii) ΔB_z between the chain and source/target qubits; (iii) Limited tunability of the exchange couplings; (iv) Noise in the qubit energy splittings ϵ_i; (v) Noise in the exchange couplings J_s and J_t. We define the transport fidelity $F_{\rm AP}$ for transporting a source state $|\psi_s\rangle$ according to Equation 6.10. Here, the required final state of the system is $|\Psi_r\rangle = |\varphi_{S_{ct}}\rangle \otimes |\psi_s\rangle$.

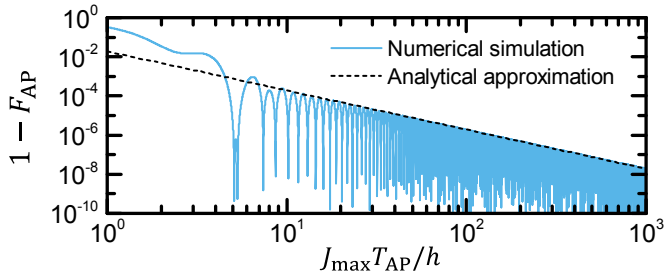

Figure 6.9: **Adiabatic transport fidelity.** The error of the transport protocol is plotted as a function of $J_{\max}T_{\mathrm{AP}}/h$, assuming $\Delta B_z = 0$ and $J_{\min} = 0$. The envelope of the transport error in the adiabatic regime is given by Equation 6.19 (dashed line). The protocol is highly robust to errors in $J_{\max}$ and T_{AP}.

6.4.1 Errors in $J_{\max}$ and T_{AP}

$J_{\max}$ and T_{AP} are the fundamental transport parameters as they determine the degree of adiabaticity of the protocol [126]. To illustrate this, it is instructive to first consider the case where $\Delta B_z = 0$. In this case, the minimum energy separations $\Delta E_{(\pm)}$ between each adiabatic passage and the nearest eigenstate in their blocks are equal to $J_{\max}/2$ [see Figure 6.6(b)]. To maintain adiabaticity, we require the transport time $T_{\mathrm{AP}} \gg h/\Delta E_{(\pm)}$, and hence the transport fidelity F_{AP} is dependent on the product $J_{\max}T_{\mathrm{AP}}/h$.

Figure 6.9 shows the transport error, $1 - F_{\mathrm{AP}}$, as a function of $J_{\max}T_{\mathrm{AP}}/h$, obtained from numerical simulations of transporting the $|\psi_s\rangle = (|\uparrow\rangle + |\downarrow\rangle)/\sqrt{2}$ state. We note that fidelities calculated here are independent of the choice of $|\psi_s\rangle$. The resonances indicate points where perfect adiabatic transport is achieved [126]. However, we focus on the envelope to provide a conservative estimate of fidelities. For large $J_{\max}T_{\mathrm{AP}}/h$, Oh *et al.* [126] showed that the envelope of the error is proportional to $1/(J_{\max}T_{\mathrm{AP}})^2$. This envelope can also be obtained analytically (derivation shown in sub-section below), and is given by

$$1 - F_{\mathrm{AP}} \approx \frac{3}{3 + (2J_{\max}T_{\mathrm{AP}}/\hbar)^2}. \tag{6.19}$$

The above equation is also plotted in Figure 6.9 as the dashed black line. This highlights that the adiabatic protocol is robust to errors in $J_{\max}$ and T_{AP}, and low transport errors of $\sim 10^{-4}$, 10^{-6} and 10^{-8} can be achieved for $J_{\max}T_{\mathrm{AP}}/h \approx 10^1$, 10^2 and 10^3, respectively [126]. Therefore, depending on the targeted fidelity, transport times $T_{\mathrm{AP}} \sim 10 - 100$ ns are required when $J_{\max}/h \sim 1 - 10$ GHz.

Note that the timescales required for T_{AP} are significantly shorter than those required for the singlet initialization protocol time T_{SP}. This is because the transport time is limited by $J_{\max}$, while T_{SP} is limited by $\Delta B_z \ll J_{\max}$.

Derivation of analytical approximation

Here we outline the method we use to quantify the fidelity of the adiabatic transport protocol. Our strategy will be to truncate the Hamiltonian of the system to the relevant 3×3 block. We then map this onto a 2×2 Hamiltonian and translate it into the adiabatic frame to estimate the fidelity.

We start with the basic Hamiltonian H_{s-c-t} for the source-chain-target system defined in Equation 6.6. As described by Oh *et al.*, H_{s-c-t} is block-diagonal, consisting of four blocks. Only two blocks play a role in adiabatic transport, as described in Section 6.4, where one transports the $|\downarrow_s\rangle$ component and the other transports the $|\uparrow_s\rangle$ component of the source qubit. When $\Delta B_z = 0$, these two blocks are identical apart from the Zeeman energy. The Zeeman energy can be ignored, as it is simply an identity offset to the diagonal elements of either block. Either adiabatic transport block is defined by the following Hamiltonian.

$$H_{\mathrm{AP}-3}(t) = \frac{1}{4}\begin{pmatrix} J_t - J_s & 2J_s & 0 \\ 2J_s & -J_s - J_t & 2J_t \\ 0 & 2J_t & J_s - J_t \end{pmatrix} \tag{6.20}$$

The basis states of $H_{\mathrm{AP}-3}$ are given by $\{|\downarrow_s\uparrow_c\uparrow_t\rangle, |\uparrow_s\downarrow_c\uparrow_t\rangle, |\uparrow_s\uparrow_c\downarrow_t\rangle\}$ for the spin-up block and $\{|\uparrow_s\downarrow_c\downarrow_t\rangle, |\downarrow_s\uparrow_c\downarrow_t\rangle, |\downarrow_s\downarrow_c\uparrow_t\rangle\}$ for the spin-down block. For this derivation, we analyze the fidelity for transporting the $|\uparrow_s\rangle$ source state. The eigenvectors of $H_{\mathrm{AP}-3}$ are given by [126]

$$|\Phi_0(t)\rangle = \frac{1}{\sqrt{3}}\begin{pmatrix} 1 \\ 1 \\ 1 \end{pmatrix}, \tag{6.21a}$$

$$|\Phi_\pm(t)\rangle = \frac{1}{\sqrt{N_\pm}}\begin{pmatrix} \sin(\zeta) \\ -\cos(\zeta) \pm \sqrt{q} \\ \cos(\zeta) - \sin(\zeta) \mp \sqrt{q} \end{pmatrix}, \tag{6.21b}$$

where $\tan(\zeta) = (J_s(t)/J_t(t))$, $q = 1 - \sin(\zeta)\cos(\zeta)$, and $N_\pm = \mp 2\left(2\cos(\zeta) - \sin(\zeta)\right)\sqrt{q} + 4q$. For adiabatic transport, the system is initialized in the $|\uparrow_s S_{ct}\rangle$ state, which is $|\Phi_-(0)\rangle$.

Recall that the eigenenergies of the $|\uparrow\rangle$-transport and $|\downarrow\rangle$-transport blocks are plotted in Figure 6.6. We see that in each block, two states anti-cross whereas the energy of one state is constant, suggesting that $H_{\mathrm{AP}-3}(t)$ can be truncated to a 2×2 Hamiltonian. For this, we write $H_{\mathrm{AP}-3}$ in the basis of the eigenstates at $t = T_{\mathrm{AP}}/2$, which can be obtained by substituting $J_s = J_t$ into Equation 6.21. The new basis states are given by

$$|\Phi_0^{'}\rangle = \frac{1}{\sqrt{3}}\begin{pmatrix} 1 \\ 1 \\ 1 \end{pmatrix}, |\Phi_+^{'}\rangle = \frac{1}{\sqrt{2}}\begin{pmatrix} 1 \\ 0 \\ -1 \end{pmatrix}, |\Phi_-^{'}\rangle = \frac{1}{\sqrt{6}}\begin{pmatrix} 1 \\ -2 \\ 1 \end{pmatrix}. \tag{6.22}$$

The Hamiltonian $H_{\mathrm{AP}-3}$ in this basis, $\{|\Phi_0^{'}\rangle, |\Phi_+^{'}\rangle, |\Phi_-^{'}\rangle\}$, is

$$H_{\mathrm{AP}-3}^{'}(t) = \frac{1}{4}\begin{pmatrix} J_t + J_s & 0 & 0 \\ 0 & 0 & \sqrt{3}(J_t - J_s) \\ 0 & \sqrt{3}(J_t - J_s) & -2J_s - 2J_t \end{pmatrix}. \tag{6.23}$$

As expected, $H_{\mathrm{AP}-3}^{'}(t)$ is block-diagonal. The initialized state of the system is $|\uparrow_s S_{ct}\rangle = (1/2)|\Phi_+^{'}\rangle - (\sqrt{3}/2)|\Phi_-^{'}\rangle$. As the initial population of the $|\Phi_0^{'}\rangle$ is zero, we truncate $H_{\mathrm{AP}-3}^{'}(t)$ to the lower 2×2 block, spanned only by $|\Phi_+^{'}\rangle$ and $|\Phi_-^{'}\rangle$. Adding $(J_s + J_t)I_2$, we obtain

$$H_{\mathrm{AP}-2}^{'}(t) = \frac{1}{4}\begin{pmatrix} J_t + J_s & \sqrt{3}(J_t - J_s) \\ \sqrt{3}(J_t - J_s) & -(J_t + J_s) \end{pmatrix}. \tag{6.24}$$

Recall that $J_s + J_t = J_{\max}$ and $J_t - J_s = J_{\max}(1 - 2t/T_{\mathrm{AP}})$. We thus complete our mapping onto a spin in a magnetic field, obtaining

$$H_{\mathrm{AP}-2}^{'}(t) = \varepsilon\frac{\sigma_z}{2} + \Delta_{\mathrm{AP}}(t)\frac{\sigma_x}{2}, \tag{6.25}$$

where $\varepsilon = J_{\max}/2$ and $\Delta_{\mathrm{AP}}(t) = (\sqrt{3}J_{\max}/2)\,(1 - 2t/T_{\mathrm{AP}})$. Note that the initialized state, $|\uparrow_s S_{ct}\rangle$ is the lower-energy eigenstate of $H_{\mathrm{AP}-2}^{'}(0)$.

With the mapping complete, we then move to calculating the fidelity of the adiabatic protocol. For this, we translate $H_{\mathrm{AP}-2}^{'}(t)$ into the adiabatic frame, by invoking the same operation used in Equation 6.14. The Hamiltonian in the adiabatic frame $H_{\mathrm{AP}-2}^{A}(t)$ can be simplified as

$$H_{\mathrm{AP}-2}^{A}(t) = \sqrt{\varepsilon^2 + \Delta_{\mathrm{AP}}(t)^2}\frac{\sigma_z}{2} - \hbar\frac{d\chi_{\mathrm{AP}}}{dt}\frac{\sigma_y}{2}, \tag{6.26}$$

where $\tan(\chi_{\mathrm{AP}}) = \Delta_{\mathrm{AP}}(t)/\varepsilon$. The eigenvectors of $H_{\mathrm{AP}-2}^{A}(t)$ are given by

$$|\Phi_{1_{\mathrm{AP}}}(t)\rangle = \begin{pmatrix} \cos(\alpha_{\mathrm{AP}}) \\ -i\sin(\alpha_{\mathrm{AP}}) \end{pmatrix}, \tag{6.27a}$$

$$|\Phi_{2_{\mathrm{AP}}}(t)\rangle = \begin{pmatrix} \sin(\alpha_{\mathrm{AP}}) \\ i\cos(\alpha_{\mathrm{AP}}) \end{pmatrix}, \tag{6.27b}$$

where $\tan(2\alpha_{\mathrm{AP}}) = \hbar\frac{d\chi_{\mathrm{AP}}}{dt}/\sqrt{\varepsilon^2 + \Delta_{\mathrm{AP}}(t)^2}$. We employ the same technique used to derive an expression for the fidelity of the singlet initialization protocol. We consider the dynamics in the adiabatic frame and assume the adiabatic limit, where the projection of the instantaneous state onto the eigenstate remains constant. The diameter of the 'circle of precession,' again, is determined by the initial eigenstates in the adiabatic frame, which is at an angle $\alpha_{\mathrm{AP}}(0)$ from the z-axis. The eigenstate at the end of the protocol is oriented at an angle $\alpha_{\mathrm{AP}}(T_{\mathrm{AP}})$ from the z-axis. From Equation 6.27, we see that $\alpha_{\mathrm{AP}}(T_{\mathrm{AP}}) = \alpha_{\mathrm{AP}}(0)$. Therefore, at the end of the protocol, the circle of precession is at exactly the same position as at $t = 0$. Recall that the fidelity of the adiabatic protocol is the projection-squared of the final state onto the z-axis.

The 'circle of precession' touches the z axis, and hence we obtain resonances in the transport fidelities as a function of T_{AP} in Figure 6.9. To obtain the worst case fidelity, however, we use the opposite point on the circle, which has the maximum angular deviation from the z-axis. This yields an expression for the envelope of transport errors given by

$$1 - F_{\mathrm{AP}} \approx \sin^2(2\alpha_{\mathrm{AP}}(0)) = \frac{3}{3 + (2J_{\max}T_{\mathrm{AP}}/\hbar)^2} \tag{6.28}$$

Note that this expression perfectly aligns with the numerical simulations in the adiabatic regime ($J_{\max}T_{\mathrm{AP}}/h \gg 1$) in Figure 6.9.

6.4.2 The effect of ΔB_z

The previous section showed that the adiabatic transport protocol is robust to errors in $J_{\max}T_{\mathrm{AP}}$. The ratio between ΔB_z and $J_{\max}$ also has an important effect on the adiabaticity of the protocol. The energy separations $\Delta E_{(\pm)}$ as a function of ΔB_z are given by:

$$\frac{\Delta E_{(\pm)}}{J_{\max}} = \frac{1 + \sqrt{9 \pm 8\frac{\Delta B_z}{J_{\max}} + 16(\frac{\Delta B_z}{J_{\max}})^2}}{8} \pm \frac{\Delta B_z}{2J_{\max}}. \tag{6.29}$$

A non-zero ΔB_z decreases $\Delta E_{(-)}$ in Equation 6.29, and can therefore reduce the adiabaticity of the $|{\downarrow_s}\rangle$ passage. Figure 6.10(a) plots the error for transporting a $|\psi_s\rangle = |{\downarrow}\rangle$ state, as a function of $\Delta B_z/J_{\max}$, for $J_{\max}T_{\mathrm{AP}}/h \approx 10^1$, 10^2 and 10^3. The plot shows that for $\Delta B_z \ll J_{\max}$, the fidelities are limited only by $J_{\max}T_{\mathrm{AP}}/h$, and are given by Equation 6.19. As ΔB_z increases past a certain point, the reduction of $\Delta E_{(-)}$ causes the $|{\downarrow_s}\rangle$ passage to lose adiabaticity. From Figure 6.10(a) we can extract the cut-off value for $\Delta B_z/J_{\max}$, such that ΔB_z does not reduce the transport fidelity, by fitting to the following expression:

$$\left(\frac{\Delta B_z}{J_{\max}}\right)_{\mathrm{cut-off}} \approx \frac{\sqrt{J_{\max}T_{\mathrm{AP}}/h}}{13} \tag{6.30}$$

Equation 6.30 shows that, that for $J_{\max}T_{\mathrm{AP}}/h \approx 10^1$, ΔB_z can be as large as $J_{\max}/4$ without affecting the fidelity. In the example of $\Delta B_z/h = 100$ MHz, $J_{\max}/h$ only needs to be as large as ≈ 400 MHz. Even higher values of $\Delta B_z/J_{\max}$ can be tolerated if $J_{\max}T_{\mathrm{AP}}/h$ is increased.

In addition to the adiabaticity, ΔB_z has another effect on the transported state. It breaks the symmetry of the $|{\uparrow}\rangle$ and $|{\downarrow}\rangle$ adiabatic passages, since $\Delta E_{(+)} \neq \Delta E_{(-)}$ in Equation 6.29. The transported state thus acquires a constant phase $\Delta\phi$ with respect to the initial source state. The phase $\Delta\phi$ can be calibrated and corrected for, because it is a function of ΔB_z, $J_{\max}$, (which are determined during the calibration stage) and T_{AP}.

6.4.3 Limited tunability of exchange couplings

So far, we have assumed that the exchange coupling can be controlled up to the point of being entirely switched off, $J_{\min} = 0$. A more realistic assumption would allow for a limited dynamic

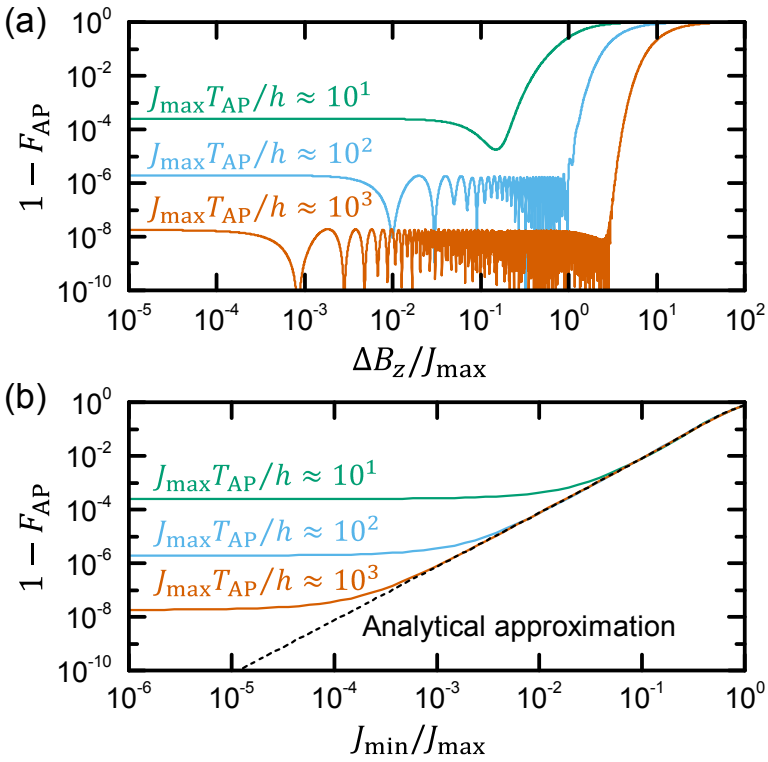

Figure 6.10: **The effect of ΔB_z and $J_{\min}$ on transport fidelity.** The transport error due to (a) ΔB_z normalized to $J_{\max}$, and (b) limited tunability ($J_{\min}/J_{\max}$) of exchange couplings. These are obtained from numerical simulations of the adiabatic protocol for $J_{\max}T_{\mathrm{AP}}/h \approx 10^1$, 10^2 and 10^3. The cut-off value of $\Delta B_z/J_{\max}$ such that ΔB_z does not affect the transport fidelity is given in Equation 6.30. The dashed line in (b) is the error due to 'spin-leakage' as described by Equation 6.31.

range in the tunability of J, such that some residual exchange coupling remains at all times. For $J_{\min} > 0$, the eigenstates of the system at $t = 0$ are not the simple tensor products of the source qubit state with the coupled states of the chain and target qubits. The transport fidelity then depends on how the system is initialized. If we assume that the system can be initialized such that the source qubit holds the state to be transported $|\psi_s\rangle$ and the chain and target are in the 'near singlet' state $|\varphi_{S_{ct}}\rangle$, the initialized state is not an eigenstate. The source qubit will then undergo partial exchange oscillations ('spin-leakage') with the chain and target, resulting in an error.

To estimate the effect of this spin-leakage, we perform simulations where we wait for a time $h/J_{\max}$ after the transport protocol, which yields the worst-case fidelity. For simplicity, we assume $\Delta B_z = 0$. Figure 6.10(b) plots the error of transporting the $|\psi_s\rangle = |\uparrow\rangle$ state as a function of $J_{\min}/J_{\max}$, for $J_{\max}T_{\mathrm{AP}}/h \approx 10^1$, 10^2 and 10^3. The fidelity here is independent of the choice of $|\psi_s\rangle$. We observe that the error traces in Figure 6.10(b) are first limited by Equation 6.19 ($J_{\max}T_{\mathrm{AP}}/h$) and then by spin-leakage for large $J_{\min}/J_{\max}$. An analytical expression for the error due to spin-leakage (derivation shown in sub-section below) is plotted

as the dashed black line in Figure 6.10(b) and is given by

$$1 - F_{\mathrm{AP}} \approx \frac{3}{4} \times (J_{\min}/J_{\max})^2. \tag{6.31}$$

The quadratic dependence in Equation 6.31 allows for low transport errors to be achieved with fairly limited tunability. One and two orders of magnitude of control over the exchange interaction result in errors of 10^{-2} and $\sim 10^{-4}$, respectively. Note that the exchange coupling that needs to be tuned in this system is that between a single donor electron operated in the bulk-like mode (source or target) and an electron at the edge of the chain operated in the interface mode. Estimation of the control on this exchange interaction is left for future work. A recent experiment has demonstrated limited tuning of the exchange coupling in a similar configuration, but the donor in that instance was located almost directly beneath the interface dot [135].

On another note, the spin-leakage error is essentially an estimate of the degree of isolation of the source qubit from the rest of the system. Figure 6.10(b) illustrates that good isolation can be achieved even with limited tunability of exchange couplings. Recall the technique described in Section 6.2 to isolate the source qubit during calibration, where J_t is maximized with respect to J_s. With two orders of magnitude of tunability of exchange couplings, i.e. $J_t/J_s \sim 100$, the source qubit can be treated as being isolated with a fidelity of $\sim 99.99\%$. This is an important result, that could perhaps be used to design an architecture robust to residual exchange interactions, as will be discussed at the conclusion of this chapter.

Derivation of analytical approximation

Here we derive an expression for the transport fidelity limited by 'spin-leakage.' We set $\Delta B_z = 0$ for simplicity, such that the $|\uparrow\rangle$ and $|\downarrow\rangle$ adiabatic passages are equivalent. In Section 6.4.3, in the example of transporting the $|\uparrow_s\rangle$ state, we have considered the system to be initialized in the $|\uparrow_s\, S_{ct}\rangle$ state. At $t = T_{\mathrm{AP}}$, the system is transported to the $|S_{sc}\uparrow_t\rangle$ state, which is not an eigenstate if $J_{\min} \neq 0$. To quantify the error due to the resulting precession, we express $|S_{sc}\uparrow_t\rangle$ as a superposition of the eigenstates of $H_{\mathrm{AP}-3}$, given by

$$|S_{sc}\uparrow_t\rangle = c_+|\Phi_+(T_{\mathrm{AP}})\rangle + c_-|\Phi_-(T_{\mathrm{AP}})\rangle, \tag{6.32}$$

where $c_\pm^2 = \left[\mp\left(2\cos\left(\zeta_0\right) - \sin\left(\zeta_0\right)\right) + 2\sqrt{q}\right]/4\sqrt{q}$ with $\tan(\zeta_0) = J_{\min}/J_{\max}$. For $J_{\min}/J_{\max} < 1$, $c_- > c_+$. The precession frequency is $\sim J_{\max}/h$. The maximum error is when the state rotates by an angle π around the eigenstate, such that the state of the system becomes $c_+|\Phi_+(T_{\mathrm{AP}})\rangle - c_-|\Phi_-(T_{\mathrm{AP}})\rangle$. This worst-case leads to a fidelity given by $F_{\mathrm{AP}} = |c_+^* c_+ - c_-^* c_-|^2$, which is the projection onto the $|S_{sc}\uparrow_t\rangle$ state. This can be simplified to

$$1 - F_{\mathrm{AP}} = \frac{3}{4} \times \frac{\left(J_{\min}/J_{\max}\right)^2}{\left(J_{\min}/J_{\max}\right)^2 - \left(J_{\min}/J_{\max}\right) + 1}. \tag{6.33}$$

In the limit $J_{\min}/J_{\max} \ll 1$, the transport error takes the form

$$1 - F_{\mathrm{AP}} \approx \frac{3}{4} \times (J_{\min}/J_{\max})^2. \tag{6.34}$$

6.4.4 Noise on the qubit energy splittings ϵ_i

Magnetic and electric noise, arising both within the device and from the external control fields, results in fluctuations in ϵ_s, ϵ_c and ϵ_t. This can lower the fidelity of the transport protocol in two ways. First, the qubit being transported will be subject to dephasing, where an error in $\Delta\phi$ is accumulated. Second, higher-frequency noise can cause fast temporal variations in the instantaneous eigenstates, which can in turn make the transport passages lose adiabaticity.

To estimate the effect of this noise, we simulate the adiabatic transport protocol with independent white Gaussian noise of power spectral density $S_{\delta\epsilon_i}$ added to ϵ_s, ϵ_t and ϵ_c in Equation 6.6. For each value of $S_{\delta\epsilon_i}$, we perform 1000 simulations and compute the mean fidelity F_{AP} for transporting the $|\psi_s\rangle = (|\uparrow\rangle + |\downarrow\rangle)/\sqrt{2}$ state, for $J_{\max}T_{\mathrm{AP}}/h \approx 10^1$, 10^2 and 10^3, with $\Delta B_z/h = 100$ MHz. We plot these errors as a function of $\left(S_{\delta\epsilon_i}/h^2\right) \times T_{\mathrm{AP}}$, as the solid lines in Figure 6.11(a). We express the noise added as $\left(S_{\delta\epsilon_i}/h^2\right)$ to yield units of $\mathrm{Hz}^2/\mathrm{Hz}$, which is consistent with the quantities discussed in this chapter.

We observe that, in the low-noise regime, the fidelities are limited by the value of $J_{\max}T_{\mathrm{AP}}/h$. As the level of noise increases, the fidelities are independent of $J_{\max}$ and instead only depend on the magnitude of the noise and the time that the noise has to act on the system.

The total error is a combination of errors due to dephasing and loss of adiabaticity. To capture the error due to the loss of adiabaticity alone, we perform a separate simulation to obtain the average error $e_A(\delta\epsilon_i)$ of transporting the $|\psi_s\rangle = |\uparrow\rangle$ and $|\psi_s\rangle = |\downarrow\rangle$ states, which are immune to dephasing. $e_A(\delta\epsilon_i)$ is computed for $J_{\max}T_{\mathrm{AP}}/h \approx 10^3$ and is plotted as the dashed purple line in Figure 6.11(a). We observe that this matches the solid orange line when $\left(S_{\delta\epsilon_i}/h^2\right) \times T_{\mathrm{AP}} < 10^{-10}$. Beyond this value, dephasing also contributes to the total error, separating these two lines, as shown by the inset.

The error due to dephasing of a single qubit, $e_\phi(\delta\epsilon_i)$ in the presence of white noise is given by [136]

$$e_\phi(\delta\epsilon_i) = \frac{1 - e^{-T_{\mathrm{AP}}/T_2}}{2} = \frac{1 - e^{-2\pi^2 S_{\delta\epsilon_i} T_{\mathrm{AP}}/h^2}}{2}, \tag{6.35}$$

where T_2 is the qubit dephasing time. We plot $e_\phi(\delta\epsilon_i)$ as the dashed gray line in Figure 6.11(a). Assuming the two sources of error to be independent, the total error is given by $e_\phi(\delta\epsilon_i) + e_A(\delta\epsilon_i) - e_\phi(\delta\epsilon_i)e_A(\delta\epsilon_i)$. This matches the solid orange line remarkably well (result not plotted). In the regime where the transport is limited by noise, we fit the error to an exponential function. This yields the fit, $e(\delta\epsilon_i)$ (plotted as the dashed magenta line in Figure 6.11(a)), given by

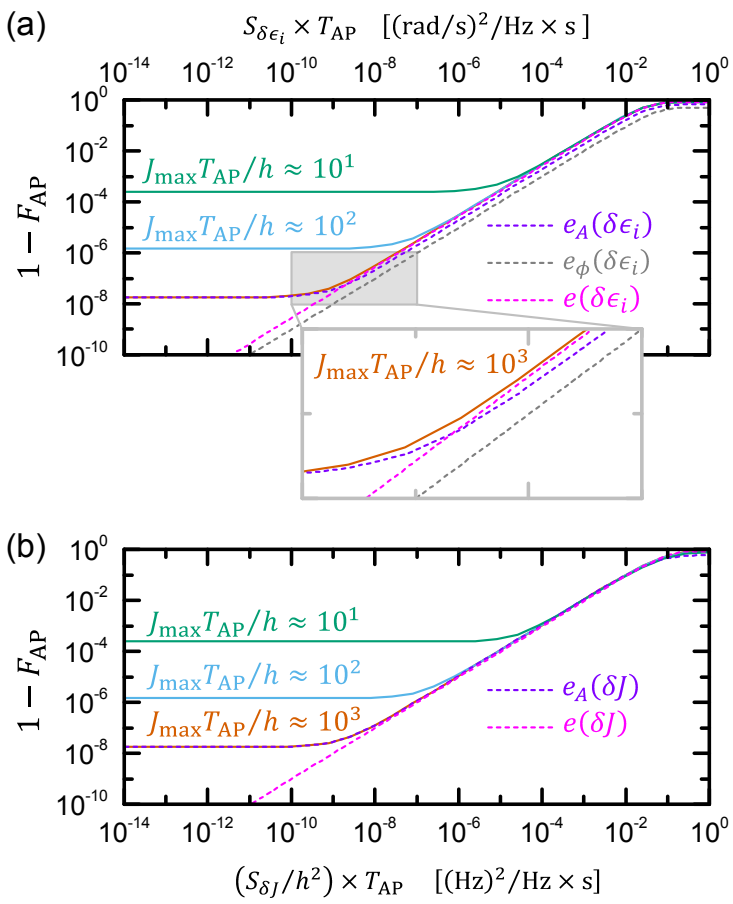

Figure 6.11: **The effect of noise on transport fidelity.** Calculations of error due to noise added to (a) ϵ_s, ϵ_c and ϵ_t and (b) J_s and J_t. The errors are plotted as a function of the product of the power spectral density of the white noise added ($S_{\delta\epsilon_i}$ and $S_{\delta J}$) and T_{AP}. We assume $\Delta B_z/h = 100$ MHz. The solid lines are obtained from numerical simulations of the adiabatic protocol for $J_{\max}T_{\mathrm{AP}}/h \approx 10^1$, 10^2 and 10^3. The dashed purple lines correspond to the error due to the loss of adiabaticity for $J_{\max}T_{\mathrm{AP}}/h \approx 10^3$. The dashed magenta lines are fits of the total error due to the noise given by Equations 6.36 and 6.37. The dashed gray line in panel (a) shows the error due to dephasing.

$$e(\delta\epsilon_i) \approx 0.83\left(1 - e^{-34\times S_{\delta\epsilon_i}T_{\mathrm{AP}}/h^2}\right). \tag{6.36}$$

Comparing these results to the experiment requires knowledge of the frequency-dependence of the power spectral density of the noise. For the device measured in Chapter 3, the noise spectrum was of the form $9\times10^{11}/\omega^{2.5} + 6$ (rad/s)^2/Hz. The frequency-dependent component is attributed to fluctuations in the external magnetic field B_0 [46], which would be homogeneous over the typical transport length-scales ($\sim$ 100 nm). This effect of this noise component can therefore be refocused with dynamical decoupling [21]. On the other hand, the white noise floor cannot be refocused. With the reported noise floor of 6 (rad/s)^2/Hz, such that $\left(S_{\delta\epsilon_i}/h^2\right) \approx 0.15$, Equation 6.36 predicts errors of $\sim 10^{-7}$ with $T_{\mathrm{AP}} \approx 100$ ns.

6.4.5 Noise in the qubit-chain couplings J_s and J_t

Electrical noise in a gated nanostructure can modify the exchange interactions J_s and J_t. For $\Delta B_z = 0$, noise in J_s and J_t modifies the $|\uparrow\rangle$ and $|\downarrow\rangle$ adiabatic passages equally, such that the phase error of the transported state is zero. However, $\Delta B_z/h \sim 100$ MHz is always finite for an interface-mode chain, breaking the symmetry of the passages and allowing this noise to potentially feed in to the phase of the transported qubit. Additionally, high frequency noise can potentially reduce the adiabaticity of transport by rapidly modifying the instantaneous eigenstates.

We estimate the transport fidelity as a function of $\left(S_{\delta J}/h^2\right) \times T_{\mathrm{AP}}$, where $S_{\delta J}$ is the power spectral density of white noise added to J_s and J_t. For each value of $S_{\delta J}$, we perform a Monte Carlo analysis of 1000 simulations to quantify the fidelity F_{AP} of transporting the $|\psi_s\rangle = (|\downarrow\rangle + |\uparrow\rangle)/\sqrt{2}$ state with $\Delta B_z/h = 100$ MHz. These errors are plotted as the solid lines in Figure 6.11(b), for $J_{\max}T_{\mathrm{AP}}/h \approx 10^1$, 10^2 and 10^3. The trend observed is the same as that of Figure 6.11(a). Note that solid orange line is hidden by the dashed purple line.

To quantify the loss of adiabaticity, we obtain the average error $e_A(\delta J)$ of transporting the $|\psi_s\rangle = |\uparrow\rangle$ and $|\psi_s\rangle = |\downarrow\rangle$ states, as they are immune to dephasing. $e_A(\delta J)$ for $J_{\max}T_{\mathrm{AP}}/h \approx 10^3$ is plotted as the dashed purple line in Figure 6.11(b). It aligns almost exactly with the solid orange line for $\left(S_{\delta J}/h^2\right) \times T_{\mathrm{AP}} < 10^{-2}$, indicating that the loss of adiabaticity is the main source of error for noise in J_s and J_t. In the regime where the transport is limited by noise, we fit the error to an exponential function. This yields the fit, $e(\delta J)$ (plotted as the dashed magenta line in Figure 6.11(b), given by

$$e(\delta J) \approx 0.83 \left(1 - e^{-11 S_{\delta J} T_{\mathrm{AP}}/h^2}\right). \tag{6.37}$$

Experimental values for noise on the exchange coupling between donors are not currently available. In any case, our analysis shows that it is favorable to perform the transport protocol in shorter times T_{AP} and larger $J_{\max}$.

Overall, we find that high-fidelity spin-qubit transport across donor chains may be achieved with the adiabatic protocol. This protocol is inherently robust to errors in the precise magnitudes of exchange couplings and the transport time (Figure 6.9). The inclusion of ΔB_z in the system is utilized to initialize the system for transport. For $\Delta B_z/h \sim 100$ MHz, we find that a minimum $J_{\max}/h$ of 400 MHz is sufficient to ensure that the fidelity is unaffected by ΔB_z (Figure 6.10(a)). In the case of limited tunability of the exchange coupling, we have found that two orders of magnitude of control is sufficient for fidelities exceeding 99.99% (Figure 6.10(b)). The magnitude of magnetic noise as measured in a recent experiment in isotopically-purified silicon still allows for errors $\sim 10^{-7}$ to be achieved (Figure 6.11(a)). As for the noise in the exchange couplings, although we have calculated the transport fidelities as a function of the noise power spectral density, we do not have compatible experimental measurements for comparison.

6.5 Summary and Outlook

This chapter provided a comprehensive assessment of the use of donor chains for the transport of electron spin qubits in a silicon quantum processor. We addressed the requirements for a chain of donors to form the necessary extended qubit and determined that the donors in the chain should be operated in the interface mode. This allows for greater donor placement inaccuracies, in line with current fabrication techniques, and greater transport distances, due to the width of the wavefunction of an electron operated in this mode. The nuclear spins of the source and target donors produce an inbuilt magnetic detuning that enables the initialization of a singlet state between the chain and target, which is required for adiabatic transport. We analyzed the performance of the transport protocol under a range of realistic experimental imperfections and noise, concluding that high fidelities should be achievable.

Qubit transport is not explicitly required by recent architectures employing the surface code layout. However, as alluded to in the introduction of this chapter, we may be able to use spin chains to aid in the design of realistic architectures. One of the main problems faced in scale-up is effectively combating residual interactions when qubits are meant to be uncoupled. Figure 6.12 shows a sketch of a surface code layout employing spin chains for their ability to couple and effectively isolate distant qubits. Isolation may be achieved using the technique described in this chapter, where neighboring qubits are strongly coupled to each other in order to isolate them from another particular qubit. Further isolation may be achieved by returning chains from the interface mode to the bulk-like mode, essentially destroying the extended qubit.

Figure 6.12(a) shows a surface-code compatible layout [50] where each orange box is one logical data qubit and each green box is one logical ancillary qubit. The black lines connecting the corners of the green boxes indicate that transport via spin chains is available between ancillary qubits. The purple connections between adjacent boxes indicate that two-qubit logic gates can be performed between data and ancillary qubits. Figure 6.12(b) shows the composition of each logical qubit. The white circles represent neutral donors. The actual qubit is held by one electron spin at a time. It can be shuttled to the different donors in the box using the spin chains and exchange-gates, represented as the black lines and gray boxes, and the adiabatic transport protocol discussed in this chapter. An idle qubit would be held at the donor in the center while the spin chains serve to decouple it from its neighbors. When a logic gate is to be performed, the qubit is transported to the edge where the purple boxes represent a weak exchange interaction such that the logic gate proposed in Chapter 5 can be performed.

This sketch is far from a complete architecture. Its purpose is simply to bring to the attention of the reader the possibility of taking advantage of spin transport in the design of a surface code quantum processor.

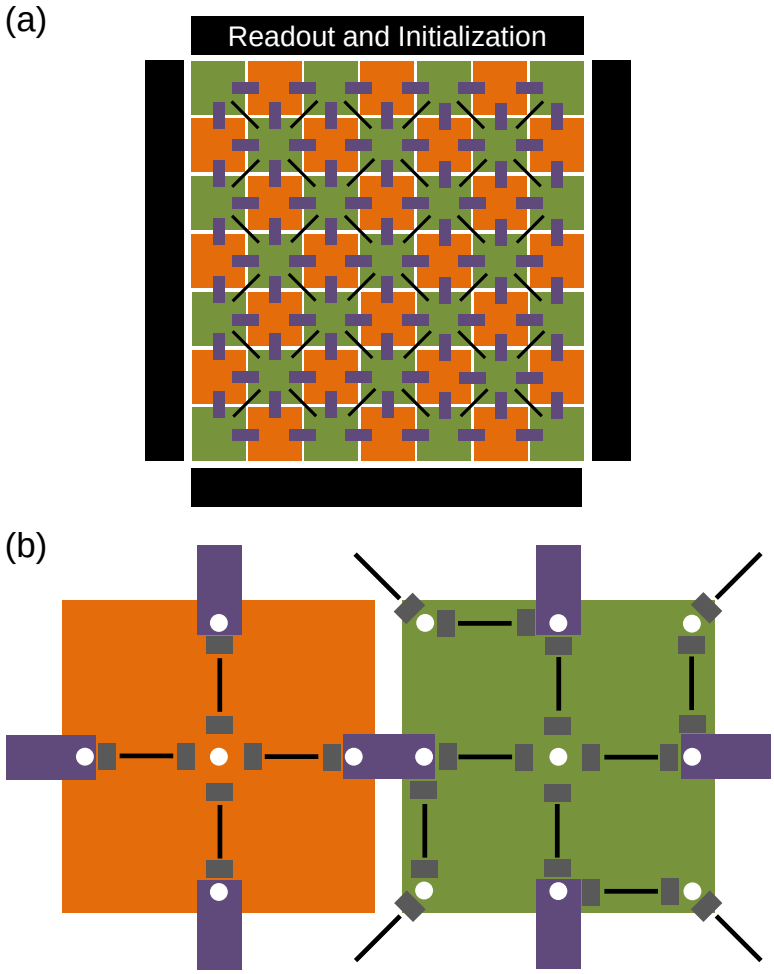

Figure 6.12: **Spin chains in a surface-code compatible architecture.** A sketch of how spin chains can be used in a surface code layout to reduce the effect of residual interactions when a qubit is meant to be idle. (a) A schematic of the surface code layout where the orange and green boxes each represent one logical data and ancillary qubit, respectively. (b) A zoom-in on the composition of the data and ancillary qubits. Each white circle is a neutral donor.

Chapter 7

Vibration-induced electrical noise in a cryogen-free dilution refrigerator

The measurements presented in this thesis thus far were performed in a traditional wet dilution refrigerator which relies on frequent replenishment of liquid helium. While this has been adequate for single qubit experiments, the limited space available for the device and supporting electronics makes it unsuitable for a full-scale quantum processor. Thus, the shift to cryogen-free dilution refrigerators is a necessary step towards scale-up. Our group recently acquired such a system which uses a pulse tube cryocooler to cool the dilution unit to below 4 K. A major disadvantage of these systems, however, is the vibrational noise from the pumps and refrigeration processes. In this chapter, we report on how these vibrations result in electrical noise measured on the cables installed in the cryostat. We test the performance of different cables designed to diagnose and tackle the noise, and find triboelectric effects to be the dominant mechanism coupling the vibrations to the electrical signal. Flattening a semi-rigid cable or jacketing a flexible cable to restrict movement within the cable successfully reduces the noise level by over an order of magnitude. Furthermore, we characterize the effect of the vibrations on the same electron spin qubit device measured in Chapters 3 and 4. Coherence measurements are used to measure the spectrum of the noise experienced by the qubit, revealing the spectral components attributed to the vibrations of the pulse tube.

The work presented in this chapter has been submitted for publication:

R. Kalra, A. Laucht, J. P. Dehollain, D. Bar, S. Freer, S. Simmons, J. T. Muhonen and A. Morello. "Vibration-induced electrical noise in a cryogen-free dilution refrigerator: characterization, mitigation, and impact on qubit coherence." *arXiv:1603.03146* (2016). Submitted to *Review of Scientific Instruments*.

The author acknowledges A. Laucht and J. P. Dehollain, with whom the majority of the work presented in this chapter was completed. J. P. Dehollain led the measurements presented in Figure 7.8.

Chapters 3 and 4 presented results from measurements on a single electron spin qubit device in a traditional 'wet' dilution refrigerator. Chapters 5 and 6 discussed theoretical proposals for scaling to multi-qubit operations. Equally important in the discussion of scale up is the shift from the 'wet fridge' to a cryogen-free system.

Perhaps the most important disadvantage of wet systems is the limited space available as a result of the narrow-neck dewars required to minimize helium boil-off. A full-scale quantum processor will require space for supporting classical electronics and for control lines to the chip. From a practical perspective, the need to refill the helium dewar every 2-4 days is inconvenient and requires manpower. Additionally, liquid helium is a limited natural resource that is becoming increasingly scare and, therefore, expensive. While a system can be installed for re-liquefaction, the necessary equipment and infrastructure is very expensive and, even then, $\sim 10\%$ losses are common.

These factors have led to the increasing popularity of cryogen-free systems, where a pulse tube cryocooler is used to cool the dilution unit to below 4 K. These 'dry fridges' do, however, have major sources of vibrational and acoustic noise [137, 138]. The necessary compressor and rotary valve, used in modern systems, are sources of tangible vibrations external to the cryostat. Inside the pulse tube, the dynamics of the helium gas can produce acoustic vibrations that are directly coupled to the cold head. Significant efforts have been made by manufacturers to minimize the coupling of these vibrations to the sample-space in the cryostat, as will be described in Section 7.1.

In this chapter, we report on how vibrations from the pulse tube significantly couple into the electrical signal measured on our cables, over a bandwidth of up to 40 kHz. This noise completely corrupts our measurement signal. We characterize this noise and, by testing the performance of different types of cables, learn that the dominant mechanism through which the vibrations couple into the electrical signal is via triboelectric effects [139]. Using the cables that yield the minimum amount of voltage and current noise, we prepare the setup for measurement of the same electron spin qubit device characterized in Chapters 3 and 4. Performing noise spectroscopy with qubit coherence measurements clearly reveals that vibrational noise from the pulse tube couples into the effective magnetic environment of the qubit.

7.1 Measurement setup

Figure 7.1(a) shows a schematic of our BlueFors LD400 dilution refrigerator setup. Pre-cooling to < 4 K is provided by a two-stage Cryomech PT-415 pulse tube cryocooler, which is driven by a CP1000 helium compressor. As shown in the schematic, the low and high pressure lines in and out of the compressor are connected to a rotary valve. This has an internal disc that is incrementally rotated at a frequency of 140 Hz by a stepper motor with a full rotation frequency of 1.4 Hz. With each half rotation, the rotary valve switches the connection of the pulse tube between the low and high pressure lines. The valve, along with the helium gas reservoirs, is

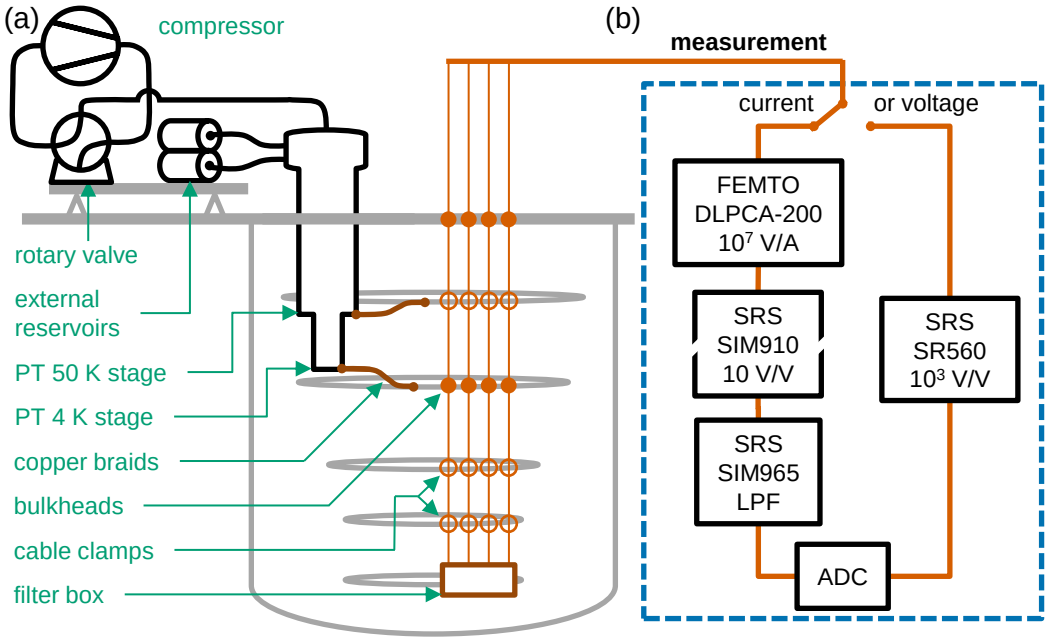

Figure 7.1: **Schematic of the cryogen-free dilution refrigerator measurement setup.** (a) The two stages of the pulse tube cryocooler and measurement cabling in the cryostat are highlighted. (b) Block diagram of the measurement instrumentation used for either current or voltage measurements.

mounted on a metal plate that stands on rubber posts to isolate the 140 Hz vibrations from the cryostat. The pulse tube is designed to be vibrationally isolated from the cryostat, where soft copper braids are used to thermally link the cold heads to their respective plates in the dilution refrigerator.

Our cables run from the measurement box, as shown in Figure 7.1(b), from room temperature down to the mixing chamber plate. Our standard setup uses cupronickel semi-rigid cables from COAX CO, part number SC-219/50-CN-CN (we refer to this cable as 'UT85 cupronickel'). We have SMA bulkheads from Huber-Suhner at two stages. The hermetically sealed 34_SMA-50-0-3/111 is used at the top plate and the standard 34_SMA-50-0-1/111 is used at the 4 K plate. On the 50 K, 1 K and cold plates, we use copper clamps made in-house for thermalization of the cables without the need for bulkheads. Finally, these cables go to a filter box made in-house at the mixing chamber plate. The filter box is identical to the one used in the wet fridge described in Chapter 2. Recall that it houses a printed circuit board with an 80 MHz LC-pi low-pass filter for each line. For the filtering of very high frequencies, each line is counter-wound around an ECCOSORB rod and the box is filled with copper powder. Not shown in this figure is the space in which the sample is mounted below the mixing chamber plate and the superconducting vector magnet from American Magnetics. Also not shown is a constantan twisted-pair 'loom' wire used to carry our low-frequency signals to the device that goes through a separate filter box.

Figure 7.1(b) shows our signal measurement setup. The setup for current measurement

is identical to that described in Chapter 2. We also show the setup used to perform voltage measurements. While we do not typically measure voltages within the scope of our experiments, this was set up to measure the noise on our lines, as we will discuss later in this chapter. For voltage measurements, we use the SR560 voltage amplifier set to a gain of either 10^3 or 10^4 V/V, with a low-pass filter at 100 kHz with 12 dB/octave roll-off. The amplifier has an input impedance of 100 MΩ and output impedance of 50 Ω. The digitizer used to acquire the final signal has an input impedance of 50 Ω as well, which halves the gain of our voltage amplifier chain. The use of the SR560 here introduces a ground loop in our system, but we focus on the spectral components of interest.

7.2 Pulse tube noise

With the system at its base temperature of ∼11 mK, we set up our measurement of the current through the SET. A 2-second trace of the current acquired with 200 kSa/s is shown in Figure 7.2(a), labeled 'PT on.' The gain of the amplifier chain (0.1 V/nA) has been taken into account to plot the magnitude of the current. We observe noise that coincides with the chirping of the pulse tube. Chirping refers to the audible 1.4 Hz cycle of connecting the pulse tube to the high and low pressure lines from the compressor. With an amplitude exceeding 10 nA, the noise would completely overwhelm our experimental signal. We temporarily switch off the pulse tube cooler, such that both the compressor and the rotary valve are switched off, without interrupting the dilution refrigeration to acquire the trace labeled 'PT off.' The noise amplitude reduces by a factor of 8, clearly indicating that the noise is caused by the operation of the pulse tube.

Figure 7.2(b) shows an audio recording of the chirping next to the setup, taken with the standard sampling frequency of 44.1 kHz. Traces (a) and (b) were not taken simultaneously, but are aligned to highlight that the spikes in amplitude do occur simultaneously. We take the Fourier transform of the current and plot its amplitude spectrum in Figure 7.2(c). The dominant noise lies between 5 and 10 kHz, which lies in the range of our typical experimental signal frequencies. We also observe a 9 pA peak at 140 Hz, caused by vibrations of the rotary valve, but this is negligible compared to the dominant noise.

Figure 7.2(d) shows a zoom-in of the dominant noise in the amplitude spectrum. We observe sharp peaks in the 5 to 10 kHz range that are regularly spaced with a separation of ∼400 Hz. We also calculate the amplitude spectrum of the audio signal and show a zoom-in of the same frequency region in Figure 7.2(e). We observe the same pattern, with the frequency peaks matching those from the current measurements. In another test, we took vibration measurements with a Wilcoxon Research 731A seismic accelerometer. While this model is low-pass filtered at 450 Hz, we still managed to acquire an appreciable signal in the kHz range. We placed the accelerometer at the top of the frame on which the fridge is mounted. Figure 7.2(f) shows the RMS value of vibration velocity as a function of frequency in the same range for an

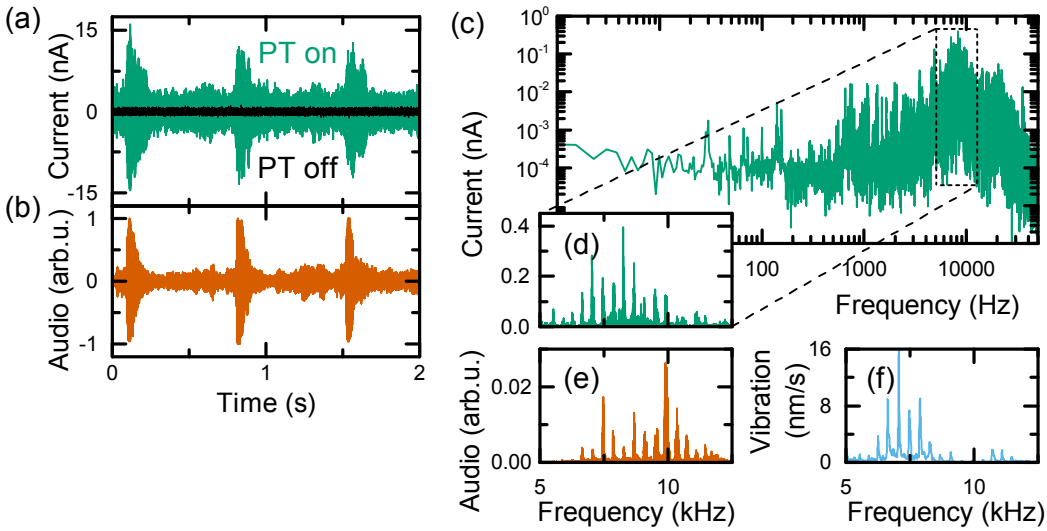

Figure 7.2: **Electrical noise induced by vibrations from the pulse tube.** (a) Current traces measured on a UT85 cupronickel cable run from room temperature to the sample at 10 mK. The green and black traces are taken when the pulse tube is on and off, respectively. (b) Audio recording of the pulse tube chirps. (c) Amplitude spectrum of the current trace with a zoom-in of the 5-12 kHz range shown in (d). (e) Amplitude spectrum of the audio trace. (f) Vibration spectrum measurement taken with an accelerometer.

average of 100 traces. We observe the same characteristic 400 Hz spacing between peaks, again with the frequencies matching the previous traces.

Figure 7.3 plots the spectrograms of both the current and audio signals to reveal how their spectra vary with time. The spectrograms are obtained by dividing the signals into 20 ms windows, with an overlap between adjacent windows of 10 ms for smoothing. A Hamming window is used to reduce spectral leakage. The power spectral density is then calculated from the Fourier transform, and the spectrograms are plotted to 40 kHz for the current signal in Figure 7.3(a) and to 20 kHz for the audio signal in Figure 7.3(b). The spectrograms reveal how the regularly spaced peaks in the 5 to 10 kHz range from Figure 7.2(d)-(f) are produced. Figure 7.3 shows three chirps of the pulse tube, occurring at times ~ 0.1 s, ~ 0.8 s and ~ 1.5 s. We see that with each chirp, the 400 Hz-spaced peaks are not produced simultaneously, but rather each peak occurs in quick succession. Each subsequent peak is spaced by roughly 400 Hz in frequency and by 10 to 20 ms in time. Following a peak, there appears to be a finite decay time in the magnitude of noise at that frequency. This is shown more clearly in the spectrogram of the audio signal, where the result is a 'slanted comb' structure. This comb also appears in between chirps, at ~ 0.5 s and ~ 1.2 s, presumably when the rotary valve connects the low pressure line from the compressor. It is interesting that these combs are slanted in the same direction as the ones where the high pressure line is connected, although they have a lower amplitude and a longer delay between successive peaks.

With the understanding that the observed electrical noise originates from (or is at least

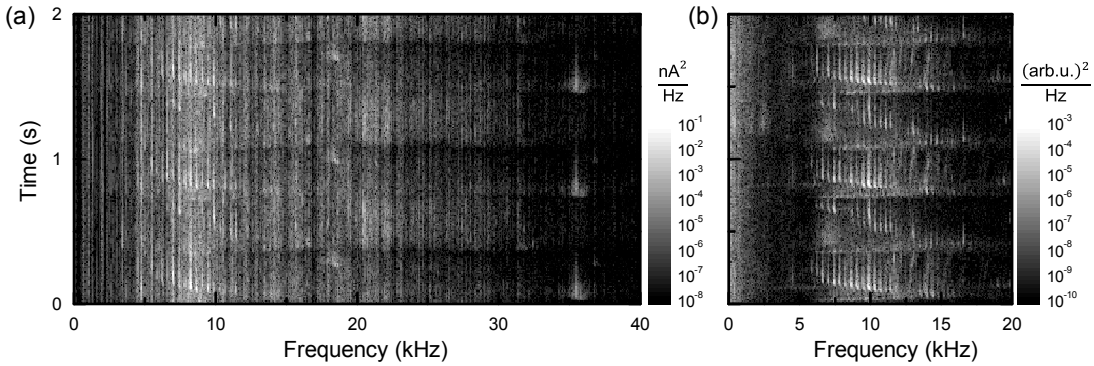

Figure 7.3: **Spectrogram of the noise signal.** Near-identical features are observed in the spectrograms of the (a) the current trace shown in Figure 7.2(a), and of (b) the audio record shown in Figure 7.2(b).

strongly correlated with) vibrational noise, we perform further tests to gain insight into the problem. We first test the effect of ambient acoustics by playing a 3 kHz tone next to the cryostat to see if it couples to the measured signal. With the volume set much louder than the chirps of the pulse tube, the amplitude spectrum still shows that the magnitude of the tone is significantly lower than the 5 to 10 kHz peaks (data not shown). This suggests that the problematic vibrations are not coupling via acoustics through the air to the top flange. We then attempt to reduce the noise by replacing the default step driver to the rotary valve with a linear ramp driver. We try this with the LNII linear micro-stepping drive from Precision Motion Controls. While this slightly reduces the amplitude of the 140 Hz peak as measured both by the accelerometer and the current signal, it does not make a difference to the dominant noise in the 5 to 10 kHz range (data not shown).

Next we test the hypothesis that the vibrations may be originating from the gas reservoir and rotary valve, combined with ineffective damping from the rubber posts supporting that plate. We therefore detach the entire plate and lift it a few centimeters over the frame. The helium lines are, of course, still connected to the pulse tube. Analyzing the amplitude spectra of the two traces, this does not make any difference to the dominant 5 to 10 kHz noise observed. However, the 140 Hz peak caused by the vibrations of the rotary valve reduces in amplitude by a factor of 11 (data not shown). This led us to investigate whether the 140 Hz peak actually couples in to the room-temperature measurement setup as opposed to the cable in the cryostat. Careful positioning of the room-temperature connection to the transimpedance amplifier reduces the 140 Hz peak close to the noise floor, while the higher frequency noise associated with the pulse tube chirps remains unaffected. This supports the hypothesis that the 140 Hz peak is being coupled through the room-temperature setup.

Finally, we investigate the dependence of the magnitude of the noise on the temperature of the system. For this test, we use a UT85 cupronickel line that terminates at an open-circuit bulkhead at the 4 K plate. Figure 7.4(a) plots the current traces at different temperatures,

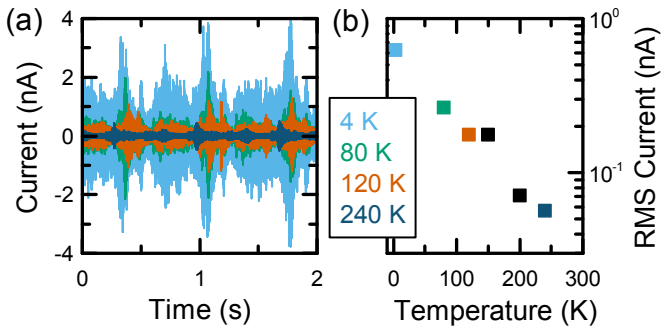

Figure 7.4: **Temperature dependence of the noise magnitude.** The current is measured at different temperatures of the second stage of the pulse tube during a cool-down. The UT85 cupronickel cable is run from the room-temperature flange to the 4 K plate. (a) The current traces are plotted for four selected temperatures. (b) The RMS current is plotted as a function of temperature.

clearly showing the increase in the magnitude of the noise with decreasing temperature. Figure 7.4(b) plots the root-mean-square (RMS) values of the current traces as a function of temperature, suggesting an exponential dependence.

While the pulse tube chirps reduce by over an order-of-magnitude from 4 K to 240 K, the 140 Hz peak reduces by less than a factor of two. This also supports the hypothesis that the 140 Hz vibrations are largely coupling in to the signal via the room-temperature cables.

The dependence of the magnitude of the pulse tube chirps on temperature must come from the origin of the vibrations within the pulse tube itself and/or the mechanism by which they couple to the electrical signal. The volume of the sound made by the pulse tube during the cool-down does not vary significantly. If this is a good measure of the magnitude of the vibrations at the source, then this would suggest that the temperature dependence lies in the coupling mechanism.

The amplitude of the current noise of the trace shown in Figure 7.2(a), where a cable reaching the device enclosure was tested, is approximately 3 times larger than that of the 4 K trace shown in Figure 7.4(a), where the cable stops at the 4 K plate. The dependence of the noise magnitude with cold cable length is consistent with vibration-to-signal coupling occurring within the cables. We have two models for how vibrations can couple to the electrical signal, both of which are based on the fact that the dielectric undergoes a greater thermal contraction than the outer conductor.

The dielectric should undergo the majority of its thermal contraction at a relatively high temperature. From Figure 7.4(b), however, the noise appears to increase continuously with decreasing temperature down to 4 K. Recall that the cable tested is fixed on one end to the room-temperature plate and on the other to the 4 K plate, resulting in a thermal gradient. Therefore, the length of the cable that is cold, and that can therefore translate vibrations to electrical noise, should increase continuously with decreasing temperature at the cold end.

The first candidate model is the creation of noise due to microphonics. We refer specifically to the effect used in a capacitor microphone, where acoustic vibrations cause fluctuations in

capacitance. A current is produced that is proportional to these fluctuations and the voltage applied across the capacitor. In our cables, the thermal contraction of the dielectric causes it to be squeezed around the inner conductor and results in a gap being formed between it and the outer conductor. Thus, vibrations can cause movement of the dielectric and inner conductor with respect to the outer conductor, which translates to variations in the effective capacitance of the line. While we have not intentionally applied a voltage on the line, one may be created by the thermoelectric effect. A voltage difference on the order of millivolts would be induced between the cold and room temperature ends of the line, and a difference may be present between the inner and outer conductors depending on their construction and assembly.

We test if the dominant mechanism is microphonics by applying a voltage on the line while measuring the current, which can be achieved with the FEMTO DLPCA-200 transimpedance amplifier. Applying biases of up to 5 V on the line, we find that the current measured is independent of the applied bias (data not shown). Based on this, we believe that the dominant effect is not capacitor microphonics.

The second candidate is the creation of noise via the triboelectric effect [139]. When the dielectric is rubbed against either the inner or outer conductor, any friction experienced will facilitate the transfer of charge that can be measured as either a current or a voltage depending on the setup. The shrinking of the dielectric with decreasing temperature allows more room for sliding and rubbing between the dielectric and outer conductor. The amount of friction and charge transfer inside a cable will vary significantly with the construction of and materials in the cable. Therefore, we proceed by installing and measuring several different types of cables in our setup, which will be discussed in detail in the following section.

7.3 Cable comparison

We prepare a measurement of the noise on different types of cables, both to understand the coupling mechanism and to reduce the noise in our measurement as much as possible. We test four variations of semi-rigid cables and four variations of flexible cables. For fair comparison, all of these cables run from room temperature to open-circuit terminated bulkheads at the 4 K plate. The semi-rigid cables tested are clamped at the 50 K stage for thermalization as described before. The flexible cables are thermalized by taping and tying them to posts both above the 50 K and 4 K plates. The system is cooled to < 4 K and the dilution unit is not operated. We record both the voltage and current noise present on the cables. Measurements are performed as described previously.

Figures 7.5 and 7.6 show the results for the semi-rigid and flexible cables tested, respectively. The first column shows a schematic of the cable, with dimensions and materials labeled. The second column shows the time traces of the current and voltage noise, where available. The traces plotted here have been filtered digitally to remove components that are not representative of the noise created in the cable. A notch filter is used to remove the 140 Hz signal that couples

in to both the current and voltage measurements in the room-temperature setup. Additionally, the voltage measurement introduces a peak at ∼30 kHz independent of the cable, which we also remove with a notch filter. The RMS values labeled in the figure are calculated using the filtered traces. The third column shows the amplitude spectra of the unfiltered current and voltage traces, so that the 140 Hz and 30 kHz peaks are visible here. Note that the voltage and current noise measurements are not normalized to the length of the cable, as they are installed with the necessary length to reach the 4 K plate with the thermalization steps in our setup.

The first cable presented in Figure 7.5 is the original cable tested, the semi-rigid UT85 cupronickel cable from COAX CO. The RMS values for the current and voltage noise traces are 620 pA and 54 μV. From this, we estimate the effective output impedance of this 'noise source' between the inner and outer conductors of the cable to be 90 kΩ. This is an important quantity in determining whether or not this noise affects particular experiments. The effect of our setup in relation to the noise both on the measurement of the current through the SET and on the voltage biases applied to electrodes on the device must be considered.

Our current measurement setup is as described before. A transimpedance amplifier with an input impedance of 150 Ω sits at room temperature and is connected to a cable that runs inside the cryostat, down to the input of the 80 MHz filter box at the mixing chamber plate. The ∼kHz noise of the pulse tube is not attenuated by the high-frequency filter, whose output is then connected to the drain contact of the SET. The impedance of the SET varies between ∼100 kΩ and an open-circuit, depending on whether it is biased to a conductance peak or in Coulomb blockade. This means that the noise source at the cable 'sees' a high impedance to its left (the SET) and a low impedance to its right (the transimpedance amplifier). Therefore, the majority of the noise current flows through the transimpedance amplifier, corrupting our experimental signal of the current through the SET. Techniques such as lock-in modulation and RF reflectometry [140] are able to modulate the readout signal to a higher frequency, thus avoiding the ∼ 10 kHz pulse tube noise. However, care must still be taken in considering the effect of this noise on the voltage biasing of the gate electrodes.

The experiments we conduct are extremely sensitive to voltage noise present at the gate electrodes of the device [44]. The gates we intend to pulse with moderately high frequencies are connected through the 80 MHz filters described previously. The setup at room-temperature is as described in Chapter 2, but is repeated here for clarity. A passive voltage summer-divider circuit, with resistors in the order ∼kΩ, is used to combine the output of a DC voltage source with voltage pulses from an arbitrary waveform generator. This means that the noise source at the cable 'sees' an open circuit to its left (the gate electrode) and a resistance of a few kΩs to its right (the output impedance of the room temperature summer-divider circuit). In this configuration, the voltage noise at the gate would be a few percent of the noise produced by the cable, since most of it is shunted by the low output impedance of the voltage divider-combiner. In Section 7.4, we quantify the effect of this noise on our electron spin qubit device.

The second row of the figure shows the noise measured on an identical cable that is flattened

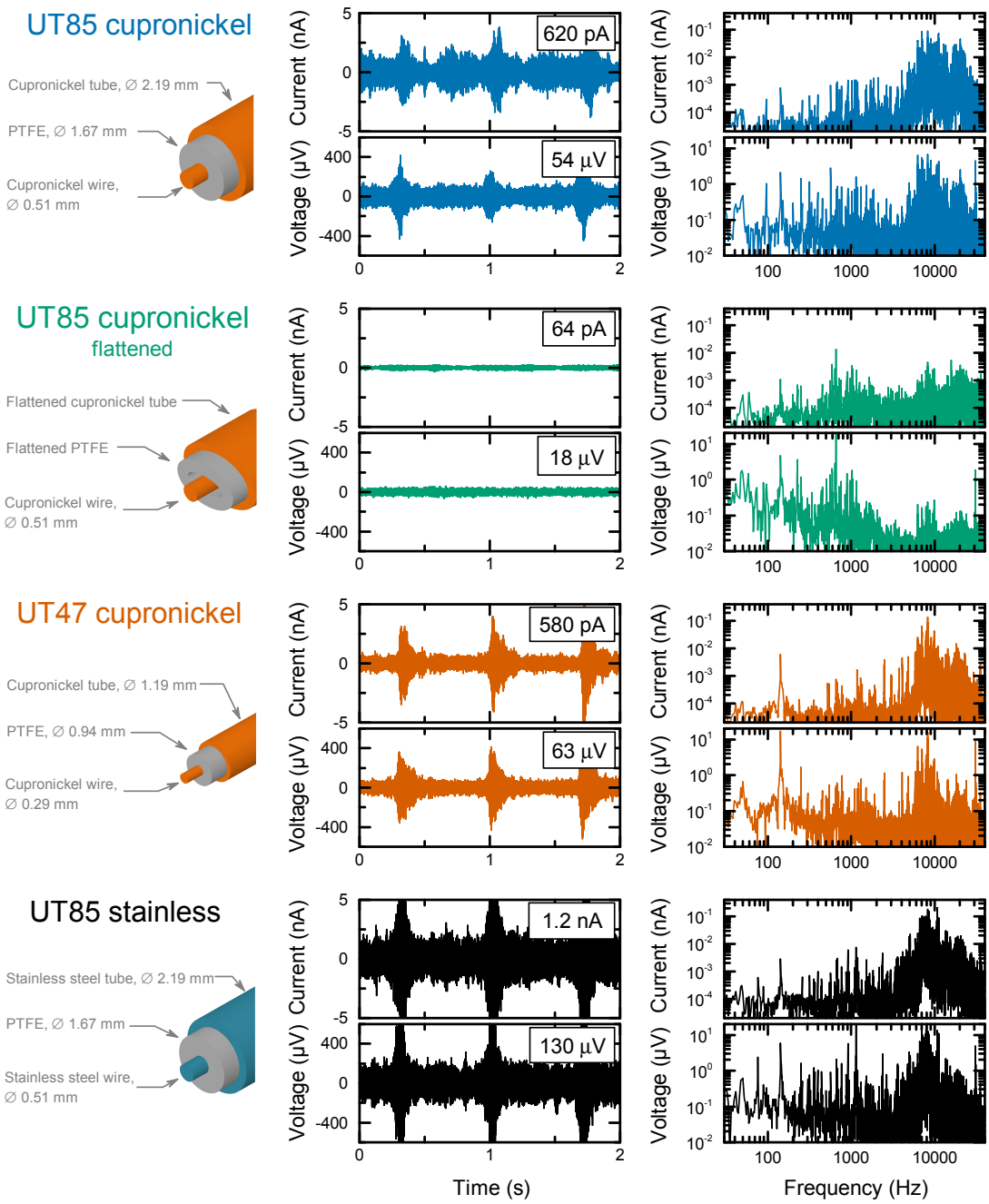

Figure 7.5: **Comparison of the noise induced in four types of semi-rigid cables.** Each row shows the noise measurements for a particular semi-rigid cable, terminating in an open-circuit at a bulkhead on the 4 K plate. A schematic of the cable is shown in the first column. The second column shows the current and voltage traces, with their RMS values written in the top-right corner of each graph. The third column show the amplitude spectra of the current and voltage traces.

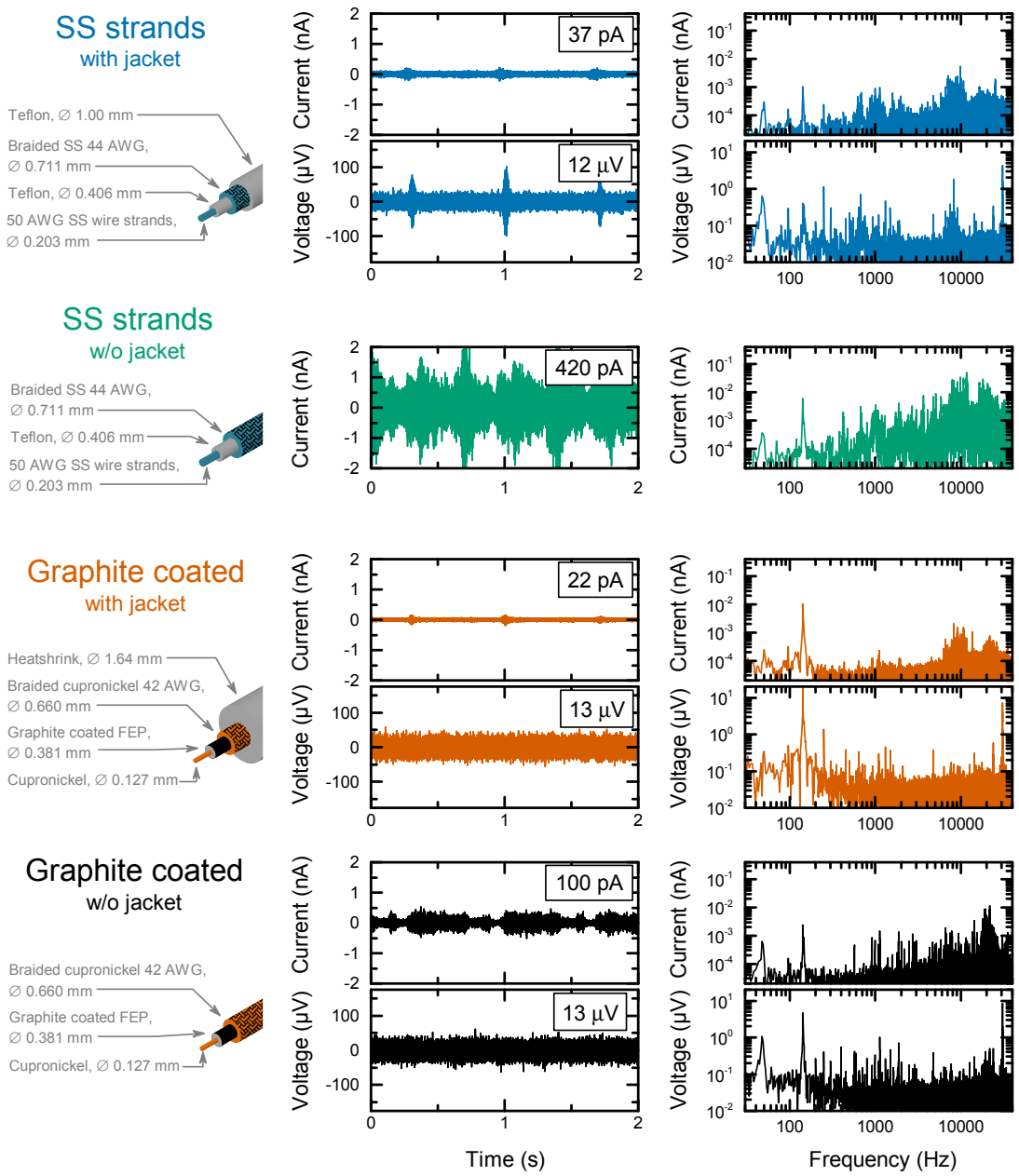

Figure 7.6: **Comparison of the noise induced in four types of flexible cables.** Each row shows the noise measurements for a particular flexible cable, terminating in an open-circuit at a bulkhead on the 4 K plate. A schematic of the cable is shown in the first column. The second column shows the current and voltage traces, where available, with their RMS values written in the top-right corner of each graph. The third column shows the amplitude spectra of the current and voltage traces.

with a vise. The entire length of the cable is flattened apart from the sections that are looped for strain relief and thermalization of the inner conductor. The purpose of the flattening is to restrict movement of the dielectric when the cable is cooled to reduce triboelectric effects. Comparing the RMS values for the current and voltage traces, the flattening yields an improvement of factor 10 and 3, respectively. From the amplitude spectra, we see that the pulse tube noise near 10 kHz has reduced by an order of magnitude for both current and voltage measurements. While the current signal for the standard cable is dominated by the spectral components in this region, the voltage noise has lower frequency contributions with comparable amplitude. The noise in the lower frequency region (30 to 3000 Hz) is not reduced by flattening the cable.

The third and fourth rows show the noise measured on a thinner cable made of the same material (UT47 cupronickel) and a cable of the same dimensions made with stainless steel (UT85 stainless), both from COAX CO. The thinner cable is the SC-119/50-CN-CN and the stainless steel cable is the SC-219/50-SS-SS. The noise amplitudes are of the same order as that of the standard UT85 cupronickel cable.

Figure 7.6 shows the noise measurements on four types of flexible cables. The first row shows the noise measured on the 'ultra miniature coaxial cable' Type SS from Lake Shore Cryotronics. This cable, as the drawing shows, has stainless steel strands for the center conductor, Teflon insulation, braided stainless steel wire as the outer conductor, and a Teflon jacket. The current and voltage noise is significantly lower as compared to the standard semi-rigid cables, with RMS values of 37 pA and 12 μV, respectively. We conjecture that the Teflon jacket serves to squeeze the braided outer conductor onto the dielectric to prevent movement within the cable when cooled. We thus take an identical cable and strip it of the jacket, as shown in the second column of the figure. The current trace has an RMS value of 420 pA, which is a factor of 11 worse than the jacketed version. The amplitude spectrum shows that this order of magnitude increase in the noise is across the entire frequency range. The record for the voltage measurement is not available for this cable.

The final cable we test is a graphite-coated cable given to us by David Goldhaber-Gordon. In their paper on vibrational noise in a pulse tube system, Pelliccione *et al.* reported the use of a cable with graphite coating on the outside of the dielectric to reduce triboelectric effects due to rubbing against the outer conductor [141]. The graphite is a conductive solid-state lubricant that is meant to reduce friction between the dielectric and outer conductor and to rapidly return any charges displaced due to triboelectrics to and from the outer conductor [139]. As stated in their paper, this cable from Calmont Wire & Cable comprises of a single 36 AWG cupronickel wire for the inner conductor and braided cupronickel for the outer conductor. The dielectric is FEP with graphite coating on the outside. This cable did not come with an outer jacket. To further validate our hypothesis that the jacket helps to reduce triboelectric effects, we made a jacket for the cable using 1.5/0.5 mm heat-shrink tubing from HellermannTyton. A schematic of the resulting cable is shown in the third column of Figure 7.6. The current noise measured is the best so far. The RMS current is 22 pA and the peak amplitude during

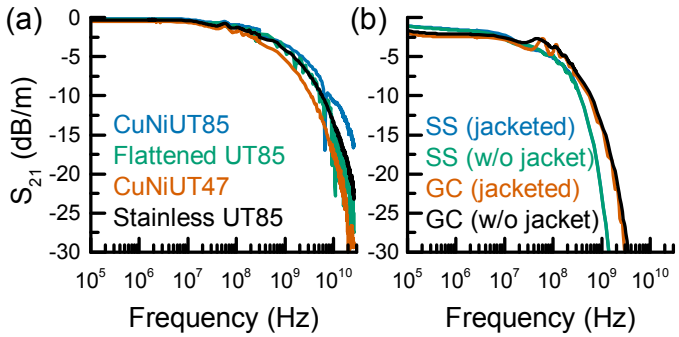

Figure 7.7: **Comparison of the frequency response of the eight cables tested.** The S_{21} measurements are plotted for the (a) four semi-rigid and (b) four flexible cables tested. The measurements are performed at room-temperature and the results are normalized to the length of the cable. 'GC' in (b) refers to the graphite-coated cable.

the chirps of the pulse tube is less than 200 pA. Note that the heat-shrink that was available to us becomes brittle at low temperatures. Although we do not know the degree to which it thermally contracts before becoming brittle, a Teflon jacket made by the cable manufacturer should improve the noise performance of the cable further.

We then test an identical cable without the heat-shrink jacket, shown in the last column of Figure 7.6. The magnitude of the noise is significantly increased, as expected, with an RMS current of 100 pA. However, the time trace looks quite different compared to the other cables tested. The amplitude spectrum reveals that the dominant noise is actually close to 20 kHz, as opposed to the usual peaks in the 5 to 10 kHz range. Surprisingly, the amplitudes of the peaks in the 5 to 10 kHz range for the jacketed and unjacketed graphite-coated cables are similar. A spectrogram of the current trace of the unjacketed cable (data not shown) reveals that the noise around 20 kHz does not appear in peaks, but as a smear, similar to the spectrogram shown in Figure 7.3(a) for the semi-rigid UT85 cupronickel cable. The same pattern is observed in comparing the voltage spectra of the jacketed and unjacketed cables. While the voltage traces look similar and both have RMS values of 13 μV, the noise near 20 kHz can be seen appearing above the noise floor for the unjacketed cable. We do not understand why the jacketing of the graphite cable reduces this 20 kHz noise, but does not affect the 5 to 10 kHz peaks.

For the reader's reference, Figure 7.7 plots the frequency response (S_{21}) of each of the cables tested at room temperature. The S_{21} measurement across the two ends of each cable is taken with the KeySight Technologies N9918A FieldFox hand-held microwave analyzer and is normalized to the length of the cable in units of dB/m. The results for the semi-rigid cables and flexible cables are plotted in sub-figure (a) and (b), respectively. From Figure 7.7(a), we see that the flattening of the UT85 cupronickel cable does not significantly worsen its frequency response. The roll-off above 1 GHz is slightly steeper and there are some ripples in the passband beyond 100 MHz. From Figure 7.7(b), we see that the frequency responses of the jacketed and unjacketed stainless steel cables are identical. This is expected, as the unjacketed cable was

obtained simply by stripping off the jacket. However, this is not the case for the graphite-coated cables. While the overall passband and roll-off are the same, the jacketed cable has some ripples beyond 30 MHz. This could be due to deformation of the dielectric during the heating of the cable to secure the heat-shrink jacket. A custom cable with a proper Teflon jacket ordered from the manufacturer should avoid this problem.

7.4 Effect of noise on qubit coherence

We then proceed to prepare the cryogen-free dilution refrigerator for measurement of the qubit device measured in Chapters 3 and 4. The purpose of this is to determine whether or not the new setup allows for successful measurement of the device, given our efforts in mitigating noise from the pulse tube. Performing coherence measurements to measure the effect of this noise on the electron spin qubit also allows for direct comparison between the two different dilution refrigerator setups. Following the investigation carried out in the previous section, we use the cables that exhibit the lowest level of noise.

The cabling used for the DC lines and broadband line are almost identical to that used in the wet fridge, as described in Chapter 2. The DC lines consist of the twisted-pair 'loom' wires with a low-frequency filter box. A UT85 silver-plated cupronickel coaxial cable is used for the broadband line. The only difference in comparison to the setup in the wet fridge is the addition of an inner-only DC block to the broadband line at the mixing chamber plate to attenuate low frequency thermal radiation. While this cable will exhibit a significant degree of triboelectric noise (Section 7.2), we currently do not have an alternative solution capable of delivering the ~ 40 GHz signals required for qubit control. As for the AC lines, we would have preferred to use the jacketed graphite-coated cable exclusively. However, due to limited supply, we were only able to use this cable for the source and drain contacts (SRC and DRN, as defined in Figure 2.3). The flattened UT85 cable was chosen for the AC gate electrodes (TGAC, DF1 and DF2).

As expected, the modified setup with low-noise cables allows us to successfully tune and measure the device in the BlueFors LD400 dry fridge, without noticeably affecting the measurement fidelity of the qubit. We thus proceed to using the electron spin qubit to probe the effective magnetic environment, as performed in Reference [46]. Recall that the technique involves measuring the coherence time of the qubit with CPMG sequences where τ, the wait time between successive refocusing pulses, is chosen to probe the power spectral density of the noise at frequency $1/\tau$. This technique allows us to probe the noise spectrum in the range 1 to 25 kHz, which coincides with the bandwidth over which we have been studying the noise from the pulse tube. A similar investigation was carried out by Britton *et al.*, where the same ESR-based spectroscopy technique was used with ~ 300 $^9Be^+$ ions in a Penning trap to probe the noise resulting from mechanical vibrations of a room-temperature bore superconducting magnet up to 1 kHz [142].

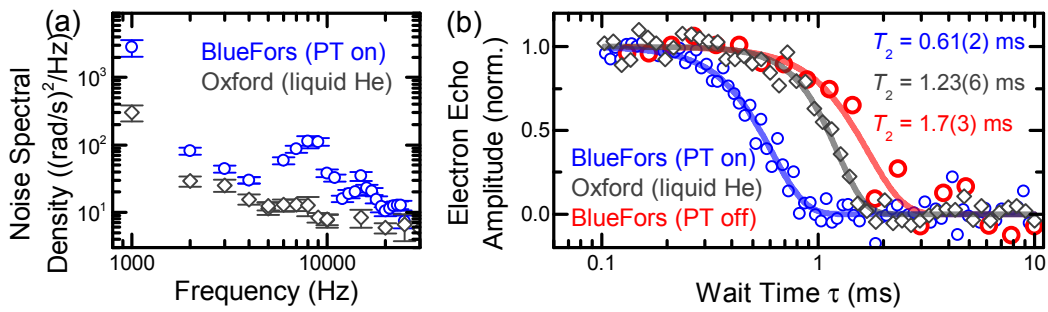

Figure 7.8: **Coherence measurements of the electron spin qubit in different dilution refrigerator setups.** In both panels, diamonds correspond to measurements taken inside an Oxford Kelvinox 100 liquid He bath dilution refrigerator, while circles correspond to measurements taken in a BlueFors LD400 cryogen free dilution refrigerator. (a) Noise spectral density of the qubit, extracted from dynamical decoupling coherence time measurements. (b) Hahn echo coherence time measurements. The two dry fridge measurements correspond to normal operation (blue) and dilution unit operating while the pulse tube is switched off (red). The time over which the pulse tube was switched off to obtain the latter measurement was ∼1 minute.

Figure 7.8(a) plots the noise spectral density as a function of frequency for this setup (blue circles). The figure also reproduces the data from Reference [46] for comparison (gray diamonds). We see a greater level of noise with the current setup in the 5 to 10 kHz region, coinciding with the peaks observed in the characterization presented earlier. As the spectral resolution of the spectroscopy technique is limited, the sharp peaks presented in the earlier sections of the chapter appear as a broad peak centered at 8 kHz. This is a first indication that the pulse tube vibrations are coupling into the effective magnetic field environment of our qubit. This is confirmed by a second experiment consisting of a quick Hahn echo T_2 measurement [20], taken with the pulse tube temporarily switched off, without interrupting the operation of the dilution unit. Figure 7.8 shows the echo decay traces with coherence times of $T_2 = 1.7(3)$ ms and $T_2 = 0.61(2)$ ms for the pulse tube being off and on, respectively. Therefore, we conclude that noise induced by the pulse tube reduces the Hahn echo T_2 by a factor ∼3. For comparison, the coherence times measured in the wet fridge was $T_2 = 1.23(6)$ ms.

There are three possible mechanisms through which the vibrations caused by the pulse tube can couple to the resonant frequency of the qubit, thus limiting its coherence. The first is based on the fact that vibrations from the pulse tube creates large current noise on the coaxial cable used for the broadband line via the triboelectric effect. The current noise created in the section of the cable above the mixing chamber plate will be attenuated by the 3 dB attenuator and the inner-only DC block at that plate before reaching the device. The attenuation of the ∼ 10 kHz noise of the pulse tube achieved by the DC block at base temperature is of order 80 dB. However, another section of cable connects the bottom of the mixing chamber plate to the transmission line on the device, designed to deliver the ∼ 40 GHz signals to the spin qubit. From the perspective of the current noise created in this portion of the cable, the lowest impedance shunting the majority of the current is exactly the short-circuit microwave antenna adjacent to the qubit. Therefore, the vibrations of the pulse tube couple into the

magnetic field experienced by the spin qubit via the creation of current noise that then flows through the antenna. Ideally, this would not have an effect on the coherence of the qubit as the magnetic field created would be exactly perpendicular to the quantization axis set by the large externally applied magnetic field. However, due to constraints in device design, a small fraction ($\sim 1/30$) of the field created by the antenna is actually parallel to the quantization axis, and can therefore contribute to dephasing. Assuming that the average power spectral density of the pulse tube current noise in the 5 to 10 kHz range is of order 10^{-1} nA^2/Hz (see Figure 7.3) and that the antenna is 100 nm from the qubit, we expect this to contribute ~ 10 (rad/s)^2/Hz in the same frequency range. This value is comparable to the observed noise power from Figure 7.8(a), indicating that this mechanism is likely to have had a significant contribution. In future experiments, an additional DC block and attenuator should be inserted directly at the device enclosure to filter pulse tube noise created from all sections of the cable. Additionally, the sample should be reoriented to eliminate the component of the field produced by the antenna that is parallel to the quantization axis.

Another mechanism that could contribute to coupling vibrations to magnetic noise is via relative displacements in an inhomogeneous magnetic field. Mechanical vibrations, of either the magnet or the cold finger to which the device is attached, would thus directly result in magnetic field noise experienced by the qubit. We have calculated that displacements on the order of few tens of μm would be sufficient to cause the experimental qubit linewidth of 4 kHz (obtained from the measured free induction decay $T_2^* = 80$ μs with the pulse tube on, data not shown). This calculation assumes that the qubit is located within $\sim$100 μm of the center of the field.

The third and final possible mechanism for coupling vibrational noise to the qubit coherence is through the creation of voltage noise via triboelectric effects on the cables connected to gate electrodes. This voltage noise would be passed on to the gates thus creating electric field noise at the position of the qubit. The resonant frequency of the qubit would then be affected via Stark shift of the hyperfine interaction and of the electron's g-factor [44]. As discussed in Section 7.3, the voltage dividers used at the room-temperature side of the pulsing lines and source-drain lines significantly reduces the amount of voltage noise created at the cable that reaches the device electrodes. From the effective impedance of the 'noise source' for the cables used in this setup, we find that voltage noise would be attenuated by at least a factor of 100. Therefore we expect gate noise in our device to be on the order of 100 nV. From the results of an experiment presented in Reference [46], we find that a gate noise $>$100 μV is needed in order to observe a similar amplitude of the noise spectral density as observed in our experiment. This evidence suggests that the more probable mechanisms coupling vibrations from the pulse tube to our qubit is through displacements of the qubits with respect to the applied magnetic field and current noise from the broadband line created by triboelectric effects.

It is interesting to note that the Hahn echo T_2 with the pulse tube switched off (Figure 7.8(b), black diamonds), is 40% longer than previously measured in the wet fridge. This could be due to additional filtering of low-frequency thermal radiation on the broadband line achieved by

the DC block at the mixing chamber plate, which was not present in the measurements of Reference [46]. The Hahn echo measurements give encouraging signs that our efforts will lead to better qubit performance, once the effects of the pulse tube noise are mitigated further.

7.5 Summary and Outlook

This chapter focused on an aspect of the scale up of a quantum computer that is often overlooked. A full-scale processor based on spin qubits in silicon would almost certainly need to be installed in a cryogen-free dilution refrigerator setup, simply for the space required for control electronics and cables. In this chapter, we characterized noise unique to the dry fridge system.

We measured electrical noise in our cables that are caused by vibrations originating from the pulse tube cryocooler. We observe the same spectral comb of peaks in both the electrical signal and in an audio recording of the chirping of the pulse tube. The magnitude of the noise is strongly temperature dependent. Our hypothesis is that the vibrations couple to the electrical signal through triboelectric effects. This is consistent with the temperature dependence of the noise amplitude given our model of the cable dielectric undergoing the greatest thermal contraction, leaving room for it to slide against the outer conductor. Flattening a semi-rigid cable or jacketing a flexible cable to reduce movement of the cable dielectric and inner conductor successfully and consistently reduces the pulse tube noise by over an order of magnitude. The two jacketed flexible cables tested perform comparably in terms of both voltage and current noise, both with a significant improvement from the standard semi-rigid cable.

Aside from introducing current and voltage noise in our lines, the pulse tube vibrations also couple into the effective magnetic field environment of our qubits. Noise spectroscopy measurements on the qubit show a noise spectrum that is qualitatively similar to the pulse tube noise spectrum. It is most likely that this coupling occurs via a combination of mechanical vibrations of the magnet or cold finger and current noise from the broadband line created by triboelectric effects. Future work to address the first issue could include improving the rigidity of the cold finger. Alternatively, a device enclosure using permanent magnets could be used to supply the quantization field instead of a superconducting magnet. In this case, vibrations would not cause relative motion between the qubit and the magnetic field. The second issue can be significantly mitigated by adding a DC block on the broadband line at the device enclosure. Additionally, reorienting the sample such that the short-circuit microwave antenna is parallel to the quantization axis will dramatically reduce the component of the field from the antenna that contributes to dephasing.

Based on the insights gained from the work in this chapter, we conclude that, with careful measurement setup design, a processor based on spin qubits in silicon can function in a cryogen-free system even in the presence of vibrations from the pulse tube.

Chapter 8

Conclusion

"*What I see in Nature is a magnificent structure that we can comprehend only very imperfectly, and that must fill a thinking person with a feeling of humility.*"

–Albert Einstein

8.1 Summary of achievements

The aim of this thesis was to advance progress towards realizing a quantum computer based on donor electron spin qubits in silicon. Following the foundational work of Pla *et al.* on a single donor, we selected five hurdles to address on the road-map towards scaling up. The device fabricated on isotopically-purified silicon enabled us to dramatically improve the fidelities of the key single qubit operations. Moving towards multi-donor operations, we realized that current proposals available in the literature pose requirements on donor placement accuracies that are too stringent for the fabrication technique that has generated our success. As a response, we proposed one technique in particular for the implementation of a two-qubit logic gate that is robust to a high degree of variability in donor separations. Moving further, we devised a scheme to achieve high-fidelity qubit transport robust to experimental imperfections, which could prove invaluable to the design of a quantum processor. Finally, we measure the spin qubit device in a cryogen-free dilution refrigerator for the first time. We show how vibrations from the system couple to the electrical signals on our cables via the triboelectric effect and report our efforts in mitigating this noise. Below we present the key results from each chapter of this thesis.

8.2 Chapter 3 - Improving single qubit operations

A donor qubit device was designed and fabricated on isotopically purified silicon substrate: the logical step towards improving the results obtained in natural silicon. This chapter reports the enhanced coherence times and fidelities for the operation of the electron spin qubit. The isotopic purification was the key to the high control fidelity achieved ($F_c \approx 99.9\%$ as measured with randomized benchmarking) and to the long qubit coherence times ($T_2 \approx 0.56$ s as measured with a 16,384-pulse CPMG sequence). The advancements made in the qubit readout and initialization fidelities came as a result of techniques devised in this thesis. The electron spin measurement fidelity, previously $\sim 97\%$, was improved to equal the control fidelity by using the nuclear spin as a resource. The initialization fidelity, previously $\sim 97\%$, also exceeded the 99.9% target using measurement induced back-action. While this chapter presented a series of successes, it also revealed an observation we do not currently understand. The limiting coherence time of the qubit appears to be dependent on the electrostatic tuning of the device. Optimizing the tuning resulted in a new record for the electron spin coherence time, $T_2 \approx 0.98$ s, as measured with a 32,768-pulse CPMG sequence.

8.3 Chapter 4 - Isotropic dynamical decoupling

The electron spin coherence time we reported in Reference [46], $T_2 \approx 0.56$ s, sparked criticism as it was measured using the CPMG sequence. In bulk NMR measurements, CPMG is known to produce anomalously long echoes that are not reflective of the true coherence times. Simulating the single spin system, we confirmed that the reported T_2 is a valid quantity. Nevertheless, this

opportunity was taken to demonstrate in the experiment that an isotropic dynamical decoupling sequence could match the performance of CPMG for the single donor electron qubit. We found that $T_2 \approx 0.45$ s for the XY128 sequence, closely matching CPMG at 16,384 pulses. The echo traces observed for lower order XY sequences, however, showed unexpected behavior. To explain these observations, we developed a model that involves the generation of a shift in the electron spin resonance frequency following the application of a microwave pulse. Our simulations of this effect matched the experiment closely in some cases, supporting the plausibility of the model.

8.4 Chapter 5 - Two-qubit gate proposal

This chapter addressed the first step towards scaling up: the development of a two-qubit logic operation. We presented two proposals for two-qubit gates that use the hyperfine interaction with the donor nuclei as a resource to produce an effective magnetic detuning between the two electrons. The first proposal is for a $\sqrt{\text{SWAP}}$ gate, where the focus is shifted from reducing the frequency of exchange oscillations, to using this detuning to switch the amplitude of exchange oscillations. This allows for a gate with an inherent fidelity of 99% to be achieved with two orders-of-magnitude tuning of the exchange interaction. The second proposal also uses the magnetic detuning provided by the nuclear spins, but improves upon the first by eliminating the need for tuning the exchange interaction. Furthermore, the susceptibility of the gate to electric field noise is reduced and its implementation is robust to a high degree of variability in inter-donor separation. This operation is the rotation of one electron spin conditional upon the state of the other. We show that the fidelity of the CROT gate can exceed 99.9% using the experimentally measured qubit linewidth. More importantly, CROT fidelities of 99% can be achieved even with two orders of magnitude variability in the magnitude of the exchange interaction. A protocol to calibrate the parameters of the system in order to demonstrate the two-qubit gate in a proof-of-principle device is also presented.

8.5 Chapter 6 - Spin transport under realistic experimental conditions

This chapter combined the concepts of linear spin chains and the adiabatic spin transport protocol to develop a complete guideline for achieving qubit transport with the donor system. A chain of donors can form an extended spin-1/2 qubit that can be used to link spin qubits separated by ~ 100 nm. Errors of ~ 5 nm in donor positioning are tolerable when operating the donors in the mode where the electrons are pulled to the interface with a gate voltage. A protocol is detailed on how to calibrate the relevant parameters required for spin transport. We showed that the system can be initialized for transport with inherent fidelity exceeding 99.99%. The calculated fidelity of the adiabatic transport protocol under realistic experimental conditions also exceeds 99.99%.

8.6 Chapter 7 - Noise in a cryogen-free dilution refrigerator

This chapter presented the first characterization of a cryogen-free dilution refrigerator setup in the context of measurement of our spin qubit devices. Large electrical noise was measured on the cables in the setup that are induced by vibrations from the pulse-tube cryocooler. An exponential dependence of the magnitude of the electrical noise on system temperature was observed. By measuring the performance of a variety of cables, we determined that triboelectric effects are responsible for coupling the vibrations to the noise on the cables. Flattening a semi-rigid cable or jacketing a flexible cable to reduce the motion of the dielectric within the cable reduces the noise by over an order of magnitude. Using the best-performing cables, we prepared the setup for measurement of the same donor qubit device measured previously in this thesis. Measurements of the electron spin qubit coherence revealed that the vibrations couple into the magnetic noise experienced by the qubit. The level observed is consistent with two models for the mechanism responsible for this coupling: (i) triboelectric effects induce current noise in the short-circuit antenna via the coaxial cable transmission line and (ii) vibrations cause relative displacements of the device with respect to the external magnetic field.

8.7 Future work and Outlook

The work of this has advanced progress in the quest to build a quantum computer based on donor spins in silicon. Indeed, numerous challenges remain.

Our work has revealed phenomena in our device that we do not currently understand. Future work by our group will include further investigations of the dependence of T_2 on device tuning as well as the shift in the electron resonance frequency following a microwave pulse. Single qubit control fidelities could also be improved, as they are currently limited by the bandwidth of the measurement instrumentation. The setup in the cryogen-free system can easily be improved using the techniques already discussed. Rotating the device such that the antenna is parallel to the externally applied field and filtering the triboelectric noise before it reaches the antenna will reveal the mechanism by which the vibrations couple to the coherence of the qubit. In regards to scaling to two qubits, an experimental effort is already underway to demonstrate the CROT gate in a proof-of-principle device. This will provide valuable information on the magnitude of the noise affecting the exchange interaction in our system. As for theoretical work, the technique we developed to decouple qubits from residual interactions warrants further attention. This may lead to the development of a robust and scalable architecture that requires very limited tuning of exchange interactions.

Perhaps the most pressing matter at hand, however, is to improve upon our technique of donor incorporation. The work of this thesis has shown that some imprecision in donor positioning can be tolerated, which means that ion implantation may continue to be suitable.

However, a more precise approach will be necessary. Techniques are currently being developed to use hybrid systems employing trapped ions to achieve implantation precisions of ~ 5 nm [143]. This technique could lead to rapid progress towards developing a donor-based quantum processor, whether it follows the architecture suggested in this thesis or other promising architectures [119]. A parallel effort towards developing the Kane quantum computer is based on scanning-tunneling microscope lithography which allows for near-atomic precision in the placement of donors [144], though the technology has not yet reached the stage where single donors can be incorporated reliably [145]. An alternative route has seen rapid progress in the past three years, where a single electron is confined to a gate-defined quantum dot fabricated with the same processes used in this thesis [52, 146]. As both the quantum dot and donor implementations have their advantages, it is likely that future work will include the development of hybrid systems [108]. This speaks to perhaps one of the most exciting aspects of research in quantum computing: the field is wide open.

References

[1] Waldrop, M. M. *Nature News* **530**(7589), 144 (2016).

[2] Feynman, R. *International journal of theoretical physics* **21**(6), 467–488 (1982).

[3] Deutsch, D. In *Proceedings of the Royal Society of London A: Mathematical, Physical and Engineering Sciences*, volume 400, 97–117. The Royal Society, (1985).

[4] Shor, P. W. In *Proc. 35th Annu. Symp. on the Foundations of Computer Science*, 124–134. IEEE Computer Society Press, Los Alamitos, California, (1994).

[5] Shor, P. W. *Physical review A* **52**(4), R2493 (1995).

[6] Divincenzo, D. P. *Mesoscopic Electron Transport*, chapter Topics in Quantum Computers, 657–677. Springer Netherlands, Dordrecht (1997).

[7] Kok, P., Munro, W. J., Nemoto, K., Ralph, T. C., Dowling, J. P., and Milburn, G. J. *Reviews of Modern Physics* **79**(1), 135 (2007).

[8] O'Brien, J. L. *Science* **318**(5856), 1567–1570 Dec (2007).

[9] Monz, T., Schindler, P., Barreiro, J. T., Chwalla, M., Nigg, D., Coish, W. A., Harlander, M., Hänsel, W., Hennrich, M., and Blatt, R. *Physical Review Letters* **106**(13), 130506 (2011).

[10] Monz, T., Nigg, D., Martinez, E. A., Brandl, M. F., Schindler, P., Rines, R., Wang, S. X., Chuang, I. L., and Blatt, R. *arXiv:1507.08852* (2015).

[11] Majer, J., Chow, J., Gambetta, J., Koch, J., Johnson, B., Schreier, J., Frunzio, L., Schuster, D., Houck, A., Wallraff, A., et al. *Nature* **449**(7161), 443–447 (2007).

[12] Ristè, D., Poletto, S., Huang, M.-Z., Bruno, A., Vesterinen, V., Saira, O.-P., and DiCarlo, L. *Nature communications* **6**, 6983 (2015).

[13] Córcoles, A., Magesan, E., Srinivasan, S. J., Cross, A. W., Steffen, M., Gambetta, J. M., and Chow, J. M. *Nature communications* **6**, 6979 (2015).

[14] Kelly, J., Barends, R., Fowler, A., Megrant, A., Jeffrey, E., White, T., Sank, D., Mutus, J., Campbell, B., Chen, Y., et al. *Nature* **519**(7541), 66–69 (2015).

[15] Benjamin, S. and Kelly, J. *Nature materials* **14**(6), 561–563 (2015).

[16] Hanson, R. and Burkard, G. *Physical review letters* **98**(5), 050502 (2007).

[17] Kim, D., Shi, Z., Simmons, C., Ward, D., Prance, J., Koh, T. S., Gamble, J. K., Savage, D., Lagally, M., Friesen, M., et al. *Nature* **511**(7507), 70–74 (2014).

[18] Eng, K., Ladd, T. D., Smith, A., Borselli, M. G., Kiselev, A. A., Fong, B. H., Holabird, K. S., Hazard, T. M., Huang, B., Deelman, P. W., et al. *Science advances* **1**(4), e1500214 (2015).

[19] Gerlach, W. and Stern, O. *Zeitschrift für Physik A Hadrons and Nuclei* **9**(1), 349–352 (1922).

[20] Hahn, E. *Physical Review* **80**(4), 580–594 Nov (1950).

[21] Viola, L., Knill, E., and Lloyd, S. *Phys. Rev. Lett.* **82**(12), 2417 (1999).

[22] Álvarez, G. A. and Suter, D. *Physical Review Letters* **107**(23) Nov (2011).

[23] Meiboom, S. and Gill, D. *Review of Scientific Instruments* **29**(8), 688 (1958).

[24] Kane, B. E. *Nature* **393**(6681), 133–137 May (1998).

[25] Tyryshkin, A. M., Tojo, S., Morton, J. J. L., Riemann, H., Abrosimov, N. V., Becker, P., Pohl, H.-J., Schenkel, T., Thewalt, M. L. W., Itoh, K. M., and Lyon, S. A. *Nature Mater.* **11**(2), 143–147 Feb (2012).

[26] Hollenberg, L., Greentree, A., Fowler, A., and Wellard, C. *Phys. Rev. B* **74**, 045311 Jul (2006).

[27] Hill, C., Hollenberg, L., Fowler, A., Wellard, C., Greentree, A., and Goan, H. *Phys. Rev. B* **72**, 45350 Jul (2005).

[28] Vrijen, R., Yablonovitch, E., Wang, K., Jiang, H., Balandin, A., Roychowdhury, V., Mor, T., and DiVincenzo, D. *Phys. Rev. A* **62**, 12306 Jun (2000).

[29] Pla, J. J., Tan, K. Y., Dehollain, J. P., Lim, W. H., Morton, J. J. L., Jamieson, D. N., Dzurak, A. S., and Morello, A. *Nature* **489**(7417), 541–545 Sep (2012).

[30] Kohn, W. and Luttinger, J. *Phys. Rev.* **98**(4), 915–922 May (1955).

[31] Morello, A., Pla, J., Zwanenburg, F., Chan, K., Tan, K., Huebl, H., Möttönen, M., Nugroho, C., Yang, C., van Donkelaar, J., et al. *Nature* **467**(7316), 687–691 Oct (2010).

[32] Pla, J. J., Tan, K. Y., Dehollain, J. P., Lim, W. H., Morton, J. J. L., Zwanenburg, F. A., Jamieson, D. N., Dzurak, A. S., and Morello, A. *Nature* **496**(7445), 334–338 Apr (2013).

[33] Morello, A., Escott, C., Huebl, H., Willems van Beveren, L., Hollenberg, L., Jamieson, D., Dzurak, A., and Clark, R. *Phys. Rev. B* **80**(8), 81307 Aug (2009).

[34] Beenakker, C. *Physical Review B* **44**, 1646–1656 Jul (1991).

[35] Kastner, M. *Reviews of Modern Physics* **64**(3), 849–858 Jul (1992).

[36] Jamieson, D., Yang, C., Hopf, T., Hearne, S., Pakes, C., Prawer, S., Mitic, M., Gauja, E., Andresen, S., Hudson, F., et al. *Appl. Phys. Lett.* **86**, 202101 Oct (2005).

[37] Elzerman, J., Hanson, R., van Beveren, L., Witkamp, B., Vandersypen, L., and Kouwenhoven, L. *Nature* **430**(6998), 431–435 Jul (2004).

[38] Dehollain, J. P., Pla, J. J., Siew, E., Tan, K. Y., Dzurak, A. S., and Morello, A. *Nanotechnology* **24**(1), 015202 Jan (2013).

[39] Sarovar, M., Young, K. C., Schenkel, T., and Whaley, K. B. *Physical Review B* **78**(24), 245302 (2008).

[40] Deal, B. E. *Journal of the Electrochemical Society* **121**(6), 198C–205C (1974).

[41] Cheng, Y. *Progress in Surface Science* **8**(5), 181–218 (1977).

[42] McCamey, D., Francis, M., McCallum, J., Hamilton, A., Greentree, A., and Clark, R. *Semiconductor science and technology* **20**(5), 363 (2005).

[43] Brower, K. *Applied physics letters* **53**(6), 508–510 (1988).

[44] Laucht, A., Muhonen, J. T., Mohiyaddin, F. A., Kalra, R., Dehollain, J. P., Freer, S., Hudson, F. E., Veldhorst, M., Rahman, R., Klimeck, G., Itoh, K. M., Jamieson, D. N., McCallum, J. C., Dzurak, A. S., and Morello, A. *Science Advances* **1**(3) (2015).

[45] Martinis, J., Devoret, M., and Clarke, J. *Physical Review B* **35**(10), 4682–4698 Apr (1987).

[46] Muhonen, J. T., Dehollain, J. P., Laucht, A., Hudson, F. E., Kalra, R., Sekiguchi, T., Itoh, K. M., Jamieson, D. N., McCallum, J. C., Dzurak, A. S., et al. *Nature Nanotech* **9**(12), 986–991 Oct (2014).

[47] Muhonen, J., Laucht, A., Simmons, S., Dehollain, J., Kalra, R., Hudson, F., Freer, S., Itoh, K. M., Jamieson, D., McCallum, J., et al. *Journal of Physics: Condensed Matter* **27**(15), 154205 (2015).

[48] Knill, E., Leibfried, D., Reichle, R., Britton, J., Blakestad, R., Jost, J., Langer, C., Ozeri, R., Seidelin, S., and Wineland, D. *Physical Review A* **77**(1) Jan (2008).

[49] Gottesman, D. In *Proceedings of the XXII International Colloquium on Group Theoretical Methods in Physics,* Corney, S. P., Delbourgo, R., and D., J. P., editors, 32–43 (International Press, Cambridge, MA, 1999).

[50] Fowler, A. G., Mariantoni, M., Martinis, J. M., and Cleland, A. N. *Phys. Rev. A* **86**(3) Sep (2012).

[51] Möttönen, M., Tan, K., Chan, K., Zwanenburg, F., Lim, W., Escott, C., Pirkkalainen, J.-M., Morello, A., Yang, C., van Donkelaar, J., et al. *Physical Review B* **81**(16), 161304 (2010).

[52] Veldhorst, M., Yang, C. H., Hwang, J. C. C., Huang, W., Dehollain, J. P., Muhonen, J. T., Simmons, S., Laucht, A., Hudson, F. E., Itoh, K. M., Morello, A., , and Dzurak, A. S. *Nature* **526**, 410–14 (2015).

[53] Dehollain, J. P., Simmons, S., Muhonen, J. T., Kalra, R., Laucht, A., Hudson, F., Itoh, K. M., Jamieson, D. N., McCallum, J. C., Dzurak, A. S., et al. *Nature nanotechnology* (2015).

[54] Kalra, R., Laucht, A., Hill, C. D., and Morello, A. *Phys. Rev. X* **4**, 021044 Jun (2014).

[55] Ashhab, S. and Nori, F. *Physical Review A* **82**(6), 062103 (2010).

[56] Pechen, A., Ilin, N., Shuang, F., and Rabitz, H. *Physical Review A* **74**(5), 052102 (2006).

[57] Wiseman, H. M. *Nature* **470**(7333), 178–179 (2011).

[58] Biercuk, M. J., Uys, H., VanDevender, A. P., Shiga, N., Itano, W. M., and Bollinger, J. J. *Physical Review A* **79**(6), 062324 (2009).

[59] Purcell, E. M., Torrey, H., and Pound, R. V. *Physical review* **69**(1-2), 37 (1946).

[60] Bloch, F. *Physical review* **70**(7-8), 460 (1946).

[61] Wrachtrup, J., Von Borczyskowski, C., Bernard, J., Orritt, M., and Brown, R. *Nature* **363**, 244–245 (1993).

[62] Köhler, J., Disselhorst, J., Donckers, M., Groenen, E., Schmidt, J., and Moerner, W. *Nature* **363**, 242–244 (1993).

[63] Dementyev, A., Li, D., MacLean, K., and Barrett, S. *Physical Review B* **68**(15), 153302 (2003).

[64] Watanabe, S. and Sasaki, S. *Japanese journal of applied physics* **42**(11B), L1350 (2003).

[65] Franzoni, M. B. and Levstein, P. R. *Physical Review B* **72**(23), 235410 (2005).

[66] Li, D., Dementyev, A., Dong, Y., Ramos, R., and Barrett, S. *Physical review letters* **98**(19), 190401 (2007).

[67] Li, D., Dong, Y., Ramos, R., Murray, J., MacLean, K., Dementyev, A., and Barrett, S. *Physical Review B* **77**(21), 214306 (2008).

[68] Watanabe, S., Harada, J., Sasaki, S., and Hirayama, Y. *Journal of Magnetism and Magnetic Materials* **310**(2, Part 3), 2167 – 2169 (2007). Proceedings of the 17th International Conference on MagnetismThe International Conference on Magnetism.

[69] Ridge, C. D., O'Donnell, L. F., and Walls, J. D. *Physical Review B* **89**(2), 024404 (2014).

[70] Mohiyaddin, F. A., Rahman, R., Kalra, R., Klimeck, G., Hollenberg, L. C. L., Pla, J. J., Dzurak, A. S., and Morello, A. *Nano Lett.* **13**(5), 1903–1909 May (2013).

[71] Pla, J. J., Mohiyaddin, F. A., Tan, K. Y., Dehollain, J. P., Rahman, R., Klimeck, G., Jamieson, D. N., Dzurak, A. S., and Morello, A. *Physical review letters* **113**(24), 246801 (2014).

[72] Souza, A. M., Álvarez, G. A., and Suter, D. *Physical Review Letters* **106**(24), 240501 (2011).

[73] Gullion, T., Baker, D. B., and Conradi, M. S. *Journal of Magnetic Resonance (1969)* **89**(3), 479–484 Oct (1990).

[74] Vandersypen, L. M. and Chuang, I. L. *Reviews of modern physics* **76**(4), 1037 (2005).

[75] Cummins, H. K., Llewellyn, G., and Jones, J. A. *Physical Review A* **67**(4), 042308 (2003).

[76] Alvarez, G. A., Ajoy, A., Peng, X., and Suter, D. *Physical Review A* **82**(4), 042306 (2010).

[77] Witzel, W. and Sarma, S. D. *Physical Review B* **76**(24), 241303 (2007).

[78] Tyryshkin, A., Wang, Z.-H., Zhang, W., Haller, E., Ager, J., Dobrovitski, V., and Lyon, S. *arXiv preprint arXiv:1011.1903* (2010).

[79] Medford, J., Barthel, C., Marcus, C., Hanson, M., Gossard, A., et al. *Physical review letters* **108**(8), 086802 (2012).

[80] Rowan, L., Hahn, E., and Mims, W. *Physical Review* **137**(1A), A61 (1965).

[81] Laucht, A., Kalra, R., Simmons, S., Dehollain, J. P., Muhonen, J. T., Mohiyaddin, F. A., Freer, S., Hudson, F. E., Itoh, K. M., Jamieson, D. N., et al. *arXiv preprint arXiv:1603.04800* (2016).

[82] Bremner, M. J., Dawson, C. M., Dodd, J. L., Gilchrist, A., Harrow, A. W., Mortimer, D., Nielsen, M. A., and Osborne, T. J. *Physical review letters* **89**(24), 247902 (2002).

[83] Hill, C. *Physical Review Letters* **98**(18), 180501 May (2007).

[84] Koiller, B., Hu, X., and Das Sarma, S. *Phys. Rev. Lett.* **88**, 027903 Dec (2001).

[85] Wellard, C. J., Hollenberg, L. C. L., Parisoli, F., Kettle, L. M., Goan, H.-S., McIntosh, J. A. L., and Jamieson, D. N. *Phys. Rev. B* **68**, 195209 Nov (2003).

[86] Meunier, T., Calado, V. E., and Vandersypen, L. M. K. *Phys. Rev. B* **83**, 121403 Mar (2011).

[87] Pioro-Ladrière, M., Obata, T., Tokura, Y., Shin, Y.-S., Kubo, T., Yoshida, K., Taniyama, T., and Tarucha, S. *Nature Physics* **4**(10), 776–779 August (2008).

[88] Luis, F., Repollés, A., Martínez-Pérez, M. J., Aguilà, D., Roubeau, O., Zueco, D., Alonso, P. J., Evangelisti, M., Camón, A., Sesé, J., Barrios, L. A., and Aromí, G. *Phys. Rev. Lett.* **107**, 117203 Sep (2011).

[89] Foletti, S., Bluhm, H., Mahalu, D., Umansky, V., and Yacoby, A. *Nature Physics* **5**(12), 903–908 October (2009).

[90] Beaudoin, F. and Coish, W. A. *Phys. Rev. B* **88**, 085320 Aug (2013).

[91] Plantenberg, J. H., de Groot, P. C., Harmans, C. J. P. M., and Mooij, J. E. *Nature (London)* **447**(7146), 836–9 June (2007).

[92] Jelezko, F., Gaebel, T., Popa, I., Domhan, M., Gruber, A., and Wrachtrup, J. *Phys. Rev. Lett.* **93**, 130501 Sep (2004).

[93] Culcer, D., Hu, X., and Das Sarma, S. *Applied Physics Letters* **95**(7), 073102–073102 (2009).

[94] Wang, Y. E., Tankasala, A., Hollenberg, L. C., Klimeck, G., Simmons, M. Y., and Rahman, R. *arXiv preprint arXiv:1507.08009* (2015).

[95] Rahman, R., Wellard, C. J., Bradbury, F. R., Prada, M., Cole, J. H., Klimeck, G., and Hollenberg, L. C. L. *Phys. Rev. Lett.* **99**, 036403 Jul (2007).

[96] Slichter, C. P. *Phys. Rev.* **99**, 479–480 Jul (1955).

[97] Jérome, D. and Winter, J. M. *Phys. Rev.* **134**, A1001–A1007 May (1964).

[98] Marko, J. *Phys. Lett. A* **27**(2), 119–120 (1968).

[99] Shimizu, T. *J. Phys. Soc. Jpn.* **25**(4), 1021–1024 (1968).

[100] Pifer, J. H. *Phys. Rev. B* **32**, 7091–7097 Dec (1985).

[101] Petta, J. R. *Science* **309**(5744), 2180–2184 Sep (2005).

[102] Burkard, G., Loss, D., and Divincenzo, D. P. *Physical Review B* **59**(3), 2070–2078 (1999).

[103] Tan, K. Y., Chan, K. W., Mottonen, M., Morello, A., Yang, C., Donkelaar, J. v., Alves, A., Pirkkalainen, J.-M., Jamieson, D. N., Clark, R. G., and et al. *Nano Lett.* **10**(1), 1115 Jan (2010).

[104] Vasilev, G. S. and Vitanov, N. V. *Phys. Rev. A* **70**, 053407 Nov (2004).

[105] Abe, E., Tyryshkin, A. M., Tojo, S., Morton, J. J. L., Witzel, W. M., Fujimoto, A., Ager, J. W., Haller, E. E., Isoya, J., Lyon, S. A., Thewalt, M. L. W., and Itoh, K. M. *Phys. Rev. B* **82**, 121201 Sep (2010).

[106] Persaud, A., Park, S., Liddle, J., Schenkel, T., Bokor, J., and Rangelow, I. *Nano letters* **5**(6), 1087–1091 (2005).

[107] Alves, A., Newnham, J., van Donkelaar, J., Rubanov, S., McCallum, J., and Jamieson, D. *Nanotechnology* **24**(14), 145304 (2013).

[108] Srinivasa, V., Xu, H., and Taylor, J. M. *Phys. Rev. Lett.* **114**, 226803 Jun (2015).

[109] Lim, W. H., Zwanenburg, F. A., Huebl, H., Mttnen, M., Chan, K. W., Morello, A., and Dzurak, A. S. *Applied Physics Letters* **95**(24), – (2009).

[110] Dial, O. E., Shulman, M. D., Harvey, S. P., Bluhm, H., Umansky, V., and Yacoby, A. *Phys. Rev. Lett.* **110**, 146804 Apr (2013).

[111] Stopa, M. and Marcus, C. M. *Nano Letters* **8**(6), 1778–1782 (2008).

[112] Nielsen, E., Young, R. W., Muller, R. P., and Carroll, M. S. *Phys. Rev. B* **82**, 075319 Aug (2010).

[113] Ramon, G. *Physical Review B* **84**(15), 1–9 October (2011).

[114] Rahman, R., Nielsen, E., Muller, R. P., and Carroll, M. S. *Phys. Rev. B* **85**, 125423 Mar (2012).

[115] Nickerson, N. H., Li, Y., and Benjamin, S. C. *Nat. Commun.* **4**, 1756 Apr (2013).

[116] Taylor, J. M., Engel, H.-A., Dr, W., Yacoby, A., Marcus, C. M., Zoller, P., and Lukin, M. D. *Nature Physics* **1**(3), 177–183 Dec (2005).

[117] Greentree, A., Cole, J., Hamilton, A., and Hollenberg, L. *Phys. Rev. B* **70**(23) Dec (2004).

[118] Rahman, R., Park, S. H., Cole, J. H., Greentree, A. D., Muller, R. P., Klimeck, G., and Hollenberg, L. C. L. *Phys. Rev. B* **80**, 035302 Jul (2009).

[119] Tosi, G., Mohiyaddin, F. A., Tenberg, S. B., Rahman, R., Klimeck, G., and Morello, A. *arXiv preprintarXiv:1509.08538* (2015).

[120] Trifunovic, L., Pedrocchi, F. L., and Loss, D. *Phys. Rev. X* **3**, 041023 Dec (2013).

[121] Tosi, G., Mohiyaddin, F. A., Huebl, H., and Morello, A. *AIP Advances* **4**(8), 087122 Aug (2014).

[122] Hu, X., Liu, Y., and Nori, F. *Phys. Rev. B* **86**(3) Jul (2012).

[123] Friesen, M., Biswas, A., Hu, X., and Lidar, D. *Phys. Rev. Lett.* **98**, 230503 Jun (2007).

[124] Bethe, H. *Zeitschrift fr Physik* **71**(3-4), 205–226 (1931).

[125] Meier, F., Levy, J., and Loss, D. *Phys. Rev. Lett.* **90**, 047901 Jan (2003).

[126] Oh, S., Shim, Y.-P., Fei, J., Friesen, M., and Hu, X. *Physical Review A* **87**(2) Feb (2013).

[127] Oh, S., Friesen, M., and Hu, X. *Phys. Rev. B* **82**, 140403 Oct (2010).

[128] Oh, S., Wu, L.-A., Shim, Y.-P., Fei, J., Friesen, M., and Hu, X. *Phys. Rev. A* **84**, 022330 Aug (2011).

[129] Oh, S., Shim, Y.-P., Fei, J., Friesen, M., and Hu, X. *Phys. Rev. B* **85**, 224418 Jun (2012).

[130] Ziegler, J. F., Ziegler, M., and Biersack, J. *Nucl. Instrum. Meth. B* **268**(11-12), 1818 Jun (2010).

[131] Mohiyaddin, F. A., Kalra, R., Laucht, A., Rahman, R., Klimeck, G., and Morello, A. *arXiv preprint arXiv:1602.07058* (2016).

[132] Calderón, M. J., Koiller, B., Hu, X., and Das Sarma, S. *Phys. Rev. Lett.* **96**, 096802 Mar (2006).

[133] Rahman, R., Park, S. H., Boykin, T. B., Klimeck, G., Rogge, S., and Hollenberg, L. C. L. *Phys. Rev. B* **80**, 155301 Oct (2009).

[134] Laucht, A., Kalra, R., Muhonen, J. T., Dehollain, J. P., Mohiyaddin, F. A., Hudson, F., McCallum, J. C., Jamieson, D. N., Dzurak, A. S., and Morello, A. *Appl. Phys. Lett.* **104**(9), 092115 Mar (2014).

[135] Harvey-Collard, P., Jacobson, N. T., Rudolph, M., Dominguez, J., Eyck, G. A. T., Wendt, J. R., Pluym, T., Gamble, J. K., Lilly, M. P., Pioro-Ladrière, M., et al. *arXiv:1512.01606* (2015).

[136] Yuge, T., Sasaki, S., and Hirayama, Y. *Physical Review Letters* **107**(17) Oct (2011).

[137] Tomaru, T., Suzuki, T., Haruyama, T., Shintomi, T., Yamamoto, A., Koyama, T., and Li, R. *Cryogenics* **44**(5), 309–317 (2004).

[138] Riabzev, S., Veprik, A., Vilenchik, H., and Pundak, N. *Cryogenics* **49**(1), 1–6 (2009).

[139] Ong, P. *European Journal of Physics* **8**(4), 280 (1987).

[140] Angus, S., Ferguson, A., Dzurak, A., and Clark, R. *Applied Physics Letters* **92**(11), 112103 (2008).

[141] Pelliccione, M., Sciambi, A., Bartel, J., Keller, A. J., and Goldhaber-Gordon, D. *Review of Scientific Instruments* **84**(3), 033703 (2013).

[142] Britton, J., Bohnet, J., Bollinger, J., Sawyer, B., Uys, H., and Biercuk, M. *arXiv:1512.00801* (2015).

[143] Jacob, G., Groot-Berning, K., Wolf, S., Ulm, S., Couturier, L., Dawkins, S. T., Poschinger, U. G., Schmidt-Kaler, F., and Singer, K. *arXiv preprint arXiv:1512.00347* (2015).

[144] Fuechsle, M., Miwa, J. A., Mahapatra, S., Ryu, H., Lee, S., Warschkow, O., Hollenberg, L. C. L., Klimeck, G., and Simmons, M. Y. *Nature Nanotech.* **7**(4), 242–246 Feb (2012).

[145] House, M., Kobayashi, T., Weber, B., Hile, S., Watson, T., van der Heijden, J., Rogge, S., and Simmons, M. *Nature communications* **6**, 8848 (2015).

[146] Veldhorst, M., Hwang, J. C. C., Yang, C. H., Leenstra, A. W., de Ronde, B., Dehollain, J. P., Muhonen, J. T., Hudson, F. E., Itoh, K. M., Morello, A., , and Dzurak, A. S. *Nature nanotechnology* **9**(12), 981–85 (2014).